UTS UNIVERSITY OF TECHNOLOGY SYDNEY

Fabrication and Characterisation of Epitaxial Graphene on SiC/Si for High-Frequency Applications

by David Alexander Katzmarek

Thesis submitted in fulfilment of the requirements for the degree of

Doctor of Philosophy

under the supervision of

Prof. Francesca Iacopi (Principal Supervisor)
Prof. Yang Yang (Co-Supervisor)

University of Technology Sydney
School of Electrical and Data Engineering
Faculty of Engineering and Information Technology

February 2023

Certificate of Original Authorship

I, David Alexander Katzmarek, declare that this thesis is submitted in fulfilment of the requirements for the award of Doctor of Philosophy in the School of Electrical and Data Engineering, Faculty of Engineering and Information Technology, at the University of Technology Sydney.

This thesis is wholly my own work unless otherwise referenced or acknowledged. In addition, I certify that all information sources and literature used are indicated in the thesis.

This document has not been submitted for qualifications at any other academic institution.

This research is supported by the Australian Government Research Training Program.

Signature:

Production Note:
Signature removed prior to publication.

Date: 7th February 2023

Abstract

Graphene attracts considerable attention for electromagnetic (EM) applications due to its electrical and plasmonic properties and the possibility of dynamic tunability with direct current (DC) to light sources.

In order to extract the electrical characteristics of graphene at high frequencies, a straightforward method to pattern graphene, preferably without the need for material etching, is necessary. Hence, this work introduces a methodology for directly synthesising planar micro and nanopatterned epitaxial graphene (EG) on SiC/Si wafers by pre-patterning a Ni/Cu metal catalyst alloy via lift-off processes. This method is compatible with electron-beam lithography (EBL) and ultraviolet (UV)-lithography, and features down to ∼200 nm pitch can be realised.

High-frequency characteristics of this graphene platform were evaluated using metal coplanar waveguides (CPWs) that employed patterned graphene as a shunt between the centre and ground planes. A strong frequency-dependent behaviour of the graphene's sheet resistance was observed. This is attributed to the progressively smaller influence of small-scale defects, such as grain sizes, at higher frequencies. While graphene and other two-dimensional (2D) materials notoriously lead to high contact resistances, this study stresses the importance of obtaining a high-quality graphene-metal contact for high-frequency applications.

In order to characterise the intrinsic electrical properties of large-area graphene without consideration of the electrical contacts, this work also devises a methodology that uses K_a-band rectangular waveguide adaptors. The high-frequency sheet impedance was extracted from S-parameter measurements using an ABCD-Matrix model. The results indicate a ∼2-fold higher sheet resistance compared to DC measurements. However, the monotonic decrease for increasing frequencies is once again confirmed.

Finally, THz EM antennas and metasurface absorbers based on the EG on SiC/Si platform were designed and numerically simulated. Results confirm the dynamic tunability of the resonance frequency by varying graphene's Fermi level and the potential for antenna miniaturisation. However, the simulations show that a trade-off must be made as graphene antennas tend to provide lower radiation efficiencies and gains compared to thicker metallic ones. At the same time, employing graphene in absorbing structures, such as SiC-based Salisbury screens and gratings, demonstrates significant absorptivity enhancement and enables the dynamic tuning of resonance and absorptivity. These examples give a perspective of how graphene could benefit future EM devices. However, note that for a truly predictive capability,

more specific input data for the numerical model deriving from measured characteristics of EG on SiC/Si at THz frequencies (or any other type of considered graphene) will be necessary.

Acknowledgment

I would like to express my most profound appreciation to my principal supervisor, Prof. Francesca Iacopi, for the opportunity to join the Integrated Nano Systems research group and for her continuous support during my PhD journey. Her exceptional advice, encouragement, and guidance were vital for realising my PhD thesis. I would also like to extend my heartfelt thanks to my co-supervisors, Prof. Richard W. Ziolkowski and Prof. Yang Yang, for their invaluable support during my PhD studies. Their ongoing advice was essential for the progress of my research.

I extend my gratitude to our collaborators, Prof. Kourosh Kalantar-Zadeh and Dr Mohammad Bagher Ghasemian, as well as Prof. Stefan A. Maier and Andrea Mancini, for their support and insightful discussions. Special thanks to the technical support staff: Geoffrey McCredie, Dr James Bishop, and Dr Blake Regan for the technical support at the Vacuum Lab and Cleanroom unit within the Faculty of Science; Dr Linda Xiao and Dr Alexander Angeloski for their help and expertise with chemistry-related works; and Herbert Yuan for the training and technical assistance at the Microstructural Analysis Unit at UTS. Furthermore, my thanks go to Lang Chen, Jingyu Lin, and Jiexin Lai for their help with conducting electromagnetic measurements at the Wireless Communications Lab at Tech Lab.

I also acknowledge the University of Technology Sydney and the Australian Government, Department of Education and Training, for their support through the International Research Training Program. Moreover, I would like to acknowledge support from the Australian Research Council through the Centre of Excellence in Transformative Meta-Optical Systems.

I would like to extend my thanks to past and present colleagues within the Integrated Nano Systems research group: Dr Aiswarya Pradeepkumar, Dr Iryna Khodasevych, Dr Patrick Rufangura, Dr Shaikh Faisal, and Dr Mojtaba Amjadipour for their continuous support and encouraging discussions shared during my PhD studies.

I am also grateful for the academic assistance and administrative support provided by the administration team of the School of Electrical and Data Engineering, in particular, Razia Osman, for her support and friendship at and outside the university.

I am incredibly grateful to my fellow PhD students and friends Fernanda Oliveira, Derick Lima, Milad Nonahal, Wafa A. Soomro, and Roumani Alabd, as well as the friends that I have made outside of university during my PhD journey and their tremendous support, motivation, and good spirits during the trying times of the COVID-19 pandemic.

Lastly, I would like to express my sincerest gratitude to my family for their unconditional love and support throughout my PhD and my entire life.

List of Publications

1. **D. A. Katzmarek**, A. Pradeepkumar, R. W. Ziolkowski, and F. Iacopi, “Review of graphene for the generation, manipulation, and detection of electromagnetic fields from microwave to terahertz,” *2D Materials*, vol. 9, no. 2, Mar. 2022, doi: 10.1088/2053-1583/ac59d1
2. **D. A. Katzmarek,** Y. Yang, M. B. Ghasemian, K. Kalantar-Zadeh, R. W. Ziolkowski and F. Iacopi, "Characteristics of Epitaxial Graphene on SiC/Si Substrates in the Radio Frequency Spectrum," in *IEEE Electron Device Letters*, vol. 44, no. 2, pp. 297-300, Feb. 2023, doi: 10.1109/LED.2022.3230358
   (Nominated as Editors’ Pick)
3. **D. A. Katzmarek**, A. Mancini, S. A. Maier, and F. Iacopi, “Direct synthesis of nanopatterned epitaxial graphene on silicon carbide,” in *Nanotechnology*, vol. 34, no. 40, 405302 , Jul. 2023, doi: 10.1088/1361-6528/ace369

Table of Contents

List of Figures

List of Tables

List of Acronyms

2D	Two-dimensional
3C-SiC	Cubic silicon carbide
3D	Three-dimensional
ADS	Advanced Design System
AFM	Atomic force microscopy
BG	Bandgap
BW	Bandwidth
CMOS	Complementary metal-oxide-semiconductor
CNT	Carbon nanotubes
CPW	Coplanar waveguide
CVD	Chemical vapour deposition
DC	Direct current
DI	Deionised
EBL	Electron beam lithography
EG	Epitaxial graphene
EM	Electromagnetic
FLG	Few-layer graphene
FT-IR	Fourier transform infrared
GFET	Graphene field-effect transistors
GNR	Graphene nanoribbons
GSG	Ground-signal-ground
HFSS	High-frequency structure simulator
ICP	Inductively coupled plasma
INSys	Integrated Nano Systems
IR	Infrared
LO	Longitudinal optical phonon
LWA	Leaky wave antenna
MEMS	Microelectromechanical systems
NEP	Noise equivalent power
NP	Nanoparticle
PCA	Photoconductive antenna

PEC	Perfect electrical conductor
PML	Perfectly matched layer
PR	Photoresist
RF	Radio frequency
RIE	Reactive ion etching
SiC	Silicon carbide
SEM	Scanning electron microscopy
SLG	Single-layer graphene
s-SNOM	Scanning near-field optical microscopy
SOTL	Short-open-through-load
SPP	Surface plasmon polariton
TDS	Time-domain spectroscopy
TE	Transverse electric
TEM	Transverse electromagnetic
TLM	Transfer length method
TM	Transverse magnetic
TMOS	Transformative Meta-Optical Systems
TO	Transverse optical phonon
TRL	Through-reflect-line
UTS	University of Technology Sydney
UV	Ultraviolet

Chapter 1 Introduction

Novoselov et al. [1] discovered the electric field effect in an atomically thin carbon layer, the so-called graphene. Its discovery has triggered a substantial amount of research into its applications and has led to the discovery of further two-dimensional (2D) materials.

An integral part of graphene research and the possibility of future commercial applications is the synthesis of high-quality, large-area graphene, such as the epitaxial growth on silicon carbide (SiC) [2-5], using chemical vapour deposition (CVD) [6-8], or the synthesis on dielectric substrates using various carbon sources [5, 9-12]. The former is currently being investigated at the Integrated Nano Systems (INSys) Lab at the University of Technology Sydney (UTS), where a catalytic alloy-mediated approach to growing epitaxial graphene (EG) on SiC on silicon (SiC/Si) substrates was developed [4, 13]. However, many current applications require precise and defect-free patterning of graphene for their respective application, i.e., meta-atoms of metasurfaces [14], graphene field-effect transistors (GFETs) [15, 16], biosensors [17], or more.

Graphene patterning techniques to date can generally be split into top-down and bottom-up approaches. Top-down approaches are based on masking a large-area graphene layer and etching the uncovered areas using, e.g., oxygen plasma-based dry etching [18]. The etching process and mask deposition can lead to edge defects and contamination, which can introduce additional defects [19], respectively. Recently, maskless approaches, such as focused ion beam [20] and direct laser writing [21, 22], have been explored that reduce the risk of damaging the graphene. However, they suffer limited patterning speeds and writing areas. Bottom-up approaches allow for the direct synthesis of patterned graphene. Recent works have introduced the site-selective growth of graphene using a lithography-patterned solid-state carbon source [23] or CVD catalyst [24], the latter requiring a subsequent transfer step of the graphene structures.

The site-selective growth of EG on Si substrates using a pre-patterned and etched SiC film on Si, as the solid-state carbon source, in combination with a Ni/Cu catalytic alloy, was previously demonstrated [25]. Since the sidewalls of the patterned SiC are also graphitised, this approach results in three-dimensional 3D graphene-coated SiC structures. This approach has been extensively used to create large-scale graphene-coated SiC micro and nanostructures for microelectromechanical systems (MEMS), electronics, and photonics applications [25-27]. Note that the above selective bottom-up patterning is inherently tied to the use of SiC/Si

pseudo-substrates to obtain a selective graphene growth only where the SiC is present. Also, there are cases where it would be beneficial to only obtain an atomically thin pattern of EG on an unpatterned SiC substrate or SiC film on Si. This approach is still challenging.

In one approach, an aluminium nitride (AlN) capping layer was used to selectively mask the sublimation of Si species from the SiC substrate to obtain EG [28]. This method was shown to significantly reduce the graphene grain size, which was attributed to volatile Al and N atoms during the graphitisation and AlN-related processing steps. In another work, $(1\bar{1}0n)$ facets of the SiC are used to grow graphene nanoribbons [29]. While useful to demonstrate the quasi-ballistic conduction of graphene, the latter approach is limited to the size and strip shape of the SiC facets.

The high-frequency characterisation of graphene's electrical properties is often used for benchmarking and can ultimately decide the faith of a processing technology. Several approaches have been studied to experimentally evaluate the conductivity of graphene from direct current (DC) to THz frequencies.

Until recently, graphene samples fabricated at UTS using the catalytic alloy-mediated approach to grow EG on SiC/Si wafers have only been analysed at DC [30] using van-der-Pauw and Hall-effect measurements, which have established themselves as the most common DC characterisation approaches for graphene.

Various high-frequency measurement techniques have enabled the characterisation of graphene's properties in the microwave range. These include resonant cavity measurements [31, 32], which provide a single-frequency evaluation; coplanar waveguide (CPW) [33-35] and rectangular [36-38] waveguide measurements; and free space measurements [36, 37].

While free space and rectangular waveguide measurements are strictly banded due to the components used, they have the major advantage of being non-contact approaches. CPW measurements, on the other hand, are broadband and can span from MHz to GHz. However, they come with intrinsic difficulties associated with probing. Two distinct CPW approaches exist to evaluate graphene: a shunt approach [33], where graphene is used as a shunt between the centre signal trance and ground, and a patch approach [34, 35], where a graphene patch replaces the centre trace of a CPW. Although the Drude conductivity model for graphene predicts a constant real part of its frequency-dependent conductivity up to the THz range, high-frequency measurements have been shown to deviate from DC conductivity measurements [36, 39]. It is attributed to the increasingly lower influence of scattering on grain boundaries and defect-induced discontinuities at high frequencies [39, 40]. Furthermore, THz characterisation

of graphene samples has been demonstrated using time-domain spectroscopy (TDS) [41-46] and far-infrared (far-IR) Fourier transform infrared (FT-IR) spectroscopy [40, 44-48].

Graphene holds great promise for electromagnetic (EM) applications, for instance, in the microwave (300 MHz to 300 GHz) and terahertz (THz) (often now taken to be 100 GHz to 30 THz) frequency ranges, which have attracted much interest in recent years due to communication, medical, sensing, imaging, defence, and other applications [49, 50]. Metals and semiconductors have generally been the dominant materials for generating, manipulating, and detecting EM fields at those frequencies. However, metals suffer from conductivity and skin depth degradation at THz frequencies [49]. Graphene's high electron mobility, dynamic tunability, and support of surface plasmon polaritons (SPPs) make it an ideal candidate to enhance or even replace established technologies.

THz antennas, in particular, benefit from graphene's high conductivity [51], optical transparency [52], flexibility [53], and tunability [54]. SPPs at THz frequencies lead to strong field confinement, which is ideal for antenna miniaturisation [55]. Recent studies have shown a 20-fold electric field enhancement compared to metallic counterparts [56]. However, the high contact resistance at graphene-metal interfaces is one of the most common issues in graphene applications and has demonstrated a significant impact on high-frequency applications [57, 58]. Surface roughness has a detrimental effect on the contact resistance [59, 60], and the effect of the increased surface roughness after the graphitisation of SiC/Si still needs exploring [4].

Using various biasing mechanisms to induce a change in the graphene's Fermi level allows for dynamic reconfiguration of various properties of antennas, such as their resonance frequencies [55] and radiation patterns [61]. The latter is a significant area of research for graphene travelling wave antennas, such as leaky wave antennas (LWAs), where frequency scanning of the main beam direction [62, 63] and scanning the main beam (beam scanning) at a fixed frequency [62, 64] have been demonstrated. Electrostatic biasing using a capacitive gate is commonly used and well-defined [64]. It can also be achieved using planar side gating [65], a solid polymer electrolyte [66], or ion gel [67]. Alternatives are optical pumping [68] and chemical doping [69]. While many graphene applications are numerically modelled, they often omit a biasing network in their design [14].

Metasurfaces are the 2D complements of 3D metamaterials and comprise an array of sub-wavelength planar structures called unit cells or meta-atoms. They have the main advantages of being low profile, lightweight, and easy to fabricate using basic nanofabrication processes. They are commonly used for generating [70], manipulating [71], and absorbing [72] EM fields

by facilitating variations of the amplitude, phase, and polarisation of EM waves exciting them. THz graphene metasurface reflectarrays [73], transmitarrays [68], high impedance surfaces [74], and absorbers [72] have been investigated. The latter is of particular interest due to the absorption enhancement when graphene is employed [75].

Addressing the challenges mentioned above in fabricating planar graphene structures on SiC substrates, this thesis introduces the direct synthesis of planar micro and nanostructured graphene based on the catalytic alloy-mediated growth of EG on SiC/Si substrates. This innovative approach can also be used on SiC ingots using simple lithography processes. Electron beam lithography (EBL)-patterned graphene nanostructures are used to determine the pitch resolution, and ultraviolet (UV)-lithography is expected to provide repeatable wafer-scale graphene patterning for future commercialisation.

Enabled by the previous work, EG, which was patterned using the introduced approach, was grown on SiC/Si substrates. It was employed in metallic CPWs to study its electrical properties at high frequencies. This study finds a strong frequency-dependant behaviour of the sheet resistance. It shows a monotonic decrease for higher frequencies, which is attributed to the progressively smaller influence of small-scale discontinuities, such as grain sizes, at those frequencies. At the same time, the importance of graphene-metal contact for high-frequency applications and the engineering thereof is addressed.

Furthermore, rectangular waveguide adaptors are used to characterise large-area graphitised SiC/Si samples. The EG/SiC/Si stack is modelled using an ABCD-Matrix model, and the high-frequency sheet impedance of graphene was extracted from S-parameter measurements. This approach eliminates the contacting issue mentioned above and avoids complex fabrication steps.

Numerical simulations of EM devices based on EG on SiC/Si at THz frequencies are conducted to evaluate the capabilities of the EG on SiC platform for EM applications. The dynamic tunability and potential for miniaturisation in antenna applications are confirmed. However, the devices suffer from low gains and radiation efficiencies due to resistive losses in the atomically thin layer. A significant absorptivity enhancement is demonstrated by introducing graphene in SiC-based Salisbury screen and grating-based absorbing metasurfaces. Resonance tuning and further absorptivity enhancement are shown by varying graphene properties.

Overall, this work provides an important technological approach for fabricating EG-based devices on SiC/Si substrates and gives fundamental characterisations of graphene's high-frequency properties and of the graphene-metal contact at high frequencies. Finally, the proposed models give a perspective for fabricating EM devices in the future.

1.1 Objectives

This thesis aims to accelerate the development of electronic high-frequency devices based on the platform of growing EG on SiC/Si substrates using a catalytic alloy-mediated graphitisation approach. The objectives are defined as follows:

- To develop a novel, simple, and scalable patterning approach for synthesising micro and nanostructures based on EG on SiC/Si.
- Conduct the first high-frequency characterisation of EG grown on SiC/Si substrates in the microwave frequency range to determine the frequency-dependent behaviour of its electrical properties.
- Set up and perform numerical modelling of THz EM components based on EG on SiC/Si.

1.2 Thesis Structure

In this thesis, Chapters 2-3 are preliminary chapters. Chapter 2 introduces graphene and its properties, including a brief overview of synthesis procedures emphasising integration capabilities. An extensive review of current graphene-patterning approaches is given. Here, the main focus lies in the fabrication of nanometer-sized sophisticated patterns that can be used for high-frequency to optical applications. Furthermore, available high-frequency characterisation techniques with a focus on the characterisation of EG grown on SiC are reviewed. Finally, an overview of the current progress of graphene antennas used to generate EM waves, using graphene to facilitate metasurface-based devices, e.g., for wavefront engineering, and realising graphene-based EM absorbers and detectors within the microwave and THz frequency ranges is given. Chapter 3 covers the methodology for the fabrication of samples, the physical characterisation thereof, the experimental characterisation techniques, and the numerical modelling tools used.

Chapters 4-6 outline the main contribution to the field and summarise the experimental and modelling work conducted. Here, Chapter 4 introduces a novel graphene patterning approach based on the pre-patterning of the metal alloy catalyst. Chapter 5 concludes the high-frequency characterisation of EG on SiC/Si. First, a probe-based characterisation of the high-frequency

conductivity of selectively grown graphene is demonstrated, which highlights the importance of the contact resistance for high-frequency applications. Secondly, it covers the K_a-band characterisation of large-area EG on SiC/Si substrates using rectangular waveguide measurements. Chapter 6 delves into the simulation-based evaluation of several graphene applications within the THz spectrum. Chapter 7 concludes the thesis and gives an outlook on future works of applications based on the platform of growing EG on SiC/Si.

Chapter 2 Literature Review

2.1 Unique Properties of Graphene

Graphene is a 2D allotrope of carbon [76]. It can be seen as the basis for the other 2D allotropes of carbon, including graphite, which is a stack of many graphene layers (typically more than 10 [77]), carbon nanotubes (CNTs), rolled-up sheets of graphene with different chirality), and fullerene molecules (sphere-like structures of wrapped graphene, or C_n) [78], see Figure 2-1. The 2D nature of carbon is enabled by sp^2 hybridised atoms naturally forming a planar, honeycomb/hexagonal lattice structure. Each atom forms three σ-bonds with neighbouring carbon atoms. They are separated by 1.42 Å [79] and are responsible for the strength of the lattice structure [78]. These orbitals form the completely filled valence band of graphene. P-orbitals are perpendicular to the lattice and form covalent bonds (π-bonds) with neighbouring atoms to create a so-called π-band [78]. Pristine graphene has one electron per carbon atom in the π-band, resulting in a half-filled band [78]. These electrons are highly mobile and are responsible for graphene's unique electrical properties.

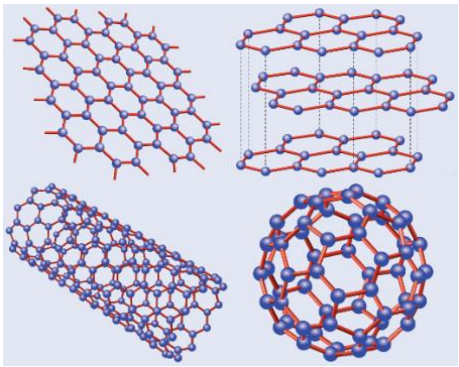

Figure 2-1 Carbon allotropes. Reprinted from [78]

2.1.1 Tight Binding Model

The carbon atoms in graphene are arranged in a hexagonal structure, but its lattice can also be seen as triangular, as illustrated in Figure 2-2(a), with the lattice vectors [78]

$$a_1 = \frac{a}{2}\left(3, \sqrt{3}\right), a_2 = \frac{a}{2}\left(3, -\sqrt{3}\right), \tag{2.1}$$

and $a \approx 1.42$ Å being the carbon atom separation distance. Accordingly, the reciprocal lattice vectors can be written as [78]

$$b_1 = \frac{2\pi}{3a}\left(1, \sqrt{3}\right), b_2 = \frac{2\pi}{3a}\left(1, -\sqrt{3}\right). \tag{2.2}$$

δ_1, δ_2, and δ_3 represent the nearest neighbour vectors and are given by [78]

$$\delta_1 = \frac{a}{2}(1,\sqrt{3}), \delta_2 = \frac{a}{2}(1,-\sqrt{3}), \delta_3 = -a(1,0). \tag{2.3}$$

The Dirac points are positioned at the corners of graphene's Brillouin zone, i.e., K and K' points, which are determined by [78]

$$K = \left(\frac{2\pi}{3a}, \frac{2\pi}{3\sqrt{3}a}\right), K' = \left(\frac{2\pi}{3a}, -\frac{2\pi}{3\sqrt{3}a}\right). \tag{2.4}$$

Using the tight-binding Hamiltonian, which considers electron hopping to the nearest and next-nearest-neighbour atoms, Wallace [79] derived the energy bands as [78]

$$E_{\pm}(k) = \pm t\sqrt{3 + f(k)} - t' f(k), \tag{2.5}$$

$$f(k) = 2\cos\left(\sqrt{3}k_y a\right) + 4\cos\left(\frac{\sqrt{3}}{2}k_y a\right)\cos\left(\frac{3}{2}k_x a\right), \tag{2.6}$$

with k representing a 2D vector from the centre of the Brillouin zone (see Figure 2-2(a)), t being the nearest-neighbour hopping energy between different sublattices, and t' being the next-nearest-neighbour hopping energy within the same sublattice. Figure 2-2(b) shows the upper (E_+) and lower (E_-)-band from equation (5) for $t = 2.7$ eV and $t' = -0.2t$. It also visualises how non-zero values for t' break the electron-hole symmetry [78].

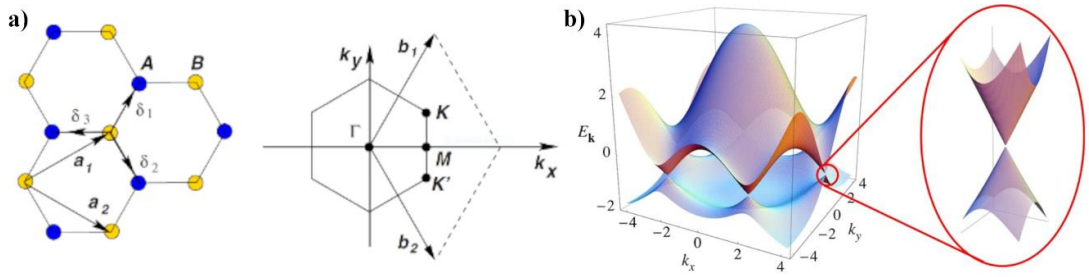

Figure 2-2 (a) Graphene's hexagonal lattice and its Brillouin zone. (left) The graphene lattice structure comprises two triangular Bravais lattices and (right) Brillouin zone with Dirac cones located at the K and K' points. (b) Electronic dispersion of graphene in a single hexagonal lattice element for $t = 2.7$ eV and $t' = -0.2t$. Reprinted from [78]

Graphene has a linear energy-momentum diagram with zero bandgap (BG) at the Dirac points. Figure 2-2(b) indicates that its dispersion surfaces form cones, which are often referred to as Dirac cones. As a result, very high intrinsic carrier mobilities, with a theoretical limit of $\sim 2 \times 10^5$ cm^2 V^{-1} s^{-1} [80], have been demonstrated for exfoliated and suspended graphene. This value is significantly higher than any metal. Graphene has a Fermi velocity of $v_F = 3ta/2 \cong 1 \times 10^6$ m s^{-1} [78]. Moreover, graphene offers a very high saturation velocity and values of $> 3 \times 10^7$ cm s^{-1} for graphene on silicon dioxide (SiO_2) [81] have been

demonstrated. Furthermore, a breakdown current density of $> 10^8$ A cm^{-2} has been shown in [1]. These properties make it an excellent material for electronic and EM applications.

Graphene's electric field effect on the carrier concentration was first demonstrated by Novoselov et al. [1]. It characterises the modulation of the carrier concentration, which leads to a variation in the conductivity of graphene. Their experiment revealed graphene's ambipolar characteristics with electrostatic biasing. Their results showed the charge neutral point, i.e., biasing voltage at which the conductivity of graphene has a minimum, is shifted towards positive voltages. This is due to the interactions between graphene and the substrate and gate dielectrics and graphene's intrinsic doping. Most manufacturing processes of graphene will result in distinct initial doping. For example, CVD graphene is generally p-type, whereas EG grown on SiC is primarily n-doped [82]. Consequently, these graphene samples will have either a hole or electron-dominant conduction in their unbiased state. Ideal graphene has its charge neutral point at $V_g = 0$ V, and its conductivity changes symmetrically as the absolute value of biasing increases, as shown in Figure 2-3(a).

Like semiconductor applications, graphene can be dynamically tuned using various biasing options and doped to manipulate its material characteristics as they induce a change in its Fermi level E_F (sometimes also referred to as its chemical potential μ_c), which also introduces a BG within the band structure [83], as illustrated in Figure 2-3(b).

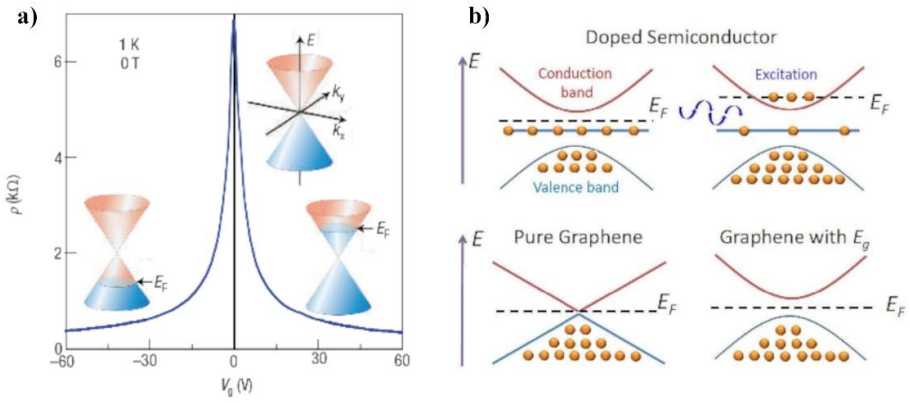

Figure 2-3 (a) Electrostatic biasing induced electric field effect in single-layer graphene. The graph shows the ambipolar modulation of graphene's resistivity and the Fermi level change with varying gate voltages. (b) Band structure of graphene for (bottom-left) pristine graphene, (bottom-right) non-ideal graphene with minimal BG, (top-left) doped graphene with slightly larger BG, and Fermi level shift, as well as (top-right) doped graphene with EM biasing. (a) Reprinted from [84] and (b) from [83]

2.1.2 The Conductivity of Graphene

One of graphene's most important properties for its use in electronic and EM applications is its conductivity and tunability. Therefore, it has been a significant area of research in the early years after graphene's discovery. Knowing the behaviour of the conductivity regarding various biasing mechanisms, as well as its temperature and frequency dependence, is crucial for the characterisation of graphene and the development of models.

The derivation of graphene's conductivity model results from consideration of the Kubo formalism [85-88]. It is dependent on ω, the angular frequency, E_F, the Fermi level, Γ, as the phenomenological scattering rate, as well as T, the temperature, and can be expressed as [89]

$$\begin{aligned}\sigma_{Gr}(\omega, E_F, \Gamma, T) \\ = \frac{\mathrm{i}e^2(\omega - \mathrm{i}2\Gamma)}{\pi\hbar^2}\left[\frac{1}{(\omega - \mathrm{i}2\Gamma)^2}\int_0^\infty \varepsilon\left(\frac{\partial f_\mathrm{d}(\varepsilon)}{\partial\varepsilon}\right.\right. \\ \left.\left. - \frac{\partial f_\mathrm{d}(-\varepsilon)}{\partial\varepsilon}\right)d\varepsilon - \int_0^\infty \frac{f_\mathrm{d}(-\varepsilon) - f_\mathrm{d}(\varepsilon)}{(\omega - \mathrm{i}2\Gamma)^2 - 4\left(\frac{\varepsilon}{\hbar}\right)^2}\right]\end{aligned} \tag{2.7}$$

where e is the electron charge, $\hbar$ is the reduced Planck's constant, i as the imaginary unit, and f_d being the Fermi-Dirac distribution. It is given by [89]

$$f_\mathrm{d}(\varepsilon) = \left(\mathrm{e}^{\frac{(\varepsilon - E_F)}{k_\mathrm{B}T}} + 1\right)^{-1} \tag{2.8}$$

where k_B is the Boltzmann's constant. The first and second terms of (2.7) represent intraband and interband contributions, respectively. It can, therefore, be written as

$$\sigma_{Gr}(\omega, E_F, \Gamma, T) = \sigma_{intra}(\omega, E_F, \Gamma, T) + \sigma_{inter}(\omega, E_F, \Gamma, T). \tag{2.9}$$

and individual contributions can be separately evaluated to be [89]

$$\sigma_\mathrm{intra}(\omega, E_F, \Gamma, T) = -\mathrm{i}\frac{e^2 k_\mathrm{B} T}{\pi\hbar^2(\omega - \mathrm{i}2\Gamma)}\left(\frac{E_F}{k_\mathrm{B}T} + 2\ln\left(\mathrm{e}^{\frac{-E_F}{k_\mathrm{B}T}} + 1\right)\right) \tag{2.10}$$

$$\sigma\ \ (\omega, E_F, \Gamma, T) \cong -\frac{\mathrm{i}e^2}{4\pi\hbar}\ln\left(\frac{2|E_F| - (\omega - \mathrm{i}2\Gamma)\hbar}{2|E_F| + (\omega - \mathrm{i}2\Gamma)\hbar}\right) \tag{2.11}$$

where the interband conductivity is approximated for $k_\mathrm{B}T \ll |E_F|, \hbar\omega$.

Given the general definition of complex conductivity $\sigma = \sigma' + \mathrm{i}\sigma''$, Figure 2-4 shows the real and imaginary parts of graphene's conductivity for $E_F = 0.5$ eV, $T = 300$ K, and $\tau = 0.5$ ps, τ being the relaxation time and related to Γ by $\Gamma = 1/2\tau$. In the case of DC and for a mobility of $\mu = 10\ 000\ \mathrm{cm^2\ V^{-1}\ s^{-1}}$, it can be estimated to be $\tau_\mathrm{DC} = \mu\hbar\sqrt{n\pi}/ev_\mathrm{F} = 0.64$ ps [90], with n as the carrier concentration.

Intraband transitions are the primary conduction mechanism in the lower frequency range. They contribute significantly to the imaginary part of the conductivity. As the frequency increases, the interband contribution becomes more dominant. $\sigma_{\min}$ represents the general optical conductivity of graphene. At low frequencies, the conductivity can reach values up to $100 \times$ the optical conductivity [36], as illustrated in Figure 2-4.

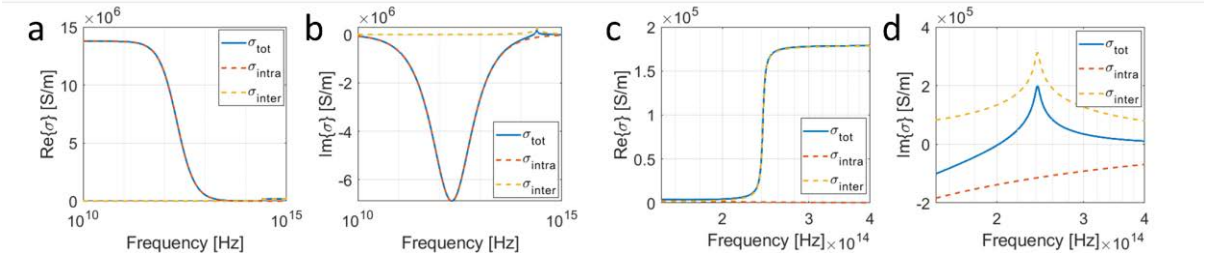

Figure 2-4 Graphene's conductivity model. (a) The real and (b) imaginary part of graphene conductivity for $E_F = 0.5\ eV$, $T = 300\ K$, and $\tau = 0.5\ ps$. (c,d) Enhancement into frequency region of interest. Reprinted from [14]

As analysed in [89], the propagation of surface waves is dependent on σ''. Transverse magnetic (TM) surface modes can propagate if $\sigma'' < 0$. This is mostly valid as the intraband contribution dominates in many cases. Although an introduction of the Fermi level can alter the conductivity, see Figure 2-4. The imaginary part of the conductivity becomes positive since $\sigma'' > 0$. In this case, σ''_{inter} dominates over σ''_{intra}. Therefore, only TE surface wave modes will exist. In the THz range, interband transitions in graphene are forbidden due to the Pauli exclusion principle [91]. It results in low losses and allows for SPP wave propagation in graphene. SPPs can propagate for frequencies $\hbar\omega < 2E_F$ [49].

2.1.3 Surface Plasmon Resonance

SPPs are an essential property of graphene and one of the main reasons it is intensively studied within the THz frequency range. It is particularly exciting in nanophotonics as it would allow the control of light at dimensions smaller than the wavelength [90, 92]. Still, it also found meaningful applications in the design of graphene antennas and other EM devices.

SPPs are EM waves that travel along the interface of a metal and a dielectric or air. They are a combination of surface plasmons (SPs), which describe quantised charge oscillations of electrons and holes at the interface, and polaritons, quasiparticles induced by coupling of dipole excitations (e.g., electron-hole pair) and EM waves.

For the existence of SPs, the SP-carrying material needs to satisfy the following criteria: the real part of its dielectric constant $\epsilon = \epsilon' + \mathrm{i}\epsilon''$ needs to be negative, i.e. $\epsilon' < 0$, and ϵ'' should

be significantly smaller than the negative real part of ϵ, i.e. $\epsilon'' \ll -\epsilon'$ [49, 90]. Their complex wave vector K_{SPP} defines SPP propagation properties. It is defined as [91]

$$K_{\mathrm{SPP}} = \frac{\mathrm{i}(\epsilon_{r1} + \epsilon_{r2})\epsilon_0 c_0}{\sigma_{Gr}} K_0 \tag{2.12}$$

with K_0 being the free space wave vector, c_0 the speed of light, σ_{Gr} being the surface conductivity of graphene, ϵ_0 representing the vacuum permittivity and ϵ_{r1} and ϵ_{r2} being the relative dielectric permittivities of the material above and the substrate below graphene. Its real part is related to the SPP wavelength by $Re\{K_{\mathrm{SPP}}\} = 2\pi/\lambda_{\mathrm{SPP}}$, which is much smaller than the free space wavelength λ_0 [49]. On the other hand, the decay and propagation length of the SPPs are related to the imaginary part of K_{SPP} by $Im\{K_{\mathrm{SPP}}\}$ and $1/Im\{K_{\mathrm{SPP}}\}$, respectively. The high inductive conductivity of graphene leads to TM modes [55], see Figure 2-5

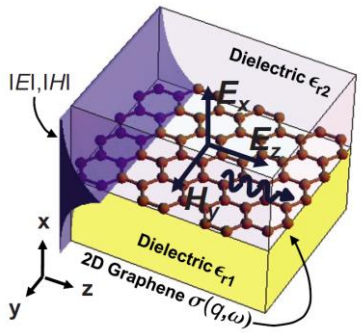

Figure 2-5 TM plasmon modes in general graphene system. Graphene is sandwiched between two dielectrics with their relative permittivities ϵ_{r1} and ϵ_{r2}. The field profile is the same as for SPs at the metal-dielectric interface. Reprinted from [90]

In conjunction with metallic materials, graphene supports SPPs at a much lower frequency, namely in the mid-IR range versus near-IR to the optical range for metals [49]. At the same time, graphene exhibits low losses in the frequency regime of interest and is tunable [90]. The latter has been demonstrated to allow for the dynamic control of the wavelength and amplitude of plasmons in graphene structures [93, 94].

2.1.4 Other Properties

High thermal conductivity is vital for various electronic applications. One of the main problems with integrated circuits is that resistive heat must be dissipated rapidly to maintain device reliability and performance. Particularly, analog high-power electronics suffer from substantial heating. The continuing trend of downsizing planar integrated technologies results in densely populated integrated circuits with long interconnects (up to above 1 km in length) and high power consumption [95], further challenging thermal management. 3D die integration

reduces the length of interconnects but leads to even higher device and power densities, with heat dissipation becoming a major bottleneck [95]. Pristine graphene has demonstrated superior in-plane thermal conductivity of $\sim 5.3 \times 10^3$ W mK^{-1}. It exceeds the best bulk crystalline thermal conductivity of diamond ($1 \times 10^3 - 2.2 \times 10^3$ W mK^{-1}) [96] and could be used as heat spreaders to aid thermal management in integrated devices [95].

The tight lattice structure of graphene makes it impermeable to even the smallest gas molecules [84]. Combined with graphene's property of compromised electrical properties upon molecular attachment on its surface, which generally is considered a disadvantage, it allows for application as molecular/gas sensors [83].

Graphene's unique lattice structure is the reason for its mechanical strength and elasticity. Electronic applications directly benefit from these characteristics. They result in more robust devices that can withstand significant mechanical stress and allow for new applications such as flexible electronics. Graphene has been shown to have a Young's modulus of 1 TPa and an intrinsic strength of 130 GPa [97]. However, the inherently poor adhesion of graphene to its underlying substrate can still pose an issue for manufacturability and thermo-mechanical reliability, particularly for transferred graphene [27]. Furthermore, a single graphene layer absorbs only about 2.3 % of the incident light, making it an interesting material for coating or invisible electronic applications, such as optically transparent antennas [52].

The properties discussed up to this point are primarily based on free-standing, single-layer monocrystalline graphene (SLG), such as exfoliated graphene [1]. However, the properties are immediately affected if the grain sizes are small [98], several graphene layers are stacked [98, 99], and when graphene is integrated due to its interaction with the underlying and overlying layers [30, 100], as is typically the case in integrated electronics.

2.2 Graphene Patterning

Quite disparate approaches for synthesising graphene have emerged ever since the development of the scotch tape method, also referred to as mechanical exfoliation, that was used to prepare the first graphene samples [1]. They all have their particular advantages and disadvantages concerning the properties of graphene, scalability, sample size, fabrication complexity, and cost. Ultimately, the particular properties of the produced graphene determine the possible applications. Therefore, only a few of these approaches are viable for use in graphene production and its use for electronics and EM applications.

As one of the main focuses early on in graphene research was the synthesis of homogenous and large-area graphene, and it commonly forms the basis for top-down patterning approaches,

the fabrication of large-area graphene via CVD and the epitaxial growth on SiC are first introduced. Furthermore, a summary of alternative manufacturing techniques is given.

2.2.1 Graphene Synthesis

2.2.1.1 Chemical Vapor Deposition

Graphene layers can be grown on various, often sacrificial, metallic surfaces using CVD. The process has been shown to produce large-area uniform polycrystalline graphene films [98] and was first introduced by Li et al. [6]. They grew graphene on copper foils, which were used as a catalyst, in a furnace in a methane atmosphere. A transfer process was developed that allowed to separate the graphene from the metal and deposit it on SiO_2/Si wafers. The growth process produces predominately SLG, with < 5 % of the area having multiple layers.

Many variations have been developed using several different catalyst metals, carbon-source gasses, and experimental setups. Yet, they are generally based on the same principles. Graphene films of a few square meters have been produced, as shown by Kobayashi et al. in [7]. They used a roll-to-roll CVD process to grow graphene on a 100 m long copper foil and transferred it onto a polyethylene terephthalate (PET) film. The transfer process itself has also significantly improved as graphene can now be transferred onto a large variety of substrates and materials, such as Si, SiO_2, Quartz, PET, and many more. Recently, Xu et al. [101] developed a CVD process for growing single-crystal graphene on copper foils by reducing the synthesis time to 20 min. This process can potentially also be scaled to m^2 sized copper foils.

CVD graphene has been demonstrated to have excellent electrical properties. Some samples of CVD graphene transferred to SiO_2, and hexagonal boron nitride substrates have been shown to match the properties of mechanically exfoliated graphene on a small scale [98]. They generally offer high homogeneity and purity and allow for reasonable control of graphene film properties. However, the fabrication process still brings a number of challenges as it is relatively labour-intensive and may produce toxic by-products. Furthermore, the transfer process can be complex and can damage the graphene. It is also prevalent for CVD graphene to have an intrinsic chemical doping profile due to the metallic catalyst used. Due to graphene's interactions with its substrate, this effect can be further enhanced with its transfer onto another material, reducing its purity and degrading its electrical and mechanical properties.

2.2.1.2 Epitaxial Growth on Silicon Carbide

SiC is a common substrate material used in the design of high-power electronics. Graphene layers can be epitaxially grown on its surface via thermal decomposition due to the sublimation of Si atoms and species on its silicon or carbon faces. It was first demonstrated by Forbeaux et

al. [2] on a Si-terminated 6H-SiC(0001) substrate. The process is relatively straightforward as it only requires the substrate to undergo an annealing process. An annealing temperature of $1\,400$℃ and ultra-high vacuum with a pressure of $< 3 \times 10^{-10}$ mbar is required. Berger et al. [3] were the first to measure the electrical properties of graphene grown using this approach. Their fabrication approaches were similar, but Berger et al. introduced several oxidation and de-oxidation steps to improve the surface quality of SiC before graphitisation. They found that this growth process results in a stack of randomly oriented graphene layers.

The main drawbacks of this approach are the high temperatures ($1\,300 - 1\,700$℃) that are required to realise the graphitisation, the cost of SiC wafers, as well as the restriction to small wafer sizes ($d_{\mathrm{SiC}} \approx 150$ mm) available compared to Si ($d_{\mathrm{Si}} \approx 300 - 450$ mm) [13, 98]. Various groups investigated the use of metal catalysts with the primary goal of reducing the temperature needed for graphitisation (≥ 750℃) [102]. The higher-quality graphene layer was found to form on the metal surface and would thus require an additional transfer process, similar to CVD-grown graphene [25].

Simultaneously, heteroepitaxial growth of cubic SiC (3C-SiC) films on Si wafers and the graphitisation thereof have been investigated [103-105]. However, the crystallographic orientation, defects, and surface roughness of the 3C-SiC/Si, significantly limit the quality of graphene formed via the thermal decomposition of the pseudosubstrates [106]. The Raman spectrum commonly shows a $I_{\mathrm{D}}/I_{\mathrm{G}}$ ratio close to unity, indicative of extremely small and patchy domains [107, 108]. Recently, a catalytic alloy approach using Cu and Ni on epitaxial SiC on Si wafers has shown the capability for wafer-scale uniform graphitisation [4, 13], see Figure 2-6. Here, the graphitisation takes place at lower temperatures ($900 - 1\,100$℃) and in high vacuum ($\sim 10^{-4}$ mbar) instead of ultra-high vacuum, which makes it compatible with current Si processing technologies [25].

The metal catalysts (10 nm of Ni and 20 nm of Cu) are sputtered onto the SiC layer and placed in a furnace where the metal catalysts undergo a liquid phase. Here, the Ni acts as the main catalyst by reacting with the SiC to form Ni silicides ($NiSi_x$), which enables the release of carbon. Cu has a twofold benefit as it dilutes and distributes the Ni, with the melting point of Cu being close to the annealing temperature. The molten metal conforms to the defective surface morphology of the 3C-SiC/Si, increasing the uniformity and quality of the graphene layer as compared to the thermal decomposition of 3C-SiC/Si [4, 13]. Furthermore, Cu acts as a catalyst, enabling the precipitation and graphitisation of the released carbon [4].

The EG grown following this procedure has recently yielded a sheet resistance comparable to that of EG on bulk SiC [109]. The sheet carrier concentration and mobility follow the inverse power-law dependence typical of supported graphene [30]. The transport properties of EG on both bulk SiC and SiC/Si are dominated by the interface between the EG and the substrate [30, 100], which is also the case for CVD graphene. Hence, the engineering of the interface needs to be carefully considered when designing integrated graphene-based devices.

In contrast to CVD graphene, epitaxial growth of graphene on SiC/Si can be used to graphitise previously patterned SiC to create 3D graphene-based structures [25, 27], as will be discussed further later. It further offers much higher adhesion to the substrate, more than $6\ \mathrm{J\ m^{-2}}$, compared to transferred graphene, $1.5 - 2\ \mathrm{J\ m^{-2}}$ [27].

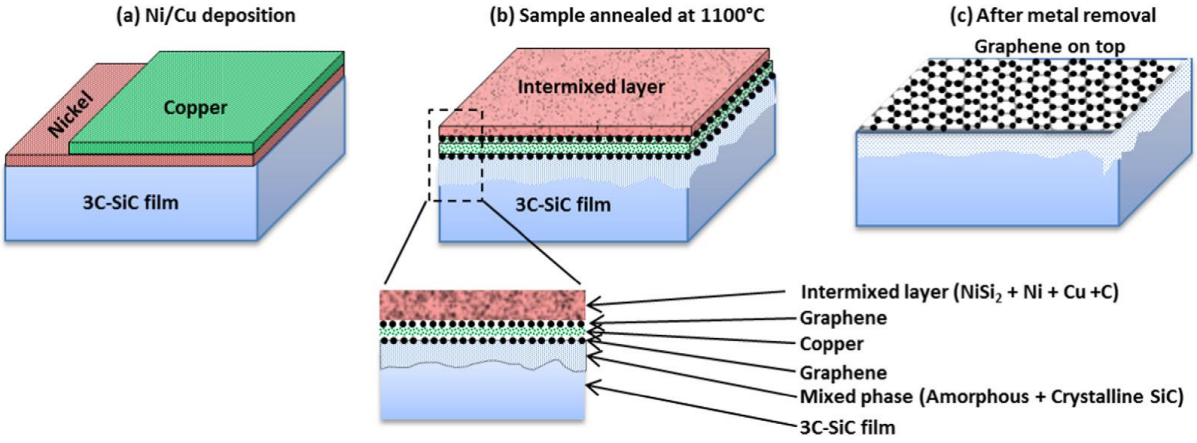

Figure 2-6 Catalytic alloy graphitisation mechanism of SiC/Si substrates. (a) Deposition of nickel and copper catalyst metals, (b) vertical profile after annealing, and (c) vertical profile after Freckle etch. Reprinted from [13]

2.2.1.3 Other Techniques

Mechanical exfoliation produces graphene samples with the best electrical properties. The samples are prepared by repeatedly exfoliating graphite until left with a single layer of graphene. It is a highly random process and generally produces only tiny flakes of graphene. This makes it only applicable to research in laboratory environments [98].

In liquid-phase exfoliation, graphite is exposed to an organic solvent. Initial sonication results in the splitting of first graphite pallets from the graphite sample. Further sonication allows for the graphene pallets to break down into graphene flakes [110]. Solution-mediated approaches are widespread, and a large number of graphene flakes can be produced this way. Their major drawback is that deposited layers can only be formed by overlapping the flakes

rather than homogenous and conjoined layers. Instead, they are ideal for the fabrication of graphene paints and inks [98].

Generally, conductive graphene inks can be divided into two categories depending on whether they have been made with or without binders [111, 112]. Binder-free graphene ink only consists of graphene flakes and an organic solvent such as N-Methyl-2-pyrrolidone, Dimethylformamide, or Dihydrolevoglucosenone, with the former two being toxic and unsustainable [113]. On the other hand, binder-based inks contain binders such as ethyl cellulose or cellulose acetate butyrate. The insulating nature of binders makes them generally unusable for high-frequency applications. However, a compromise in the graphene ink's conductivity can be acceptable in some cases, depending on the application.

Graphene ink has the advantage that it can easily be printed on various substrates, such as polytetrafluoroethylene (PTFE), glass, paper, cardboard, and more, depending on the type of ink used [112, 114]. However, due to the thickness of the ink films, graphene ink-based devices lose their transparency and can not be considered graphene anymore. Instead, they can be referred to as graphitic films, laminates, or layers. Graphitic films with metallic-like conductivities of up to $\sim 1.43 \times 10^6$ S m^{-1} have been reported [115]. They lead to lower ohmic losses and improved antenna performances, making them an excellent alternative to typical metal films in flexible antenna applications

CNTs were discovered before graphene. They can be seen as rolled-up graphene sheets. Several methods have been developed that allow for the unzipping of CNTs to form GNRs [116]. Other graphene fabrication processes are available but will not be discussed here due to the lack of utility towards electronic and EM applications.

2.2.2 Top-Down Approaches

To this date, numerous approaches have been developed to pattern graphene. The main processes can be split into top-down and bottom-up processes and are discussed more thoroughly. The emerging field of chemical patterning, unconventional techniques that do not physically pattern the graphene, and substrate-dependent techniques are only discussed briefly.

2.2.2.1 Lithography-Based Techniques

Reactive ion etching (RIE)-based dry etching of graphene is currently the most common top-down approach for graphene patterning [18]. Generally, oxygen (O_2) gas plasma is used, and graphene is chemically etched via the oxidation of the carbon atoms [117-119]. Alternatively, physical etching via the Ar plasma-induced sputtering of carbon atoms has been reported [118]. A mask, i.e., metal or photoresist (PR), is commonly used to cover the graphene

that is not to be etched [117, 119]. These processes may introduce additional defects and damage the graphene [19]. One of the most common techniques used to pattern the mask is using EBL. It is particularly useful due to its flexibility and high resolution. However, the lithography process itself can be relatively complex.

Han et al. [15] used an EBL-structured hydrogen silsesquioxane (HSQ) mask to pattern $10-100$ nm wide and $1-2$ µm long GNRs. The uncovered graphene was removed using an oxygen plasma. They used the GNRs to engineer the BG of graphene. Similarly, the poly methyl methacrylate (PMMA) layer used to transfer CVD graphene onto another substrate was EBL patterned and used as an etching mask to pattern graphene [120], as illustrated in Figure 2-7. In a more recent study, Sun et al. [16] created GNR-based transistors with channel widths of < 10 nm. While these two studies used exfoliated graphene flakes, the patterning of few-layer graphene (FLG) using this approach is synthesis-independent and has also been achieved using CVD graphene [121] and epitaxially grown graphene [122].

The main advantage of using lithography-based processing is the possibility of creating any pattern imaginable. The resolution is limited by the used lithography process, with EBL creating GNRs as little as 10 nm [123], while UV- or direct-laser Writing lithography are able to achieve resolutions of a few 100 nm. However, EBL generally suffers from a limited write field, and large-scale patterning is not viable. Furthermore, photomask deposition on top of the graphene can lead to PR contamination that is inherently difficult to remove [123]. Choi et al. recently introduced a process to mitigate this issue by using a buffer layer underneath the PR. Here, AZ nLOF 2035 PR, propylene glycol monomethyl ether acetate (PMAc), and sodium dodecyl sulphate (SDS) were used as the buffer layer, solvent, and surfactant [124].

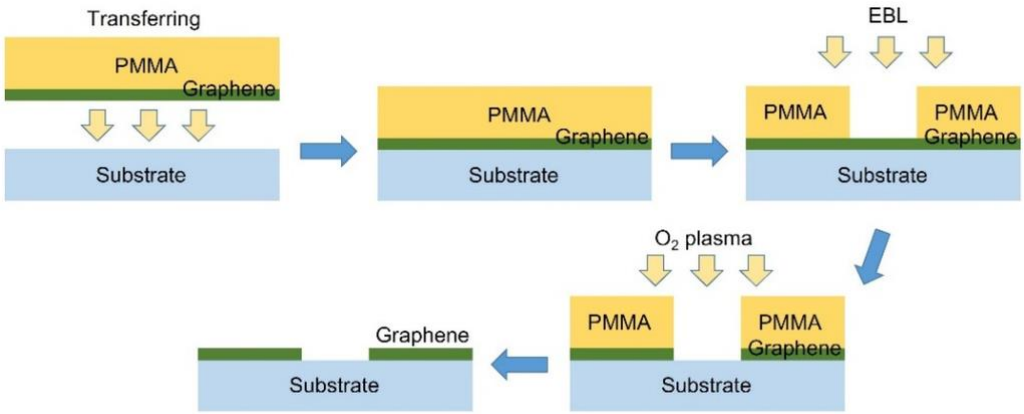

Figure 2-7 EBL-based patterning of CVD graphene. An oxygen-based plasma is used to etch the uncovered graphene. Reprinted from [120]

Instead of using a PR, nanostructures such as nano-spheres and nanowires can be used as a mask [125-127]. Cong et al. [125] created a graphene nano-disk array (diameter of ~186 nm) using polystyrene nano-spheres as an etching mask. The nano-spheres were deposited on the surface of the graphene, and by exposing the samples to O_2 plasma RIE, the uncovered graphene was etched. A subsequent bath in chloroform was used to remove the polystyrene spheres and reveal the graphene nano-disks. In a similar fashion, Bai et al. [126] used Si nanowires as an etching mask to create GNRs. The fabricated GNRs had widths as little as $6\,nm$. While nano-particle lithography processing initially lacked design flexibility as the shape of the graphene patterns was predetermined by the particles used as an etching mask, Liu et al. [127] recently introduced a programmable approach to pattern graphene using ultra-long Si nanowires. However, it is still limited to the geometrical dimensions of the nanowires.

As an alternative to the plasma-based etching of graphene, several groups have explored UV-based processes to pattern graphene [18, 128]. For example, Yuan et al. [18] explored the possibility of using a UV-ozone treatment for graphene patterning. CVD graphene was transferred onto a SiO_2/Si substrate, and a PR mask was patterned using lithography processing. Exposing the uncovered graphene resulted in a photochemical reaction, transforming graphene to graphene oxide and creating local insulating and conducting areas. Lee et al. [128] used a similar approach but deposited patterned TiO_2 on the substrate before transferring the graphene on top of it. The TiO_2 acted as a photocatalyst during the UV-Ozone treatment and facilitated the oxidation of the graphene.

Many other lithography-based patterning approaches exist. They will not be discussed in detail here. Instead, they are briefly mentioned, and a detailed overview can be found in [119, 123]. Nanoimprint lithography and soft lithography are very similar in that a patterned stamp is created on a solid or flexible material before it is transferred onto the graphene [123]. Soft-lithography does not require a PR, and instead, a PMMA layer is structured using a polydimethylsiloxane (PDMS) stamp [129]. After contacting the PDMS stamp with the PMMA, which leaves an imprint within, it was exposed to an O_2 plasma to etch the uncovered graphene [129]. Modified PDMS coated with dimethyl sulfoxide (DMSO) increased the adhesion to the graphene, exceeding the adhesion of the graphene and substrate. Hence, the graphene can be patterned by pealing off the stamp-contacted graphene [130].

In contrast to soft lithography, nanoimprint lithography uses a solid stamp that is transferred onto the PR using high pressure and high temperature. The pattern is then transferred to the underlying graphene using plasma dry etching [131, 132]. Tweedie et al. [133], on the other

hand, used a simple lift-off technique to pattern graphene. PR was initially patterned on a Si substrate, and using a thin layer of PMMA, graphene was then transferred to the substrate, covering the PR and hard-baked to ensure proper graphene-substrate contact. PMMA and PR removal were facilitated using Acetone sonication, leaving behind the patterned graphene.

Furthermore, scanning probe lithography has recently been employed to pattern graphene. It also eliminated the use of a PR. An atomic force microscopy (AFM) tip was used to induce high electrical fields into the graphene, which leads to localised oxidation thereof [134].

Very recently, advances in the wet chemical etching of graphene were made by Zhang et al. [135]. This lithography-based process used a sodium-hypochlorite (NaClO) solution together with UV irradiation to remove unwanted graphene. Graphene not to be etched was covered using a previously patterned masking layer.

2.2.2.2 Nanoparticle Assisted Etching

Already in 2006, cobalt nanoparticles (NPs) have been demonstrated to etch straight channels into highly oriented pyrolytic graphite upon heating ($> 600°C$) and under H_2/N_2 (10:90) atmosphere [136]. Several metallic NPs, such as Ag [137], Co [136], Cu [138], Ni [139, 140], and Fe [138, 141], have since been demonstrated to facilitate the process of etching graphene along crystallographic directions. Generally, the mechanism is based on a reaction between carbon and hydrogen, with the metal NPs acting as catalysts.

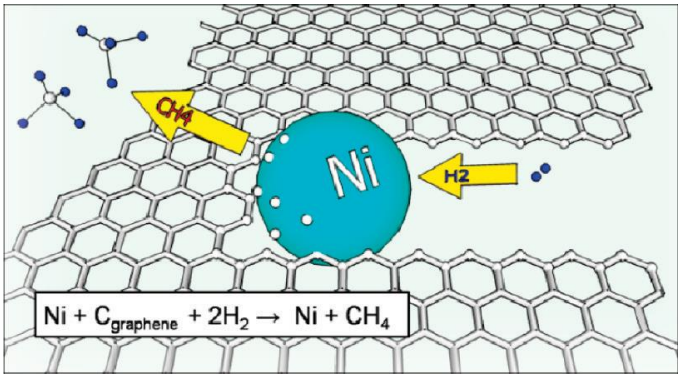

Figure 2-8 Visualisation of Ni NP etching a graphene sheet via the absorption of carbon from the graphene edges, which then react with H_2 to create methane. Reprinted from [140]

Figure 2-8 shows the main mechanics of NP-assisted etching using Ni. The process is relatively simple, where NiCl is deposited onto the sample and submitted to a two-step process in an Ar and H_2 environment. First, it needs to be annealed for 20 min at 500°C to facilitate the NP formation, and then it is annealed at 1 000°C for 25 min for the etching process. During the etching process, carbon from graphene edges dissociates into the Ni NP and then reacts

with hydrogen at the Ni surface [140]. The etching occurs along the crystallographic lattice of graphene and creates 60° and 120° rebound angles. Alternating the cutting direction facilitates the creation of shapes, i.e., ribbons, triangles, and more [142].

The NP-based etching of graphene was, for a long time, exclusively conducted using metal NPs due to the lack of nonmetallic catalytic NPs. Gao et al. [143] introduced SiO_x. While the process provides high crystallographic selectivity and smooth edges, the trajectories of the NPs cannot be controlled and, thus, are unfit for precise patterning.

2.2.2.3 Carbon-Nano-Tube Unzipping,

CNTs can be regarded as rolled-up sheets of graphene. This inspired the idea of unzipping nanometer-scale CNTs to form GNR. Several approaches have been developed, with the main figures-of-merit being the with of the GNR, defectively, and scalability.

Kosynkin et al. [144] developed an oxidative solution-based process that requires strong chemical agents such as sulphuric acid and potassium permanganate to split carbon bonds within the CNT. The process allows for the bulk preparation of GNR and creates nanoscale GNR by unzipping narrow-diameter CNTs, but it has the main drawback that defects are introduced to the GNR. Using molecular intercalation of sulphate nitrate and potassium ions into the CNTs followed by solution-based oxidisation using potassium permanganate, the process can be scaled up to industry-scale production due to the decreased amount of strong acid needed for the unzipping [145]. Shinde et al. [146] introduced a hydrothermal approach using high-temperature intercalation of potassium, sulphate and nitrate ions to partially split CNTs. Subsequent intercalation steps facilitated the complete unzipping of the CNTs.

GNR with widths of $10 - 20$ nm were prepared using a plasma-assisted etching approach [116]. The CNTs were partially embedded in a polymer film before they were etched using an Ar plasma. The final GNR had well-defined edges, and their widths could be controlled by selecting CNT with different diameters and varying the etching time. The approach suffers from limited scalability. Hence, they later developed a process based on a gas phase oxidation and sonication in an organic solvent [147]. A high yield of smooth-edged GNRs was achieved. CNT unzipping can merely be used to create GNRs, and structuring of larger, i.e. few 100 nm, and more sophisticated patterns are not attainable.

2.2.2.4 Direct Writing

The major advantage of direct laser writing patterning approaches compared to lithography-based ones is the lack of requiring a mask for the patterning. They thus provide superior flexibility and allow for rapid prototyping. The idea behind this approach is to create laser-

heating-induced local changes to the graphene lattice, either physical or chemical. For example, Singh et al. [148] used a 1 064 nm wavelength and 7 ns long laser pulses to selectively oxidise EG. The laser-modified EG was identified as graphene oxide or reduced graphene oxide. In [149], CVD graphene on top of Au films was patterned using direct UV laser machining to create graphene-based capacitors. Here, the laser-exposed graphene also underwent oxidation. Tian et al. [150], on the other hand, have demonstrated the physical milling of suspended graphene using a 517 nm laser. The negative thermal expansion coefficient of graphene causes it to shrink and rupture when exposed to laser-induced heating.

Graphene's superior thermal conductivity, coupled with the exposure to lasers, leads to heat diffusion to surrounding areas, thus limiting the resolution of long pulse direct laser writing. Hence, the use of femtosecond lasers was proposed to mitigate this issue. Aumanen et al. [151] used fs laser pulses, wavelengths of 540 nm and 590 nm, to create 2 µm × 2 µm square graphene oxide patterns in suspended and substrate-backed SLG. They demonstrated the tuning of the oxidation rate by controlling the intensity and dose of irradiation, as well as the oxygen content in the atmosphere during the writing process.

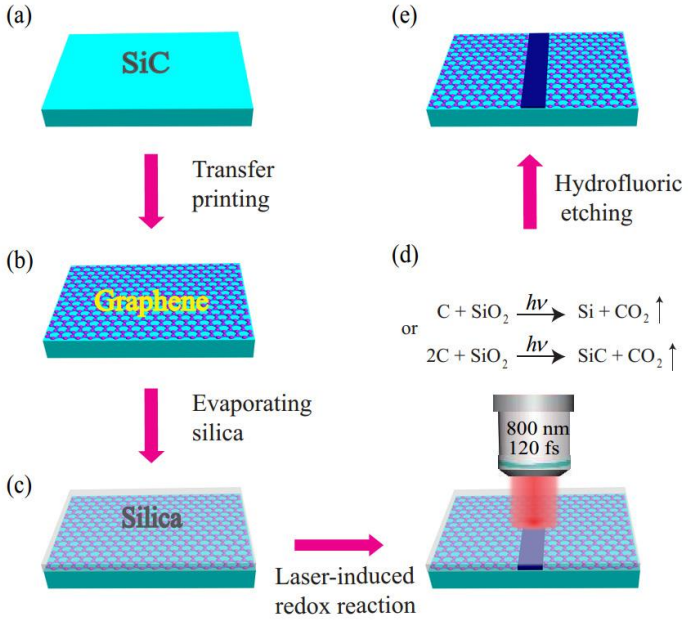

Figure 2-9 High-precision femtosecond direct laser writing. (a) Bare substrate material onto which (b) graphene is transferred before it is (c)covered by a thin layer of SiO_2. (d) Diagram and chemical reactions of femtosecond laser writing process. (e) Removal of the silica layer using etching in hydrogen fluoride exposes patterned graphene. Reprinted from [21]

High-precision fs direct-laser writing was demonstrated by Xu et al. [21]. Depositing SiO_2 on top of graphene on SiC and irradiating it using a femtosecond laser resulted in a redox reaction between the graphene and silica, see Figure 2-9. An 800 nm laser with a 120 fs pulse duration was used. The process achieved a resolution of ±7 nm and created gratings as little as 100 nm wide, much smaller than the diffraction limit.

Another direct writing patterning approach is based on ion beams. Recently, Helium ion microscopy was used to pattern graphene [152]. Its main advantage is the short Broglie wavelength that is almost $100\times$ smaller than the wavelength of an electron and results in a beam resolution of 0.5 nm [119, 153]. Using this approach, graphene quantum dot devices with a minimum feature size of 3 nm were fabricated [154]. The issue of hydrocarbon contamination, which resulted in residual conductivity, was mitigated using an annealing step and facilitated the complete removal of graphene using the helium ion beam [154]. The process requires precise ion dose calibration, as the graphene changes from a conductor to an insulator before it is etched, depending on the dosage [155]. Insufficient He^+ dosage would again result in residual conductivity, while high dosage would result in He^+ diffusion into the SiO_2/Si substrate and degradation of the patterned graphene [119, 155].

Simultaneously, various ion plasma etching methods were developed, such as Ar, Ar/H_2, Ga, and N_2-based approaches [119]. For example, Luo et al. used a Ga^+-focused ion beam to pattern graphene into circular resonators with a diameter of as little as 30 nm [20]. Exposure of graphene to Ga^+ results in its amorphisation.

2.2.3 Bottom-Up Approaches

2.2.3.1 Substrate-Assisted Synthesis

The substrate-assisted synthesis approach relies on the principle of restricting the growth of patterned graphene to a predefined catalyst area. As previously discussed, various metals stand out due to their catalytic properties for synthesising graphene. At the same time, it is crucial to provide a sufficient carbon source for graphene growth.

Tosic et al. [156] used a graphene-nano-dot mediated electroplating mechanism to create Ni-C nanowires. These were subsequently deposited on a SiO_2/Si substrate and exposed to a rapid thermal anneal process at $500-800°C$ to facilitate the carbon dissolution within and the precipitation onto the surface of the Ni nanowires. The graphene-coated Ni nanowires were then etched using nitric acid to remove the Ni core and form GNR with widths of ~32 nm.

Kato and Hatakeyama [157] used a CVD process to coat Ni-Nanowires instead. They used EBL to pattern Ni into nano-bars on top of a SiO_2/Si substrate. Exposing the structures to a

rapid heating plasma CVD process in a methane and hydrogen atmosphere and a subsequent rapid cooling process resulted in the coating of the Ni nano-bars with graphene while the Ni was simultaneously volatilised, leaving GNRs with widths as little as 23 nm behind.

The main drawback of the processes introduced thus far is that they merely result in the formation of GNR. Larger and more sophisticated patterns require different approaches. Nakagawa et al. [23] enabled the direct patterning of graphene using a combination of lithography and rapid thermal anneal, see Figure 2-10. 300 nm of SiO_2 was initially grown on Si wafers using thermal oxidation. 20 nm of Ni and 5 nm of amorphous carbon (a-C) were deposited to be used as the catalyst and solid carbon source, respectively. The samples were then subjected to a rapid thermal anneal at 1 100°C to initiate the graphitisation process. The residual metal catalyst was then removed by immersing the sample in a $FeCl_3$ acid bath. This approach allows for the creation of patterned graphene with superior design freedom. The minimal line width was determined to be 5 μm, which is rather large.

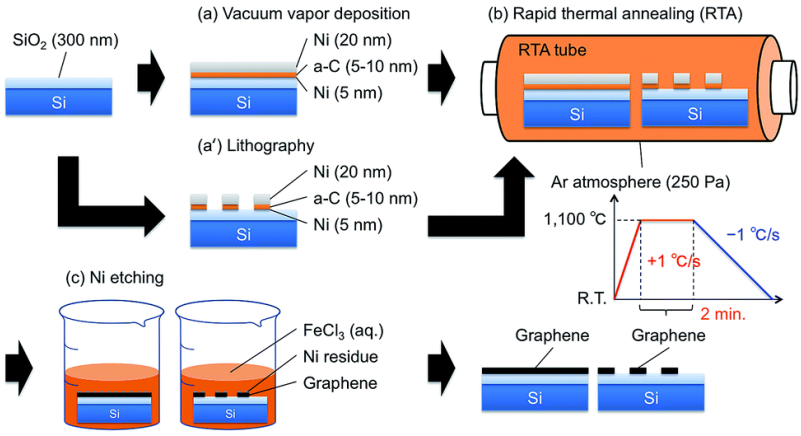

Figure 2-10 Diagram visualising a direct patterning approach. Here (a) lithography processing is used to pattern the catalyst and carbon source, Ni and a-C, respectively, before (b) a rapid thermal anneal step. (c) The Ni residue is subsequently removed using $FeCl_3$. Reprinted from [23]

Next to Ni, Cu has also been found useful for the patterning of graphene [158, 159]. In particular, the crystal facets, such as Cu(111) or Cu(100), can enhance the diffusion of carbon atoms through the surface. This particular effect was utilised in [160] to grow Moiré patterned graphene. Recent work has shown the synthesis of patterned CVD graphene using a pre-patterned nickel catalyst layer on top of a Si substrate [24], as illustrated in Figure 2-11. Here, 300 nm of Ni were deposited onto a SiO_2(300 nm) on Si substrate and placed in a furnace at 1 000°C in a methane/hydrogen/argon atmosphere. This approach requires a subsequent

transfer step of the graphene structures to their final substrate. Two different approaches are used, such that the graphene was transferred by using a PDMS stamp and etching the Ni layer using $FeCl_3$, or by etching of the SiO_2 and Ni layer using hydrogen fluoride or a buffered oxide etchant.

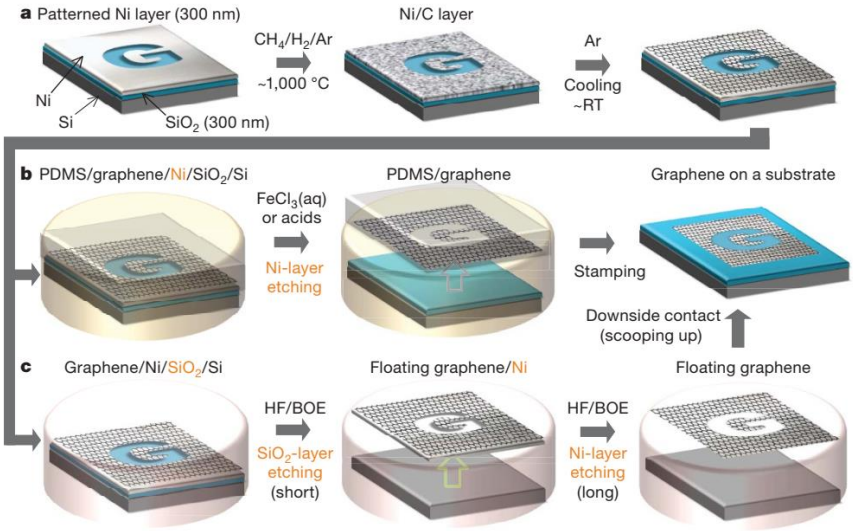

Figure 2-11 Diagram visualising a direct patterned growth approach using CVD. (a) Synthesis of CVD graphene, (b)transfer of graphene using a PDMS stamp by etching of the Ni layer using $FeCl_3$, and (c)transfer of graphene by etching of the SiO_2 and Nickel layer using hydrogen fluoride or a buffered oxide etchant. Reprinted from [24]

Various metallic substrates, such as Au [161], In [162], Ge [163], and Pt [164], have since been shown to allow for the patterned growth of graphene [123]. Of particular interest is the research of Jacobberger et al. [163] that demonstrated the synthesis of < 10 nm wide GNR with predominantly smooth armchair edges on a Ge (001) substrate. However, this process limits the orientation of the GNR to the crystallographic lattice of the substrates.

2.2.3.1.1 Patterned Epitaxial Graphene on Silicon Carbide

As previously introduced, SiC is a common substrate used for the growth of EG and was first applied to pattern GNR by Camara et al. [28]. Their approach was based on thermal decomposition, and an AlN capping layer was used to selectively mask the sublimation of Si species from the substrate. However, the increased I_D/I_G ratio of Raman measurements of the patterned graphene samples indicated significantly reduced graphene grain sizes. The researchers suggested that the sublimation of AlN in the furnace chamber during the anneal step, impedeed the graphitisation process [28].

Sprinkle et al. [29] grew graphene along $(1\bar{1}0n)$ facets of the SiC, see Figure 2-12. Here a Ni line was initially defined on the (0001) or $(000\bar{1})$ crystal faces of semi-insulating 4H-SiC. Fluorine-based RIE was used to etch patterns into the SiC, and an ultrasonic treatment in nitric acid removed the Ni mask before the samples were annealed. Initial heating to $1\,200 - 1\,300°C$ under vacuum induced a step flow and relaxation to the $(1\bar{1}0n)$ facet [29]. Further heating to $\sim 1\,450°C$ facilitates the growth of 40 nm wide GNR on the facet. Their approach, while useful to demonstrate the quasi-ballistic conduction of graphene, does not allow patterning with free designs and dimensions because of the limitation to GNR shape and sizes as defined by the facets of the SiC substrate.

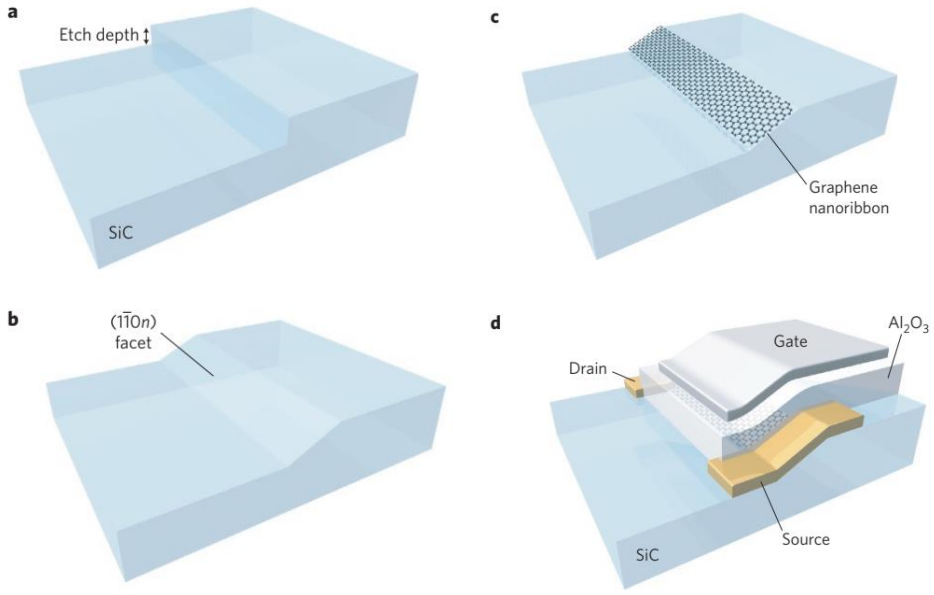

Figure 2-12 Diagram the growth of EG GNRs on the $(1\bar{1}0n)$ facet of SiC using thermal decomposition to demonstrate the quasi-ballistic conduction of graphene. (a) Wet etching of SiC using a Ni masking layer to create a step in the SiC. (b) Annealing step to induce the step flow to the $(1\bar{1}0n)$ facet. (c) Second anneal step induces the graphitisation of the SiC layer. EG that grows on the (0001) or $(000\bar{1})$ crystal faces was removed via RIE with the ion current parallel to the $(1\bar{1}0n)$ facet. (d) The GNRs were studied in a GFET configuration. Reprinted from [29]

The site-selective growth of graphene on Si substrates using a pre-patterned and etched SiC film on Si, as the solid-state carbon source, in combination with a Ni/Cu catalytic alloy, was previously demonstrated [25]. Since the sidewalls of the patterned SiC are also graphitised, this approach results in 3D graphene/SiC instead of planar graphene structures. This approach has been extensively used to create large-scale graphene-coated SiC micro and nanostructures

for MEMS, electronics, and photonics applications [25-27], as illustrated in Figure 2-13. Here, a PR mask or metal hard mask was used to cover the areas of the SiC that were not to be etched. The etching of SiC was then performed using Inductively coupled plasma reactive ion etching (ICP-RIE) plasma dry-etching. Using a polymer-based PR as a mask is generally inadequate for the plasma-based dry-etching of SiC due to the addition of O_2 to the etching process. It would result in gradual consumption of the masking layer and, inevitably, a deviation of the as-designed layout or complete removal and partial etching of the not-to-be-etched SiC regions. Hence, the etching of thick (several μm) SiC layers or the need for high spatial resolution require the use of a metal hard mask. This would add additional processing steps and further complicate the patterning approach.

Note that the above selective patterning cannot apply to EG on SiC wafers. Also, there are cases where it would be beneficial to only obtain an atomically thin pattern of EG on an unpatterned SiC substrate or SiC film on Si. This approach is still challenging.

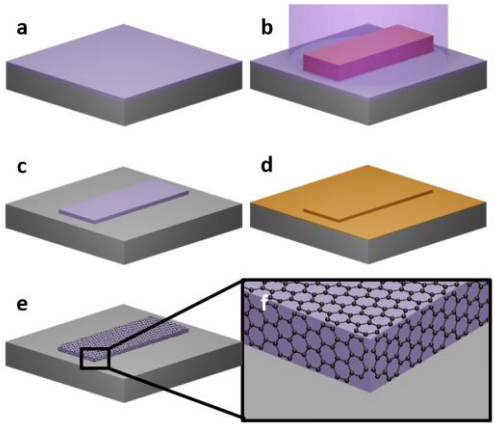

Figure 2-13 Graphitisation of the pre-patterned SiC on Si substrate. The SiC layer is used as the solid-state carbon source. (a) The process starts with a SiC/Si substrate. (b) A Photoresist mask is deposited on the substrate using lithography, and the SiC layer is etched using RIE. (c) Removing the PR layer reveals the patterned SiC. (d) The Ni and Cu catalyst metals are deposited on the sample. After an anneal, the sample is submerged in a Freckle etch bath to reveal (e) the graphitised SiC structures. All sides of the SiC covered by the catalyst metals are graphitised to create 3D graphitised structures. Reprinted from [165]

2.2.3.2 Liquid-Phase Synthesis

Liquid-phase synthesis enables the creation of large quantities of GNRs with widths as little as $0.69 - 1.13\,\text{nm}$ and lengths of $> 200\,\text{nm}$ [166]. Similar to the solution-mediated exfoliation of graphene flakes, it allows for varying the physical and chemical properties of the

GNRs during their synthesis [123]. Due to the limitation of only synthesising GNR, this process will not be discussed further. However, further reading is available in [123, 167].

2.2.4 Others

Several patterning techniques exist that do not fit the previously mentioned categories as they are either highly graphene synthesis-dependent or do not physically pattern the graphene. One such field is the emerging research field of chemical patterning. Alternatively to etching graphene, defined areas of an unpatterned graphene layer are covalently functionalised [123]. Furthermore, localised chemical doping or biasing [168-170] can be used to achieve the effect of a patterned structure. For example, localised biasing creates patches within the same layer of graphene that have different conductivities [170]. On the other hand, graphene-ink films can be patterned using inkjet printing, doctor-blading, or screen printing [113].

2.3 High-Frequency Characterisation

Graphene's electrical conductivity or sheet resistance are some of the main properties used to simulate graphene-based electronic devices and to benchmark graphene samples and their synthesis procedures. Several measurement techniques have been employed to quantify this property from DC up to the optical frequency range. Measurement results provide valuable information about the properties of the sample and are essential for simulation. They can be used to validate the Drude conductivity model, which is commonly utilised for accurate modelling and design of electronic devices. Currently, graphene samples fabricated at UTS using the catalytic alloy-mediated approach to growing EG on SiC/Si wafers [4, 13] have only been analysed at DC [30].

While the Drude conductivity model for graphene predicts the real part of the conductivity to be constant up to the THz range, some high-frequency measurements of the electrical properties of CVD graphene have been shown to deviate from DC conductivity measurements as the measured conductivities experienced a monotonic increase with increasing frequency [36, 39]. This is expected to be related to the discontinuities in the graphene layer that play a significant role in DC measurements but show less influence in high-frequency measurements [39, 40]. Several measurement techniques have been developed, each within a specific frequency range, as there is no universal measurement method available to quantify the electrical properties of graphene from DC to THz and above. They are listed in Table 2-1.

Table 2-1 High-frequency and THz conductivity characterisation of graphene

Approach	References	Frequency Range	CVD	EG/SiC	EG/SiC/Si
Van der Pauw	[36, 37, 39]	DC	✓	✓	✓
Resonant Cavity	[31, 32, 171]	~10 GHz (single frequency)	✓	✓	✗
Rectangular Waveguide	[36-38]	$7 - 40$ GHz	✓	✗	✗
CPW	[33-35]	MHz – 110 GHz	✓	✗	✗
Free Space	[36, 37]	$75 - 110$ GHz	✓	✗	✗
TDS	[41-46]	$0.1 - 2.5$ THz	✓	✓	✗
FT-IR Spectroscopy	[40, 44-48]	$1 - 600$ THz	✓	✓	✗

2.3.1 Direct-Current Characterisation

The main measuring approaches used for determining the DC conductivity and characteristics of graphene are the four-point probe [37, 172], the van der Pauw method and the Hall effect measurement [33, 173]. The four-point probe method uses four probes that are set up in line to measure the conductivity/resistivity of the sample. It is also possible to calculate the mobility of the charge carriers using this method. Apart from the requirement of contacts, the measuring procedures do not require complicated fabrication steps and are non-destructive. The van der Pauw method and Hall effect measurement use four probes that are placed around the perimeter of the graphene sample. They allow for evaluating its conductivity/resistivity, the charge carrier type (electrons or holes), the sheet carrier concentration, and their mobility. They are superior to the in-line four-point probe method due to directly determining a large number of properties and providing averages of the properties over the sample area. In contrast, the four-point probe measurement technique only evaluates the properties in line with the probes. The van der Pauw method and the Hall measurement are extensively used on a wide variety of graphene samples, including EG on SiC, and have proven to be reliable and the preferred characterisation methods.

2.3.2 High-Frequency and Terahertz Characterisation

2.3.2.1 Rectangular Waveguide

In this approach, graphene samples are inserted into the rectangular waveguide, perpendicular to the direction of the waveguide [38], or wedged between two coaxial adaptors

[36], see Figure 2-14. Rectangular waveguides are strictly banded, and their dimensions determine the frequency range of this measurement approach. Graphene samples within frequency ranges of $7-13$ GHz [36, 37], as well as $8-12$ GHz and $25-40$ GHz [38], have been evaluated this way.

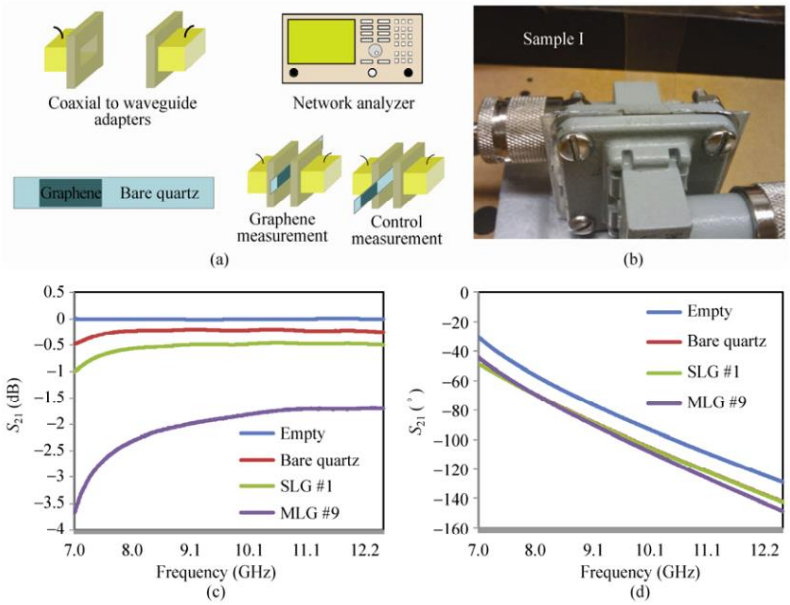

Figure 2-14 Rectangular waveguide-based measurement setup to characterise graphene's conductivity in the X-band. (a) Schematic view of the measurement setup. (b) Image of graphene on quartz sample sandwiched within the waveguide. (c,d) The measured magnitude and phase of the transmission coefficient S_{21} for the empty waveguide, bare quartz, SLG, and 9-layer FLG on a quartz substrate. Reprinted from [36]

The conductivity of the graphene layer can be evaluated by determining its impedance using a transmission line model where graphene is treated as a lumped impedance. Therefore, the transmission and reflectance coefficients can be evaluated by considering the wave impedances of the substrate used and air. Using those and the results of transmission and reflection S-parameter measurements allows for calculating the complex graphene conductivity. Gómez-Díaz et al. [38] estimated the extraction error using reflection measurements to be 50 % and suggested an alternative approach using an $ABCD$-matrix model. It is calculated using transmission line models of the individual layers of the substrate and graphene. The impedance of graphene is then evaluated from S-parameter measurements. They estimated the error using this method to be only 5 %.

The rectangular waveguide approach is non-destructive but requires the matching of sample sizes to the waveguide dimensions. High resistivity substrates should be used to enhance

transmission, and it is generally necessary to conduct reference measurements with the bare substrate for control and accuracy.

2.3.2.2 Coplanar Waveguide

As the name suggests, CPWs are used to characterise the conductivity of graphene samples. The main structure of the CPW is made up of metal as it can generally be deposited as a thick layer and will therefore improve its transmission properties [34, 35]. Graphene is characterised by creating a small gap in the centre trace of the CPW and placing a graphene patch in it, see Figure 2-15. The dimensions of the structures are generally tiny and require the measurement of S-parameters using a network analyser, a probe station, and dedicated ground-signal-ground (GSG) probes. Complex fabrication is required to create the CPW structures, and additional open, short, and thru structures are needed for de-embedding [174-176]. De-embedding is crucial as it removes the influences of metallic traces, probes, and parasitic elements. The frequency range is generally determined by that of the network analyser and the probes used, and frequency ranges of up to $0.01 - 110$ GHz [33] have been measured.

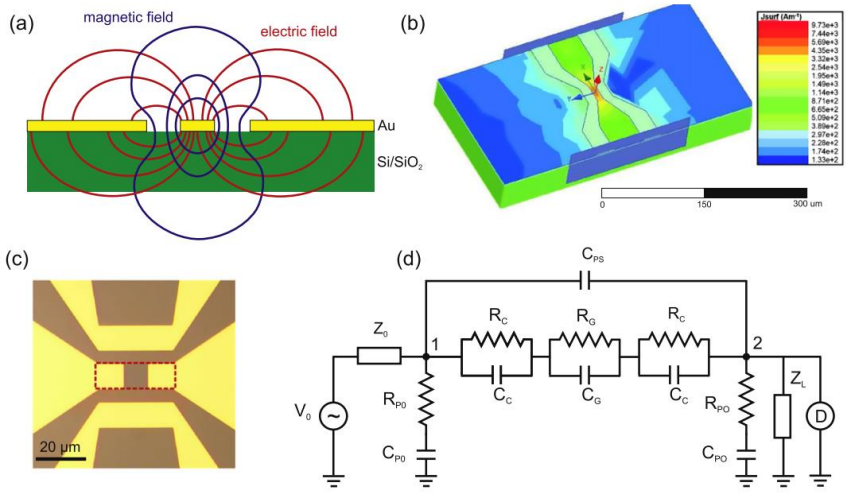

Figure 2-15 CPW-based characterisation of graphene's conductivity. (a) TEM mode propagation within metallic CPW and the electric and magnetic field distributions. (b) Full-wave simulation of the surface current density in the CPW at 13.5 GHz. (c) Image of the fabricated CPW with the graphene patch placed within the centre signal trace. (d) An equivalent circuit model of graphene patch-loaded CPW that was used for the extraction of the conductivity of the graphene patch. Reprinted from [35]

The conductivity of the graphene is calculated by first extracting the impedance of the graphene patch alone from the S-parameter measurements and then de-embedding those values. Then, an equivalent circuit model is matched to the impedance parameters (Z-

parameters), and values for the resistance of graphene are extracted. Although a wide frequency range is measured, the conductivity is assumed to be constant and extracted as a single real value. The frequency-dependent behaviour is not determined. Yet, it is still a valid assumption as the conductivity does not change in those frequency regions according to the Drude conductivity model. Generally, each research group will use their unique equivalent circuit model, and no consensus has been found yet. It is also the main critique point of this approach, though measurement results have been shown to match DC measurements [33-35].

Skulason et al. [33] introduced an alternative method to determine the conductivity of graphene using CPW structures. They used graphene as a shunt between the centre trance and ground instead of replacing part of the centre trace. The $RLCG$-parameters of the transmission line are then extracted from S-parameter measurements and compared to those of a CPW structure with equal dimensions but without graphene. This approach evaluates the frequency-dependent conductivity and has also shown to agree well with DC-measurement results.

As these approaches favour dielectric substrates to reduce transmission losses, only CVD graphene has been analysed this way. However, measurements of EG on SiC should be possible and still need investigating.

2.3.2.3 Resonant Cavity

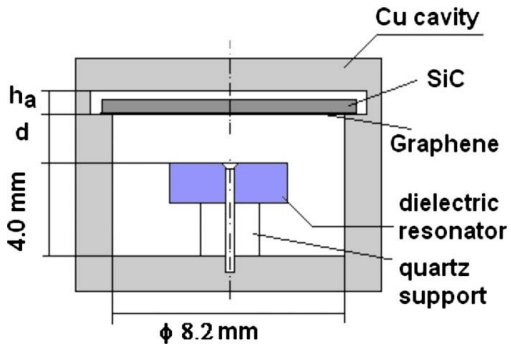

Figure 2-16 Schematic of resonant cavity loaded with EG on SiC sample. Reprinted from [31]

Placing a thin film sample into a resonant cavity shifts its resonant frequency and quality factor (Q-factor) [31, 32, 171]. This non-contact approach requires little fabrication as sample sizes only need to match the resonant cavity dimensions, see Figure 2-16. A network analyser is used for the measurement, but the conductivity can only be evaluated for a single frequency. It depends on the design of the resonant cavity, and conductivities at individual frequencies between ~9 GHz and ~13.4 GHz have been evaluated [31, 32, 171]. This approach has been applied to both CVD graphene and EG grown on SiC. Krupka et al. [171] estimated the

measurement error to be ± 5 % and have shown good agreement between the DC and high-frequency measurement results of metallic samples.

2.3.2.4 Free Space Measurement

Rouhi et al. [36, 37] used a free space measurement approach to determine the conductivity of CVD graphene on an insulating Quartz substrate. No dedicated fabrication steps are necessary, although the sample needs to be large enough to be characterised in the dedicated frequency band. In their works, it was $75 - 110$ GHz. The setup consisted of a source and detector horn antennas, a focal lens, and a 2D adjustable mount for the sample. The adjustable mount enabled a large-area scan of the sample, resulting in a 2D evaluation of the surface conductivity. Difficulties in this approach arise from possible reflections from the lens and mount and need to be filtered out. The conductivity is calculated from the S-parameter measurements using a network analyser. Similar to the waveguide approach, two additional measurements of the bare substrate and air-only cases were required. Rouhi et al. found that the conductivity in this higher frequency range was slightly higher compared to DC and rectangular waveguide measurements.

2.3.2.5 Coherent Photomixing Spectrometer

This approach was first used on graphene by Rouhi et al. [36, 37]. Two coherent photomixers were used as transmitters and receivers, and a circular polarised normal-incident Gaussian beam was generated to penetrate the sample. The conductivity is determined via the Airy transmission formula. A frequency range of $0.1 - 1$ THz was analysed using this approach. Again, two additional measurements using the bare substrate and air-only cases are needed. Rouhi et al. found that this approach cannot be used on SLG samples as the difference in transmission between the bare quartz and the graphene sample was too low and resulted in a low signal-to-noise ratio. The measurement of FLG, on the other hand, was performed but gave highly fluctuating measurement results, see Figure 2-17. Similar to the free space measurement, it showed an increased conductivity compared to measurements in a lower frequency range.

2.3.2.6 Time Domain Spectroscopy

Another measuring approach for graphene conductivity in the THz range is TDS. An fs laser source is used to generate a THz pulse. It passes through the sample in the direction normal to its faces, and the power of the transmitted signal is measured at the receiver. Figure 2-18(a) shows a schematic view of the general setup. The impedance mismatch between the air and the substrate causes multiple reflections, Fabry-Pérot effect, that interfere with the main pulse [41].

The use of very short laser pulses creates a temporal separation of higher-order reflections, and they can thus be ignored [39, 43], see Figure 2-18(b). The time-domain signal of the received pulse is then transformed to the frequency spectrum using the Fourier transformation to create the transmittance spectrum. Applying the Fresnel formulation, the conductivity of the graphene layer can be calculated. Here, graphene is treated as a boundary condition instead of a bulk material, such as for the substrate. It is beneficial to use high-resistivity substrates to improve the transmission of the pulse [39]. As with some previous approaches, measurements of the bare substrate are necessary, and they can also be used to characterise the substrate itself.

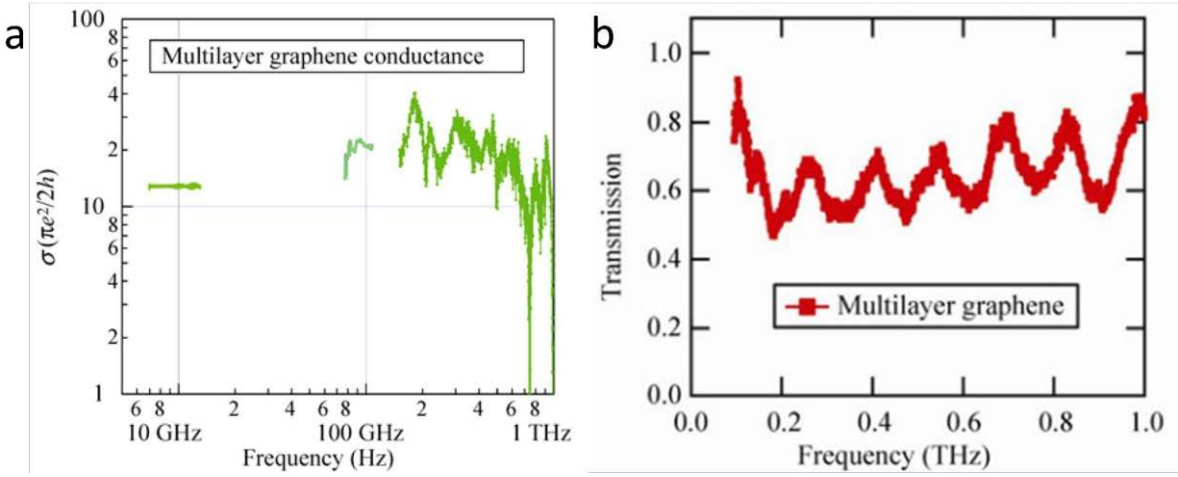

Figure 2-17 FLG high-frequency conductivity evaluation using waveguide, free space, and coherent photomixer spectrometer approaches. (a) Measured conductivity of graphene. (b) Measured normalised transmission of FLG using photomixer spectroscopy. Reprinted from [36]

TDS has been used on a wide variety of SLG and FLG samples and substrates. These include CVD graphene on glass or quartz [41-43], high resistivity Si [39, 46], and SiO_2/p-Si [44], as well as thermal decomposition graphene on SiC [45]. Moreover, a wide range of frequencies, such as $0.1 - 2.2$ THz [44] and $0.5 - 2.5$ THz [43], have been analysed.

As not all substrates allow for accurate transmission measurements using TDS, Feng et al. [43] investigated the possibility of evaluating the conductivity of their graphene from the reflectance spectrum. They suggest that the signal-to-noise ratio is higher using this approach due to residual contamination on the top and bottom of substrates used in transmission-based measurement setups. Furthermore, a large area analysis of the graphene conductivity can be evaluated, showing the 2D profile of the sample [39, 43].

As the electrostatic biasing capabilities are one of the most exciting features of graphene, Ren et al. [44] used the bottom p-type doped Si layer of a SiO_2/p-Si substrate as a gate to bias the graphene sample. Their results clearly show the biasing dependence of the conductivity as predicted by the Drude model. The major drawback of this approach is the significant error that results from a substantial attenuation of the substrates. The measured conductivity spectrum generally results in a large variability.

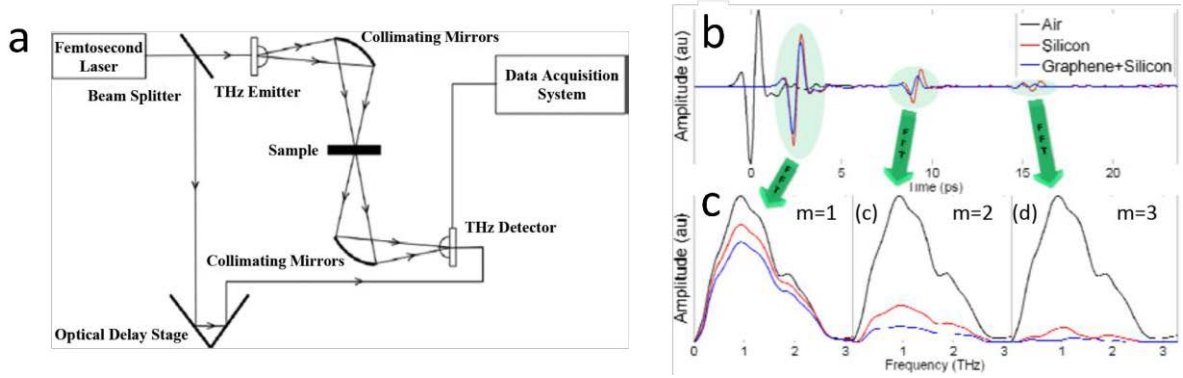

Figure 2-18 (a) Schematic of a TDS characterisation setup. [41] (b) THz pulses transmitted through air, Si, and graphene on Si, as well as the first two internally reflected pulses. (c) The Fourier transform spectrum of each pulse is evaluated. Reprinted from [39]

2.3.2.7 Fourier-Transform Infrared Spectroscopy

All measurement techniques introduced to this point generally range just below the Drude roll-off frequency, where graphene exhibits a constant surface conductivity. The use of FT-IR allows for evaluating the graphene conductivity for even higher frequencies, spanning the complete IR spectrum. The exact frequency range depends on the FT-IR system used. Horng et al. [48] reported measurements at $0.9 - 180$ THz, whereas Choi et al. [45] characterised graphene conductivity at $4.8 - 600$ THz using FT-IR. A similar selection of SLG and FLG samples and substrates have been analysed compared to TDS. This includes CVD graphene on quartz [40] and SiO_2/p-Si [44, 48], as well as thermal decomposition graphene on SiC [40, 45]. The main drawback of using SiC as a substrate is its significant absorption in the Reststrahlen band ($18 - 54$ THz), which thus does not allow for accurate measurement results [40, 47]. The conductivity of the graphene film is determined, just as for TDS measurements, by considering the transmission spectrum. Santos et al. [177] have further evaluated the reflectance spectrum of EG grown via thermal decomposition on bulk SiC. Both Ren et al. [44] and Horng et al. [48] used the bottom p-type doped Si layer of their SiO_2/p-Si substrate as a gate to bias their

graphene sample during FT-IR measurements and fitted the results to the Drude model, as illustrated in Figure 2-19.

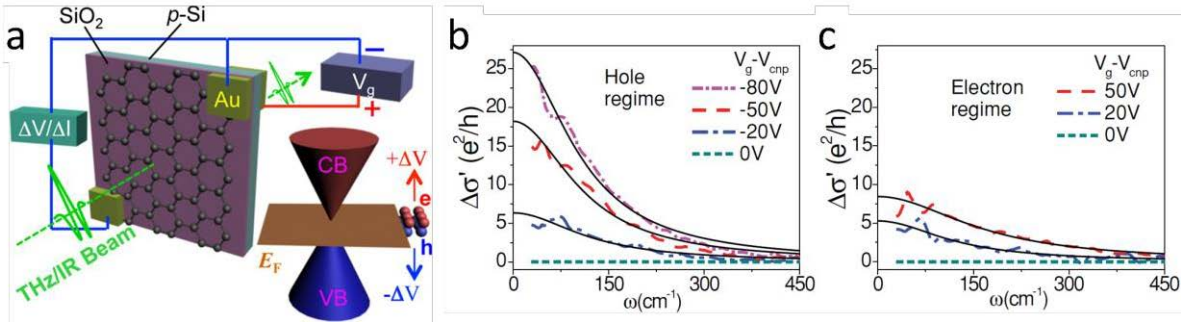

Figure 2-19 FT-IR spectroscopy characterisation of graphene's conductivity. (a) Schematic representation of characterising gated large-area graphene using FT-IR spectroscopy [44]. (b,c) The frequency-dependent conductivity of CVD graphene fit to the Drude model. Modulation of the conductivity spectrum due to gate-induced biasing for the (b) hole and (c) electron regime, respectively. Reprinted from [48]

2.4 High-Frequency Applications

2.4.1 Antennas

Most antennas are currently realised with a variety of different metals. Metals offer high electrical conductivity and are relatively inexpensive, and many antenna fabrication processes are available [178]. Copper is currently the most widely used material for fabricating antennas in the high-frequency and microwave frequency range. However, metals suffer from significant conductivity and skin depth degradation in the THz regime, resulting in high ohmic losses [49, 179].

Using graphene allows for the design of optically transparent antennas [52, 180, 181], flexible antennas for wearable electronics [111, 182], and miniaturised nanoantennas for high-speed data transmission at the nanoscale [183, 184]. Furthermore, graphene's tunability can reconfigure antennas in various ways, such as dynamically changing its radiation pattern [61, 185, 186]; resonance frequency [49, 55, 183, 186] and frequency scanning [62, 63]; and beam scanning at a fixed frequency [62, 64].

The use of metal in conjunction with graphene, e.g., at graphene metal contacts for biasing or feeding the EM wave emitters, has previously been shown to result in large contact resistances [187]. This has been identified as an issue, particularly in GFET applications, as it hinders the achievement of significant gain values [188, 189], and reducing the contact resistance can significantly improve their performance [189]. This can be achieved in various

ways, with the most prominent one being the use of high work-function metals, i.e., nickel [187, 190] or platinum [189], and the use of edge contacts [187, 190]. Jiang et al. [190] managed to reduce the contact resistance down to $4 - 8\ \Omega\ \mu m$ using nickel and edge contacts.

The effect of metal contacts in antenna applications has not been studied to date. However, they have been previously shown to reduce the transmission properties of graphene-loaded transmission lines [191]. The contact resistance is proportional to the contact dimensions, which could pose an issue in the THz region. However, it is generally not considered.

2.4.1.1 Microwave Frequency Range Graphene Antennas

Early near-field characterisation of the exposure of CVD graphene patches deposited on metal microstrip lines to EM fields indicated that graphene is dominated by losses in the X-band ($7.0 - 11.2$ GHz) due to its high sheet resistance. Comparing the effectiveness of the fields radiated by a FLG patch to a copper patch of identical dimensions, it has been shown that their radiation efficiencies were on the order of 20.7 % and 80 %, respectively [192]. A later study on the near-field radiation of capacitively coupled CVD graphene-based patches consisting of one to five layers of graphene indicated that no microwave resonance is present for patches with sheet resistances of $> 0.6\ k\Omega\ \square^{-1}$ and predicted that sheet resistances of $< 10\ \Omega\ \square^{-1}$ are necessary for microwave antenna applications [51]. Regardless, researchers have successfully demonstrated that antennas based on graphene with inferior conductivities still perform sufficiently well depending on their application, e.g., radio frequency (RF) identification devices [112]. However, measured radiation efficiencies are rarely reported as the high surface impedance of a single graphene layer results in high resistive losses at microwave frequencies. Instead, researchers focus on the mechanical properties of the fabricated antennas, such as their flexibility, lightness, and optical transparency.

2.4.1.1.1 Microwave Resonant Antennas

Resonant antennas get their name from their fundamental operating characteristic. They exhibit resonant current and voltage standing waves arising from internal reflections that occur from their structure, such as from edges or open ends. They are also known as standing wave antennas [193].

Dragoman et al. [194] fabricated antennas from RIE-patterned CVD graphene that was transferred onto metal-backed SiO_2/Si wafers (see Figure 2-20(a)). The wideband antenna had two distinct resonances at 8.8 GHz and 11.4 GHz with corresponding reflection coefficients of -12.2 dB and -13.4 dB, respectively. Biasing was applied via a surrounding gold plane,

resulting in a 24 MHz blueshift, as shown in Figure 2-20(b), of the spectrum caused by an impedance mismatch [194].

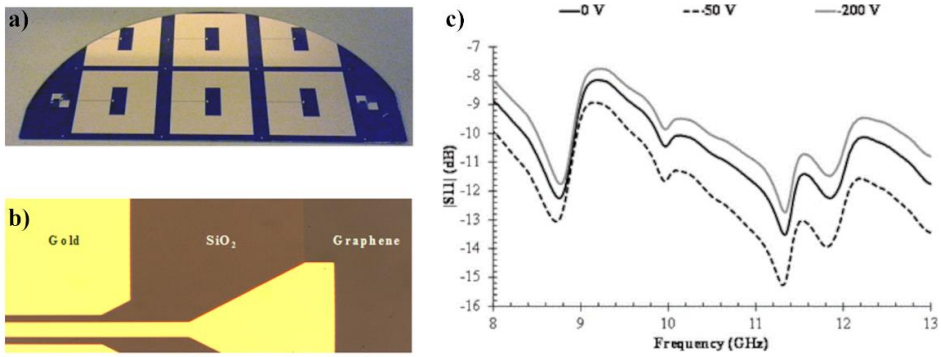

Figure 2-20 (a) Printed graphene patch antennas on the SiO_2/Si substrate surrounded by a gold ground plane. (b) Magnification of the gold, SiO_2, and graphene interface. (c) Measured $|S_{11}|$ values in the X-band for 0, 50, and 200 V biasing voltage. Reprinted from [194]

Kosuga et al. [180, 181] designed optically transparent UV-ozone patterned CVD dipole antennas on quartz, see Figure 2-21(a). The graphene antenna appears electrically larger with its resonance at 20.7 GHz, while a gold antenna with equal dimensions resonated at 9.2 GHz, which is not desirable. Both show similar absorption coefficients of around −10 dB [180].

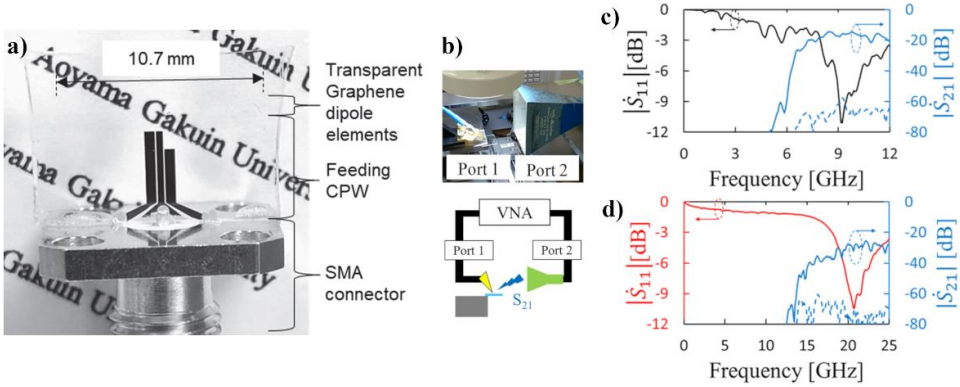

Figure 2-21(a) Optically transparent CVD graphene-based dipole antenna (b) Probe station measurement setup for characterisation of the reflection and transmission coefficients. (c,d) S-parameter measurement results for the (c) gold and (d) graphene antennas. (a) Reprinted from [181] and (b) from [180].

Similar resonances were measured in [181] at 21.6 GHz for the graphene and at 9.5 GHz for the gold dipole, while absorption coefficients varied significantly with −11 dB and −20 dB, respectively. The graphene antenna has a higher directivity compared to the Au antenna, with

6.2 dBi and 5.2 dBi, respectively. It was suggested that SLG behaves like a dielectric rather than a metal [181], making the antenna appear physically smaller.

The dielectric behaviour of graphene was further investigated in [52]. Stacking six thionyl chloride doped CVD graphene layers resulted in sheet resistance of $18\,\Omega\,\square^{-1}$. Stacking individual graphene layers only works for a limited number of layers due to interlayer interactions and impurities [52, 99]. The antenna provided a -10 dB bandwidth (BW) of greater than 3.5 GHz and an average gain of -1 dBi with an average efficiency of 21 %.

Graphene behaves as a variable frequency-independent resistor in the microwave range when subjected to biasing [194]. Metal implementations still significantly outperform graphene ones but lack transparency. Current transparent alternatives are indium tin oxide [195, 196], indium-zinc-tin-oxide [197], fluoride-doped tin oxide [195], silver-coated thin films [198], and metal mesh patches [197, 199]. In particular, metal mesh layers provide sheet resistivities as little as $0.18\,\Omega\,\square^{-1}$ [197] and antenna implementations outperform graphene ones.

2.4.1.1.2 Flexible Graphene Ink Antennas

Due to its high elasticity and mechanical robustness, graphene can be used for flexible antenna applications [200]. Conductive graphene inks, along with metal NPs, conductive polymers, and liquid metals [201], have established themselves for flexible antenna applications [53, 111-115, 182, 202-206].

Huang et al. [112] applied rolling compression to commercially available binder-free graphene ink to increase the conductivity of the deposited film. A half-wavelength dipole antenna was cut out using a doctor-blading technique and showed a reflection coefficient of -11.6 dB at 960 MHz, a 130 MHz -10 dB BW, and a realised gain of -0.6 dBi, which is much lower than the theoretical gain of 2.14 dBi.

In recent publications, Huang et al. [111, 202] analysed the properties of flexible transmission lines and various antenna designs made of graphene ink-based graphitic films. Repeated bending of a transmission line had little effect on its transmission properties (see Figure 2-22(g)). The antenna had resonated at 1.97 GHz and 3.26 GHz with a -18.7 dB and -19.2 dB reflection loss, respectively, and was insensitive to bending, see Figure 2-22(e,f).

Song et al. [114] deposited graphene ink on a PTFE substrate to fabricate a flexible microstrip antenna array. It resonated at 2.46 GHz, had a return loss of -40.28 dB, BW of 120 MHz. It had a maximum gain of 6.78 dB and was comparable to its copper counterpart with a resonance at 2.44 GHz, -33 dB return loss, 80 MHz BW, and 7.11 dB maximum gain. Tang et al. [204] investigation of the sensitivity of graphitic film-based patch antennas showed

a higher sensitivity at 9.8, compared to their copper counterpart at 5.39. In a later study, Zhang et al. [205] increased the sensitivity of graphitic film-based antennas to 35.6 using a poly-based substrate. Their results show the possibility for graphitic film-based antenna applications in human health or motion detection.

Owning to the possibility of depositing thicker layers of graphene ink, the introduction of rolling compression, and the use of binder-free graphene inks, graphitic films with metal-like conductivities can be fabricated. These techniques could resolve the issue of high impedance dominating EG microwave antennas. Graphitic films are particularly well-suited for lightweight, flexible, wearable antenna applications due to their superior robustness when compared to metallic films. Moreover, they are low-cost and readily available.

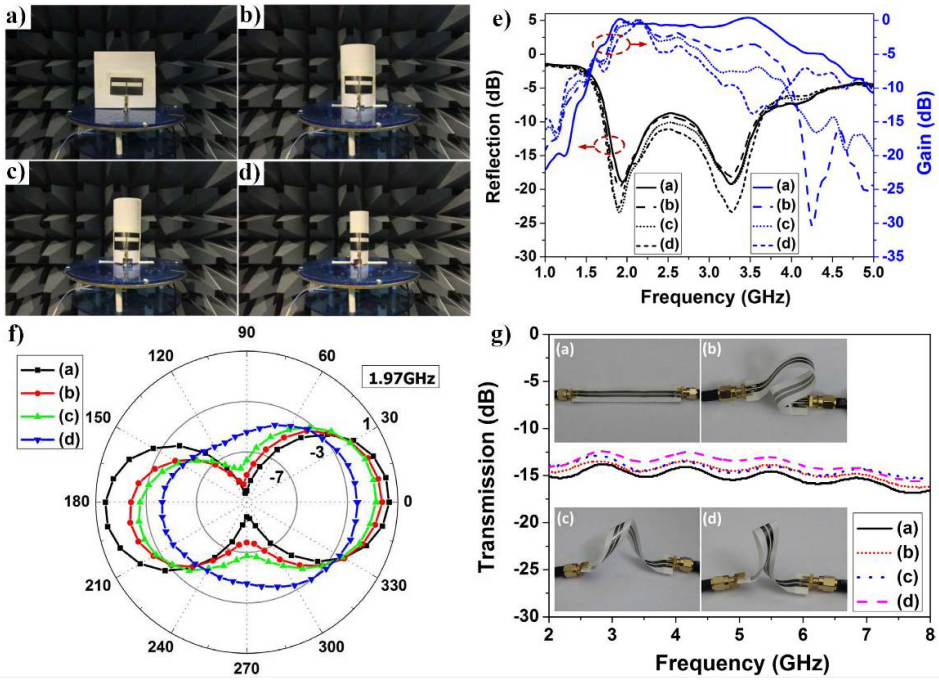

Figure 2-22 Flexible complementary dipole antenna made of binder-free graphene ink-based graphitic film. (a-d) Antenna under different bending radii: (a) un-bend, (b) bend with $5\ cm$*, (c)* $3.5\ cm$*, and (d)* $2.5\ cm$ *radius. (e, f)) Measurement results of graphitic film antenna for different bend scenarios (a-d) (e) Reflection coefficient and realised gain, (f)* $1.97\ GHz$ *radiation patterns. (g) Transmission performance of (a) un-bent, (b) bent, and (c,d) twisted transmission line made out of the graphitic film. Reprinted from [111]*

2.4.1.1.3 Graphene-Assisted Tunable Antennas

Metallic antennas can be designed to exhibit dynamic tunability by linking them with graphene or graphene-derived devices, so-called graphene-metal-hybrid antennas. Various metallic antennas that have been combined with patches made of either graphene flakes [53,

54, 207] or CVD graphene [208], or CVD graphene-based capacitors [209, 210] have been demonstrated.

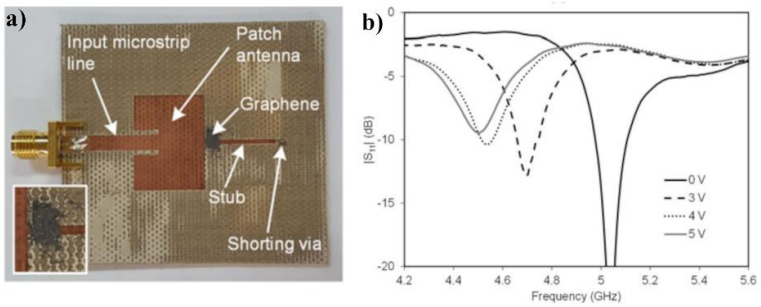

Figure 2-23 Experimental evaluation of tunable graphene-assisted metal patch antenna. (a) The fabricated copper patch antenna is connected to a stub via a graphene-flake-based patch. (b) Measured reflection coefficient under different graphene patch biasing conditions. Reprinted from [54]

Table 2-2 Comparison of microwave antenna implementations

Technology	Design	Operation Frequency [GHz]	Conductivity/ Sheet Resistance	Return Loss [dB]	Gain	Ref.
Copper on acryl	Patch antenna (36 mm × 40 mm)	2.45	$0.02\ \Omega\ \square^{-1}$	-12.5	4.75 dB	[197]
CVD SLG on SiO_2/Si	Tunable folded slot antenna (9.5 mm × 2.9 mm)	8.8, 11.4	-	-12.2, -13.4	-	[194]
Gold on quartz	Dipole antenna (10.7 mm)	9.5	$4.1 \times 10^7\ \mathrm{S\ m^{-1}}$	-20	5.2 dBi	[181]
Multilayer film IZTO/Ag/IZTO	Transparent patch antenna (36 mm × 40 mm)	2.45	$2.52\ \Omega\ \square^{-1}$	-8.4	-4.23 dB	[197]
Copper mesh on acryl	Transparent patch antenna (36 mm × 40 mm)	2.45	$0.18\ \Omega\ \square^{-1}$	-14.5	2.63 dB	[197]
$SOCl_2$ doped CVD FLG on quartz	Transparent wide planar antenna (75 mm × 25 mm)	4 (3.5 GHz BW)	$18\ \Omega\ \square^{-1}$	-40	-1 dBi (avg.)	[52]
Indium tin oxide on glass	Transparent patch antenna (12 mm × 8.85 mm) with frequency-selective surface	5.725 − 5.850	$7\ \Omega\ \square^{-1}$	< -10	-6 dBi	[196]
CVD graphene on quartz	Transparent dipole antenna (10.7 mm)	21.6	$4 \times 10^6\ \mathrm{S\ m^{-1}}$ ($750\ \Omega\ \square^{-1}$)	-11	6.2 dBi	[181]

Ag-NP ink on PET	Flexible Z-shaped microstrip patch antenna (34 mm × 25 mm)	0.9, 2.4	-	−16.45, −26	16.74, 16.24 dBi	[211]
Graphene ink on paper	Flexible half-wavelength dipole antenna (68.82 mm)	0.96 (112 MHz BW)	4.3 $\times 10^4$ S m^{-1} (3.8 Ω □$^{-1}$)	−11.6	−0.6 dBi	[112]
Copper film on PTFE	Flexible microstrip array antenna (2 × 2)	2.44 (80 MHz BW)	-	−33	7.11 dB	[114]
Graphene ink on PTFE	Flexible microstrip array antenna (2 × 2)	2.46 (120 MHz BW)	1×10^6 S m^{-1}	−40.28	6.78 dB	[114]
Copper on polyimide	Flexible hybrid-shaped patch antenna (30.4mm × 38mm)	3.5, 6.7, 12	-	> 1.69	1.69 dBi	[212]
Graphene ink on PDMS	Flexible circularly polarised patch antenna (13.9 mm × 14 mm) over an artificial magnetic conductor	5.8 (1.4 GHz BW)	1.13 $\times 10^6$ S m^{-1}	−37.5	6 dBic	[182]
Copper on RT/Duroid 5880 or Wangling Ltd.	Diode reconfigurable circularly polarised antenna array (1 × 4) over an artificial magnetic conductor	1.65 (350 MHz BW)	-	< −10	13 dBic	[213]
Copper on Teflon (Graphene assisted)	Tunable slot antenna (25 mm × 15 mm) with graphene ink extension	2.83–6	-	< −10	−1.7 dBi	[53]
Copper on PCB (Graphene assisted)	Tunable patch antenna with biased graphene ink stub	5.05, 4.5	< 100− > 1 000 Ω □$^{-1}$	< −20	2.38 dB	[54]
Copper on PCB (Graphene assisted)	Beam steering (± 16°) phased array with biased CVD graphene phase shifter	4.5	580 − 2 500 Ω □$^{-1}$	−20	3.3 dB (V_{bias} = 0.7 V)	[214]
Copper on PCB (Graphene assisted)	Beam steering (90°, 270°) dual Vivaldi printed antenna with biased graphene nanoplate resistors	30	-	< −10	3.8 dBi	[207]

Wang et al. [214] realised a beam-direction reconfigurable antenna array using a CVD graphene capacitor-based reflective phase shifter. Applying 0.7 V and 5.0 V bias voltages to the graphene-based capacitor changed the main beam direction in the azimuth plane from 16° to −16°. Yasir et al. [54] connected a metallic patch antenna to a stub using a graphene-flake-

based patch. A 0.55 GHz frequency shift was achieved with 5 V applied to the patch, as shown in Figure 2-23.

The radiation pattern and polarisation of microwave antennas are readily reconfigured, for instance, using ferrite elements as phase shifters [178] or RF switches such as MEMS [215] or diodes [213, 216]. These approaches have been designed while striving to maintain relatively high radiation efficiencies [216]. A comparison of several graphene and non-graphene-based microwave antennas is given in Table 2-2.

2.4.1.2 Terahertz Antennas

The EM wavelength confinement associated with SPPs in graphene at THz frequencies is one of the main reasons why the focus in graphene antenna research lies in the THz range [55, 217]. Furthermore, graphene's dynamic tunability can be used for reconfiguration of their resonance frequency [49, 55, 183], directivity [61, 179], and radiation pattern [61, 185]. The results of the references presented in this section are all based on numerical modelling. The models of graphene THz antennas are based on the Kubo conductivity formula introduced in 2.1.2. Here, I focus mainly on research that considered resonant antennas, Yagi-Uda, and LWAs.

2.4.1.2.1 THz Resonant Antennas

The main focus around resonant graphene antennas is on dipole [55, 99, 184, 218, 219], patch [183, 184, 217, 220-224], and bowtie [225] antennas due to their simple planar design and fabrication potential. In simulations, tunability is achieved by varying the Fermi level E_F within graphene's conductivity model. It is crucial that researchers use conservative values that can realistically be achieved using common biasing concepts. For unbiased graphene, a E_F of $0 - 0.2$ eV and a relaxation time of $\tau = 0.5 - 1$ ps are often chosen because they give a good representation of real graphene [49, 55, 90]. At the same time, biasing structures should be considered in a realistic design.

Tamagnone et al. [55] designed a plasmonic dipole using a two-layer graphene stack. Due to the high input impedance, they can be matched to THz photomixers. Increasing E_F resulted in higher conductivity and improved radiation efficiency. The total efficiency, including the photomixer, was $0.25 - 3.2$ %, compared to ~ 20 % for their metallic counterpart, which lacks tunability and is roughly $\times 20$ larger, see Figure 2-24. The high input impedance of graphene antennas is often seen as a drawback, as many RF sources are currently designed with an output impedance of $50\ \Omega$. The capacitively coupled graphene patch antenna in [183] provided a $50\ \Omega$ input impedance. The graphene antenna resonated at 1.0193 THz, had directivity and gain of

6.82 dB and 5.08 dB, respectively, and a radiation efficiency of 66.72 %. A comparable copper antenna resonates at 1.0541 THz; it had a directivity and gain of 6.92 dB and 6.05 dB, respectively, and a radiation efficiency of 82.67 %. The resonance frequency was tuned within $959.39 - 1028.03$ GHz, which was a rather small range, by varying E_F between $0 - 0.45$ eV.

Dash and Patnaik [223] designed a 50 Ω circular off-centre-fed planar graphene antenna on a Si substrate with a metallic backplane. The graphene antenna design resonated at 0.75 THz with an ultra-wideband impedance BW of 370 % (≈ 2.8 THz). A comparable copper antenna resonated at 1.25 THz and was narrowband with a 2 % (≈ 0.2 THz) BW. Dash and Patnaik [49] also compared graphene, CNT, and copper-based dipole antennas with equal dimensions. The antennas were designed with a length of $L = 71$ µm on top of SiO_2 substrate. The graphene, CNT, and copper antennas had resonance frequencies of 0.81, 1.42, and 1.9 THz, as well as directivities of 4.5, 3.5, and 2.2 dBi, respectively.

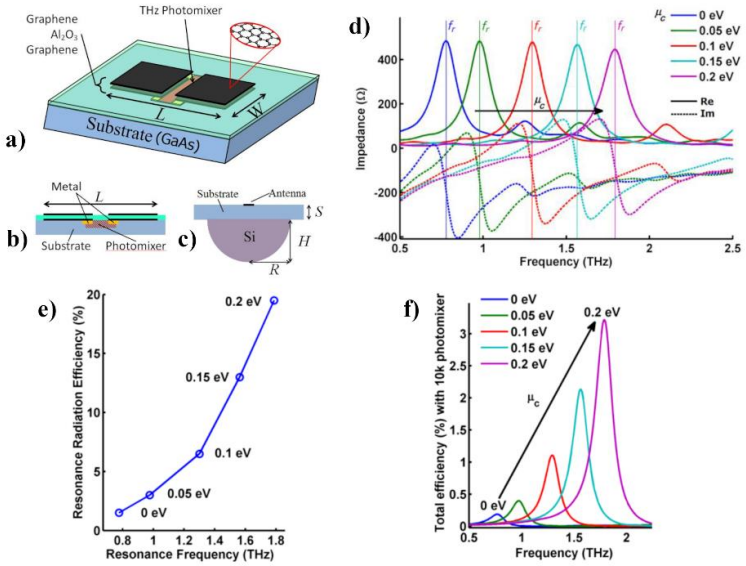

Figure 2-24 (a-c) Chematic of the photomixer-coupled two-layer graphene stack dipole antenna. (d) Real and imaginary parts of the graphene antenna's input impedance and its dependence on E_F. (e-f) Simulated (e) resonance radiation efficiency and (f) total antenna efficiency. Reprinted from [55]

Bowtie antennas are a planar variant of biconical antennas consisting of triangular radiating patches that permit wideband operation [178]. Zhang [225] designed a graphene-based bowtie antenna. It had a -10 dB BW of < 10 % and showed a wide tunability range. Graphene resonant THz antennas have demonstrated dynamic reconfiguration of their resonance frequency and radiation patterns. They generally operate with wider BWs compared to metallic

implementations, and SPP resonances facilitate up to 20-fold antenna miniaturisation. However, their radiation efficiencies suffer from SPP dispersion losses. Operating resonant graphene THz antennas outside of the SPP range could improve the antenna performance but at the cost of reconfigurability and size [64]. Table 2-3 gives an overview of several graphene and non-graphene implementations of THz resonant antennas.

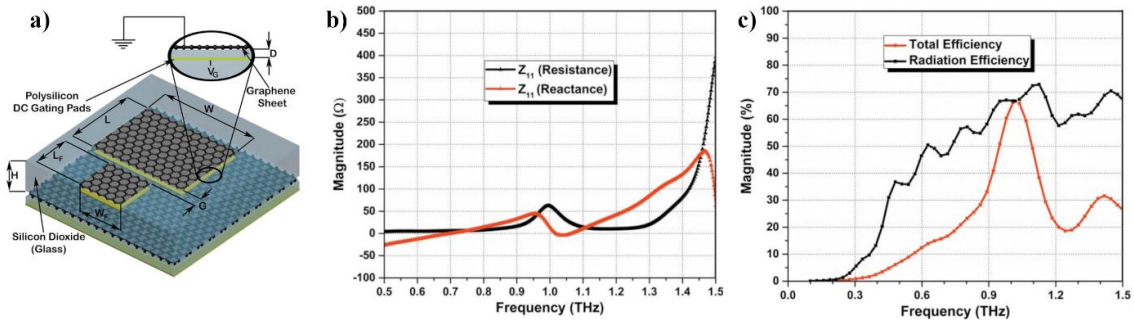

Figure 2-25 (a) 50 Ω capacitively-coupled graphene patch antenna on a glass substrate. (b) Antenna's frequency-dependent input impedance. (c) Antenna's radiation and total efficiency. Reprinted from [183]

2.4.1.2.2 Yagi-Uda Antennas

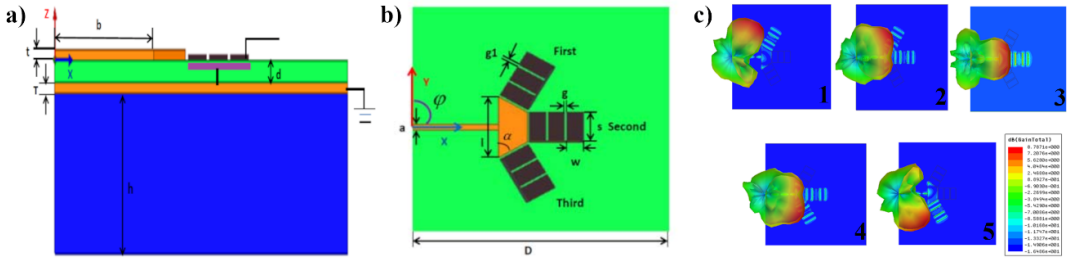

d)

The group which is applied by 15V	First	First Second	Second	Second Third	Third
Minimum return loss(dB)	-35dB	-23dB	-38dB	-23dB	-35dB
-10dB Return Loss Bandwidth	7%	9.2%	7.1%	9.2%	7%
Peak Gain(dB)	6.8	7.79	7.56	7.79	6.8
Deflection Angle (φ)	50°	30°	0°	-30°	-50°
Efficiency	91.2%	92.7%	92.3%	92.7%	91.2%

Figure 2-26 (a) Schematic representation of a graphene-Metal hybrid Yagi-Uda antenna. (b) Top-view of the antenna showing three 60° separated graphene-based director patch arrays. (c) 3D radiation patterns for five (1-5) operating states: (1) only top antenna, (2) top and middle antennas, (3) only middle antenna, (4) middle and bottom antennas, and (5) only bottom antenna in operation. (d) Table of antenna parameters for those five (1-5) operation conditions. Reprinted from [61]

Table 2-3 Comparison of numerically modelled THz resonant antennas

Technology	Design	Frequency [THz]	Return Loss [dB]	Directivity (Gain)	Radiation Efficiency [%]	Ref.
Metal on various substrate	THz antennas ($r = 100$ μm) on photonic BG-based crystal polyimide	$0.626 - 0.63$ (BW of $26.47 - 29.79$ GHz)	-28.49 to -59.15	$8.9 - 10.1$ dBi ($8.34 - 9.45$ dB)	$82.6 - 90.6$	[226]
Graphene on polyimide	GNR patch antenna (88.98 μm × 133.2 μm)	0.75	< -35	5.71 dBi (5.09 dB)	86.58	[220]
Graphene on Si	Circular planar antenna ($r = 22$ μm)	0.75 (2.8 THz BW)	-28	5 dBi	-	[223]
Graphene on SiO_2	Dipole antenna (71 μm)	0.81	-39	4.5 dBi	-	[49]
Copper on SiO_2	Capacitive coupled patch antenna (60 μm × 100 μm)	1.0541 (77.43 GHz BW)	-	6.92 dBi (6.05 dB)	82.67	[183]
Copper on Si	Circular planar antenna ($r = 22$ μm)	1.25 (0.2 THz BW)	-12.5	-	-	[223]
CNT on SiO_2	Dipole antenna (71 μm)	1.42	-25	3.5 dBi	-	[49]
Copper on SiO_2	Dipole antenna (71 μm)	1.9	-20	2.2 dBi	-	[49]
Gold on graphene on SiO_2/Si	Switchable gold dipole antenna (120 μm) on large-area graphene	1.05	-	'On': 2.72 dBi 'Off': -43 dBi	95.8	[185]
Graphene on Al_2O_3 on GaAs	Tunable plasmonic dipole PCA (11 μm × 7 μm)	$0.8 - 1.8$ ($E_F = 0 - 0.2$ eV)	-	-	$2 - 20$	[55]
Graphene on SiO_2	Tunable capacitive coupled patch antenna (60 μm × 100 μm)	$0.96 - 1.03$ (~80 GHz BW) ($E_F = 0 - 0.45$ eV)	-24 to -39.2	6.82 dBi (5.08 dB)	66.72	[183]
Graphene on quartz	Tunable bowtie PCA (12 μm × 5 μm)	$1.8336 - 4.3825$ ($E_F = 0.1 - 0.6$ eV)	-29.5 to -51	-	-	[225]
Indium tin oxide on glass	Transparent patch antenna (95 μm × 147 μm)	2.15 (2.3 THz BW)	-32	4.97 dBi	79.6	[227]

Yagi-Uda antennas are a type of low-profile travelling wave antenna and are generally used in high directivity/gain applications. THz Graphene Yagi-Uda antennas are a common research

topic for various high-gain applications due to their plasmonic effects and dynamic tunability [61, 179, 186, 228-230].

Nissiyah and Madhan [179] designed a graphene-based Yagi-Uda photoconductive antenna (PCA) with directivity and gain of 9.57 dB and 8.64 dBi, respectively, while a comparable bare graphene antenna had lower directivity and gain of 6.77 dB and 4.88 dBi, respectively.

Hai-Qiang et al. [61] created a Yagi-Uda antenna array of three 60° spaced graphene director regions that were coupled to one metal radiating patch, as shown in Figure 2-26. Biasing the graphene director array enabled or disabled the emission in a particular direction, resulting in reconfigurable radiation patterns. Similarly, Luo et al. [186] extended this technique to cover a full 360°, in 60° increments. Six Yagi-Uda arrays were placed in a hexagonal arrangement around a point feed.

2.4.1.2.3 Leaky Wave Antennas

LWAs are a type of travelling wave antennae where, in contrast to resonant antennas, the EM wave is guided along a specific structure. Designs have achieved high directivity, narrow beamwidth radiation patterns, and broadband frequency responses [62, 64, 70, 74, 231-234]. They also offer frequency and fixed-frequency beam scanning capabilities. Planar designs are generally easy to fabricate, and they do not require complex feeding networks [178].

Distinctions are made between their uniform or periodic guiding structures, modulating elements, and the number of dimensions of the guiding structure. Thus, the main LWA types are one-dimensional (1D) uniform/quasi-uniform, 1D periodic, 2D uniform/quasi-uniform, and 2D periodic [178]. Graphene's tunability has been used to demonstrate frequency scanning of the main beam direction [62, 63] and scanning the main beam (beam scanning) at a fixed frequency [62, 64].

Esquius-Morote et al. [63] used the principle of a sinusoidally modulated reactance surface. The 1D LWA consisted of a periodically arranged set of polysilicon pads that created a grating on a back-metalised SiO_2 substrate, as illustrated in Figure 2-27. Changing the number of polysilicon pads N, resulted in beam scanning at a fixed frequency. The radiation patterns were calculated using both full-wave simulations and LWA analytical theory [178]. A radiation efficiency of about 11 % was achieved. Gómez-Díaz et al. [62] also sinusoidally modulated the reactance of a graphene strip by periodically widening and narrowing its width, see Figure 2-28(a). A much simpler biasing structure was employed, and the biasing of graphene resulted in beam scanning at a fixed frequency. The LWA operates at various frequencies and permits frequency scanning, as shown in Figure 2-28(d-e).

Fuscaldo et al. [64] placed a single graphene sheet inside a grounded dielectric multilayer stack to form a Fabry-Pérot cavity 2D LWA. Here, ordinary (non-plasmonic) propagating leaky modes were excited to reduce plasmonic losses. Two separate graphene LWAs were designed – a graphene-based single layer and a graphene-based double-layer antenna. The single-layer antenna had an efficiency of ~70 % and suffered from low directivity. The double-layer antenna had a much higher directivity and could reach efficiencies of ~95 %. Both surpass the upper limits of the SPP-based antenna designs. Furthermore, high efficiencies come at the cost of reconfigurability, and a trade-off between directivity, efficiency, and tunability must be made [64].

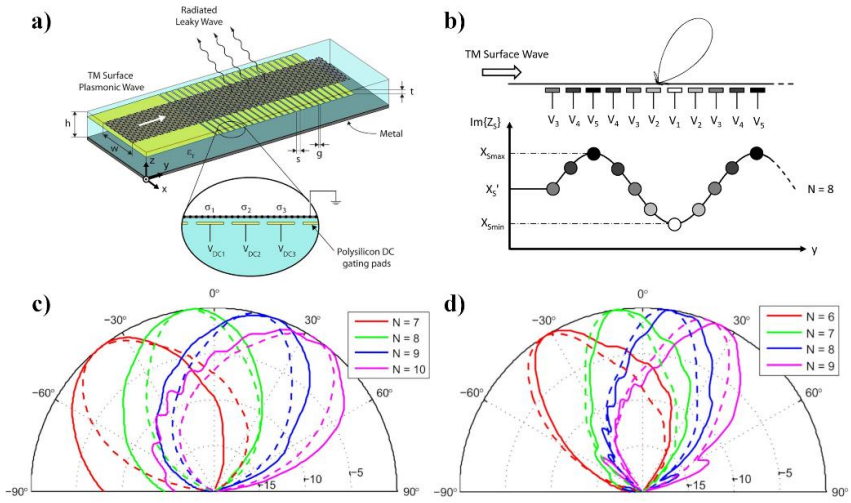

Figure 2-27 Graphene microstrip-based tunable leaky-wave antenna. The graphene strip is sinusoidally biased to achieve the desired reactance profile. (a) Schematic diagram of the leaky-wave antenna. The conductivity of the graphene strip is modulated via electrostatic biasing using polysilicon pads below the graphene strip to achieve the emission of leaky modes. (b) Biasing profile: Dependence of surface reactance on biasing voltage. (c, d) Comparison of the radiation pattern from full-wave simulation (solid) and leaky-wave antenna theory (dashed lines) for different permittivity substrates (c) $\epsilon_r = 3.8$ and (d) $\epsilon_r = 1.8$. Reprinted from [63]

Soleimani and Oraizi [70] proposed the use of complementary graphene patch cells, which they also extended to create a holographic 2D LWA. The antenna was edge-fed and designed for an operating frequency of $f_0 = 2$ THz and for the maximum radiation direction $(\theta, \phi) = (45°, 45°)$. Simulations indicated the maximum radiation direction to be $(\theta, \phi) = (53°, 45°)$ with a directivity of about 13.5 dBi and a radiation efficiency of 20 %. Tuning E_F within a range of $0.4 - 0.65$ eV enabled beam scanning in the elevation plane within $43° < \theta < 73°$.

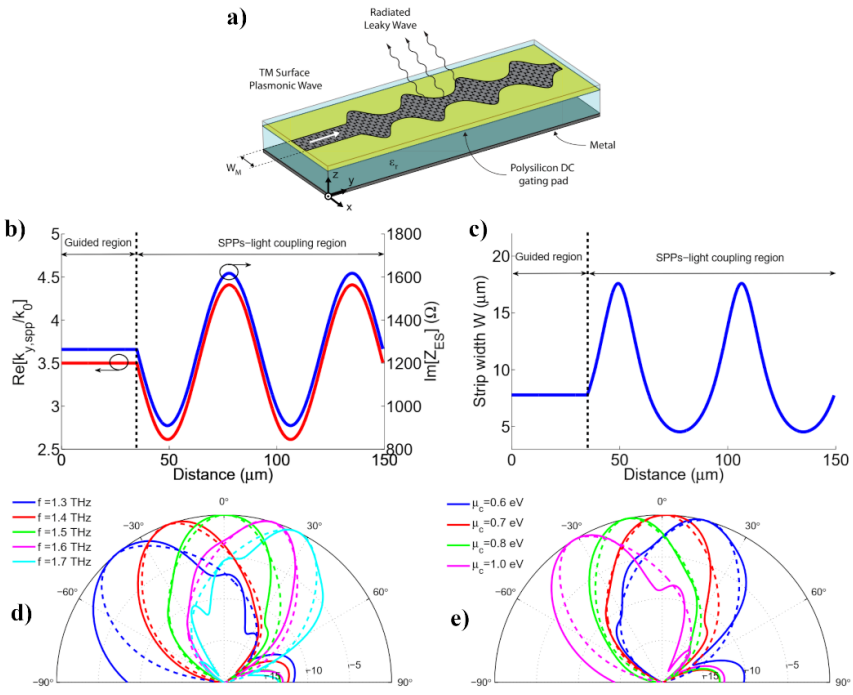

Figure 2-28 Graphene-based tunable leaky-wave antenna. (a) Schematic diagram of periodically width modulated graphene waveguide for the emission of leaky modes. (b) Normalised phase constant and surface reactance along the y-axis, the long direction of the waveguide. (c) Non-sinusoidal profile of the graphene strip width along the y-axis. (d, e) Comparison of the radiation pattern from full-wave simulation (solid lines) and leaky-wave antenna analytical theory (dashed lines) to visualise scanning capabilities: (d) frequency scanning of the beam and (e) beam scanning at fixed frequency $f = 1.5\ THz$. Reprinted from [62]

LWAs are highly suitable for complementary metal-oxide-semiconductor (CMOS) integration [235]. Most non-graphene implementations focus on the microwave frequency range [235-238], with fewer implementations exploring the THz range [235, 238-240]. The main focus has been on the development of highly efficient, high directivity, and wide scan angle implementations for communication applications. As such, much interest has been in the reconfiguration of their polarisation [237], beam scanning [236], and multiplexing [239, 240]. RF switches, such as diodes [235] or MEMS [241], are commonly used to achieve reconfigurability. Table 2-4 gives an overview of several graphene and non-graphene-based travelling-wave antenna implementations.

Table 2-4 Comparison of numerically modelled THz travelling-wave antennas

Technology	Design	Frequency [THz]	Steering/ Scanning range	Directivity (Gain)	Radiation Efficiency [%]	Ref.
Metal on GaAs	Yagi-Uda PCA on low-temperature grown GaAs	0.636	-	10.8 dBi	80.1	[242]
Graphene on GaAs	Graphene-based Yagi-Uda PCA	1	-	9.57 dBi (8.64 dB)	-	[179]
Au/Ti on glass	Double-sided planar quasi-Yagi-Uda antenna with complementary dipole excitor	2	-	(4.97 dB)	~95	[243]
Graphene-copper hybrid on SiO_2/Si	Beam steering three armed Yagi-Uda antenna with graphene directors	0.5	$\pm 50°, \pm 30°, 0°$	$(6.8 - 7.79$ dB)	> 91	[61]
Graphene-metal hybrid on polyimide	Beam steering three-layer multi-beam Yagi-Uda antenna with graphene dipoles	$1.136 - 1.220$	360° in 60° steps	$5.7 - 6.5$ dB	-	[186]
Graphene on SiO_2/poly-Si	Beam scanning LWA through N-periodic modulation of graphene	2	$-45.4°$ to 37.5° (for $N = 6 - 9$)	-	11	[63]
Graphene on SiO_2/poly-Si	Frequency and beam scanning LWA via width-modulated graphene	$1.3 - 1.7$	$\sim -40°$ to 30° for $f_0 = 1.3 - 1.7$ THz $\sim -30°$ to 20° for $E_F = 0.6 - 1$ eV	-	$5 - 20$	[62]
Graphene on SiO_2/poly-Si	Beam steering complementary graphene patch metasurface 2D LWA with	2	$43° - 73°$ for $E_F = 0.4 - 0.65$ eV	13.5 dBi	20	[70]
Metal on indium phosphide/Si	Frequency scanning periodic microstrip line LWA	$0.23 - 0.33$	$-46°$ to 42°[1] for $f_0 = 0.23 - 0.33$ THz	11 dBi [1]	60	[238]
Dielectric slab RO6010/ RT/duroid 5880 /alumina	Frequency scanning multilayer dielectric slap with periodic metallic discs	$0.1575 - 0.2015$	$-23°$ to 38° for $f_0 = 0.1575 - 0.2015$ THz	$(10.5 - 15$ dBi)	> 60	[244]

[1] Experimentally validated result

2.4.1.3 Graphene Antennas on SiC

CVD graphene or graphene ink antennas have only been experimentally characterised to date. Similarly, simulations usually consider quartz, SiO_2, or Si substrates. However, SiC is of particular interest in high-power and high-temperature applications [245] and has recently been demonstrated to have a high level of biocompatibility [246].

Over 250 polytypes of SiC exist, but their dielectric properties in the upper microwave and THz range are generally not researched due to the lack of available high-quality samples and limited interest in it [247]. Measurements of the loss tangent of bulk 6H-SiC within the microwave and THz range were conducted. As Figure 2-29 indicates, they demonstrated that the possibility of low dielectric losses exists. Semi-insulating SiC offers a high dielectric constant ($\epsilon_r \cong 9.7$), low conductivity ($\sigma \cong 10^{-5}\ \mathrm{S\,m^{-1}}$), and low loss tangent ($\tan(\delta) \cong 10^{-6}$). It has the potential to facilitate achieving high antenna efficiency and miniaturisation [245]. The latter is strictly dependent on the relative permittivity and dimensions of a patch antenna, which, for example, reduce to $\sim\lambda_0/5$ for a dielectric medium with $\epsilon_r = 10$ [178]. However, this reduction in size comes at the cost of reduced BW [178].

Further research will need to be conducted, particularly on epitaxial SiC on Si, and the direct growth of EG on SiC/Si [13] could offer an exciting platform for graphene applications from the microwave to THz regimes. Being bound to the SiC, the material properties would need to be understood and considered in the design of any subsequent graphene-based devices. This would be particularly true in the Reststrahlen band of SiC owing to the near-total reflection of EM waves from it and the surface plasmon-phonon coupling [26, 248].

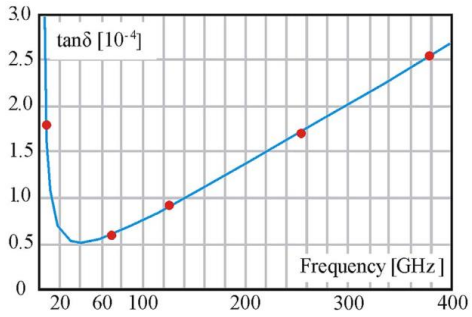

Figure 2-29 Experimentally measured values of the loss tangent tan(δ) of bulk 6H-SiC at five frequency points and their curve fit. Reprinted from [247]

2.4.2 Beamforming

Apart from using antenna arrays, beams can be generated and controlled with metamaterials or metasurfaces. Ideally, the emitted EM waves should experience no amplitude modulation

and beamformers that provide a complete 360° phase response are highly desired [249]. Most commonly, graphene reflectarray and transmitarray metasurfaces are considered for beamforming applications.

2.4.2.1 Reflectarray Antennas

Reflectarray antennas are made up of an array of unit cells in which each acts as a reflecting element. They combine the simplicity of reflector-based antennas with the versatility of array-type antennas [250]. Furthermore, one of their main advantages when compared to phased arrays, for example, is that no complex feeding network is necessary. Reflectarrays are a type of aperture antenna and are most commonly used in the microwave frequency range [251].

Metasurface-based reflectarrays would be particularly well suited in the THz range. Planar metasurfaces are easy to fabricate at micrometre dimensions due to well-defined nanofabrication technologies. Graphene's dynamic can be used for various beam shaping [71, 73, 252, 253], scanning [73, 254-259], polarisation [252, 255], cloaking [260], and many more applications within a wide frequency range from microwave [253, 258, 259], over THz [71, 73, 252, 254-257, 260], to the mid-IR [261, 262].

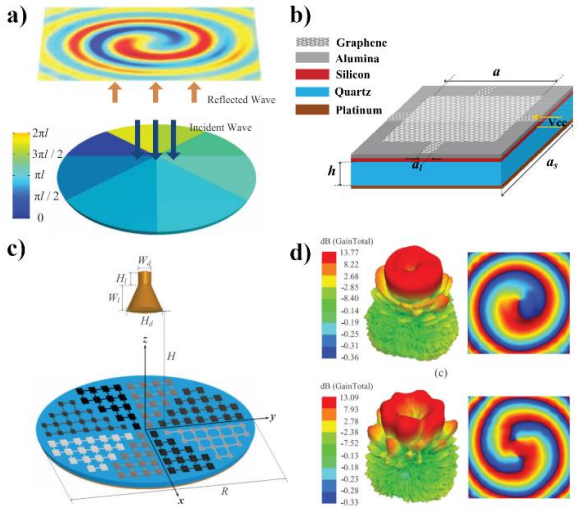

Figure 2-30 (a) Schematic representation of a vortex beam generating reflective surface with N-sectors of varying phase increments. (b) The graphene patch unit cell consists of a platinum-backed quartz substrate and is biased via the Si and alumina dielectric. (c) Horn-antenna fed circular reflectarray consisting of eight equal angular sectors. (d) Radiation pattern and phase front of (top) $l = 1$ vortex beam and (bottom) $l = -2$ vortex beam. Reprinted from [71]

Carrasco et al. [256, 257] compared a graphene reflectarray to comparable metal implementations. Their unit cells were based on simple square patches, and varying graphene's Fermi Level resulted in changes in its surface impedance and, hence, the phase and amplitude

modulation response of the individual unit cells. The modulation response of the unit cells was analysed using equivalent circuit models and full-wave simulations.

Chang et al. [71] designed a vortex beam generating graphene-based reflectarray. The reflective surface of a reflectarray was split into N sectors, that each introduce a phase change between 0 to $2\pi l$, as shown in Figure 2-30(a). $N = 8$ sectors, and $l = 0, \pm 1, \pm 2$ modes led to phase increments of $0°, \pm 45°, \pm 90°$. The patch dimensions and E_F were selected to match the required phase increments and reduce attenuation and, hence, maximise radiation efficiency.

Hosseininejad et al. [73] designed a reprogrammable metamirror that focused the reflected beam to an arbitrary and reconfigurable point. The Fabry-Perot cavity-like unit cells of the metasurface consisted of two graphene patches, which were individually biased, with high-density polyethylene between them on top of a gold-backed Si substrate. Four different values of E_F were each 2-bit coded to yield four states with a 90° phase separation and an amplitude close to 0.7. An elliptical off-centre beam was focused using the proposed reflectarray.

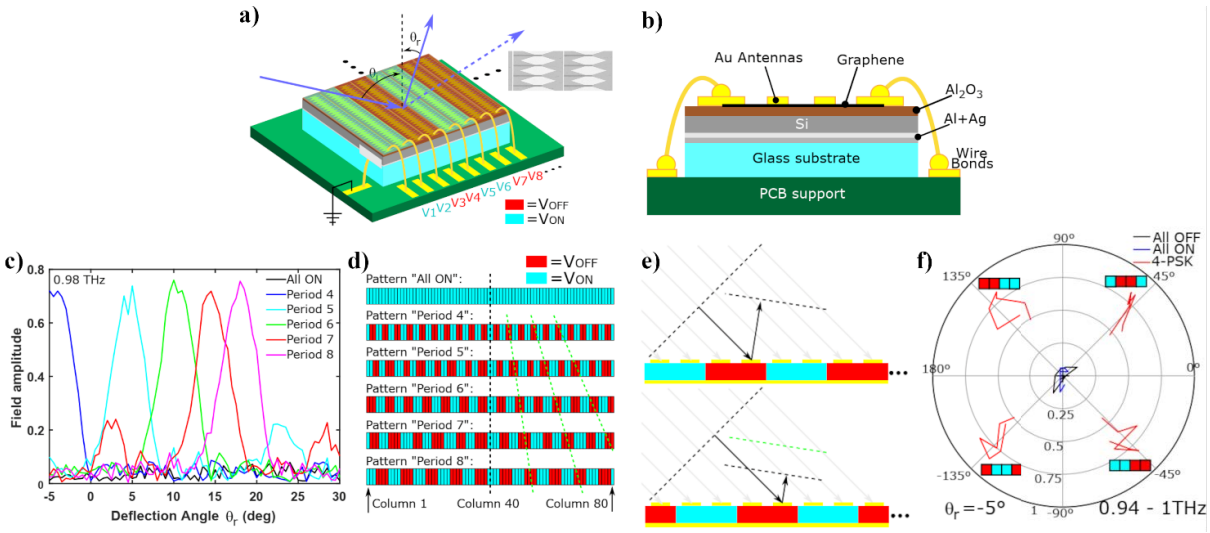

Figure 2-31 Experimental evaluation of the phase modulation over a graphene-based metasurface reflectarray intended for beam scanning. (a) Schematic diagram of the fabricated reflectarray. Inset: Bowtie-based graphene metasurface, including the, interconnects for electrostatic biasing of individual columns. (b) The vertical profile of the reflectarray shows the Si in its biasing structure. (c) Measured results for beam scanning at a fixed frequency by varying the period of a column's 'On' and 'Off' states. (d) Visualisation of the column-based period that was used for the beam scanning results in (c). (e) Example of the phase modulation by moving the period of the 'On' and 'Off' states horizontally, perpendicular to the biasing columns. (f) Measured phase and amplitude of the 4-phase shift keying implementation using the designed reflectarray. Reprinted from [254]

Much of the research on utilising graphene in the THz frequency range focuses on numerical and analytical studies of their designs. One of the first experimentally demonstrated CVD graphene-based metasurface reflectarray was reported by Tamagnone et al. in [254]. It is shown in Figure 2-31(a, b) and was designed to manipulate the phase of an incident s-polarised beam. The unit cell consisted of a gold bowtie antenna chosen for its wideband response and an SLG patch in its centre placed on top of a Salisbury screen configuration [254, 263]. The two operating states, termed 'On' and 'Off', required a $180°$ phase change between each other while maintaining a similar amplitude modulation. The reflectarray was characterised using TDS. Figure 2-31(c, d) shows how periodically biasing the individual columns resulted in controlled tunability of the reflection angle within $-5°$ to $20°$. The reflectarray was further used to demonstrate phase shift keying, see Figure 2-31(e, f). The radiation efficiency was determined to be ~ 6.3 %, while the maximum of an ideal system is limited to 15.8 %.

Graphene acts as a variable resistor in the microwave range, and the lack of reactance complicates phase control [258]. Therefore, most beamforming devices based on graphene are studied at THz frequencies and above. Nevertheless, dynamically controllable examples have been demonstrated in [253, 258, 259]. While the results seem promising, graphene still suffers from high ohmic losses at microwave frequencies, i.e., the reflection amplitude of the EM waves reflected from the metasurface designed by Chen et al. [258] is 0.33, while the structure absorbed the rest.

The concept of graphene-based metasurface reflectarrays shows great potential for dynamic beam steering and beam shaping applications in the THz frequency range. However, the biasing of graphene still poses a technological challenge. Further improvements in efficiency and biasing concepts are required for practical THz reflectarray implementations.

Non-graphene reflectarray implementations currently focus on employing metallic or dielectric resonators [249]. Passive implementations as a lens using aluminium resonators on polypropylene have achieved efficiencies of 80 % at 350 GHz [264], efficiencies of $30-60$ % at 0.7, 1.0, and 1.5 THz using Si as the dielectric [265], and 90 % at ~ 480 GHz using Si/SiO_2 resonators in an all-dielectric metasurface mirror [266]. Reconfiguration has also been achieved using varactor diodes [267], MEMS [268], liquid crystals [269], and more.

Reconfigurable intelligent surfaces [270, 271] are currently highly researched and focus on 5G applications. Here, the phase responses of the reflectarray elements are discretised and binary coded and digitally controlled. First examples of reconfigurable intelligent surfaces have been demonstrated at microwave frequencies.

2.4.2.2 Transmitarray Antennas

In contrast to reflectarrays, where an incident EM wave is modulated and then re-radiated by the metasurface, in transmitarrays, the incident EM wave couples with its metasurface as it passes through it. Their major advantage in comparison to reflectarrays is avoidance of the feed antenna and its supporting structures blocking the fields reflected from its metasurface [250].

Researchers have applied graphene-based transmitarrays in dynamic beamforming applications by modulating the amplitude [272-274], phase [68, 273, 275], and polarisation [68, 276] of the incident EM fields. Tavakol and Khavasi [275] designed a meta-coupler based on hybrid metal-graphene metasurfaces that capture incident propagating waves and couple them to either port of an underlying waveguide. A coupling efficiency of $C = 46\ \%$ (ratio of the surface wave's power at the target port to that delivered by the incident wave to the system) and directivity $D = 19$ dB (ratio of the surface wave power at the target port and at the other port) were achieved.

A polarisation-transforming graphene-based metasurface was designed by Masyukov et al. [68]. A FLG dielectric-metal hybrid structure was employed to induce a chiroptical response. The individual unit cells were formed with dimensionally identical FLG and gold chiral petal ring resonators deposited on the top and bottom, respectively, of a polymethyl pentene substrate. Variation of the ellipticity angle by $20°$ was achieved.

Transmitarrays are less often considered at THz frequencies in comparison to reflectarrays. Generally, a tradeoff between the efficiency and phase control of transmitarrays and reflectarrays needs to be made. For example, a two-layer copper and benzocyclobutene (BCB) based transmitarray reported in [277] achieved a maximum transmission of $95\ \%$ and a y-polarisation beam deflection of $2.4°$ for a single layer at 1.2 THz, and a maximum transmission of $70\ \%$ at 1.15 THz and y-polarisation beam deflection of $6.1°$. A flexible gold and polyimide-based three-layer transmitarray achieves a maximum transmission of $44\ \%$ at 0.9 THz and a beam deflection of $35°$ [278]. However, neither system is reconfigurable.

Reconfigurable non-graphene implementations use the same tunable elements as metasurfaces introduced earlier, e.g. pin diodes [279]. On the other hand, graphene's tunability can reconfigure the characteristics of graphene transmitarrays dynamically. Their biasing architecture needs to be carefully designed as the impinging EM waves will couple to them.

2.4.3 Absorbers

The absorption of EM fields has a wide range of applications, such as EM interference shielding [280], cloaking [281], sensing, spectroscopy, and more. Most absorbers can be

categorised into resonant and broadband absorbers [282]. Resonant absorbers operate at a specific frequency f_0, and generally consist of multiple layers separated by $\lambda_0/4$. Notable examples of resonant absorbers are the Salisbury screen, Jaumann absorber, Dällenbach layer, crossed grating absorber, and circuit analog absorber [282]. For example, a Salisbury screen structure consists of a thin resistive sheet deposited on a ground-backed $\lambda_0/4$ thick dielectric that forms a Fabry-Perot resonator. Its main disadvantage is its sensitivity to the angle of incidence of the fields [263, 283].

A Jaumann absorber is based on the same concept as the Salisbury screen, but several layers of resistive sheets and dielectrics above a ground plane are stacked [263, 284]. An example model is shown in Figure 2-32(a). Stacking many layers results in multiple resonances and, thus, the broadband response of the absorber [282].

Integrating graphene elements into THz absorber applications is of particular interest due to its tunability [72], compatibility with nanofabrication, broadband absorption characteristics [285], and demonstrated absorption enhancements [75]. Many examples of graphene-based absorbers have been demonstrated in the microwave [281, 284, 286-289], THz frequency ranges [66, 69, 72, 285, 290-293], and well into the IR frequency range [75, 294].

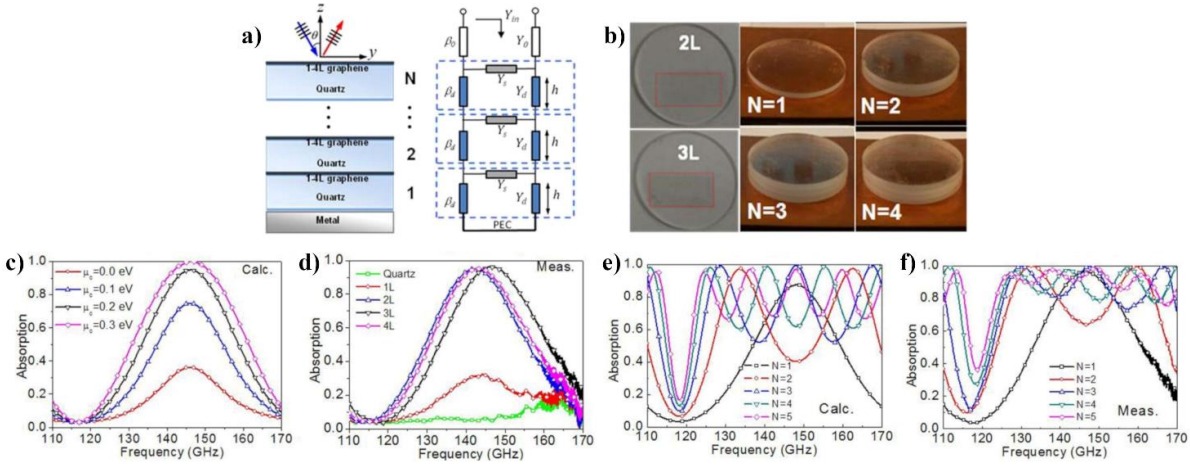

Figure 2-32 Salisbury screen and Jaumann stack absorbers. (a) Schematic and transmission-line model of a graphene Jaumann absorber. (b) CVD graphene on quartz-based Salisbury screen ($N = 1$) and Jaumann stack ($N = 2, 3,$ and 4) absorbers with varying layer count N. (c) Modelled dependence of the absorption of a Salisbury screen absorber on E_F. (d) Measured absorption characteristics of a Salisbury screen absorber for varying numbers of graphene layers. (e) Analytical evaluation of the dependence of the absorption characteristics of a Jaumann absorber on the layer count N. (f) Measured absorption characteristics of graphene-based Jaumann absorbers with different numbers of layers N. Reprinted from [284]

Wu et al. [284] designed a graphene-based absorber in the microwave frequency range using both Salisbury screens and Jaumann stacks. Figure 2-32(b) shows the fabricated absorbers. Each layer consists of numerous CVD SLGs transferred onto a quartz substrate. Simulations showed that varying E_F from 0 eV to 0.3 eV results in a significant increase in the absorption as the impedance of graphene matched to the free space, such that measurements showed that SLG only showed a peak absorbance of ~ 30 %, two layers resulted in the absorption of ~ 95 %. The performance of Jaumann absorbers with up to five layers ($N = 5$) was analysed, which showed an increased BW with increasing layer count. The 5-layer Jaumann stack achieved an absorption of ~ 90 % between $125 - 165$ GHz with a fractional BW of 28 %, as shown in Figure 2-32(e, f).

Tunable graphene-based absorbers in the microwave range generally consist of self-gated graphene-electrolyte-graphene capacitors [281, 286-289]. Similar to the example above, Balci et al. [281] designed a Salisbury screen absorber that operated at 10.5 GHz. Applying a bias of $0 - 1.5$ V allowed for dynamic tuning of the reflection from -3 dB to -45 dB. The graphene-based capacitor itself absorbed $21 - 45$ % of the EM waves, for $V_{\text{bias}} = 0 - 3.5$ V. Zhang et al. [287] explored the possibility of exclusively using graphene-electrolyte-graphene capacitors as absorbers. A single capacitor within a rectangular waveguide absorbed between $50 - 99.79$ % of the EM waves within the spectrum of the waveguide ($3.4 - 4.9$ GHz) with a biasing voltage of $0 - 3$ V.

Long et al. [66] designed and fabricated an absorber based on a graphene sheet covering a SiC-based metasurface, as illustrated in Figure 2-33(a-c). The graphene was electrostatically biased using a solid polymer electrolyte made of lithium perchlorate and polyethylene oxide [295]. Figure 2-33(d, e) illustrate the absorbance spectra measured with FT-IR spectroscopy, and a shift in the absorbance resonance with the application of a biasing voltage was demonstrated. The strong magnetic confinement within the groves of the SiC metasurface and the counter-clockwise electrical current around the grove suggest that magnetic polaritons were excited [66, 296], which had been demonstrated previously by Wang and Zhang [296].

Wu et al. [284] experimentally demonstrated wideband absorption in the microwave range, with total absorption being the desired property. Bao et al. [72] developed a graphene multiband absorber consisting of two SiO_2/graphene/SiC resonator stacks layered on top of each other. The two stacks had dedicated absorption characteristics, and by layering them, their absorption responses were superimposed. Increasing E_F of graphene blueshifted the absorption spectrum and enhanced the absorption. Total absorption was achieved for $E_{\text{F}} = 0.8$ eV.

While the absorption region of graphene-based absorbers is closely linked to their dimensions, they provide limited or no frequency tunability. Researchers suggest combining graphene absorber structures with metallic metasurfaces and tunable elements [288, 289]. Zhang et al. [289] designed a graphene-electrolyte-graphene capacitor-based absorber and coupled it with a varactor-based metallic metasurface. The absorber operates in the microwave range. The absorption frequency can be tuned from $3.1 - 6.1$ GHz by applying a voltage to the varactor diodes, which modifies their capacitance. On the other hand, graphene's tunability is used to modulate the absorption itself, and the reflection amplitude can be tuned from -3 dB to -30 dB. Table 2-5 gives a brief comparison of several graphene and non-graphene implementations of microwave and THz absorbers.

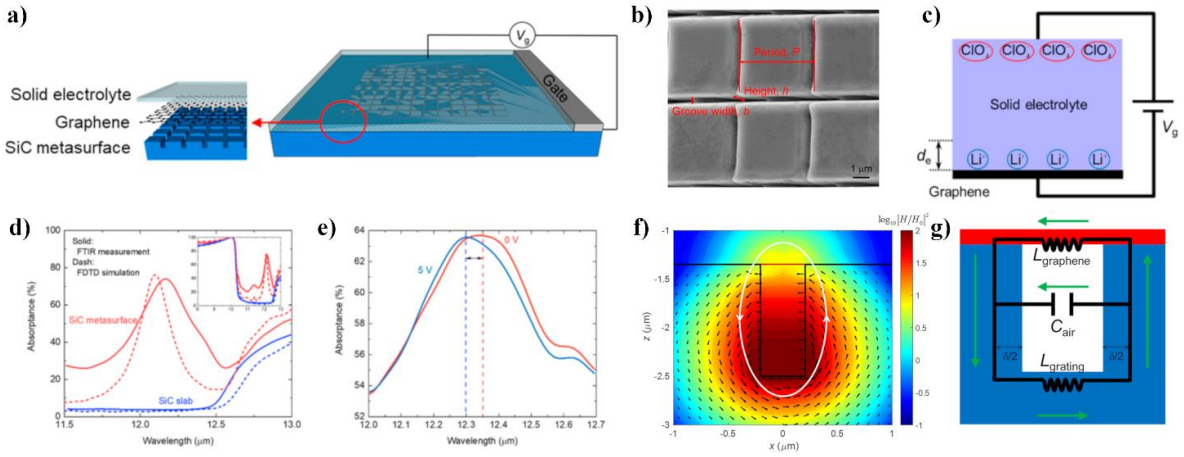

Figure 2-33 (a) Schematic representation of the absorber based on a graphene sheet covering a SiC metasurface. (b) SEM image of the SiC-based metasurface. (c) Application of a voltage to the electrolyte results in the formation of a capacitor due to the movement of free ions (Li^+ and ClO_4^-) (d) Comparison of the measured and simulated (using the finite-difference time-domain method) absorbance spectra of bare SiC (red) and SiC-based metasurface (blue). (e) Measured biasing voltage-dependent absorbance spectrum of the graphene-based absorber. (f) Numerical simulation of magnetic field distribution within the metasurface unit cell. (g) Equivalent circuit model used for the evaluation of the magnetic polariton resonance frequency. Reprinted from [66]

2.4.4 Photodetectors

Apart from the emission and manipulation of EM fields using graphene devices, their detection has become a significant research area [297] owing to graphene's properties. Specifically, its small heat capacity [297, 298], weak electron-phonon coupling [297, 299], and large Seebeck coefficient [299] have been considered. Furthermore, graphene combines several

photocurrent generation mechanisms, such as the photovoltaic effect, the photo-thermoelectric effect (Seebeck effect), the bolometric effect, the photo-gating effect, and the plasma-wave assisted mechanism [300]. The latter is often referred to as the Dyakonov-Shur mechanism [301].

Table 2-5 Comparison of absorber implementations

Technology	Design	Frequency	Absorption [%]	Ref.
Graphene/ electrolyte/ graphene capacitor on top of varactor-based metasurface	Independently tunable graphene/ electrolyte/ graphene-capacitor and varactors metasurface absorber stack	$3.1 - 6.1$ GHz	-	[289]
Graphene/ electrolyte/ graphene capacitor	Tunable N-layer ($N = 1 - 3$) graphene electrolyte capacitor-based Salisbury screen and Jaumann stack absorbers	$3.4 - 4.9$ GHz	$50 - 99.79$ ($N = 1$, $V_{\text{bias}} = 0 - 3\ V$)	[287]
Graphene/ electrolyte/ graphene capacitor	Tunable graphene electrolyte capacitor-based Salisbury screen absorber	10.5 GHz	$21 - 45$ ($V_{\text{bias}} = 0 - 3.5\ V$)	[281]
CVD FLG on quartz	Salisbury screen and Jaumann stack absorbers of $N = 1 - 5$ layers.	$125 - 165$ GHz	~95 ($N = 2$) ~90 ($N = 5$)	[284]
SiO_2/Graphene/SiC	Tunable multiband absorber made of multiple layer stack ($N = 2 - 4$) of SiO_2/ graphene-square-rings/ SiC resonators over a metal layer	$3.67, 4.73, 5.9, 6.9$ ($N = 4$)	98.6 ($N = 4$) 100 ($N = 2$, $E_F = 0.8$ eV)	[72]
Electrolyte-biased CVD SLG on SiC metasurface	Tunable graphene-based metasurface absorber consisting of electrolyte/ graphene/ SiC metasurface stack	24.6 THz ($V_{\text{bias}} = 0\ V$) 25.6 THz ($V_{\text{bias}} = 5\ V$)	~80	[66]
Copper on Fr-4 substrate	Wide-angle TE and TM absorber based on N-blade ($N = 4 - 12$) unit-cell metamaterial	~5 GHz	~99	[302]
Polyimide/ copper/ liquid crystal/ polyimide	Tunable wideband absorber based on liquid crystal	130 GHz (unbiased) 119 GHz (biased)	> 90	[303]
VO_2/Al_2O_3	Tunable absorber based on VO_2 and optical laser pumping	$0.2 - 1$ THz	18.9 (no pumping) 74.7(6 mJ cm^{-2})	[304]

Early adaptations of graphene-based detectors focused on the visible spectrum using the photovoltaic effect [305, 306]. Creating p-n junctions in graphene using metal contacts or gates and electrostatic biasing facilitates the formation of thermocouples in which photogenerated hot electrons result in a photovoltage due to the photo-thermoelectric effect [299, 307].

The thermocouples at graphene-metal interfaces are subpar due to electro-cooling [299], and now, the photo-thermoelectric effect dominates the research interests. Graphene-based detectors now cover a wide variety of frequency ranges: microwave [299, 308-310], THz [297, 298, 308, 309, 311-314], IR [297, 298, 306, 307, 310, 315, 316], visible spectrum [297, 305, 315] and in the UV frequency range [310]. Depending on the detector response time, even single photons can be detected [310]. Bolometric and antenna-coupled GFET-based detectors are mainly found in practice within the microwave and THz frequency ranges [297-299, 308-314].

2.4.4.1 Bolometers

EM detectors are devices in which the incident field energy is absorbed. Calorimeters are EM detectors in which the absorption results in a temperature increase that is subsequently read out. Bolometers, in general, use the same basic working principle and are employed specifically to measure the power of incident EM fields.

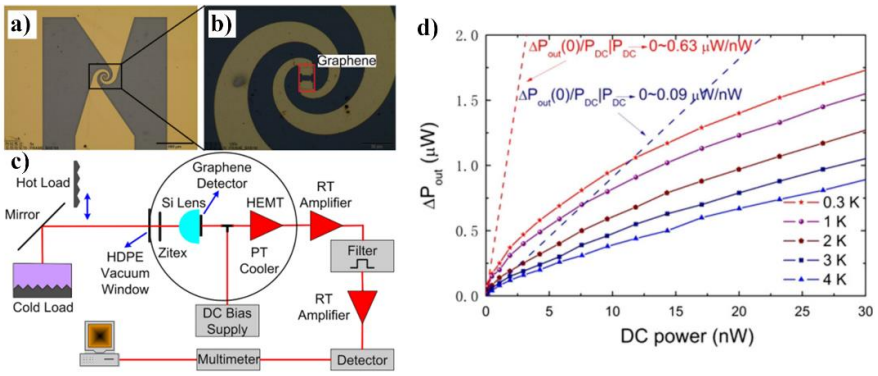

Figure 2-34 Graphene-based hot-electron bolometer. (a) Image of the fabricated hot-electron bolometer, (b) magnification of graphene structure, and (c) schematic setup for the Johnson noise measurement of the hot-electron bolometer. (d) Measured dependence of noise power variation on dc power at different bath temperatures. Reprinted from [313]

Skobin et al. [299] designed a bolometer using exfoliated graphene that was transferred onto a Parylene-N/SiO_2/Si substrate. Two metal contacts were added to measure the photo-generated voltage, and a log-periodic antenna coupled incident EM fields to the graphene via two separate gates, as illustrated in Figure 2-34(a). A photoresponsivity of $\sim 700\ \mathrm{V\,W^{-1}}$ and a

noise equivalent power (NEP) of $\sim 200\ \mathrm{pW\ Hz^{-1/2}}$ was determined at an operating temperature of 50 K. The photogenerated signal showed minimal variation, $\sim 600\ \mu\mathrm{V}$, at temperatures of $4 - 100$ K, but it was significantly lower at room temperature, i.e., $\sim 10\ \mu\mathrm{V}$.

Miao et al. [313] designed a hot-electron bolometer with EG grown on 4H-SiC substrate. The graphene was integrated with a microbridge and directly connected to a log-spiral antenna that covered the frequencies within $0.1 - 1.4$ THz. An elliptical Si lens was attached to the device. It operated at $0.3 - 10$ K. Johnson Noise Thermometry was employed to read out the response of the detector by measuring the noise emission of the incident EM field generated from blackbody loads. The NEP was estimated to be $5.6\ \mathrm{nW\ Hz^{-1/2}}$ at 3 K.

2.4.4.2 Graphene Field Effect Transistor-based Detectors

GFET-based THz detectors exhibit different photocurrent generation mechanisms compared to thermal detectors/bolometers. Wideband metallic bowtie antennas are used to couple the incident EM fields into the GFET. One of their main advantages is that they can be operated at room instead of cryogenic temperatures.

Bianco et al. [308] introduced a THz detector that consists of a log-periodic circular-toothed antenna-coupled GFET, as shown in Figure 2-35(a). The GFET was based on EG grown on a SiC substrate (semi-insulating, 4H-SiC(0001)) via thermal sublimation. Two independent detection mechanisms, the rectification of over-damped plasma waves (Dyakonov-Shur) and graphene's thermoelectric effect, were identified as they competed with each other, see Figure 2-35(c,d). The photoresponsivity and NEP were determined to be $\sim 0.25\ \mathrm{V\ W^{-1}}$ and $\sim 80\ \mathrm{nW\ Hz^{-1/2}}$, respectively. For comparison, the CVD graphene-based photodetector introduced by Zak et al. in [312] achieved a photoresponsitivity that was two orders of magnitude higher, as compared to the results from [308], with a photoresponsivity and NEP of $> 14\ \mathrm{V\ W^{-1}}$ and $\sim 515\ \mathrm{pW\ Hz^{-1/2}}$, respectively. Their design consisted of a split bow-tie antenna coupled to a GFET, as shown in Figure 2-36.

Murali et al. [311] analysed the primary mechanism to improve the sensitivity of GFET-based THz detectors. They used a split bow-tie antenna coupled to a GFET based on monolayer EG grown on a SiC substrate (semi-insulating, 4H-SiC(0001)). High-resistance contacts to the source and drain of the GFET were used deliberately, and they showed that the THz coupling onto the channel and the control thereof was more important than the initial conductivity of the channel and the contact resistances. The designed detector operated at 0.8 THz and achieved a photoresponsivity and NEP of $> 535\ \mathrm{V\ W^{-1}}$ and $< 100\ \mathrm{pW\ Hz^{-1/2}}$, respectively.

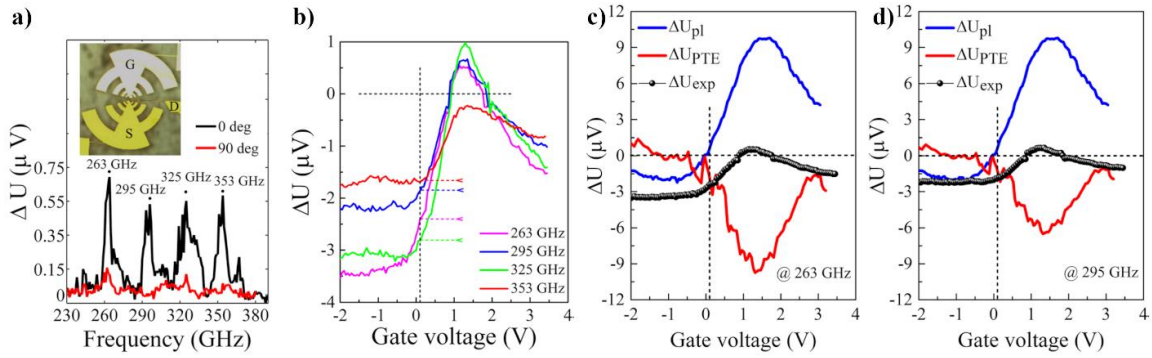

Figure 2-35 Photo-voltage measurement using a GFET-based detector of THz fields. (a) Frequency dependence for polarisations of $0°$ *and* $90°$ *relative to antenna axis at* $V_g = 1.2\ V$ *and* $V_{sd} = 0\ V$*. (b) Gate voltage dependence for a variety of frequencies at* $V_{sd} = 0\ V$ *and* $0°$ *polarisation. (c, d) Plasmonic (blue) and thermoelectric (red) photo-voltages analytically extracted from the measured values (black) at (c)* $263\ GHz$*, and (d) at* $295\ GHz$*, for* $V_{sd} = 0\ V$ *and* $0°$ *polarisation. Reprinted from [308]*

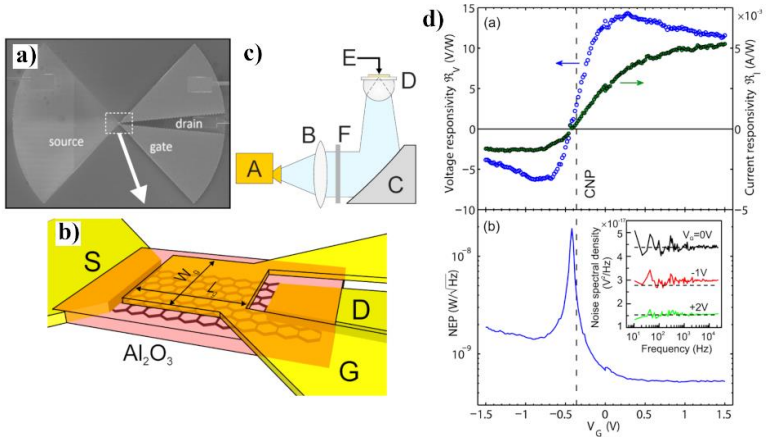

Figure 2-36 CVD GFET-based THz detector. (a) SEM picture of the device. (b) Schematic of the device. (c) Measurement setup. A: THz source, B: lens, C: paraboloid mirror, D: hyper-hemispherical Si lens, E detector, F: power meter. (d) Measured voltage and current photoresponsitivity (top) and NEP (bottom). Reprinted from [312]

Graphene-based EM field detectors are most commonly studied at THz frequencies and offer wideband detection owning to the metallic antennas used for the coupling of the EM fields into them. Moreover, they offer a great alternative to common pyroelectric [317], micro-bolometer [318], and Si CMOS detectors [319-321]. Graphene-based detectors have been demonstrated to cover a wide frequency spectrum and are easy to fabricate due to their planar design. The latter is important to compete with alternative designs that can already be fabricated

using standard Si CMOS processes, e.g., using the Taiwan Semiconductor Manufacturing Company (TSMC) 180 nm process [319].

The main figures of merit for detectors are photoresponsitivity, NEP, and response time. Graphene-based detectors in the microwave and THz ranges already offer high photoresponsitivities of $\sim 700\ \mathrm{V\,W^{-1}}$ and NEP as little as $100\ \mathrm{pW\,Hz^{-1/2}}$, comparable to commercially available room temperature THz detectors [314]. However, devices based on alternative materials are at least one order of magnitude better, with photoresponsitivities of up to $8\,600\ \mathrm{V\,W^{-1}}$ [317] and a NEP as little as $10\ \mathrm{pW\,Hz^{-1/2}}$ [320], see Table 2-6.

Table 2-6 Comparison of photodetector implementations

Technology	Design	Frequency [GHz]	Photoresponsivity [$\mathrm{V\,W^{-1}}$]	NEP [$\mathrm{pW\,Hz^{-1/2}}$]	Ref.
Exfoliated graphene on Parylene-N/SiO_2/Si substrate	Cryogenic bolometer based on log-periodic antenna	94	~ 700	~ 200	[299]
EG grown on 4H-SiC substrate	Cryogenic hot-electron bolometer with Johnson Noise Thermometry	$100 - 1400$	-	5 600	[313]
EG grown on semi-insulating, 4H-SiC(0001)	Log-periodic circular-toothed antenna-coupled GFET	$230 - 375$	0.25	80 000	[308]
EG grown on semi-insulating, 4H-SiC(0001)	Split bow-tie antenna coupled to a GFET	800	> 535	< 100	[311]
CVD SLG on	Split bow-tie antenna coupled to a GFET	600	14	515	[312]
Exfoliated bilayer graphene on SiO_2/Si	Log-periodic circular-toothed antenna coupled GFET	$290 - 380$	~ 1.2	$\sim 2\,000$	[314]
TSMC 180 nm SiO_2/Si process	Circular antenna coupled to a nMOS detector	$270 - 320$	1 286.6	210	[319]
130 nm Si CMOS process	Bowtie antenna coupled to nMOS rectifying element	$270 - 1\,050$	5 000	< 10	[320]
Lithium tantalate Crystal on Si	Detector array with pixel readout circuit	2 520	8 600	1 500	[317]

2.5 Summary

In the early stages of graphene research, a significant amount of research was conducted in the synthesis of large-area graphene. However, many applications require complex and precise patterning of graphene. Several patterning approaches start out with large-area graphene that is subsequently patterned using various etching techniques, so-called top-down approaches. These generally introduce edge defects during the etching and require masking layers that can further contaminate and damage the graphene layer. For future commercialisation and the fabrication of electronic devices, precise, simple, and scalable patterning techniques are required. Hence, there is an inherent need for graphene patterning techniques that are compatible with common Si processing techniques.

The catalytic alloy-mediated approach to growing EG on SiC/Si substrates is compatible with Si processing techniques. However, the patterning of graphene requires the etching of the SiC layer, which makes it incompatible with bulk SiC and results in 3D patterned graphene rather than planar structures. The EG grown following the catalytic alloy-mediated graphitisation approach has previously only been electrically characterised at DC using van-der-Pauw and Hall measurements. They have demonstrated a sheet resistance comparable to that of EG on bulk SiC. Furthermore, the sheet carrier concentration and mobility follow the inverse power-law dependence typical of substrate-supported graphene. The transport properties of EG on both bulk SiC and SiC/Si are dominated by the interface between the EG and the substrate, which is also the case for CVD graphene.

Several techniques, from the microwave to the THz frequency range, exist to electrically characterise graphene, such as CPW-based, free space, TDS, and more. The high-frequency behaviour of graphene is commonly modelled using the Drude conductivity model. While it predicts the real part of the conductivity to be constant up to the Drude roll-off at THz frequencies, measurements of the microwave conductivity of CVD graphene samples have shown to deviate from DC measurements, and the conductivities experience a monotonic increase for higher frequencies. This effect is expected to be related to scattering on grain boundaries and defect-induced discontinuities in the graphene layer that play a significant role in DC measurements but show less influence in high-frequency measurements. Graphene grown following catalytic alloy mediated graphitisation approach has demonstrated ~ 100 nm grain sizes, and their influence on the electrical properties in microwave range still needs to be determined.

Graphene's unprecedented properties make it an ideal candidate for EM applications within the microwave to THz frequency spectrum. They can benefit from its high electrical conductivity, mechanical flexibility and robustness, transparency, support of surface-plasmon-polaritons, and the possibility of dynamic tunability with DC to light sources. Several graphene-based EM devices, such as antennas, absorbers, and detectors, have already been numerically evaluated or experimentally verified.

In particular, the numerical modelling of graphene devices is crucial for the initial evaluation of a device's performance. Furthermore, demonstrating the potential of emerging technologies early on can determine the potential for commercial success. Consequently, it is crucial to conduct a first evaluation of EM applications based on the catalytic alloy-mediated synthesis of EG on SiC/Si and determine their potential.

Chapter 3 Methodology

This chapter describes the foundation for this study's investigative process. It comprises four key sections: the fabrication, the physical and experimental characterisation, as well as the numerical modelling methodology. These interconnected sections collectively enable a comprehensive exploration of the research questions.

3.1 Fabrication Methodology

3.1.1 Substrate Material

In this work, commercially available SiC/Si wafers were used. The 3C-SiC layer was heteroepitaxially grown on (100) or (111) crystalline-oriented 4″ lowly p-doped and on 2″ intrinsic Si. Wafers. The 3C-SiC/Si wafers were diced into $1.1\ \text{cm} \times 1.1\ \text{cm}$ coupons. Table 3-1 gives an overview of the used 3C-SiC/Si wafers.

Table 3-1 Overview of substrates used

Wafer Type	Wafer Size	Supplier	Si resistivity [Ω cm]	Si thickness [μm]	SiC thickness [μm]
3C-SiC/intrinsic Si (111)	2″	NOVASIC	$> 10\,000$	235	0.5
3C-SiC/intrinsic Si (100)	2″	NOVASIC	$> 10\,000$	235	0.5
3C-SiC/lowly p-doped Si (111)	4″	NOVASIC	$1 - 10$	527	0.5
3C-SiC/lowly p-doped Si (100)	4″	NOVASIC	$1 - 10$	680	0.5

For the high-frequency characterisation of EG grown on SiC/Si, SiC on intrinsic Si samples are used exclusively. This is due to superior dielectric properties, lower losses, and reflections, as well as inseparable parallel conduction observed in EG grown on 3C-SiC/doped Si [30, 322].

3.1.2 Graphene Synthesis

A catalytic alloy mediated-graphitisation process was used to grow graphene on SiC/Si samples [4, 13]. The process remains the same, independent of the wafer type used. Figure 2-6 shows an overview of the graphitisation process. The individual steps required for a large-area graphitisation are explained here in more detail:

1. **Sample Preparation**

   Individual samples are initially cleaned via sonication (5 min) in 50/50 Acetone and isopropyl alcohol (IPA). Next, the samples are rinsed with deionised (DI) water and dried using compressed nitrogen (N_2) gas.

2. **Metal Deposition**

   The alloy used to facilitate the graphitisation process consists of Ni (10 nm) and Cu (20 nm). They are deposited separately using DC-Magnetron-sputtering in a Moorfield Nanotechnology nanoPVD S10A sputtering system. The Ni and Cu sputtering targets had purities of 99.95 % and 99.999 %, respectively.

3. **Annealing**

   The graphitisation process itself takes place under high heat and in a high vacuum. A CARBOLITE GERO STF 15/450 vacuum furnace was used for this process. The system was set to ramp up the temperature at a rate of $25°C\ min^{-1}$ until it reached the annealing temperature of 1 100°C. The samples were annealed for 60 min at a pressure of $< 5 \times 10^{-5}$ mbar, after which the system slowly cooled down to room temperature while keeping the samples under a high vacuum.

4. **Wet Freckle Etch**

   The annealing step facilitates the graphitisation process, where the Ni reacts with the SiC to form various silicides, i.e., Ni_2Si. They intermix with the alloy catalyst while releasing carbon, which then settles during the cooling phase. It should be noted that some of the SiC is consumed during graphitisation.

   The intermixed layer that consists of metal silicides, remaining alloy catalyst, and excess carbon is removed using a wet Freckle etch. The Freckle etch solution consists of 85 % Phosphoric acid (H_3PO_4): Glacial acetic acid (CH_3COOH): 70 % Nitric acid (HNO_3): 48 % Tetraflouroboric acid (HBF_4): DI water (H_2O) in a ratio of 70:10:5:5:10. The solution was further diluted for the etching process by mixing equal parts of the Freckle etch solution with DI water. The samples are then placed in the diluted etching solution for 14 h. Finally, the samples are removed from the solution, rinsed using DI water, and dried with compressed N_2 gas. In previous works, an x-ray photoelectron spectroscopy study of graphitised samples has indicated very low residual metal and etchant contamination, i.e. fluorine (0.7%), nitrogen (0.7%), and nickel (0.15%), after the Freckle etch [4].

3.1.3 Metal Deposition

As already introduced above, DC-Magnetron-sputtering with a Moorfield nanotechnology nanoPVD S10A sputtering system was used for the deposition of metals. The main deposited metals were Al, Cu, and Ni, and the sputtering targets had purities of 99.99 %, 99.999 %, and 99.95 %, respectively.

For the deposition, the chamber was first pumped down to a base pressure of $< 8 \times 10^{-6}$ mbar. Ar gas was introduced into the chamber to facilitate the plasma and, thus, the sputtering process. To improve the repeatability of the deposition process, the sputtering process was performed at a constant deposition pressure by automatically regulating the Ar gas inflow, usually 5×10^{-3} mbar. A 30 s soaking process at a lower power was utilised before each individual sputtering step to stabilise the plasma and remove possible surface oxidation on the targets. After the deposition process, N_2 gas was used to vent the chamber.

3.1.4 Lithography Processes

Various lithography procedures were used to enable the patterning of graphene and metal structures depending on structure sizes, availability, and urgency.

- **UV-Lithography**

  A Suss MJB4 Mask Aligner was used for masked UV-lithography-based patterning of various PRs. A 4" photomask was previously designed using Siemens L-Edit IC layouting software. Both positive PR MicroChemicals AZ 1518, as well as negative PR MicroChemicals AZ nLOF 2020 were used for the fabrication of samples. The PRs were spun coated onto the samples using a Laurell WS-650-23PPB Spin Coater and exposed using the mask aligner. Depending on the PR, the spin coating speed, exposure time, and soft bake time, as well as post-exposure bake time, were adjusted. AZ 726 MIF developer was used to develop the PR, while sonication in Acetone was used to remove the PR.

- **Maskless Aligner**

  For high-urgency samples, a Heidelberg MLA100 Maskless aligner was used. It utilises direct laser writing to transfer a layout into a MICROPOSIT S1813 PR. MICROPOSIT MF321 was used for development, and the PR was removed in a hot-acetone bath followed by a brief sonication step.

- **Electron Beam Lithography**

  EBL was performed using a Zeiss Supra 55VP high-resolution field-emission scanning electron microscope and Raith Elphy Plus pattern processor. Positive ALLRESIST E-

Beam Resists AR-P 6200.18 was diluted using Anisole to reduce the solids content from 18 % down to 4 %. For the exposure, an accelerating voltage of 30 kV was used, and the dosage was set to 140 µC cm^{-2}. The PR was developed in ALLRESIST AR 600-546 developer, and ALLRESIST AR 600-60 was used as a stopper. The samples were subsequently rinsed using IPA. ALLRESIST AR 600-71 was used to remove the PR.

Since all lithography processes are very similar, only a single process for patterning MicroChemicals AZ nLOF 2020 using UV-lithography is given below:

1. Samples were cleaned using sonication in 50/50 Acetone and IPA, followed by a rinse with DI water and blow dry using compressed N_2 gas.
2. The MicroChemicals AZ nLOF 2020 PR was deposited using a Laurell WS-650-23PPB Spin Coater by rotating the samples at 5000 rpm for 60 s.
3. A soft bake was performed by placing the samples on a hot plate at 110°C for 60 s.
4. The layout of the photomask was transferred onto the PR by exposing the samples to UV light for 3 s using the Suss MJB4 Mask Aligner.
5. A post-exposure bake was performed by placing the samples on a hot plate at 110°C for 60 s.
6. The PR was developed by placing the samples in an AZ 726 MIF bath for 50 s and rinsing them with DI water, following a blow dry using compressed N_2 gas.
7. An O_2 de-scum procedure using a TRION Phantom RIE ICP Plasma Chamber was performed to remove PR residue (5 s, $P_{ICP} = 10$ W, $P_{RIE} = 30$ W, 10 mTorr, O_2:12 sccm)
8. To remove the PR again, such as for the lift-off of metal structures, the samples were sonicated in acetone for 30 s and rinsed with DI water, following a blow dry using compressed N_2 gas.

3.1.5 Inductively Coupled Plasma Reactive Ion Etching

ICP-RIE dry etching was performed using a TRION Phantom ICP-RIE Plasma Chamber. It was most prominently used to remove PR residues after the development process. The O_2-based de-scum process was performed at a pressure of 10 mTorr with an O_2 gas inflow of 12 sccm. The samples were exposed to a plasma with an ICP power of $P_{ICP} = 10$ W and RIE power of $P_{RIE} = 30$ W for 5 s.

During the characterisation of the high-frequency characteristics of EG on SiC/Si, it was determined that an ICP-RIE-based Ar-treatment was necessary to enable the graphene-metal contact. The Ar treatment was performed at a pressure of 20 mTorr with an Ar gas inflow of 20 sccm. The samples were exposed to a plasma with an ICP power of $P_{ICP} = 50$ W and RIE power of $P_{RIE} = 30$ W for 60 s. While the O_2 de-scum process makes use of the chemically reactive plasma where the O_2 reacts with the polymer-based PR, the Ar-treatment rather describes a physical sputtering process where highly energised Ar ions bombard the sample.

3.2 Physical Characterisation

The physical characterisation of the fabricated samples was conducted using the following instruments:

3.2.1 Raman Spectroscopy

Raman spectroscopy was performed using a WITec alpha300 confocal Raman microscope that was operated at room temperature and in backscattering geometry. A 532 nm argon-ion laser ($P_0 < 30$ mW) was used for the excitation in combination with a WITec ultra-high throughput spectrometer (UHTS 300 SMFC VIS). A Zeiss EC Epiplan-Neoflua $100\times/0.90$ DIC objective was used for Raman mapping and resulted in a spot size of ~ 300 nm.

Before each measurement, the system was calibrated using a Si sample by evaluating the Si peak's spectral position ($\sim 520\ \mathrm{cm}^{-1}$). Large-area mapping was utilised for improved statistical accuracy and to confirm uniform graphitisation. In general, an area of $30\ \mu\mathrm{m} \times 30\ \mu\mathrm{m}$ was mapped with 150×150 points and an integration time of 0.1 s per point. The spectral positions and intensities of graphene's D, G, and 2D peaks, as well as SiC's longitudinal optical (LO) phonon peak in the Raman spectrum, were identified. The intensity ratios I_D/I_G , I_{2D}/I_G, and I_{LO}/I_{2D} were calculated and recorded to evaluate the quality of fabricated graphene samples.

Of particular importance is the I_D/I_G ratio as it is an accurate indicator of the number of defects. Graphene's D peak is stimulated due to broken lattice symmetry, i.e., from edges or defects in the graphene layer, while the G peak results from in-plane vibrations of sp^2 hybridised carbon atoms. Hence, a low ratio depicts graphene with fewer defects, while a large ratio represents more defective graphene.

Additionally, the graphene grain size can be estimated using the I_D/I_G ratio and the laser wavelength (λ_l) using [323]

$$L_a = (2.4 \times 10^{-10})\lambda_l^4 \left(\frac{I_D}{I_G}\right)^{-1} \quad (3.1)$$

3.2.2 Scanning Electron Microscopy

For a high-resolution analysis of surface topographies, scanning electron microscopy (SEM) was performed using a Zeiss Supra 55VP high-resolution field-emission scanning electron microscope. Acceleration voltages were set to $5 - 15$ kV to analyse the samples. Due to the inherently high conductivity of graphene and metal structures, no extensive sample preparation or additional coatings were necessary for performing the characterisation on fabricated samples.

3.2.3 Atomic Force Microscopy

For the evaluation of nanometer-sized graphene patterns at UTS, a Park SE7 AFM was used. MikroMasch HQ:NSC16/NO AL AFM tips were mounted and used to perform the topographical analysis.

3.2.4 Scattering-type Scanning Near-field Optical Microscopy

Nearfield imaging was performed using a commercial scattering-type Scanning Near-field Optical Microscopy (s-SNOM) equipped with a nano-FT-IR module (Neaspec). The mid-IR output was obtained by passing the output light of an optical parametric oscillator laser (Stuttgart Instruments) that was powered by a pump laser ($\lambda = 1035$ nm, 40 MHz repetition rate, and $\sim$500 fs pulse width), through a difference frequency generation module [324] and further sharped using a monochromator. A parabolic mirror is used to focus the p-polarised emission onto a metal-coated (Pt/Ir) AFM tip (Arrow-NCPt, Nanoworld) oscillating at $\sim$280 kHz with a tapping amplitude of $\sim$80 nm. The back-scattered light was directed towards a pseudo-heterodyne interferometer and demodulated at the third harmonic [325].

3.3 Experimental Characterisation

3.3.1 Hall Effect Measurement

For the DC characterisation of large-area graphitised samples, an Ecopia HMS-5300 Hall effect measurement system, together with an AMP55T temperature control unit, were used. The Ecopia Hall effect measurement system determines the characteristics of conductive materials by conducting Hall effect measurements and van der Pauw measurements at the same time. It determines sample characteristics, such as the temperature-dependent $(80 - 300$ K) sheet resistance, sheet carrier concentration, charge carrier type (hole or electron) mobility, and more. The setup consists of a probing stage that places four brass probes around the perimeter of the sample (in the four corners of a square sample). The Hall effect method works by

measuring the Hall voltages that originate from sweeping a range of currents of charge carriers that flow through the material while the sample is exposed to a known magnetic field that is oriented perpendicular to the direction of the current. The van der Pauw method, on the other hand, measures the voltage parallel to a range of currents that are passed along one side of the sample.

3.3.2 Transfer Length Method using Probing Station Measurements

The transfer length method (TLM) is a valuable characterisation method to determine the sheet and contact resistance of thin films. TLM is based on simple I-V measurements between adjacent metal contacts that are situated in a linear array where the distance between two neighbouring contacts increases linearly with the number of contacts. A EVERBEING C-2 MINI PROBE STATION is used to contact the TLM structures, and the measurements are conducted using a Keithley 4200A-SCS parameter analyser. The resistance $R_T = U/I$ between two contacts is characterised by applying a constant voltage and measuring the current. The resistance becomes a function of the spacing between two contacts that carries information about the contact and sheet resistance and is given by

$$R_T = \frac{R_{sh}}{a} d + 2R_c \tag{3.2}$$

where R_T is the total resistance measured, a is the width of the metal contact, d is the distance between two contacts, and R_{sh} and R_c are the sheet and contact resistances, respectively.

When plotted, the measured data point can be fitted to a line, and a multiple of two of contact resistance can be read from the y-intercept, while the slope is related to the sheet resistance and the contact width a, as illustrated in Figure 3-1.

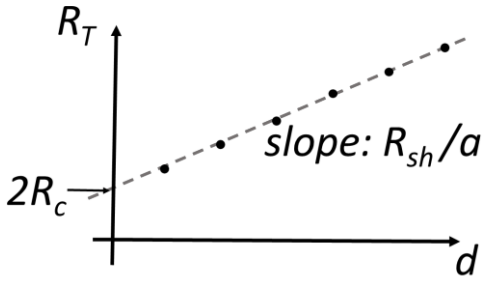

Figure 3-1 TLM line fit and extraction of contact resistance R_c and sheet resistance R_{sh}.

3.3.3 Probe Measurements

The high-frequency properties of EG grown on SiC/Si substrates using the pre-patterning of the metal catalyst were characterised in the RF spectrum using CPWs. Two CPW approaches

were evaluated. The first is a graphene patch approach, where part of the centre trace of a metallic CPW is replaced with graphene. The second is the shunt approach, where graphene is placed between the centre trace and the pair of return traces.

The Probe measurements were conducted on a Cascade MPS150 probe station. FORMFACTOR Infinity Probes I50-A-GSG-100 50 GHz probes with a 100 µm pitch were connected to a Keysight N5225B PNA Network Analyser using 2.93 mm 40 GHz cables, as shown in Figure 3-2. A FORMFACTOR 101-190D calibration substrate was used for the short-open-through-load (SOTL) calibration of the Network analyser and probes.

3.3.4 Rectangular Waveguide Measurements

For the characterisation of large area EG on SiC/Si samples, a rectangular waveguide approach was used. A pair of YERKON BJ320 (WR-28) rectangular waveguide coaxial adapters were connected to a Keysight N5225B PNA Network Analyser using $2.93\,mm$ 40 GHz cables. The coaxial adapters are banded within $26.3 - 40$ GHz, which covers the K_a-band. Figure 3-3 gives an overview of the components used and the measurement procedure. The reference plane for the measurements was set to the mating planes of the two coaxial adapters via a through-reflect-line (TRL) calibration, as illustrated in Figure 3-4.

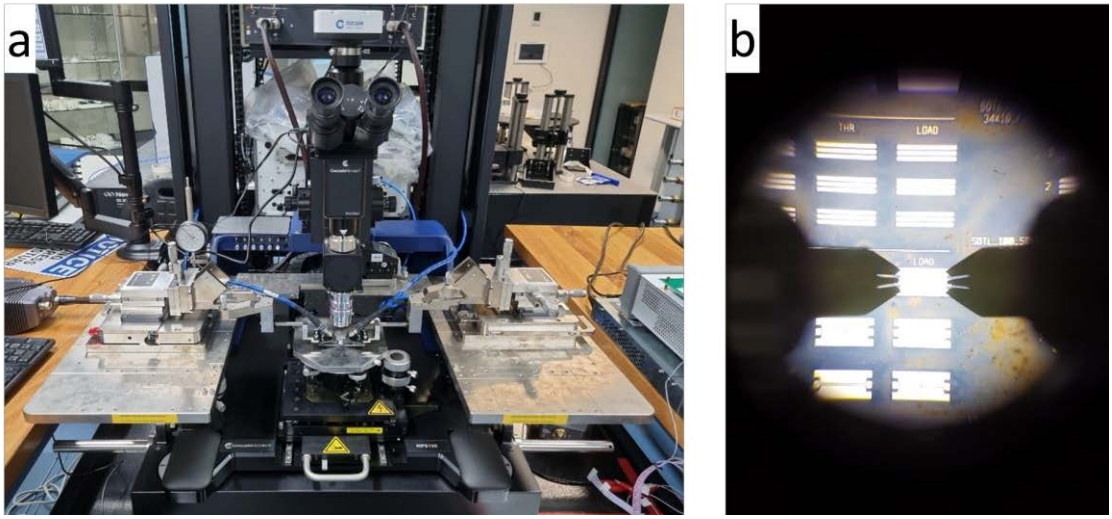

Figure 3-2 (a) Cascade MPS150 Probe station used for the probe-based high-frequency characterisation of EG-based CPWs.(b) view through the microscope of the probe station while probing CPW structures.

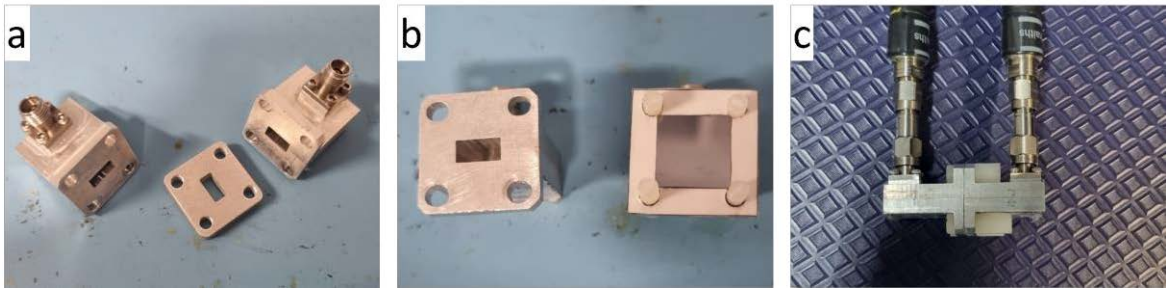

Figure 3-3 (a) YERKON BJ320 (WR-28) $26.3 - 40\ GHz$ *rectangular waveguide coaxial adapters and Wr-28 line element used for the TRL calibration. (b) Paper-based holder used for repeatable sample alignment. (c) Coaxial adapters are directly connected to each other (through connection) using nylon hardware during the TRL calibration procedure.*

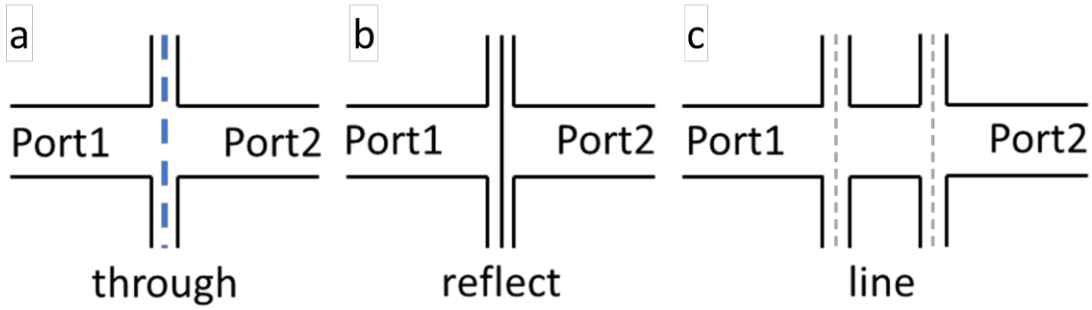

Figure 3-4 TRL calibration procedure for coaxial rectangular waveguide adaptors to set the reference plane as indicated using the blue dashed line in (a) the through measurement. (b) Reflect measurement uses a solid metal reflection surface, while (c) the line measurement uses a defined line element.

3.4 Numerical Modelling

Numerical modelling has established itself as a fundamental tool for engineering and scientific research, thanks to ongoing advancements in the computational power of the modelling hardware, as well as the accuracy, capabilities, and usability of modelling software. In the latter, the numerical methods used for the modelling are based on mathematical models and physical laws and intended to predict the performance of a designed system as accurately and quickly as possible.

Generally, the design of components, devices, or experimental setups is quite challenging and requires complete knowledge of the designed system. Sometimes, several iterations are required to optimise a setup, which can be very time- and cost-ineffective. In particular due to the possibility of using-up or destroying samples in the process. Therefore, researchers and

engineers favour the use of numerical simulation tools to optimise a designed system before it is physically constructed and experimentally validated.

In this study, numerical modelling was used to design, simulate, and optimise experimental setups as well as model first THz applications of the used EG on SiC/Si platform. Here, two distinct tools, COMSOL Multiphysics, in combination with the RF-Module, as well as ANSYS high-frequency structure simulator (HFSS), were used. They are both based on the finite element method, which is regarded as one of the most accurate, fast, and reliable modelling techniques used for investigating high-frequency applications.

3.4.1 COMSOL Multiphysics – RF Module

COMSOL Multiphysics is a finite element method-based solver. It is commonly used for a variety of physics and engineering simulations, such as for acoustics, chemical, electrical, mechanical, and fluid applications. It enables the combined simulation of various physics concepts; hence, the name "Multiphysics". Various expansion modules exist, such as the RF module used for high-frequency EM analyses. These extend the features of the basic software pack for more complex problems.

COMSOL Multiphysics was initially used due to an available graphene model developed by a co-worker [26] and previous experience with the tool. It was used to design the CPWs and experimental setup of the probe measurement used for the high-frequency characterisation of EG on SiC/Si, see 5.1, and the THz graphene dipole antenna and absorber, see Chapter 6. Details about the simulation models are given in their respective sections. However, due to the limited availability of licenses for the RF-Module and the increased demand for modelling during the COVID-19 pandemic, I later switched to using ANSYS HFSS.

3.4.2 ANSYS HFSS

ANSYS HFSS is a finite element method-based solver specifically for EM structures. It was used to design and optimise the K_a-band characterisation setup used in 5.2. Details about the model are given in that chapter.

Chapter 4 Graphene Patterning Approach based on Pre-patterning of the Metal Alloy Catalyst

4.1 Novel Bottom-Up Graphene Patterning Approach

The basic graphene synthesis mechanism makes use of a Ni/Cu catalytic alloy-mediated graphitisation, as introduced in previous works [4, 13] and as outlined in 2.2.1.2. Previously, pre-patterning the SiC as the solid-state carbon source to selectively grow the graphene patterns on Si would form three-dimensional structures made of SiC coated with graphene, as illustrated in Figure 2-13. Here, it is shown that it is alternatively possible to pre-pattern the catalytic alloy to define the areas where the graphene will selectively be grown, forming this time a 2D pattern of EG on the SiC. Figure 4-1 shows an illustration of the patterning steps. They are described in detail here:

a) Individual samples were initially cleaned via sonication (5 min) in 50/50 Acetone and Isopropyl Alcohol (IPA). Next, the samples were rinsed with DI water, dried using compressed nitrogen (N_2) gas, and placed in a Diener Electronics YOCTO-B plasma cleaner (5 min) for further cleaning, see Figure 4-1a).
b) The graphene was patterned by pre-patterning of the metal catalysts used to facilitate the graphitisation process. This was achieved using a simple lift-off process. PR lift-off layers were patterned using masked UV-lithography for large-area patterning and EBL for nanometre patterning, as outlined in 3.1.4., and illustrated in Figure 4-1(b). A very brief O_2 de-scum treatment using RIE dry plasma can be used to remove residual PR contamination on the SiC surface (not shown in the illustration).
c) Subsequently, the metal catalysts, consisting of Ni (10 nm, 99.95 %) and Cu (20 nm, 99.999 %), were deposited consecutively using DC-Magnetron-sputtering in a Moorfield Nanotechnology nanoPVD S10A sputtering system and lifted off by dipping the samples in the applicable PR stripper. Doing so using sonication can alleviate PR and residual catalyst contamination issues, see Figure 4-1(c)
d) The graphitisation process itself takes place under high heat and in a high vacuum. The samples were annealed for 60 min at a pressure of $< 5 \times 10^{-5}$ mbar in a CARBOLITE GERO STF 15/450 vacuum furnace. After the annealing step, the samples are placed in a Freckle etch bath for ~14 h to remove the residual metal catalyst and formed silicides and to reveal the planar graphene patterns, as shown in Figure 4-1(d).

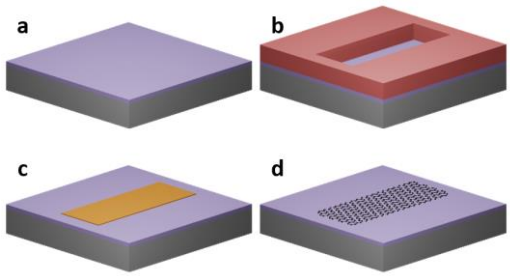

Figure 4-1 Graphene patterning via the pre-patterning of the metal catalysts. (a) The process starts with a SiC/Si substrate. (b) A Photoresist mask is deposited on the substrate using lithography. (c) The Ni and Cu catalyst metals are deposited on the sample and lifted off by removing the PR. After an anneal, the sample is submerged in a Freckle etch bath to reveal the (d) planar graphene patterns on the surface of the SiC. Reprinted from [165]

4.2 Discussion

4.2.1 Patterning using Masked UV-Lithography

The selection of the lithography process is crucial for the scalability and maximum obtainable resolution of any patterning approach. The MJB4 Mask Aligner used in this study enables the exposure of 4″ wafers. Under optimal conditions, a maximum resolution of 0.5 µm can be achieved.

As a first demonstration, showing the possibility of patterning arbitrarily large and complex graphene patterns, we have transferred the university logo onto the PR masking layer on top of a lowly p-doped 3C-(100) SiC/Si coupon. The dimensions of the structure were $\sim 2\ \text{mm} \times 4\ \text{mm}$, and an optical microscope image of the final patterned graphene in the shape of the university logo can be seen in Figure 4-2. It also shows the Raman spatial map ($2.5\ \text{mm} \times 4\ \text{mm}$ of 50×80 points) of the 2D peak ($\sim 2700\ \text{cm}^{-1}$) to confirm the graphitisation.

Subsequently, planar 2 µm wide graphene gratings with a 6 µm pitch were fabricated, exploiting the maximal resolution of the used equipment. Figure 4-3 shows an optical microscope image of the patterned graphene gratings on the SiC/Si substrate as well as the D ($\sim 1350\ \text{cm}^{-1}$), G ($\sim 1580\ \text{cm}^{-1}$), and 2D ($\sim 2700\ \text{cm}^{-1}$) peak intensity maps of the Raman map ($12\ \mu\text{m} \times 12\ \mu\text{m}$ of 36×36 points), showing the well-resolved gratings.

While the structures were fabricated on $1\ \text{cm} \times 1\ \text{cm}$ SiC/Si coupons for the sake of this demonstration, the approach can be scaled up to create wafer-scale graphene patterns with UV-lithography.

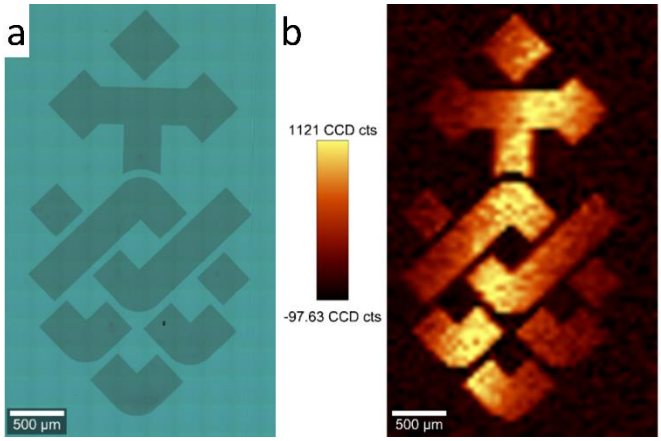

Figure 4-2 Example of $2\ mm \times 4\ mm$ *large patterned EG on a SiC/Si substrate. The metal catalysts were pre-patterned using masked UV-lithography. EG was grown in the shape of the UTS logo, as can be seen in the (a) optical microscope image and (b) 2D (*$\sim 2700\ cm^{-1}$*) peak intensity map of the Raman map (*$2.5\ mm \times 4\ mm$ *of* 50×80 *points). The drop-off of the peak intensity towards the edges of the map is an artifact due to the laser moving out of focus over the large sampled area. Reprinted from [165]*

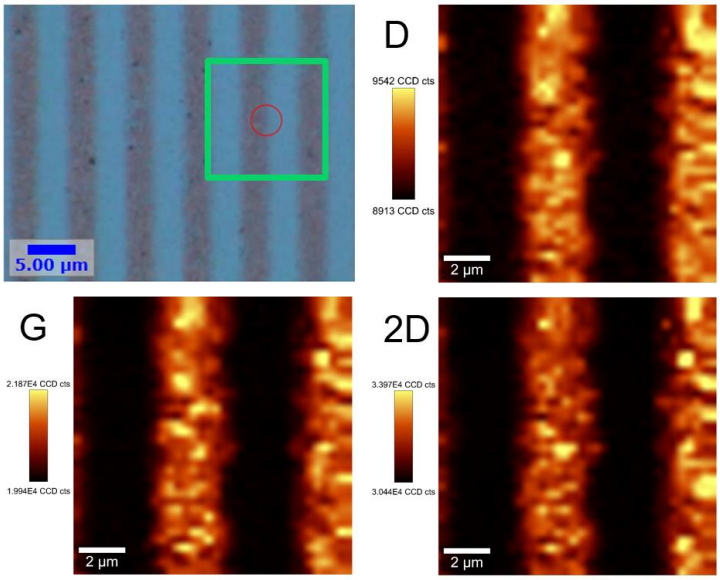

Figure 4-3 Example of planer graphene gratings with a width of $2\ \mu m$ *and a pitch of* $6\ \mu m$ *patterned on a SiC/Si substrate. The metal catalysts were pre-patterned using masked UV-lithography. The figure shows the (top-left) optical microscope image of the graphene gratings and marks the location of the large-area Raman map (*$12\ \mu m \times 12\ \mu m$ *of* 36×36 *points) with a green square. Furthermore, the Raman intensity maps of the D (*$\sim 1350\ cm^{-1}$*), G (*$\sim 1580\ cm^{-1}$*), and 2D (*$\sim 2700\ cm^{-1}$*) peaks are shown. Reprinted from [165]*

4.2.2 Patterning using Electron Beam Lithography

EBL was used to produce nanometre-sized graphene structures. It was performed using a Zeiss Supra 55VP FESEM and Raith Elphy Plus pattern processor. In order to explore the minimum pitch resolution obtainable with our patterning process, the designed mask consisted of four sets of graphene gratings and circular resonators with widths/diameters of 50 nm, 100 nm, 200 nm, and 400 nm, and their respective pitches being 100 nm, 200 nm, 400 nm, and 800 nm.

For the determination of the optimal e-beam dosage to resolve the 50 nm structures, the base dosage of 140 µC cm^{-2} was increased from 100 % to 140 %, in 5 % increments, by writing nine equal masks. Figure 4-4 shows a schematic of the designed mask as well as an optical microscope image of the patterned PR on top of a lowly p-doped 3C-(100) SiC/Si substrate at different dosages.

As before, the deposition of the metal catalyst, following an anneal for the graphitisation, and, finally, a Freckle etch was performed to create the graphene structures.

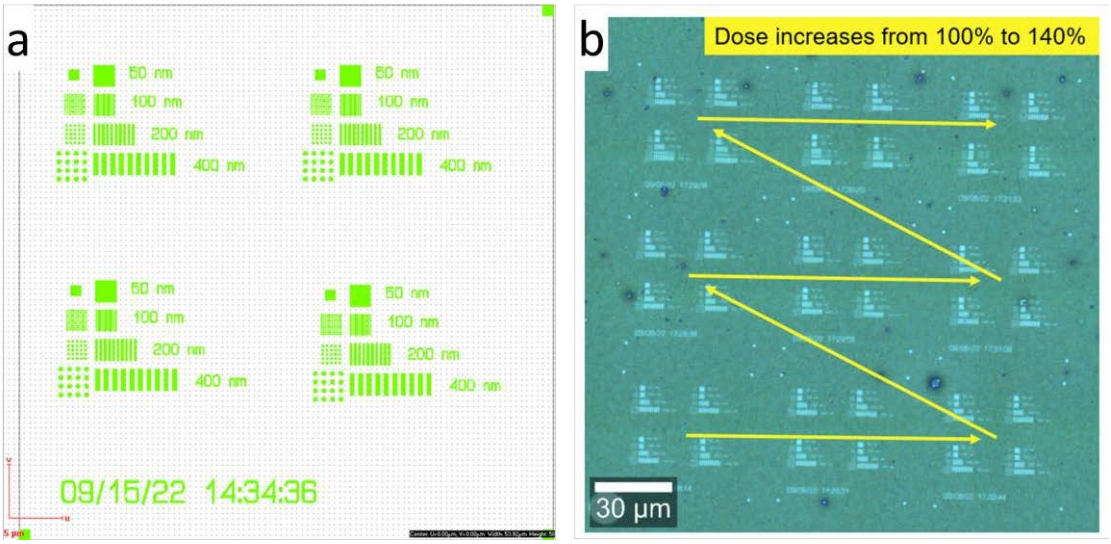

Figure 4-4 (a) Design of EBL masked used to evaluate the resolution of the patterning approach. It contains four sets of 50 *nm,* 100 *nm,* 200 *nm, and* 400 *nm wide/diameter graphene gratings and circular resonators. (b) Optical microscope image of patterned e-beam resist. For the determination of the optimal e-beam dosage, to resolve the 50 nm structures, the base dosage of* 140 µ*C cm*$^{-2}$ *was increased from* 100 % *to* 140 %*, in* 5 % *increments, by writing nine equal masks.*

Due to the dimensions of the fabricated structures, SEM was used for the optical inspection of the fabricated samples. In a first patterning attempt, the pre-patterned metal catalyst was

analysed using SEM to determine the effect of the e-beam dosage on the PR patterning and lift-off process. Most structures were well resolved; however, the metal catalyst did not completely lift off of some of the 50 nm gratings exposed to higher dosages, i.e., > 130 % of the base dosage.

Figure 4-5(a) shows an SEM image of the well-resolved patterned metal catalyst after lift-off, while Figure 4-5(b) shows the SEM image of the patterned graphene after the Freckle etch. It should be noted that the contrast of the graphitized areas, in comparison to the SiC layer, depends on the layer count as well as the SEM voltage and working distance (WD) [326]. In general, thicker graphene, i.e., few-layer graphene, appears darker, and thinner graphene, i.e., monolayer graphene, is lighter in colour. To resolve the nanostructures, a relatively high acceleration voltage of 5 kV and a low working distance of 4.3 mm were used in this study, which are not ideal conditions for the imaging of graphene.

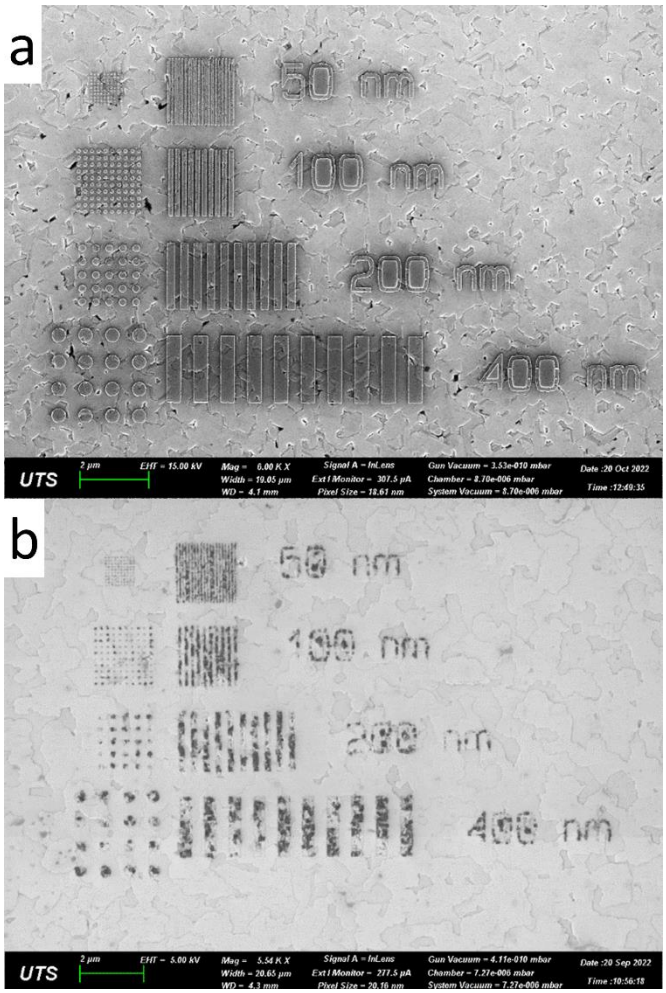

Figure 4-5 SEM images of EBL patterned (a) metal catalyst for the direct growth of 50 *nm,* 100 *nm,* 200 *nm, and* 400 *nm wide graphene gratings and circular resonators, as well as the (b) final graphene structures after the graphitisation and Freckle etch. Reprinted from [165]*

SEM images of the 50 nm (100 nm pitch) and 100 nm (200 nm pitch) gratings in Figure 4-6, show the presence of graphene (dark regions). Darker regions show the location of thicker EG, while brighter regions within the gratings indicate thinner graphene, which have lower contrast to the SiC [326]. The catalytic alloy-mediated graphitization of SiC has previously been shown to form few-layer graphene with up to 7 layers [30].

Furthermore, the images also indicate some growth of EG in areas beyond the initial catalyst pattern. This leads to potential shorting of the graphene gratings as their pitch decreases. This effect is not pronounced on the 100 nm gratings but obvious for the 50 nm graphene gratings. This suggests that the lower pitch resolution of this patterning approach is roughly equal to or smaller than 200 nm.

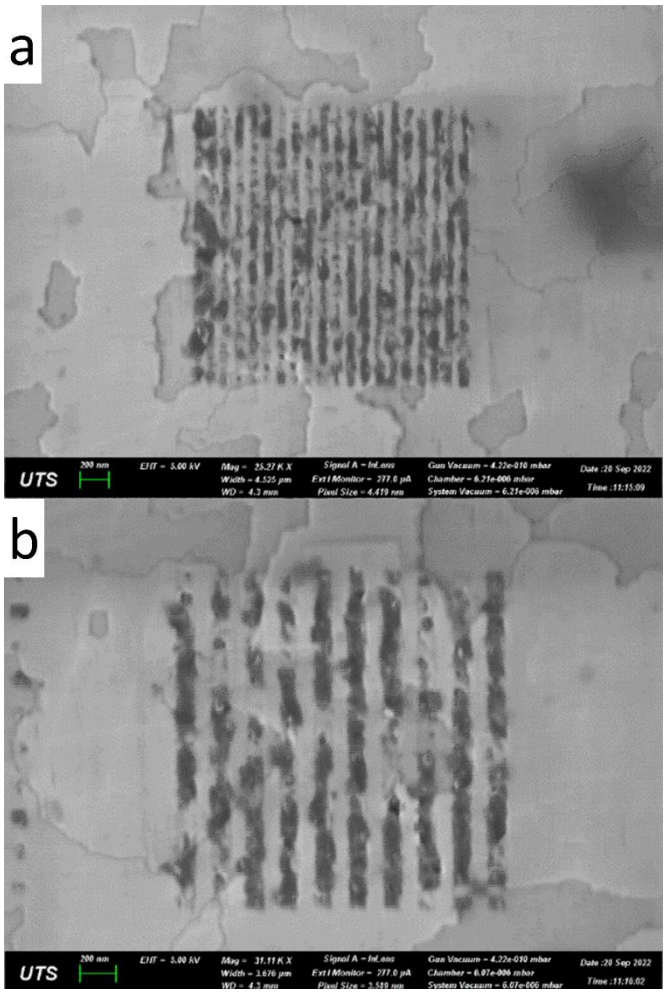

Figure 4-6 SEM images of (a) 50 nm and (b) 100 nm wide graphene gratings show that, visually, the 100 nm gratings mostly resolve fine while the 50 nm ones appear to merge in some places. Reprinted from [165]

This pitch limitation is attributed to the liquid flow of the metal catalyst during the graphitization process at $1100°C$ and a residual and undesirable metal build-up due to the sputtering and lift-off process.

The flow is a consequence of most of the catalysts being effectively in a liquid phase during the annealing step [4, 13], which results in a loss of line definition, and hence resolution, as illustrated in Figure 4-7 (a). The loss of the line definition is hence transferred to the EG layer pattern. This issue becomes a limitation as the structures get smaller, however, it appears less crucial for larger ones, as schematically illustrated in Figure 4-7 (b) and (c) exemplifying $50\ nm$ and $200\ nm$ gratings, respectively.

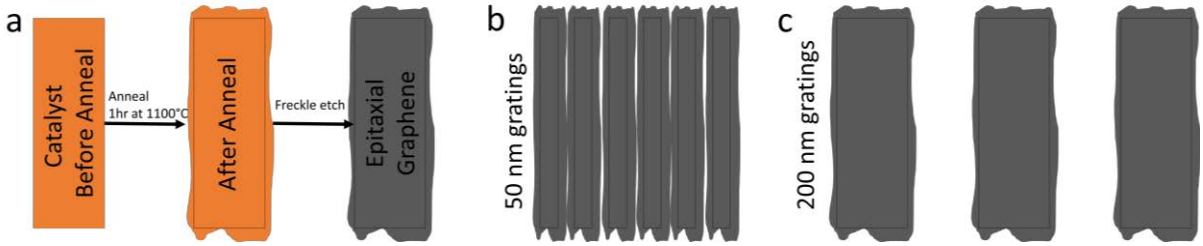

Figure 4-7 (a) Schematic of the flow of metal catalyst as it passes through a liquid phase during the anneal process and its influence on the graphitization process. (b) and (c) show a schematic representation of $50\ nm$ *and* $200\ nm$ *graphitised gratings under the consideration of the flow of the metal catalyst. (Figures are not to scale). Reprinted from [165]*

In fact, the AFM profile across a 400 nm metal catalyst grating before the graphitisation, as illustrated in Figure 4-8, shows the excess metal build-up of about 15 nm thickness at the edges of the metal pattern. We attribute this build-up to the accumulated metal on the PR sidewalls during the sputtering process, which is not effectively eliminated during the lift-off process. The metal build-up is expected to exacerbate the flow effect and contribute to further loss of line definition. Optimisation of the deposition and lithography approach to reduce the side wall deposition, for example, using highly directional evaporation techniques, is hence expected to mitigate the build-up and thus the extent of the catalyst flow during the graphitisation, improving overall the pattern definition and resolution.

Raman large-area mapping was conducted on a large graphene patch (located on the same sample as the nanostructures) and 400 nm graphene structures to further characterise the patterned graphene. The D ($\sim 1350\ \mathrm{cm}^{-1}$), G ($\sim 1580\ \mathrm{cm}^{-1}$), and 2D ($\sim 2700\ \mathrm{cm}^{-1}$) peak intensity maps of the Raman map ($12\ \mu m \times 12\ \mu m$ of 30×30 points) as well as the averaged Raman spectrum are shown in Figure 4-9 (a) and confirm a uniform graphitization of

the SiC. The I_D/I_G and I_{2D}/I_G Raman intensity ratios are evaluated from the averaged spectrum, see Figure 4-9 (a), to be 0.23 and 1.3, respectively.

The grain sizes of the EG are estimated from the Raman measurement ratio using (3.1), with $\lambda_a = 532$ nm being the excitation laser wavelength. The average grain size is estimated to be ~84 nm using the averaged I_D/I_G Raman intensity ratio. From the same measurement, the maximum and minimum of the I_D/I_G ratio were determined to be 01.13 and 0.18, respectively. Therefore, we can estimate the minimum and maximum of the grain ~17 nm and ~107 nm, respectively. Note that the Raman ratios and estimated grain sizes are in line with large-area graphitised samples.

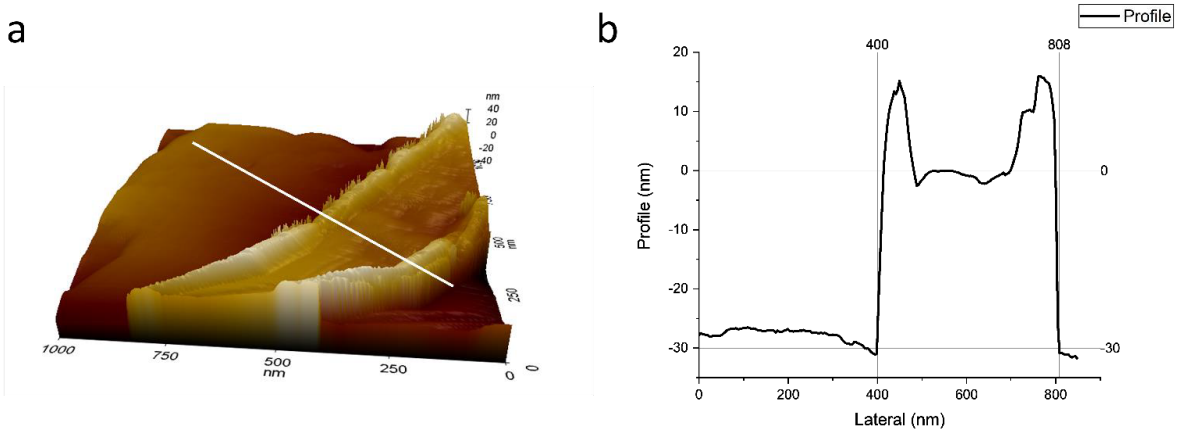

Figure 4-8 AFM topographical map (1000 nm × 1000 nm) of a single 400 nm catalyst metal grating. (a) 3D image of the metal grating with the white line indicating the location of (b) the measured profile of the grating. It shows the built-up metal on top of the grating after the lift-off process. This is due to the deposition of metals on the sidewalls of the PR during the sputtering process. Reprinted from [165]

Furthermore, two Raman spectral maps (5 µm × 5 µm of 20 × 20 points) were performed on the 400 nm graphene resonators and gratings. Figure 4-9 shows the 2D peak intensity maps of the measurements and their locations. The patterns can be clearly seen and distinguished from one another. However, our Raman spot size of ~300 nm impedes the accurate evaluation of the nanostructures.

Near-field imaging was performed using s-SNOM to analyze the patterned graphene at the nanoscale further. Figure 4-10 shows near-field imaging measurements of 100 nm and 400 nm gratings that were excited by tuning the laser source at 9.6 µm. The near-field imaging

clearly highlights the resonances of individual and groups of graphene grains within the gratings.

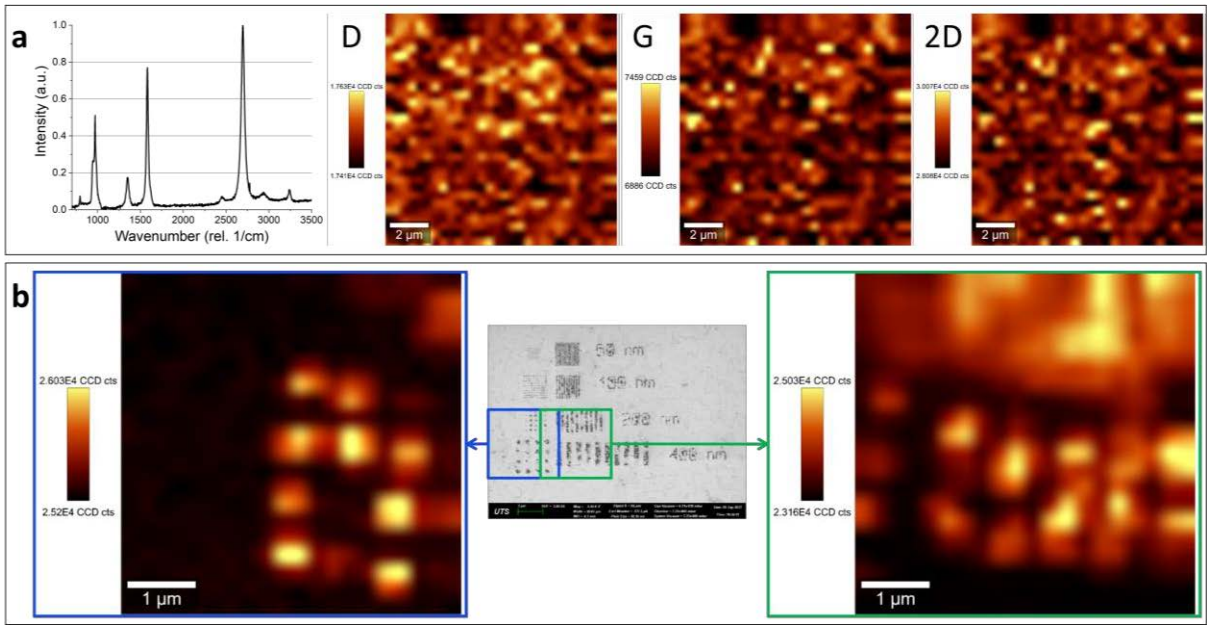

Figure 4-9 Raman characterization of patterned graphene samples. (a) Raman map ($12\ \mu m \times 12\ \mu m$ of 30×30 points) on the masked UV-lithography patterned graphene sample (university logo). The figure shows the Raman intensity maps of the D ($\sim 1350\ cm^{-1}$), G ($\sim 1580\ cm^{-1}$), and 2D ($\sim 2700\ cm^{-1}$) peaks, as well as an averaged Raman spectrum. (b) Large-area Raman map on the $400\ nm$ resonators and gratings on the EBL patterned graphene sample. (middle) Illustration of the location of the two Raman maps (each $5\ \mu m \times 5\ \mu m$ of 20×20 points). (left and right) Raman 2D ($\sim 2700\ cm^{-1}$) Intensity maps of (left) the resonators with a $400\ nm$ diameter and (right) the $400\ nm$ wide gratings. Reprinted from [165]

Figure A-1 and Figure A-2 show the amplitude and phase plots of the 100 nm and 200 nm gratings, respectively. While the near-field imaging results at a single wavelength may give the impression that some gratings are not fully graphitized, further near-field imaging of the 400 nm gratings using additional wavelengths of 7.5 µm, 8.5 µm, and 10.7 µm, as illustrated in Figure 4-11, show that graphene grains of different sizes resonate at different wavelength excitations. The background intensity change for the 10.7 µm amplitude map results from the high density of states related to the excitation of surface phonon polaritons in SiC [327].

Note that our previous work has indicated the support of plasmonic resonances in EG grown on SiC nanowires using the catalytic alloy-mediated graphitization approach used in this work [26].

The near-field images further show that some of the graphene grains conform to the shape of the gratings, particularly for the smaller 100 nm gratings, see Figure 4-10. This confirms that some of the grains approach ~100 nm sizes. For completeness, both the O2A and O2P plots of the 100 nm and 200 nm wide gratings are shown in Figure A-1 and Figure A-2.

4.3 Conclusion

In this work, we introduce the direct synthesis of planar (2D) micro and nanopatterned epitaxial graphene on silicon carbide that can be carried out at the wafer -scale. This is done by pre-patterning the Ni/Cu catalyst metals using simple lift-off processes prior to the graphene growth. This approach eliminates the need for chemical or ion and laser-based etching of the graphene, which carry the risk of potentially damaging or contaminating the two-dimensional layer. While this demonstration was carried out on a SiC/Si pseudo-substrate, this methodology could be extended to EG on bulk SiC wafers.

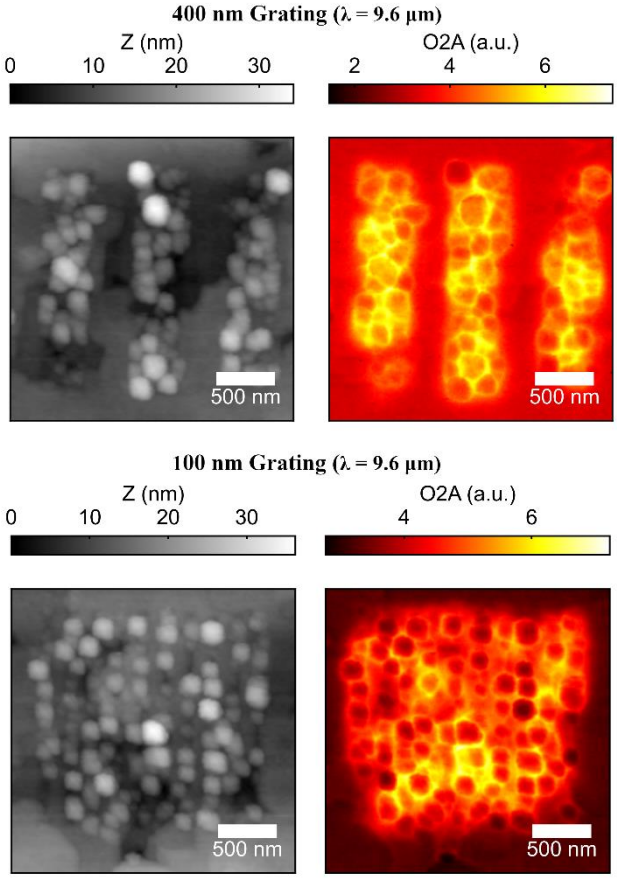

Figure 4-10 Near-field imaging characterisation of (top) 400 nm *and (bottom)* 100 nm *gratings. For the excitation, a wavelength of* 9.6 µm *was used. The image of the topographical scans are shown on the left, respectively, while the O2A plots show the amplitude of the measured fields. Reprinted from [165]*

It is estimated that the resolution of this patterning approach can currently enable grating sizes down to roughly ~100 nm width/space. This limit is mainly determined by the flow of the metal catalysts which are in liquid-phase during the graphitization, causing a loss of definition of the EG pattern. This effect is exacerbated by the metal build-up at the edges of the metal patterns due to the low anisotropy of the sputtering deposition in combination with the lift-off process. It is hence anticipated that the current pitch resolution could be improved by reducing the build-up using a highly-directional metal deposition method.

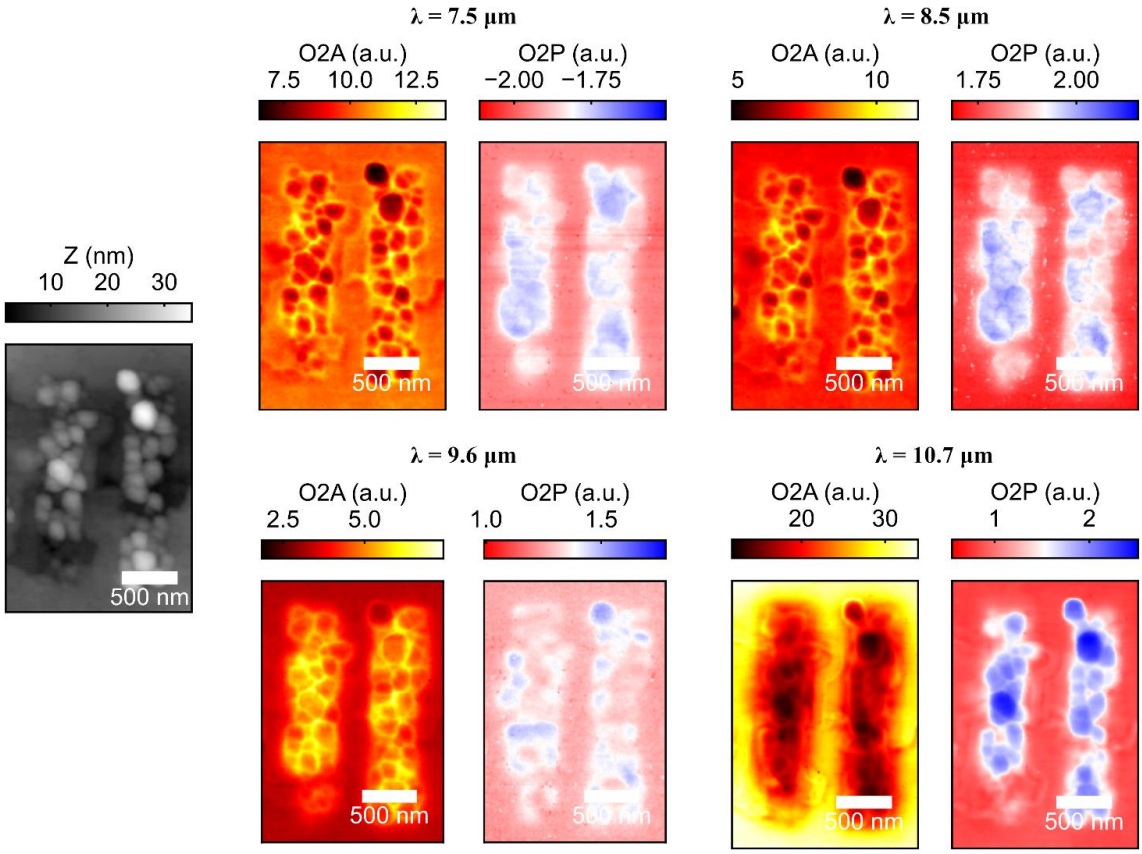

Figure 4-11 Near-field imaging characterization of two 400 nm gratings. For the excitation, wavelengths of 7.5 µm, 8.5 µm, 9.6 µm, and 10.7 µm were used. The O2A plots show the amplitude of the measured fields, and the O2P plots show the respective phase. The image of the topographical scan can be seen on the left. Reprinted from [165]

Chapter 5 High-Frequency Characterisation

5.1 Probe-based Characterisation

5.1.1 CPW Design

The initial step to characterising graphene samples using CPWs is to design the metallic CPW structures. The dimensions of the CPW are subjected to equipment-specific constraints. These need to be considered in the design:

1. For the lithography process, a Suss MJB4 Mask Aligner with a resolution limit of 0.5 µm is used. However, a Heidelberg µPG101 direct-write laser system was used to write the photolithography chrome mask. It has a resolution limit of 2 µm. Considering the cost and write time, the minimal feature size was chosen to be 5 µm.
2. The Probe measurements were conducted on a Cascade MPS150 probe station. FORMFACTOR Infinity Probes I50-A-GSG-100 50 GHz probes with a 100 µm pitch were connected to a Keysight N5225B PNA Network Analyser using 2.93 mm 40 GHz cables. A FORMFACTOR 101-190D calibration substrate was used for the SOTL calibration of the Network analyser and probes. The design rules of the pads used for the GSG probes require a minimal pad width of 25 µm.
3. The design rules further set the minimal length of the CPWs as the minimal distance between the probes, i.e., to be 150 µm.

The substrate itself is a double-layer dielectric, see Figure 5-1. SiC is heteroepitaxially grown on top of a Si wafer. Therefore, the CPW dimensions need to be analytically determined considering the permittivities and thicknesses of the individual layers.

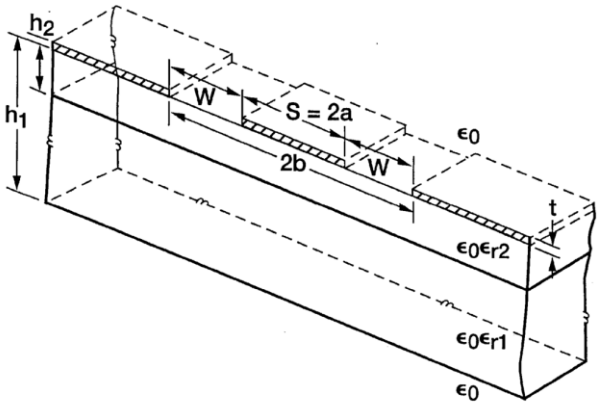

Figure 5-1 Schematic layout of conventional CPW structure on top of a double-layer dielectric substrate. Reprinted from [328]

Conformal mapping techniques are employed to calculate the effective permittivity ϵ_{eff} of the substrate and the characteristic impedance Z_0 of the CPWs. They assume the propagation of a quasi-static transverse electromagnetic (TEM) mode along the CPW [328, 329]. Furthermore, the metallic conductors have zero thickness and are perfect conductors, while the dielectric layers have perfect relative permittivity and are isotropic. The structure is, therefore, considered to be lossless.

The structure is separated into partial regions that are assumed to be divided by magnetic walls, and the electric fields in each region are thus confined in each particular region. Partial capacitances are determined for those regions, and the total capacitance is given by their sum. The capacitances are determined using the complete elliptical integral of the first kind. It is determined by [330]

$$K(k) = \int_0^{\pi/2} \frac{d\phi}{\sqrt{1 - k^2 \sin^2 \phi}} \tag{5.1}$$

with k being the modulus.

Three specific capacitances determine a CPW on a double-layer dielectric [328, 329]:

A. C_{air} is the partial capacitance of the CPW without any dielectric layers surrounding it. It is defined as

$$C_{air} = 4\epsilon_0 \frac{K(k_0)}{K(k_0')} \tag{5.2}$$

with the moduli $k_0 = \frac{S}{S+2W}$ and k_0' following $k_n' = \sqrt{1 - k_n^2}$.

B. C_1 originates from the lower dielectric layer and is given by

$$C_1 = 2\epsilon_0(\epsilon_{r1} - 1) \frac{K(k_1)}{K(k_1')} \tag{5.3}$$

with

$$k_1 = \frac{\sinh\left(\frac{\pi S}{4h_1}\right)}{\sinh\left(\frac{\pi(S+2W)}{4h_1}\right)} \tag{5.4}$$

and k_1' again following $k_n' = \sqrt{1 - k_n^2}$.

C. C_2 originates from the combination of the upper and lower dielectric. It is determined by

$$C_2 = 2\epsilon_0(\epsilon_{r2} - \epsilon_{r1}) \frac{K(k_2)}{K(k_2')} \tag{5.5}$$

with

$$k_2 = \frac{\sinh\left(\frac{\pi S}{4h_2}\right)}{\sinh\left(\frac{\pi(S+2W)}{4h_2}\right)} \tag{5.6}$$

and $k_2' = \sqrt{1-k_2^2}$.

The sum of the partial capacitances is given by

$$C_{CPW} = C_{air} + C_1 + C_2 \tag{5.7}$$

The effective permittivity, phase velocity, and characteristic impedance are defined as [329]

$$\epsilon_{eff} = \frac{C_{CPW}}{C_{air}} \tag{5.8}$$

$$v_{ph} = \frac{c_0}{\sqrt{\epsilon_{eff}}} \tag{5.9}$$

$$Z_0 = \frac{1}{C_{CPW} c_0} \tag{5.10}$$

where c_0 is the speed of light.

The thickness of the SiC layer of the NOVASIC substrates is variable. For the intrinsic 3C-(111) SiC/Si substrates, the thickness of the SiC layer is 500 nm, while the Si substrate has a thickness of 235 µm. The relative permittivities of SiC and Si are $\epsilon_{r,SiC} = 9.7$ and $\epsilon_{r,Si} = 11.7$, respectively.

The CPW is designed for a characteristic impedance of $Z_0 = 50\ \Omega$. Using (5.1)-(5.10) and 2D COMSOL modelling, as illustrated in Figure B-3, several combinations for S and W have been determined, see Table 5-1, that match the given constraints:

1. Since W is generally the smallest dimension of the CPWs, its width is set to the minimum feature size achievable using the available lithography processing. S is determined accordingly.
2. To create straight CPWs without any widening or narrowing of either S or W, CPWs are designed where S matches the minimal width of the contact pads used for the GSG probes. Here the characteristic impedance $\mathrm{Z_0} = 50\ \Omega$ was determined for $\mathrm{f} = 10$ GHz using a COMSOL 2D model.
3. Simulation of the shunt approach has identified this CPW to result in accurate extraction of graphene's conductivity. Here the characteristic impedance $\mathrm{Z_0} = 50\ \Omega$ was determined for $\mathrm{f} = 1$ GHz using a COMSOL 2D model.
4. The dimensions of S and W are set to match the pitch of 100 µm probes with $S + W = 100$ µm.

Table 5-1 CPW dimensions S and W and characteristic impedance were determined through the analytical model and numerical simulation. The dimensions of S and W within the COMSOL 2D model were optimised for impedance matching, $Z_0 = 50\ \Omega$, at $f = 10\ GHz$, or $f = 2\ GHz$, for case 3.

Case	Analytical Model		COMSOL 2D Model	
	S	**W**	**S**	**W**
1. W equivalent to minimal feature size	8.86 µm	5 µm	11 µm	5 µm
2. S equivalent to minimal pad width	25 µm	14.55 µm	25 µm	11 µm
3. S equivalent to minimal pad width	-	-	25 µm	5 µm
4. S and W optimised for 100 µm pitch	63.63 µm	36.37 µm	67 µm	33 µm

5.1.2 Approaches

Two approaches are used to determine the conductivity of graphene using CPWs. The often-considered patch approach and the less-considered shunt approach. The patch approach consists of placing a graphene patch within the centre trace of a metallic CPW. The impedance of the patch is de-embedded from the measurement results. Following the Drude conductivity model of graphene, its resistance is considered to be constant within the microwave frequency range. The extracted patch impedance is modelled in Advanced Design System (ADS) using an equivalent circuit model of the patch, and the conductivity of graphene is extracted.

Alternatively, the shunt approach is considered. Here, graphene is placed in between the centre trace and ground planes of a metallic CPW. A CPW without graphene is used as a reference. The conductivity of graphene can be determined by extracting the $RLCG$-parameters of the graphene loaded and reference CPW. It is assumed that the graphene shunt will only affect the admittance G, and the subsequently added admittance of graphene can then be determined from G_{ref} and G_{shunt}.

5.1.2.1 Graphene Patch Approach

In addition to calibrating the measurement setup using the SOTL calibration procedure, SOTL-based de-embedding is employed to isolate the electrical properties of the graphene patch and remove the influences of metallic traces, probes, and parasitic elements. Figure 5-2 illustrates the required SOTL structures for the de-embedding process. The three-step SOTL de-embedding was first introduced in [174] and later improved on by Vandamme et al. [176]. It was initially developed for the characterisation of high-frequency transistors. However, the approach can be used for any device under testing, in this case, for a graphene patch.

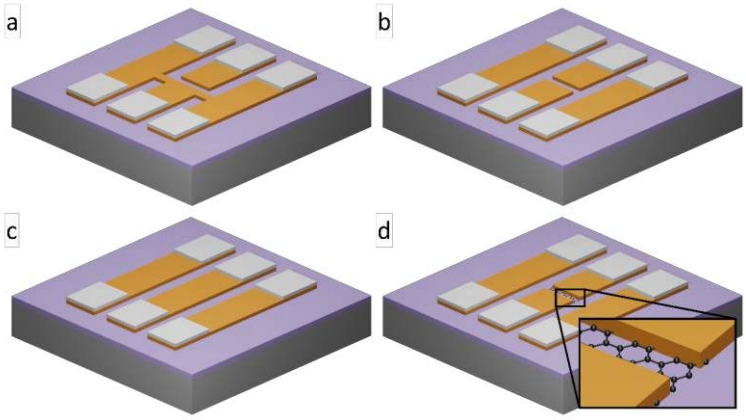

Figure 5-2 Illustration of the required (a) short, (b) open, (c) through, and (d) load structures for SOTL de-embedding. The loaded structure features a graphene patch that extends beneath the metal trace to form contacts, as shown in the inset in (d).

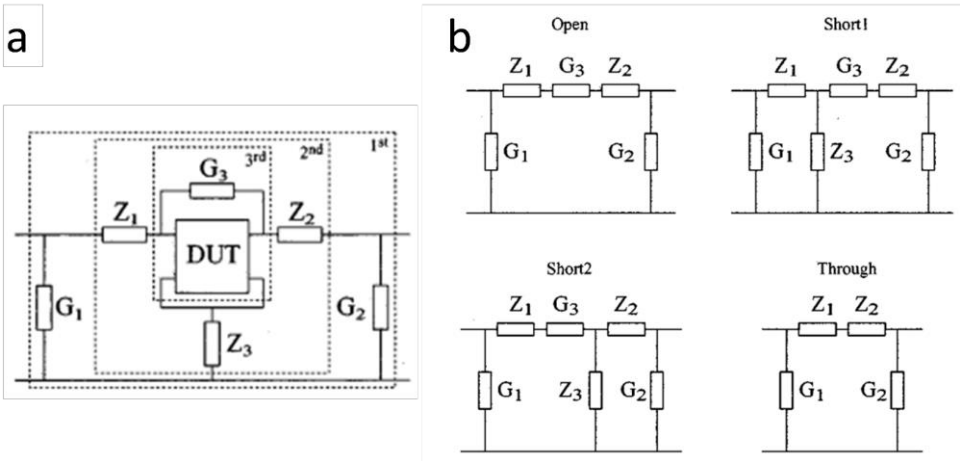

Figure 5-3 Equivalent circuit representation of CPW-based high-frequency testing and SOTL de-embedding structures. (a) Three steps of the de-embedding procedure and the equivalent circuit model of the high-frequency testing structure and the parasitic components that originate from the contact pads and interconnects. (b) Y-parameter equivalent circuits of the parasitic components of the open, short1 (left port shorted), short2 (right port shorted), and through de-embedding structures. Reprinted from [176]

Figure 5-3 shows the parasitic components of the test structure. They comprise the admittances G_1, G_2, and G_3, as well as the impedances Z_1, Z_2, and Z_3. Here, G_1 and G_2 represent the coupling that originates between the port interconnects and the substrate. G_3 is the coupling between the two port interconnects themselves. The series impedances arise from

the metal interconnects where Z_1 and Z_2 are impedances of the port interconnects and Z_3 is the impedance of the ground traces.

The calculations for de-embedding the graphene patch electrical parameters follow those in [176]. First, the individual values for the parasitic components are evaluated. For this, the S-parameter measurement values of the short, open, and through structures are transformed to Y-parameters using the two-port-network conversion table in [251] (p.192). The parasitic admittances can thus be calculated using

$$G_1 = Y_{11,open} + Y_{12,open} \tag{5.11}$$

$$G_2 = Y_{22,open} + Y_{12,open} \tag{5.12}$$

$$G_3 = \left(-\frac{1}{Y_{12,open}} + \frac{1}{Y_{12,thr}} \right)^{-1} \tag{5.13}$$

and the parasitic impedances are given by

$$Z_1 = \frac{1}{2}\left(\frac{-1}{Y_{12,thr}} + \frac{1}{Y_{11,short1} - G_1} - \frac{1}{Y_{22,short2} - G_2} \right) \tag{5.14}$$

$$Z_2 = \frac{1}{2}\left(\frac{-1}{Y_{12,thr}} - \frac{1}{Y_{11,short1} - G_1} + \frac{1}{Y_{22,short2} - G_2} \right) \tag{5.15}$$

$$Z_3 = \frac{1}{2}\left(\frac{1}{Y_{12,thr}} + \frac{1}{Y_{11,short1} - G_1} + \frac{1}{Y_{22,short2} - G_2} \right) \tag{5.16}$$

The values for the parasitic components are then used to de-embed the measurement values of the graphene patch-loaded structure. From here on out, the calculations can be made using the matrix representation of two-port-network parameters. Here, again, the S-parameter values are first converted to their Y-parameter equivalent to form Y_{load}. Using

$$Y_A = Y_{load} - \begin{bmatrix} G_1 & 0 \\ 0 & G_2 \end{bmatrix} \tag{5.17}$$

the influence of G_1 and G_2 are removed first. Then the series impedances Z_1, Z_2, and Z_3 are subtracted

$$Z_B = Z_A - \begin{bmatrix} Z_1 + Z_3 & Z_3 \\ Z_3 & Z_2 + Z_3 \end{bmatrix}. \tag{5.18}$$

Finally, G_3 is removed using

$$Y_{Gr,patch} = Y_B - \begin{bmatrix} G_3 & -G_3 \\ -G_3 & G_3 \end{bmatrix}. \tag{5.19}$$

and the de-embedded impedance matrix of the graphene patch $Z_{Gr,patch}$ can be determined from $Y_{Gr,patch}$.

Using the equivalent circuit model in Figure 5-4 and the impedance of the intrinsic impedance of the graphene patch can be written as [35]

$$Z_{21,Gr,patch} = \frac{2R_C}{1+j\omega C_C R_C} + \frac{R_G}{1+j\omega C_G R_G}. \tag{5.20}$$

where R_C and C_C are the contact resistance and capacitance, and R_G and C_G are the resistance and capacitance of the graphene patch. Furthermore, the real and imaginary parts of the impedance can be determined from

$$R_{Gr,patch} = Re\{Z_{21,Gr,patch}\} = \frac{2R_C}{1+\omega^2 C_C^2 R_C^2} + \frac{R_G}{1+\omega^2 C_G^2 R_G^2}. \tag{5.21}$$

$$X_{Gr,patch} = Im\{Z_{21,Gr,patch}\} = -\left(\frac{2\omega C_C R_C^2}{1+\omega^2 C_C^2 R_C^2} + \frac{\omega C_G R_G^2}{1+\omega^2 C_G^2 R_G^2}\right). \tag{5.22}$$

To determine the individual contributions of R_C, C_C, R_G, and C_G, the equivalent circuit model in Figure 5-4 is set up in ADS, and its impedance $Z_{21,ADS}$ is matched to $Z_{21,Gr,patch}$.

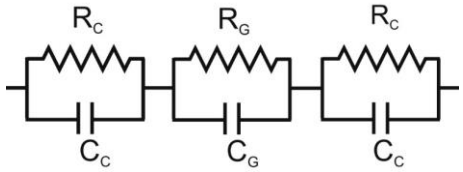

Figure 5-4 Equivalent circuit model of de-embedded graphene patch. The intrinsic impedance of the graphene patch is equal to $Z_{21,Gr,patch}$. Reprinted from [35]

5.1.2.1.1 Numerical Modelling

COMSOL and its RF-Module were used to model the graphene CPWs, and MATLAB was used to analyse the de-embedding procedure. To verify the model, previously published S-parameter measurement results of SOTL de-embedding structures were used [35]. Here the CPW design and substrate used in the study were recreated in COMSOL. Comparing the simulation output to the published values, as illustrated in Figure B-1, shows good agreement and confirms the validity of the used model. At the same time, the de-embedding procedure was implemented in MATLAB and used to extract the properties of the simulated graphene patch and its contacts. Here the contacts were simulated as lumped impedance boundary conditions, matching the values determined in the study. Figure B-2 shows good agreement between the de-embedded properties of the COMSOL model and the measurement results.

To simulate the Graphene is modelled as a transition boundary condition with constant conductivity and with a thickness of $t_{Gr} = 0.34$ nm. Typical values for EG on SiC/Si are assumed, which were determined from DC measurements [173]. The CPW structures are modelled in 3D, and several CPW structures with dimensions according to Table 5-1 were

modelled. The total width of the CPWs was determined from the 100 µm pad pitch and the pad dimensions of 50 µm × 50 µm to be 250 μm. The total length of the CPW, on the other hand, was determined from the probe pitch. Two lengths of 150 µm and 300 µm were considered, and the pad dimensions to be 200 µm and 350 µm, respectively. The CPWs were modelled as a $t_{Cu} = 100$ nm thick Cu layer.

The relative permittivities $\epsilon_{r,SiC} = 9.7$ and $\epsilon_{r,Si} = 11.7$, respectively, were assumed for the SiC and Si simulations. The SiC layer has a thickness of $t_{SiC} = 500$ nm according to the manufacturer's specifications. While the Si substrate has a thickness of 235 µm, it was simulated with a thickness of 100 µm, as the majority of the EM fields are confined close to the CPW. This choice resulted in reduced model complexity. The width and length of the substrate were determined from the width and length of the CPWs by extending those dimensions by 50 µm in each direction.

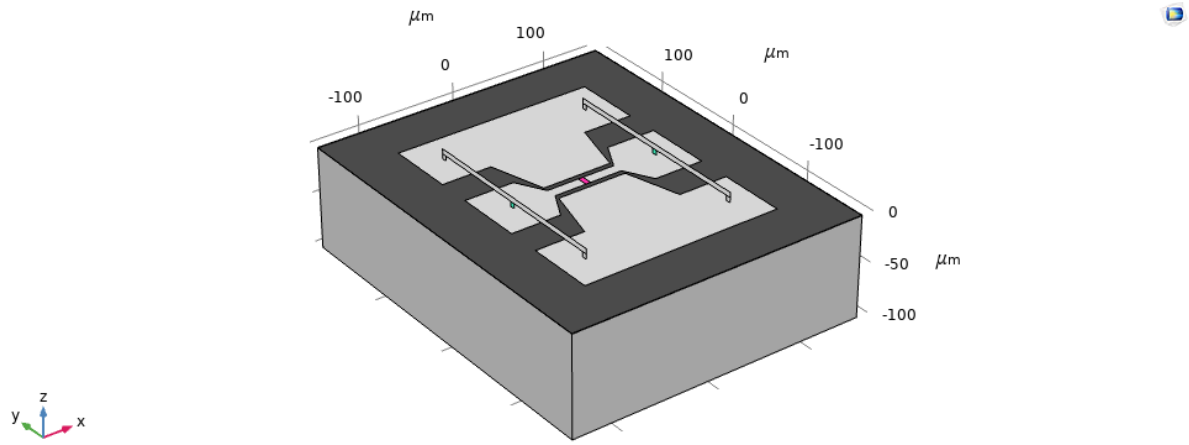

Figure 5-5 3D COMSOL model used to simulate CPWs on SiC/Si wafers. The structure is surrounded by a PML (not pictured). This particular CPW is used for the SOTL approach as it has a graphene patch (pink patch) within the centre trace. The lumped ports are rectangular patches (teal patches in the figure) between the pads of the centre trace and PEC bridges that span across the CPW to connect the outer ground planes. The dimensions of the CPW are: probe pitch of 150 µm; S is 11 µm; W is 5 µm; pad pitch is 100 µm; and the patch has a length of 5 µm.

Two 5 µm wide, perfect electrical conductor (PEC) boundary bridges that connected the two outer ground traces of the CPW together with 5 µm × 5 µm big uniform lumped ports between the bridges and centre trace were used for the excitation. The substrate was surrounded by air ($\epsilon_{r,air} = 1$) and engulfed with an exterior boundary having a radius of 5 mm. A perfectly

matched layer (PML) absorbing boundary condition with a thickness of 0.5 mm covered that boundary, effectively emulating a free space far-field domain. To determine the performance of the CPW, $1 - 60$ GHz frequency sweeps, with 10 steps per decade, were performed. The S-parameters were then extracted, and MATLAB was used for further processing.

Figure 5-5 shows the COMSOL model used to simulate the CPWs. In total, four structures, as illustrated in Figure 5-2, need to be simulated. Figure 5-6 and Figure 5-7 show the dependence of the S-parameter on the variation of the CPW structure length and CPW structure design, as per Table 5-1, respectively.

An accuracy evaluation was performed as the de-embedding technique removes parasitic components and their influence on the extracted patch impedance. However, slight variations are to be expected due to the limitations of the de-embedding procedure. Figure 5-8 shows the de-embedded graphene patch impedance Z_{21} and compares it to the extracted impedance of the whole loaded structure. Since the contact of the graphene patch and the centre trace can be simulated without a contact impedance, the lower frequency limit of the real part de-embedded patch impedance $Re\{Z_{21}\}$ represents the patch resistance. Its variation is ~ 0.1 %.

For comparison, the de-embedded impedances of the graphene patch for different CPW lengths and different CPW geometries are shown in Figure 5-9 and Figure 5-10, respectively. The former shows that a sorter CPW length results in a more accurate extraction of the patch impedance. At the same time, there is also a strong correlation between the CPW geometry and the extracted patch impedance, as indicated by Figure 5-10. The vertical change in $Re\{Z_{21}\}$ is due to the change of the patch width with the respective geometries, wider patches resulting in lower impedances. More importantly, $Im\{Z_{21}\}$ experiences a lower variation if '*full*' structures are used. The term '*full*' refers to CPWs where the width of the centre trace and gap to the ground planes does not change throughout the length of the CPW. This eliminates geometrical changes in the traces and the introduction of parasitics.

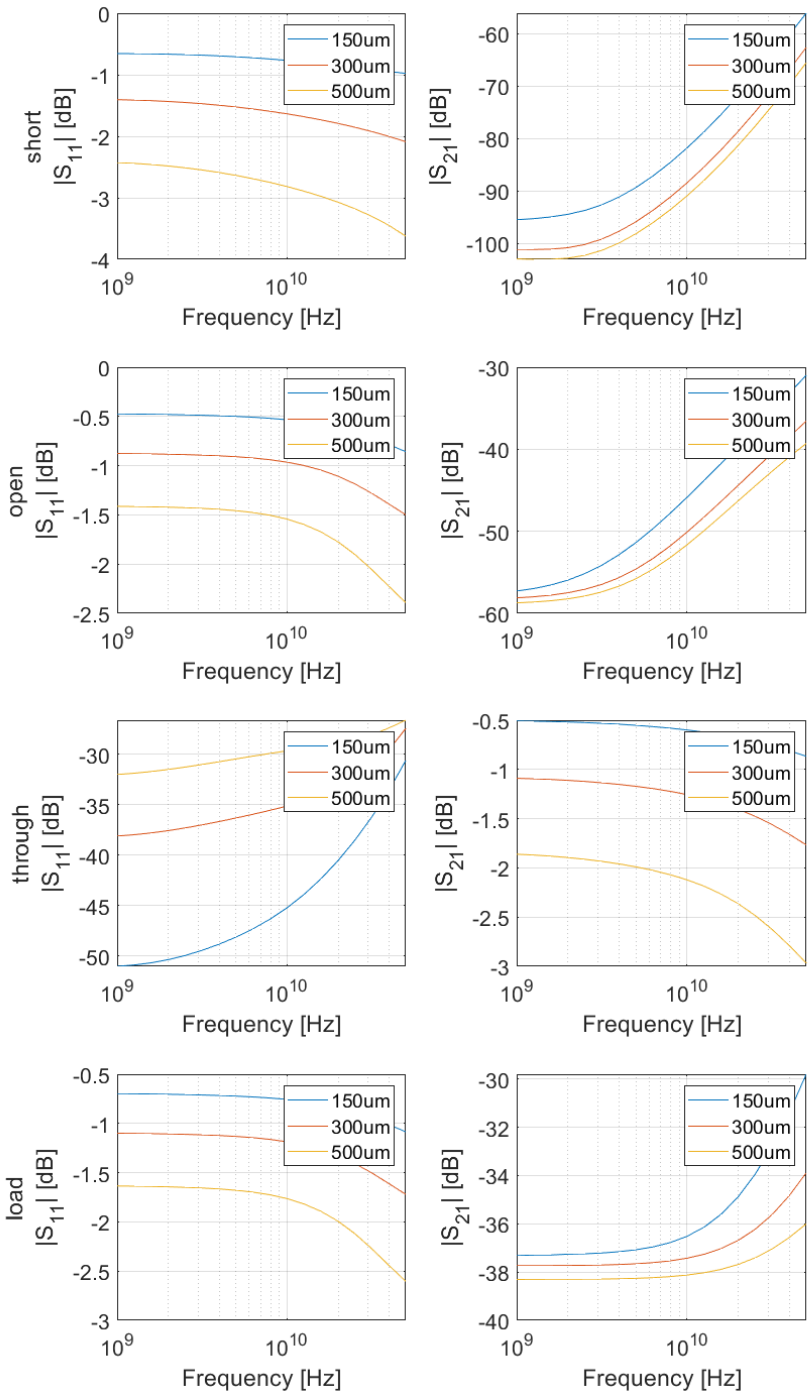

Figure 5-6 Comparison of the simulated S-parameter values of $S = 11\ \mu m$ and $W = 5\ \mu m$ CPWs with a $5\ \mu m$ long graphene patch within the centre trace for different structure lengths.

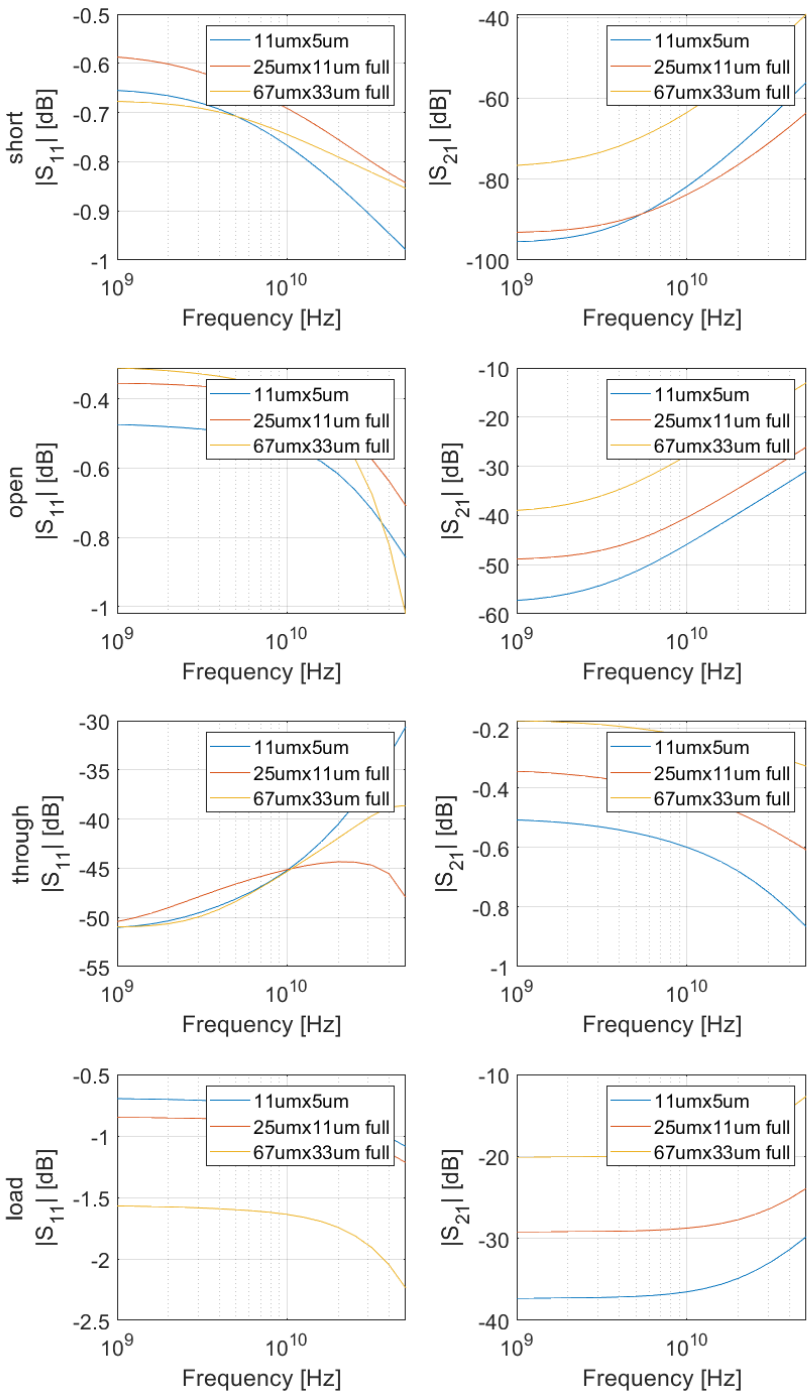

Figure 5-7 Comparison of the simulated S-parameter values of different CPW geometries (varying S and W) with a 5 μm *long graphene patch within the centre trace. The length of the CPWs is kept the same. The index 'full' refers to CPWs where the width of the centre trace and gap to the ground planes does not change throughout the length of the CPW.*

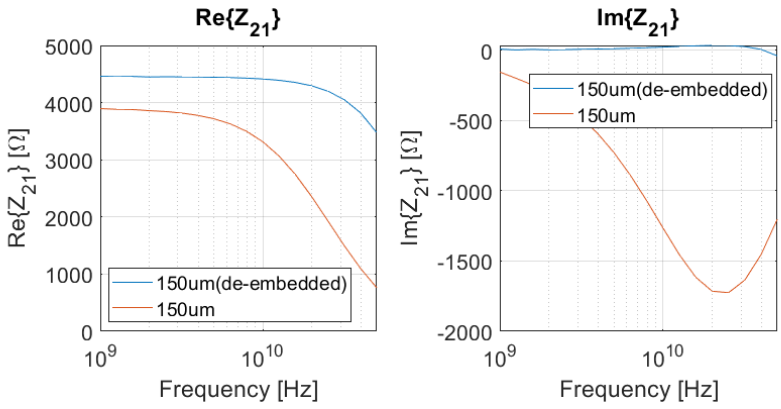

Figure 5-8 Comparison of the extracted patch impedance after de-embedding to the impedance of the graphene patch loaded CPW. The real part of the de-embedded patch impedance approaches $Re\{Z_{21}\} = 4461.1\ \Omega$ *towards the low-frequency limit. It matches the patch resistance well with* $R_{Gr,patch} = \frac{1}{\sigma_{Gr}}\frac{l}{wt_{Gr}} = \frac{1}{3\times10^5\ S\ m^{-1}}\frac{5\ \mu m}{11\ \mu m\times0.34\ nm} = 4456.3\ \Omega$. *This is the case because no contact resistance is considered in the simulation, as this data was not available at the time.*

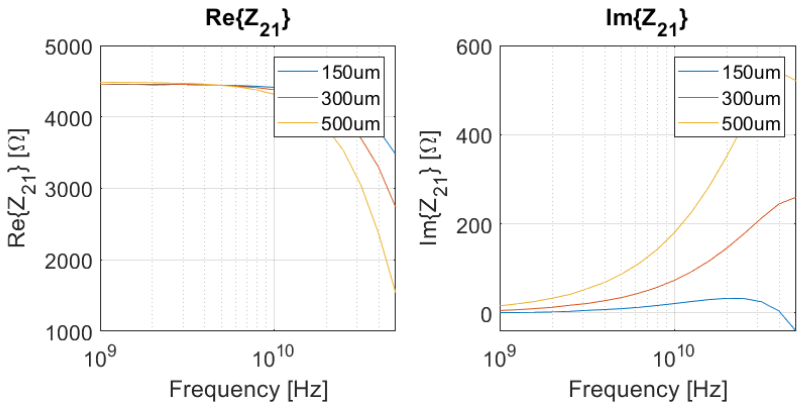

Figure 5-9 Comparison of the extracted patch impedance after de-embedding of $S = 11\ \mu m$ *and* $W = 5\ \mu m$ *CPWs with a* $5\ \mu m$ *long graphene patch within the centre trace for different structure lengths.*

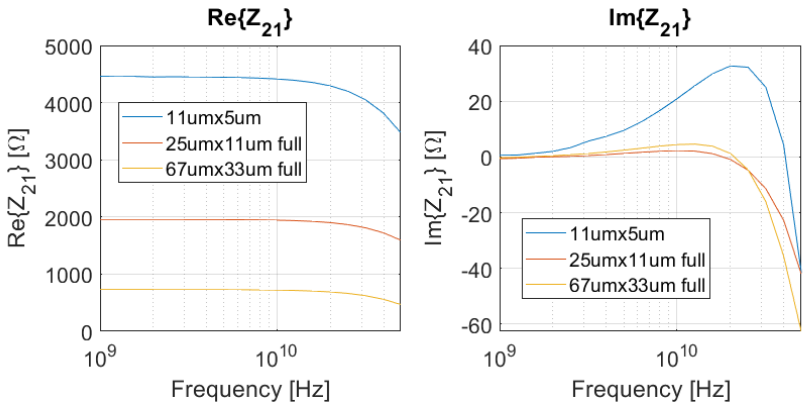

Figure 5-10 Comparison of the extracted patch impedance after de-embedding of different CPW geometries (varying S and W) with a $5\ \mu m$ long graphene patch within the centre trace. The lengths of the CPWs are kept the same.

5.1.2.2 Shunt Approach

The shunt approach has not received much attention in the past. However, it provides an alternative to the patch approach. Here, graphene is placed in between the centre trace and the ground planes as a shunt, as illustrated in Figure 5-11. The $RLGC$-parameters of the transmission line are extracted from the shunted CPW and compared to the reference structure.

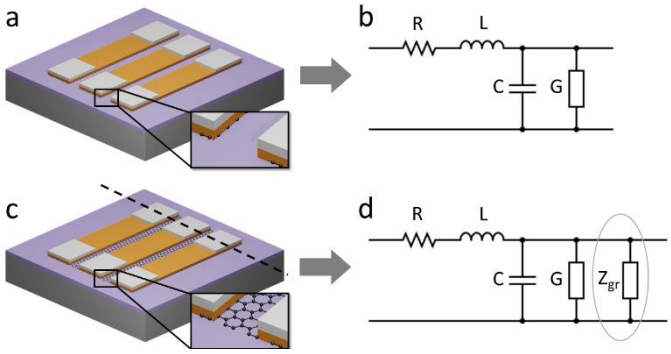

Figure 5-11 (a) Illustration of a graphene un-shunted CPW on SiC/Si substrate. The inset shows that graphene is only underneath the metal CPW, not between the signal and ground traces. (b) RLCG model of the un-shunted CPW in (a). (c) Illustration of a graphene-shunted CPW. The dashed line visualises the plane for the fabrication description in Figure 5-20. The inset shows that the graphene lies in the gaps of and underneath the signal and ground traces and, hence, acts as a shunt. (d) RLCG model of the shunted CPW in (c). Reprinted from [331]

The extraction of the $RLCG$-parameters from S-parameter measurements closely follows [332]. It is based on the Telegrapher's transmission line equations [251]. The S-parameter matrix for a two-port network is defined as

$$[S] = \begin{bmatrix} S_{11} & S_{12} \\ S_{21} & S_{22} \end{bmatrix} \tag{5.23}$$

For a lossy and unmatched transmission line, it can be written as [332]

$$[S] = \frac{1}{D_s}\begin{bmatrix} (Z^2 - Z_0^2)\sinh\gamma l & 2ZZ_0 \\ 2ZZ_0 & (Z^2 - Z_0^2)\sinh\gamma l \end{bmatrix} \tag{5.24}$$

where γ is the propagation constant, Z is the characteristic impedance of the transmission line, Z_0 is the impedance of the measurement system, $D_s = 2ZZ_0\cosh\gamma l + (Z^2 + Z_0^2)\sinh\gamma l$, and l is the length.

Converting the S-parameter matrix from (5.24 to the $ABCD$-parameter representation leads to

$$\begin{bmatrix} A & B \\ C & D \end{bmatrix} = \begin{bmatrix} \cosh\gamma l & Z\sinh\gamma l \\ \dfrac{\sinh\gamma l}{Z} & \cosh\gamma l \end{bmatrix} \tag{5.25}$$

with the $ABCD$-matrix representation being related to the S-parameter matrix via

$$\begin{bmatrix} A & B \\ C & D \end{bmatrix} = \begin{bmatrix} \dfrac{(1+S_{11})(1-S_{22}) + S_{12}S_{21}}{2S_{21}} & Z_0\dfrac{(1+S_{11})(1+S_{22}) - S_{12}S_{21}}{2S_{21}} \\ \dfrac{1}{Z_0}\dfrac{(1-S_{11})(1-S_{22}) - S_{12}S_{21}}{2S_{21}} & \dfrac{(1-S_{11})(1+S_{22}) + S_{12}S_{21}}{2S_{21}} \end{bmatrix} \tag{5.26}$$

from the two-port-network conversion table in [251] (p.192).

Combining (5.25 and (5.26 leads to [332]

$$e^{-\gamma l} = \left(\frac{1 - S_{11}^2 + S_{21}^2}{2S_{21}} \pm K\right)^{-1} \tag{5.27}$$

$$K = \left(\frac{(S_{11}^2 - S_{21}^2 + 1)^2 - (2S_{11})^2}{(2S_{21})^2}\right)^{\frac{1}{2}} \tag{5.28}$$

$$Z^2 = Z_0^2\frac{(1+S_{11})^2 - S_{21}^2}{(1-S_{11})^2 - S_{21}^2} \tag{5.29}$$

Using the formulas for γ and Z where

$$\gamma = \alpha + j\beta = \sqrt{(R + j\omega L)(G + j\omega C)} \tag{5.30}$$

$$Z = \sqrt{\frac{R + j\omega L}{G + j\omega C}} \tag{5.31}$$

the $RLGC$-parameters of the CPWs can be determined as

$$R = Re\{\gamma Z\} \tag{5.32}$$

$$L = Im\{\gamma Z\}/\omega \tag{5.33}$$

$$G = Re\{\gamma/Z\} \tag{5.34}$$

$$C = Im\{\gamma/Z\}/\omega \tag{5.35}$$

Because the Drude conductivity model predicts a purely real conductivity in this frequency band, the graphene is assumed to behave as a resistor. Because it is placed in between the centre trace and the ground planes, one can assume it will only affect the G-parameter of the CPWs. Using the extracted values of $G_{Gr,shunt}$ and G_{ref} for the shunted and reference CPW, respectively, the admittance of the graphene patch $G_{Gr,patch}$ and the conductivity of graphene σ_{Gr} and its sheet resistance $R_{s,Gr}$ can be determined using

$$G_{Gr,patch} = G_{Gr,shunt} - G_{ref} \tag{5.36}$$

$$\sigma_{Gr} = G_{Gr,patch}\frac{w}{2l} \tag{5.37}$$

$$R_{s,Gr} = \frac{W}{2lG_{Gr,patch}} \tag{5.38}$$

where W is the CPW's gap width, and l is the length of a single graphene shunting patch. Since the exact thickness of EG grown on SiC/Si is not known, the evaluation of the sheet resistance is preferred during measurements, while in the simulations, the conductivity is used due to the simple setting in the model parameters.

5.1.2.2.1 Numerical Modelling

The shunt approach requires two separate CPWs to evaluate the high-frequency conductivity of graphene, namely a through and a shunted structure. As above, the CPWs with the dimensions described in Table 5-1 were simulated using COMSOL. The model was set up the same way as those used to simulate the patch approach, see Figure 5-12, i.e., the graphene was modelled using a surface impedance boundary condition with a constant and real conductivity $\sigma_{Gr} = 3\ \mathrm{S\ m^{-1}}$ determined from previous measurements [30]. Figure 5-13 shows the extracted S-parameters of the CPW that resulted in the most accurate extraction of graphene's conductivity. The $RLCG$-parameters were then determined using (5.23)-(5.35). Figure 5-14 shows the $RLGC$-parameters of the through and shunt CPW structures with the dimensions: (150 µm × 25 µm × 11 µm; 200 µm shunt). Here it can be clearly seen that the shunt only affects G. The deviations at high frequencies can be attributed to the inaccuracy of the extraction procedure [332]. Using (5.36)-(5.38), the conductivity of graphene is extracted. Furthermore, the deviation (error) is calculated.

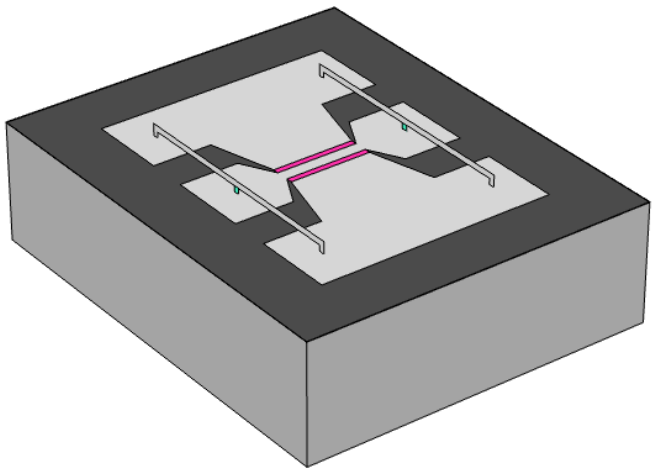

Figure 5-12 3D COMSOL CPW model used for the shunt approach. It has graphene shunts (pink patches) between the centre trace and the ground planes. The dimensions of the CPW are: probe pitch of 150 *µm; S is* 11 *µm; W is* 5 *µm; pad pitch is* 100 *µm; and the shunts have a length of* 70 *µm.*

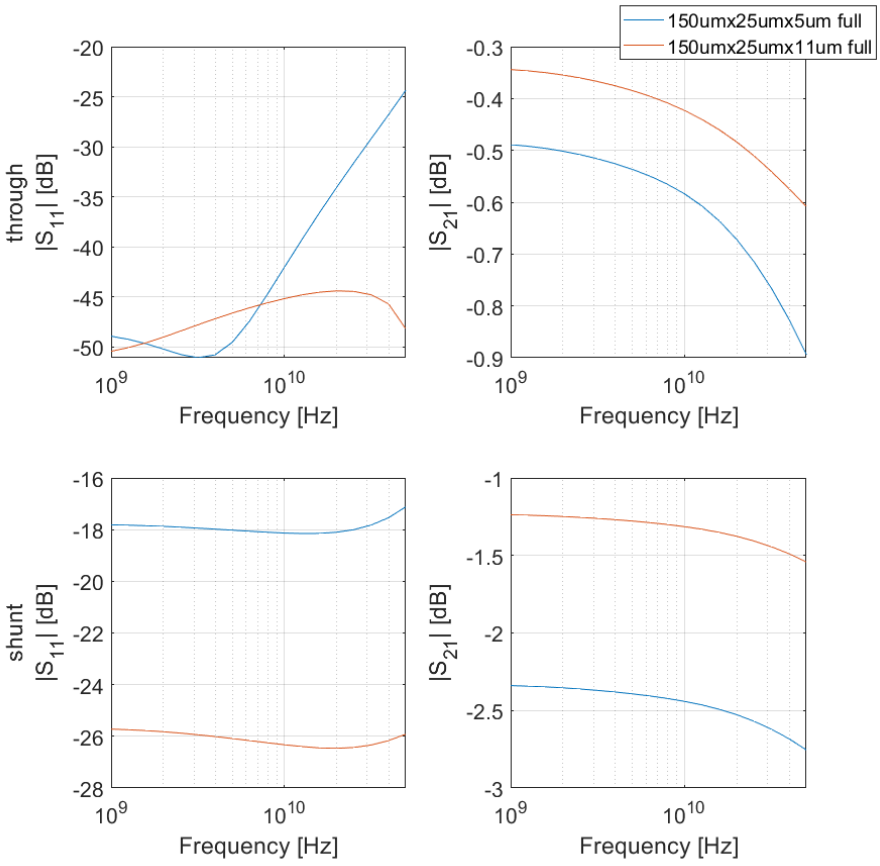

Figure 5-13 Extracted S-parameters of the two most accurate CPW geometries separated for the through (un-shunted) and shunted structures.

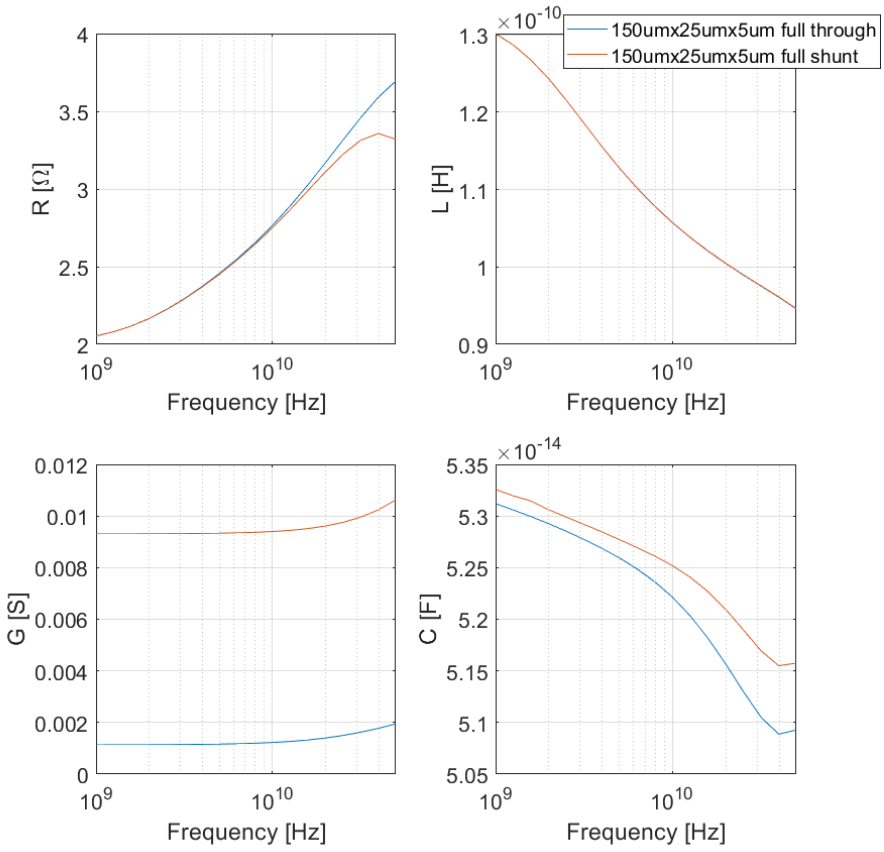

Figure 5-14 Extracted RLCG transmission line parameters using (5.23)-(5.35) of the most accurate CPW. From the measurements, it can be clearly seen that G is most influenced by the added graphene shunt. Deviations at high frequencies can further be attributed to the inaccuracy of the extraction procedure.

The accuracy of this approach can easily be determined using simulations, see Figure 5-15. Changing various design aspects of the CPW structures can significantly influence the accuracy. Figure 5-16 shows that the accuracy decreases with increasing CPW length. Moreover, it is preferred that the shunt spans the entire length of the CPW, as illustrated in Figure 5-17. However, this is only possible with CPWs where the width of the centre trace S and gap W do not change. Figure 5-18 illustrates that a tight CPW where the width of the centre trace and gap take on minimal dimensions, i.e., $25\ \mu m \times 11\ \mu m$ compared to $67\ \mu m \times 33\ \mu m$ for S and W respectively, results in more accurate results. Furthermore, using CPW structures that have smaller dimensions but have a varying S and W profile, i.e., $11\ \mu m \times 5\ \mu m$, to accommodate for the pads, also results in less accurate results. Therefore, the ideal structure for evaluating the conductivity of graphene using the shunt approach is the $150\ \mu m \times 25\ \mu m \times$

11 µm structure with a shunt that spans the entire length of the CPW. Lastly, the influence of the conductivity of the graphene patch is evaluated. Figure 5-19 shows that the extraction approach improves with increasing conductivity. Both conductivities represent the upper and lower limit of the conductivity of EG grown on 3C-(111) SiC/Si from [30]

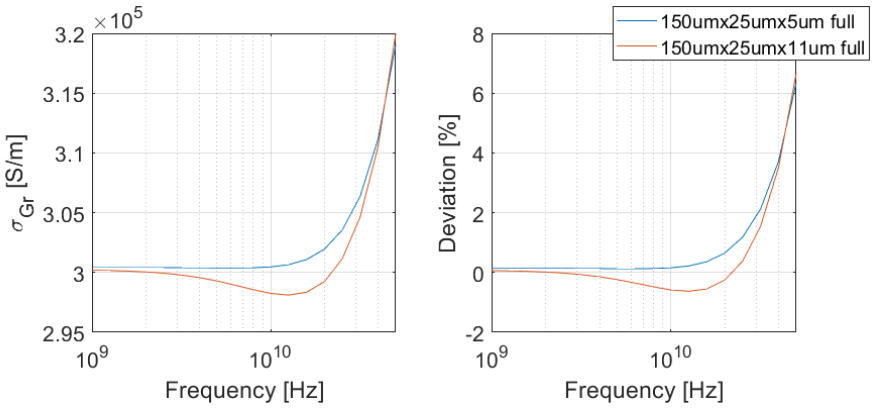

Figure 5-15 Extracted conductivity of graphene and the deviation for the two most accurate CPW geometries. Calculated using the extracted RLGC-parameters and equations (5.36)-(5.37).

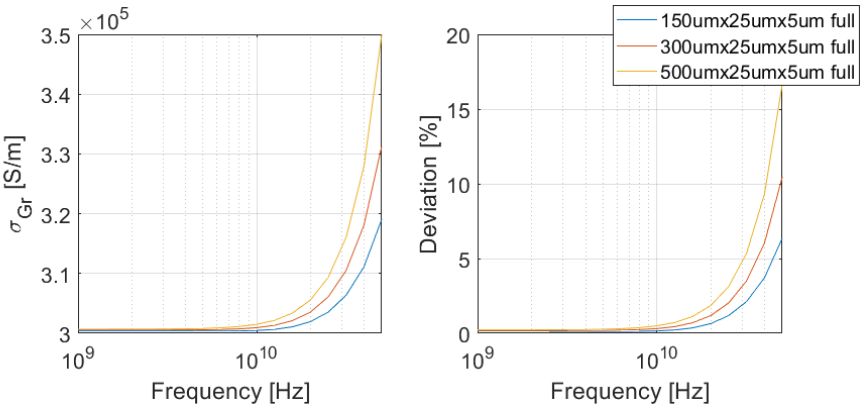

Figure 5-16 Influence of CPW length on the accuracy of the extracted conductivity. Short structures result in more accurate measurements.

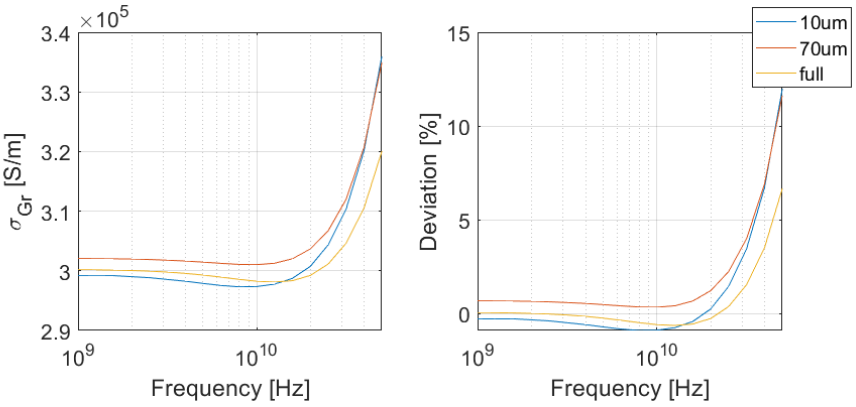

Figure 5-17 Influence of graphene shunt length on the accuracy of the extracted conductivity. Shunts that span the full length of the CPW are preferred.

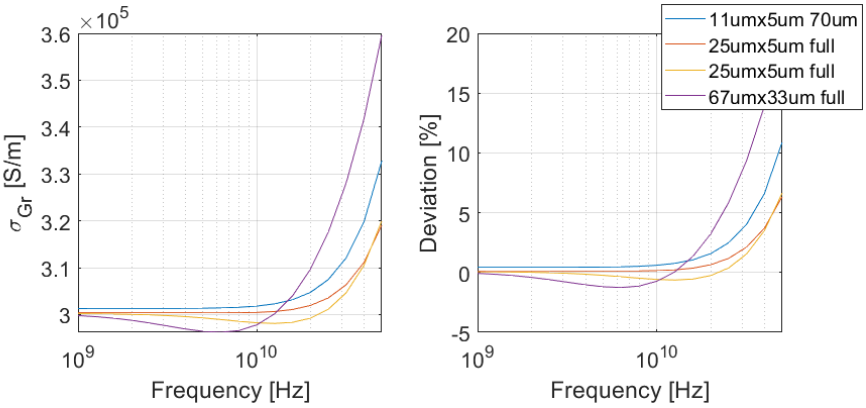

Figure 5-18 Influence of CPW structure on the accuracy of the extracted conductivity. Straight CPWs without any variation of S and W result in more accurate results.

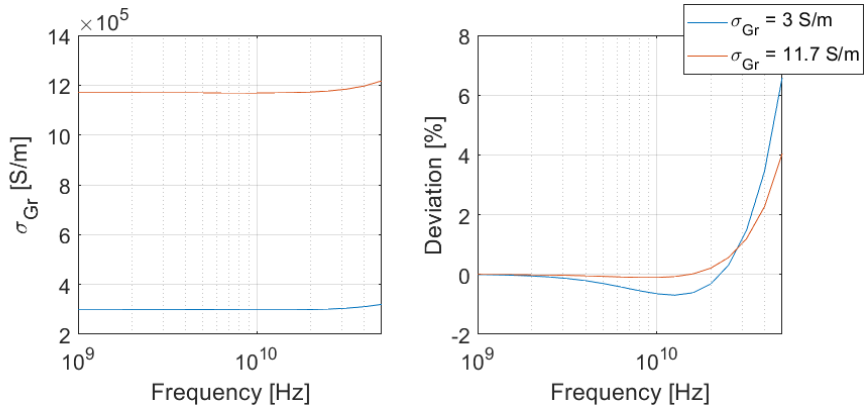

Figure 5-19 Influence of the graphene conductivity on the accuracy of the extracted conductivity. A higher conductivity results in a more accurate result.

5.1.3 Fabrication of Coplanar Waveguides

The CPW structures are fabricated using standard lithography processing steps. The main structure of the CPWs consisted of metal (5 nm of Ni and 100 nm of Cu), as it can be deposited as a relatively thick layer in comparison to graphene. This improves the transmission properties of the CPW [34, 35]. The thin layer of Ni is crucial for contacting graphene as the selection of the metal can have a significant influence on the graphene-metal contact resistance. The reason for this is the significant work function difference between the two [333]. Cu was chosen as the main CPW metal over Al due to its availability and high conductivity. Furthermore, the tetramethylammonium hydroxide-based PR developer significantly etched Al during the development of the photomask for the deposition of the contact pads, which would result in insufficient contact between the two, see Figure B-4. Aluminum was used for the contact pads due to the requirement of using the GSG probes.

The individual fabrication steps are illustrated in Figure 5-20 and outlined in Table 5-2. EG was grown on intrinsic 3C-(111) SiC/Si substrates using a catalytic alloy-mediated graphitisation process [4, 13]. It was patterned by pre-structuring the metal catalyst using UV-lithography patterned PR and a lift-off technique, as introduced in Chapter 4.

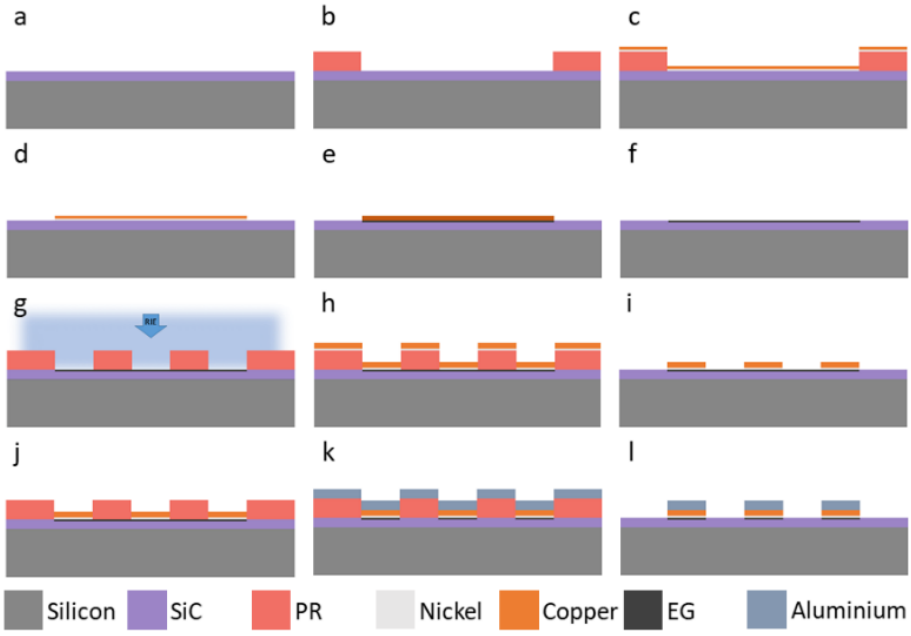

Figure 5-20 Schematic illustration of the fabrication steps required to manufacture metal CPWs on SiC/Si substrates employing EG as a shunt. EG is structured via the pre-structuring of the catalyst metals before graphitisation. A description of individual steps is given in Table 5-2. Reprinted from [331]

Table 5-2 Description of fabrication steps for the schematics in Figure 5-20.

Step	Description
a	Bare SiC/Si intrinsic substrate
b	Patterning of PR via UV lithography for lift-off of metal catalysts
c	Deposition of Ni (10 nm) and Cu (20 nm) for graphitisation
d	Lift-off using sonication in acetone
e	Graphitisation via annealing at $1100°C$ for one hour
f	Freckle etch to remove metal catalysts and silicides
g	Patterning of PR via UV lithography for lift-off of metal CPW as well as O_2 de-scum and Ar treatment via ICP-RIE
h	Deposition of Ni (5 nm) and Cu (100 nm) to form the CPW structure
i	Lift-off using sonication in acetone
j	Patterning of PR via UV lithography for lift-off of Al contact pads
k	Deposition of Al contacts
l	Lift-off using sonication in acetone

CPWs with various dimensions were fabricated for both the patch and shunt approach. An example of a shunted and un-shunted CPW used for the shunt approach is given in Figure 5-21. The CPWs have the following dimensions: their total length and width are 350 µm and 250 µm, respectively; the width of the centre trace is 25 µm; the gap width is 5 µm; and the pad dimensions are 25 µm × 50 µm. The final fabricated structures can be seen in Figure 5-21. The magnified view of the gap between the signal and the ground planes of a shunted CPW shows the graphene area. Raman large area mapping (30 µm × 30 µm) spectroscopy was used to identify the graphene shunt and confirm that it is only located in the gap.

During the fabrication process, significant difficulties with the adhesion of the metal CPW to the graphene were experienced. Lifting off the contact pads would invariably result in a complete or partial delamination of the CPW structures, as shown in Figure 5-22(b). A brief oxygen (O_2) plasma de-scum treatment (5 s, $P_{ICP} = 10$ W, $P_{RIE} = 30$ W, 10 mTorr, O_2: 12 sccm) using ICP-RIE was introduced to mitigate the poor adhesion attributed to PR residues, as shown by the intact CPWs in Figure 5-22(a). Furthermore, a mild Ar plasma treatment of the graphene-metal contact area using ICP-RIE was introduced (60 s, $P_{ICP} = 50$ W, $P_{RIE} = 30$W, 20 mTorr, Ar: 20 sccm) to create defects in the graphene for an increased extent of edge contact with the metal, hence reducing the contact resistance [334].

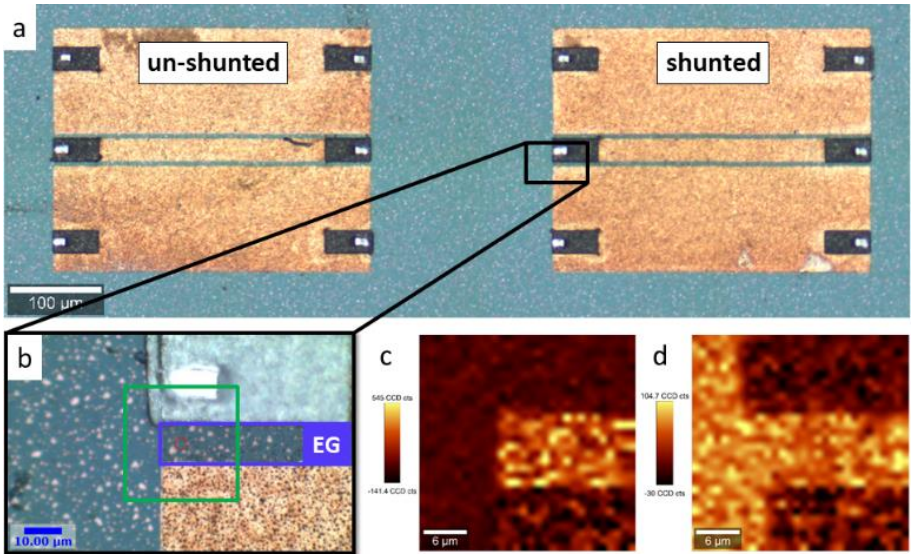

Figure 5-21 (a) Structures of (left) regular CPW and (right) graphene-shunted CPW. (b) Microscope image of the Raman mapping area (green square) showing the bare SiC substrate on the left, the Al pad on the top-right, and the Cu CPW on the bottom-right, with the graphene shunt in between (blue square). (c-d) Raman intensity maps of (c) graphene's 2D (~2700 cm^{-1}) and (d) the SiC LO (~970 cm^{-1}) peaks. Reprinted from [331]

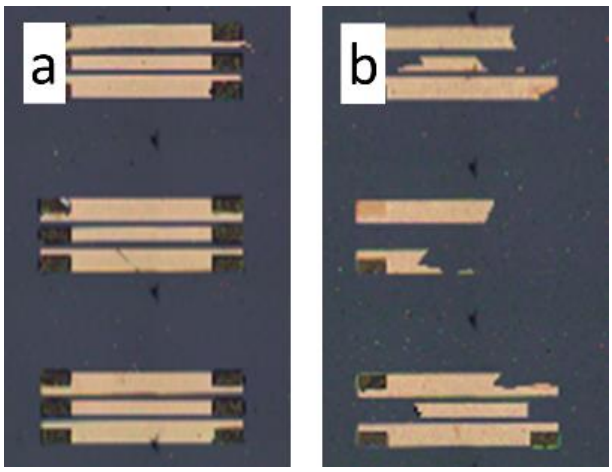

Figure 5-22 Influence of O_2 de-scum on the adhesion of the metal CPW to the graphitised surface during the lift-off of the contact pads. (a) Graphene was exposed to brief O_2 de-scum and Ar treatment, and (b) graphene was only exposed to Ar treatment using ICP-RIE.

Figure 5-23 shows fabricated samples for the SOTL approach and a close-up and Raman map of a graphene patch. It validates the position of the patch as well as the proper contact with the CPW traces.

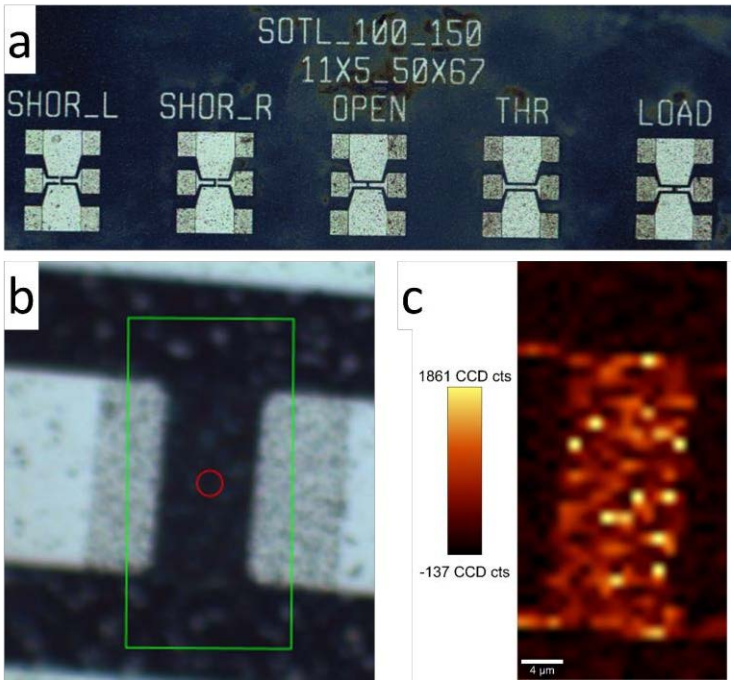

Figure 5-23 (a) Fabricated CPW structures for SOTL approach. Dimensions: 150 *µm; S is* 11 *µm; W is* 5 *µm; pad pitch is* 100 *µm; and the patch has a length of* 5 *µm. (b)Close up of graphene patch and metal interface of loaded CPW in Figure 27. The green rectangle indicates the area of the Raman map. (c) Raman spectroscopy 2D peak intensity map of the graphene patch and its surroundings. The image clearly shows the graphene patch within the centre trace, as well as that the graphene patch extends below the centre trace. Furthermore, no graphene is present in the gap between the centre trace and the ground planes*

An additional annealing step was performed after the initial measurement of the CPWs, as it has been shown to improve the contact resistance at the graphene-metal interface due to the dissolution of carbon into the metal and the formation of edge contacts [335]. The samples were annealed at 200°C for one hour in an Ar environment at atmospheric pressure. However, due to the induced stress between metals (Cu and Al) with different expansion coefficients, the Al pads detached from the CPWs, and further measurements were not possible.

5.1.4 Fabrication of Transfer Length Method Structures

Interactions between graphene and the substrate on which it resides or other surrounding materials [336], as well as achieving adequate electrical contact due to the high contact resistance at graphene-metal interfaces [57, 58], are some of the most prominent issues encountered when integrating graphene. A high contact resistance, although not ideal, would normally not impede the operation of a device at direct current (DC) operation. Nevertheless,

the impact of high contact resistance in high-frequency applications has been shown to be quite significant [57, 58].

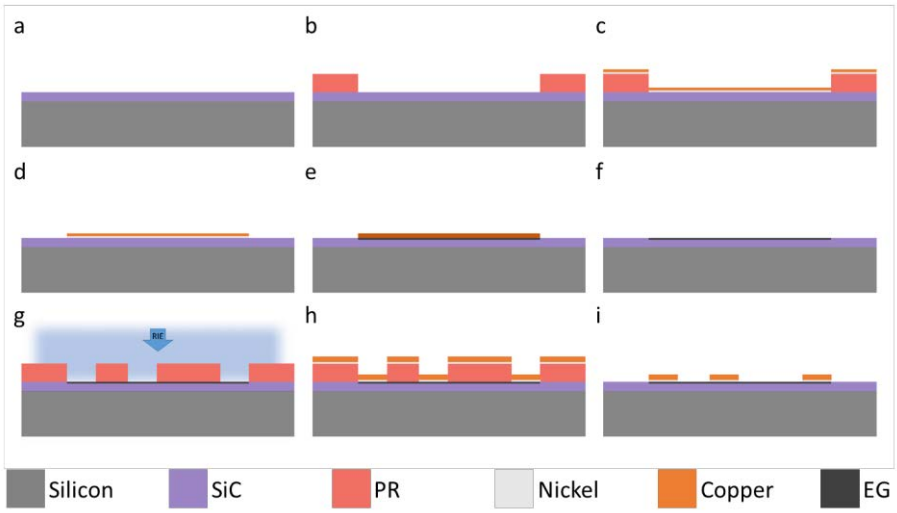

Figure 5-24 Schematic illustration of the fabrication steps required to manufacture TLM structures. EG is structured via the pre-structuring of the catalyst metals before graphitisation. A description of individual steps is given in Table 5-3.

Table 5-3 Description of fabrication steps for the schematics in Figure 5-24.

Step	Description
a	Bare SiC/Si intrinsic substrate
b	Patterning of PR via UV lithography for lift-off of metal catalysts
c	Deposition of Ni (10 nm) and Cu (20 nm) for graphitisation
d	Lift-off using sonication in acetone
e	Graphitisation via annealing at 1 100°C for one hour
f	Freckle etch to remove metal catalysts and silicides
g	Patterning of PR via UV lithography for lift-off of metal TLM contact as well as O_2 de-scum and Ar treatment via ICP-RIE
h	Deposition of Ni (5 nm) and Cu (100 nm) to form the CPW structure
i	Lift-off using sonication in acetone

To determine the graphene-metal contact resistance, TLM structures were used. The individual processing steps are shown in Figure 5-24, while the steps are described in Table 5-3. To achieve a comparison of the influence of the Ar treatment on the contact resistance, and thus draw conclusions towards the CPW measurements, the TRL structures employ the

exact same fabricating process as the CPW structures. Al pads were not deposited as they were not needed.

Two sets of TRL structures were fabricated for each, the Ar-treated and not-Ar-treated sample. First, graphene strips of $800\ \mu m \times 2350\ \mu m$ and $800\ \mu m \times 3000\ \mu m$ were patterned. Subsequently, metal contact pads (5 nm of Ni and 100 nm of Cu) were deposited. They had dimensions of $720\ \mu m \times 180\ \mu m$ and were slightly narrower than the graphene strip to simplify the alignment. The first graphene strip employed contact spacings between $10\ \mu m$ and $100\ \mu m$ with $10\ \mu m$ increments. The second strip employed contact spacings between $50\ \mu m$ and $350\ \mu m$ with $50\ \mu m$ increments.

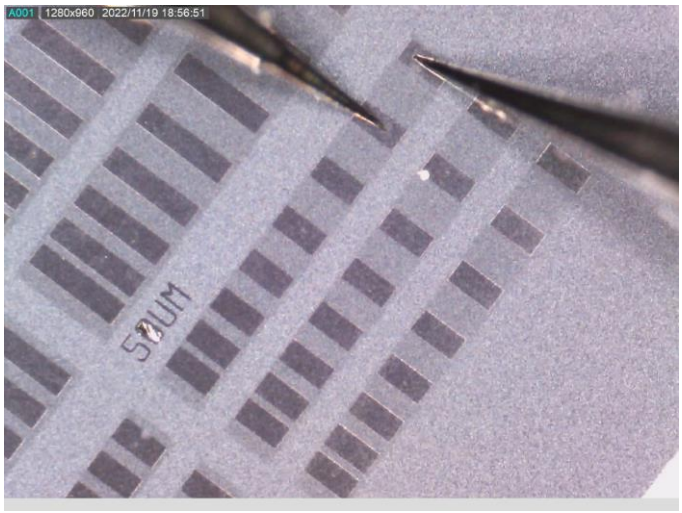

Figure 5-25 Probing of TLM structures to determine the contact resistance between graphene and the Ni/Cu contacts.

5.1.5 Discussion

5.1.5.1 Contact Resistance Extraction

The plots for the determination of the contact resistance using TLM structures are shown in Figure 5-26. The contact resistance can easily be determined from the y-intercept and shows that the mild Ar-treatment reduced the contact resistance from $16.3\ k\Omega$ ($\sim 2.9\ M\Omega\ \mu m$) down to $14.78\ k\Omega$ ($< 2.7\ M\Omega\ \mu m$) which is an improvement of $\sim 10\ \%$. The sheet resistances of the untreated and treated samples were determined to be $\sim 30\ k\Omega\ \square^{-1}$ and $\sim 38.7\ k\Omega\ \square^{-1}$, respectively. It should be noted that the graphene traces were not exposed to the Ar plasma but merely the contact area to the metal. Hence, the difference originates from the graphitisation process itself. However, the values are about $\times\ 4 - 5$ higher than previously reported values that were measured using van-der-Pauw and Hall measurements [30].

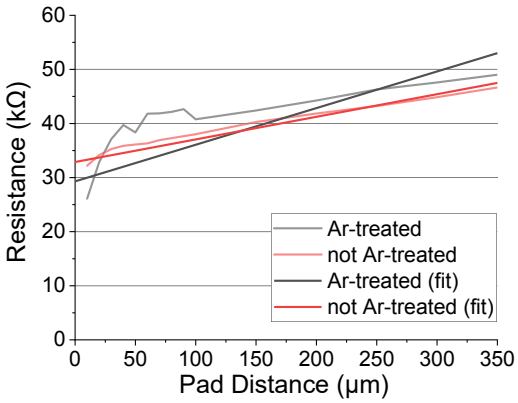

Figure 5-26 TLM measurement resistance plots for determining the sheet and contact resistance of the graphene and the graphene-metal contact, respectively. The graph shows the resistance values of TLM structures where graphene was Ar-treated, and graphene was not Ar-treated before the deposition of the metal contacts.

5.1.5.2 Patch Approach

A comparison of the measured S-parameters of the short, open, through, and load CPW structures that were either exposed or not exposed to the Ar treatment are shown in Figure 5-27 and Figure 5-28, respectively. Here, the S-parameter measurements of the short, open and through structures, respectively, give similar results, as expected, as the bare metal structures are not exposed to the Ar treatment. They further demonstrate typical behaviour, with the short and open structures having high reflection coefficients and low forward transmission, while the through structures experience low reflection coefficients and high forward transmission.

The two most important measurements here are those of the open and loaded structures. The only difference between those structures is that the loaded structures contain a graphene patch in the gap of the centre trace. Hence, the graphene-loaded structure would exhibit lower $|S_{11}|$ and higher $|S_{21}|$ values. This should be visible by directly comparing the S-parameter values of those two measurements, as shown in Figure 5-29 and Figure 5-30. The plots show no difference between the open and loaded CPW structures, neither for the not-Ar-treated nor for the Ar-treated sample. It is suspected that the contact between the graphene and the metal is still insufficient, even after Ar-treatment, to couple charge carriers from the metal into the graphene and vice-versa.

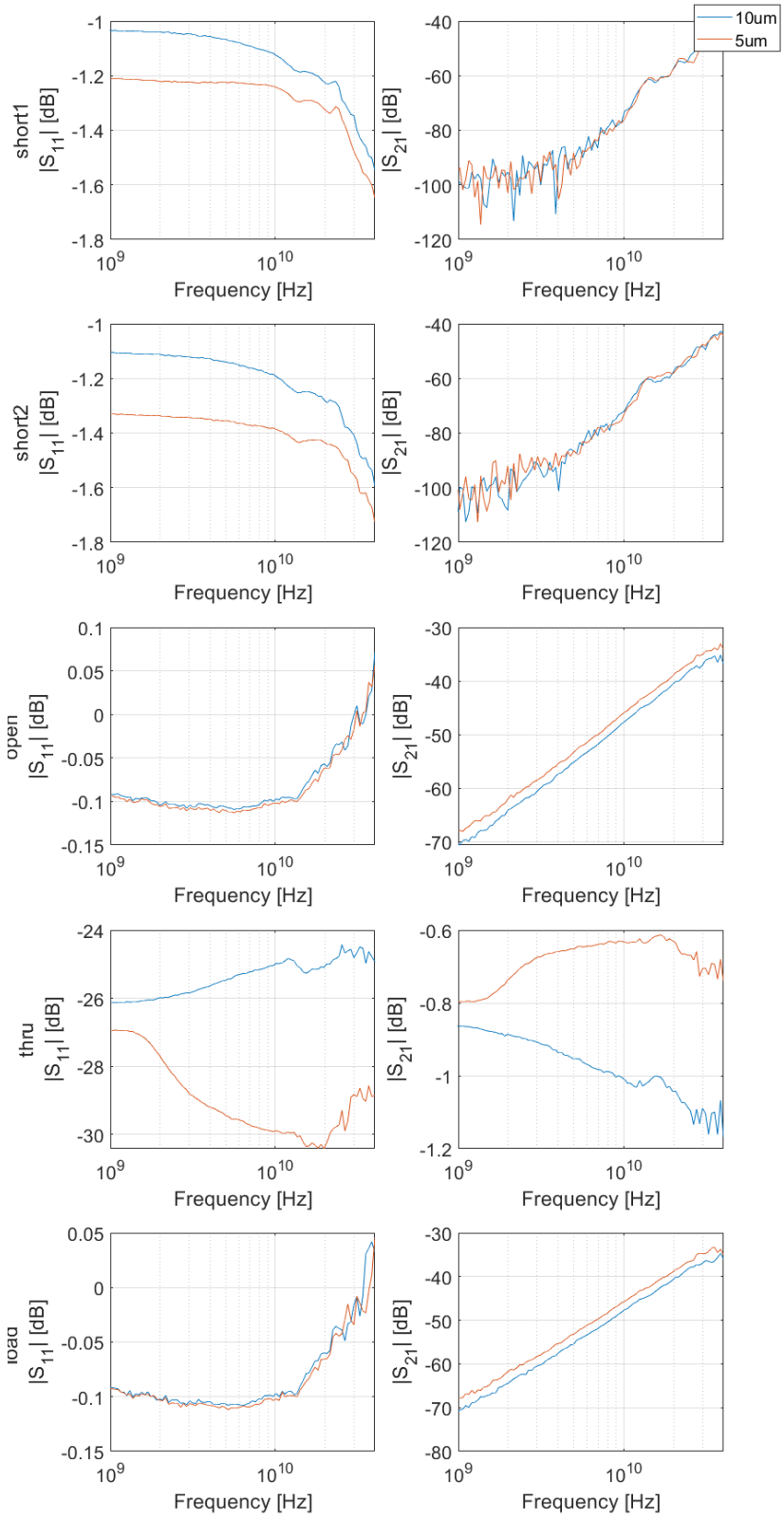

Figure 5-27 Comparison of $|S_{11}|$ and $|S_{21}|$ measurements of SOTL structures that were not Ar-treated. CPW dimensions: $l = 150\ \mu m$, $S = 11\ \mu m$, $W = 5\ \mu m$, and patch length of 5 & 10 μm.

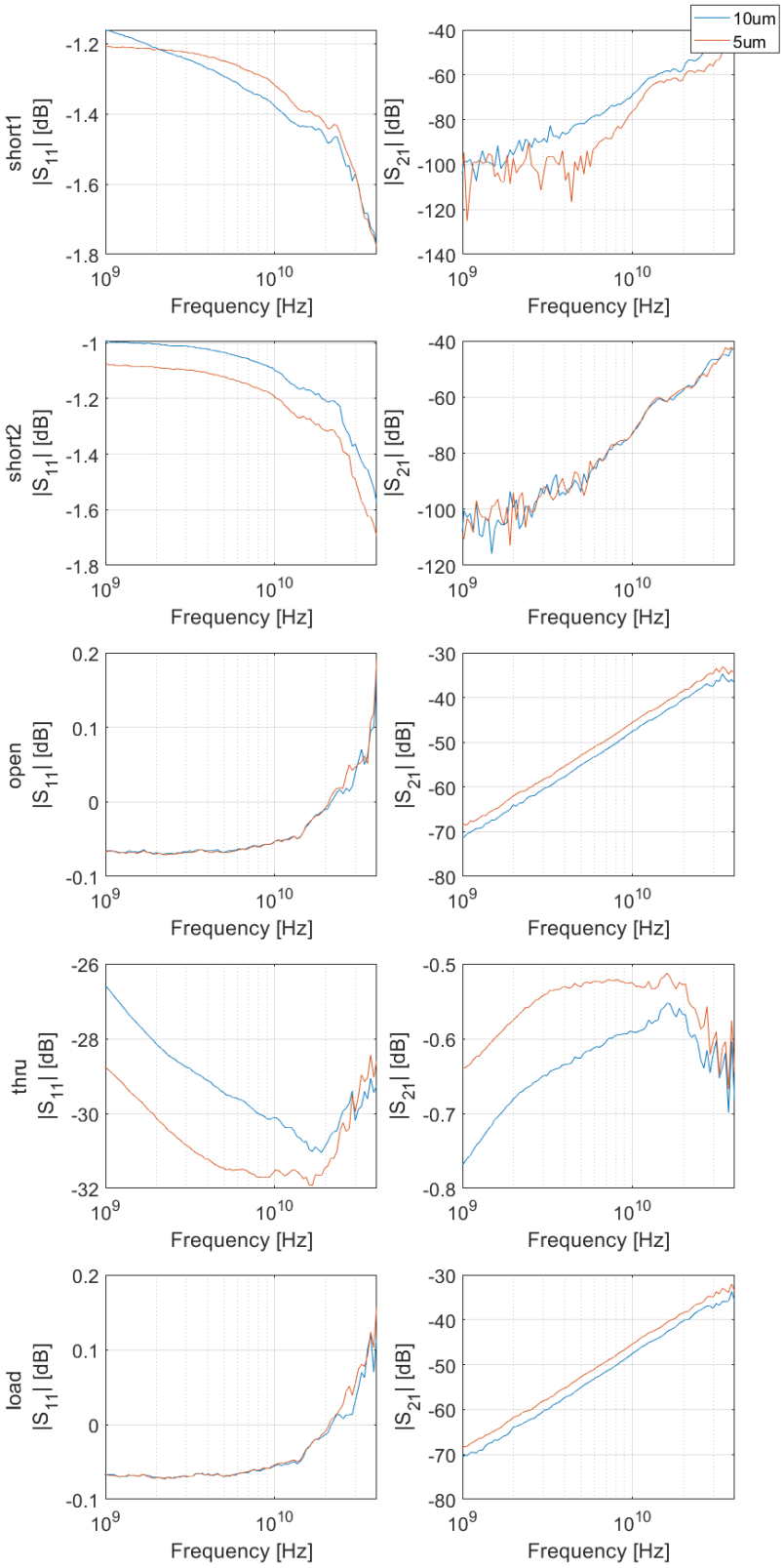

Figure 5-28 Comparison of $|S_{11}|$ and $|S_{21}|$ measurements of SOTL structures that were Ar-treated. CPW dimensions: $l = 150\ \mu m$, $S = 11\ \mu m$, $W = 5\ \mu m$, and patch length of 5 & 10 μm.

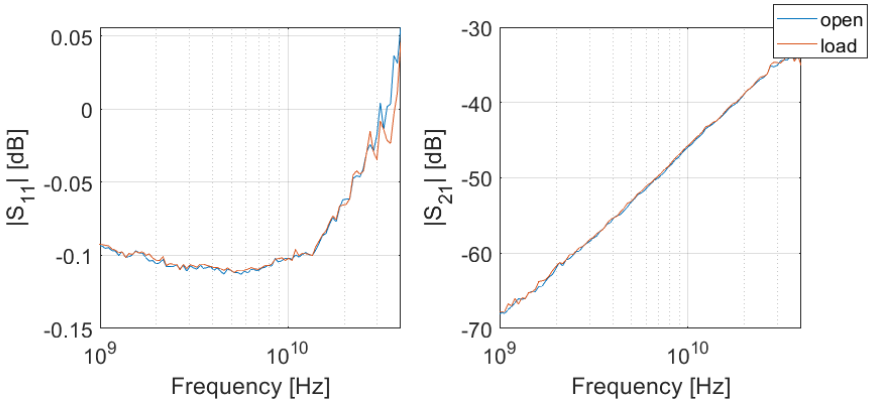

Figure 5-29 Comparison of $|S_{11}|$ and $|S_{21}|$ of the not Ar-treated open and graphene-loaded CPW structures. Dimensions: $l = 150\ \mu m$, $S = 11\ \mu m$, $W = 5\ \mu m$, and patch length of $5\ \mu m$.

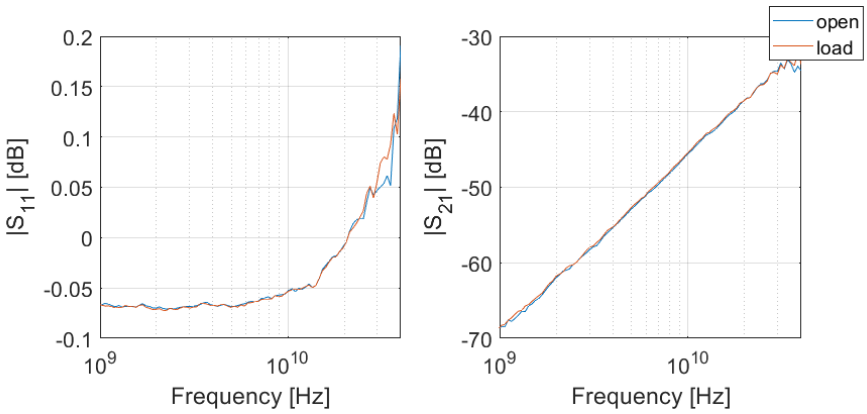

Figure 5-30 Comparison of $|S_{11}|$ and $|S_{21}|$ of the not Ar-treated open and graphene-loaded CPW structures. . Dimensions: $l = 150\ \mu m$, $S = 11\ \mu m$, $W = 5\ \mu m$, and patch length of $5\ \mu m$.

5.1.5.3 Shunt approach

A comparison of the S-parameters of the shunted and un-shunted CPW structures on the samples where the graphene-metal contact areas were either exposed or not exposed to the Ar treatment is shown in Figure 5-31. While the untreated CPWs show no difference between the shunted and un-shunted CPWs, with $|S_{11,1\ \mathrm{GHz}}|$ and $|S_{21,1\ \mathrm{GHz}}|$remaining constant at about -27.4 dB and -0.8 dB, respectively, the treated ones show a significant difference. $|S_{11,1\ \mathrm{GHz}}|$ increases from $-25.18\ (\pm 0.14)$ dB to $-21.79\ (\pm 0.51)$ dB and $|S_{21,1\ \mathrm{GHz}}|$ decreases from $-1.01\ (\pm 0.04)$ dB to $-1.41\ (\pm 0.07)$ dB. These characteristics arise from the improved contact to the underlying graphene due to the Ar treatment of the graphene at the interface to the metal CPW, resulting in the graphene shunt shorting the signal and ground planes of the CPWs. Indeed, placing the graphene shunt in the CPW structure results in higher

reflections due to a mismatch of the characteristic impedance of the CPW to the RF probe and a consequent increase in $|S_{11}|$ and a decrease in $|S_{21}|$.

In contrast, there is only a minor difference in the $|S_{11,1\ \mathrm{GHz}}|$and $|S_{21,1\ \mathrm{GHz}}|$ values of the un-shunted CPWs of the two samples (~1.8 dB and ~0.2 dB, respectively) as illustrated in Figure 5-31 (a, c). This result is attributed to the variability of the sample-to-sample dimensions of the CPWs, which is due to the individual UV lithography processing on each sample. The graphene shunt's frequency-dependent sheet resistance is evaluated by extracting the RLCG parameters [332] of the shunted and reference un-shunted CPWs that otherwise have the same dimensions.

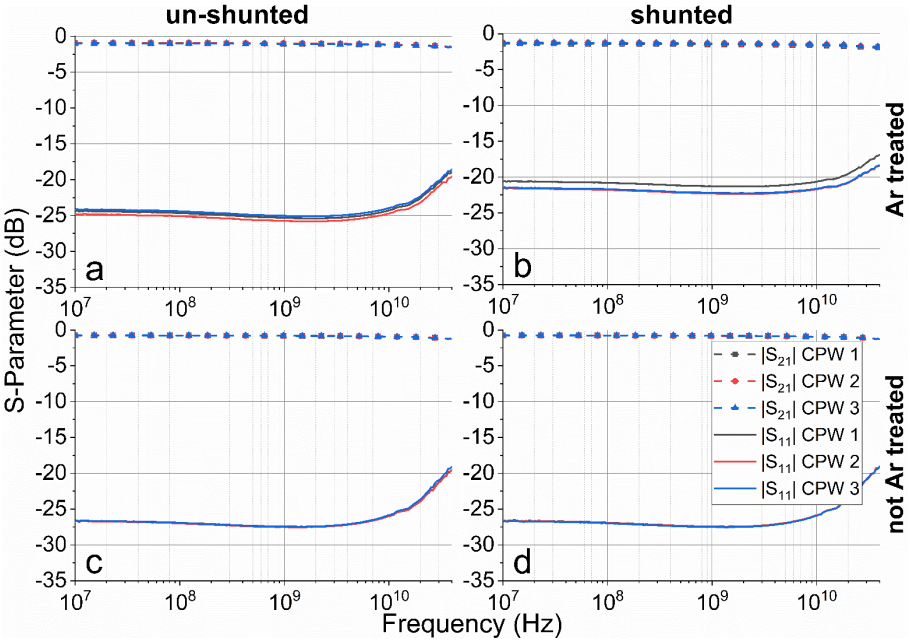

Figure 5-31 Comparison of the S-parameters of CPWs where (a,b) the graphene at the metal contacts were Ar-treated (using ICP-RIE) before metal deposition and (c,d) the graphene was not exposed to Ar plasma. (Legend in (d) applies to all graphs.). CPW dimensions: $l = 300\ \mu m$, $S = 25\ \mu m$, $W = 5\ \mu m$. Reprinted from [331]

The EG employed in this study has a relatively high charge carrier concentration of $3.3 - 7 \times 10^{12}$ cm^{-2} [30], which typically tends to deliver a lower contact resistance [57]. However, surface roughness has a detrimental effect on the contact resistance [59, 60], and this EG on 3C-(111) SiC/Si has an inherent root mean square roughness of ~9 nm [4]. As previously mentioned, using TLM structures, an initial contact resistance of ~2.9 MΩ µm was evaluated. Nevertheless, the mild Ar treatment that brought down the contact resistance to a value of $<$ 2.7 MΩ µm, was necessary to ensure optimal coupling.

Figure 5-32 plots the extracted sheet resistance of three shunted CPWs. Between 10 MHz and 80 MHz, the measurement data is very noisy and does not allow for reliable data extraction. This could potentially be mitigated using longer CPW structures. Between 80 MHz and 1 GHz, the extraction of the sheet resistance is relatively steady and shows a monotonic decline of the sheet resistance starting above/around ~100 MHz from 1.5 kΩ (value in line with the DC measurements [30]) down to 0.9 kΩ for CPW 1 and CPW 2 and from 0.9 kΩ down to 0.5 kΩ for CPW 3. This effect is attributed to the decrease in the influence of grain-boundary scattering on the sheet resistance of the graphene. Recall that the EG has grain sizes of < 100 nm in size [30] in comparison to an EM field wavelength of about 3 m at 100 MHz. Therefore, the small-scale defects within the graphene layer that play a significant role in DC measurements tend to show less influence in the high-frequency measurements [39, 40]. Furthermore, CPW 3, which has the lowest sheet resistance, has the highest $|S_{11}|$, see Figure 5-31(b). This result is attributed to the increased reflection due to the low resistance shunt.

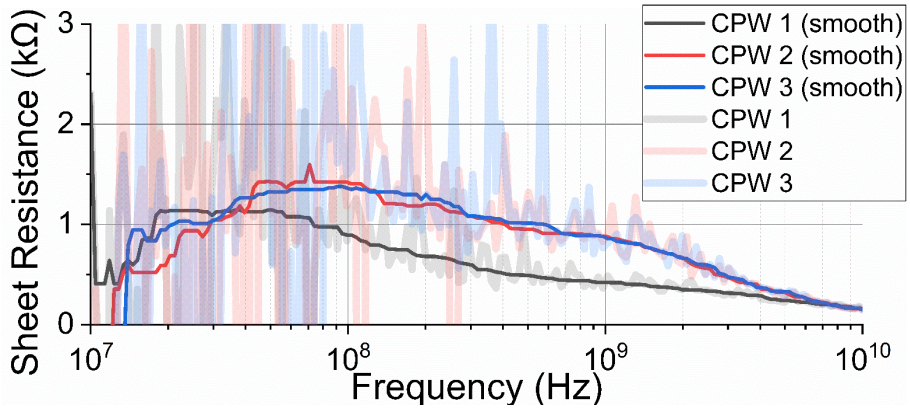

Figure 5-32 Extracted sheet resistance of the EG shunts of three samples of shunted CPWs. Reprinted from [331]

5.1.6 Conclusion

This work determined the high-frequency characteristics of EG grown on SiC/Si substrates using a catalytic alloy-mediated graphitisation process. The patterned graphene was employed as a patch within the centre trace, as well as a shunt between the centre and ground traces of metal CPWs. No current injection into the graphene patches was achieved, which is attributed to an insufficient quality of the electrical contact. In contrast, a mild Ar RIE treatment on the graphene at the interface to the metal CPW enabled the contact to the graphene shunts. It affirms the importance of achieving a sufficiently low graphene-metal contact resistance for adequate current injection in the 2D material at high frequencies. The contact resistance between metal and EG on SiC/Si grown via the catalytic alloy-mediated synthesis process

suffers from increased surface roughness after the graphitisation. Therefore, contact engineering needs to be carefully considered when designing high-frequency devices based on this technology. This suggests that even lower contact resistances may be needed to observe the graphene effects in the investigated patch approach. Furthermore, a strong frequency dependence of graphene's sheet resistance was observed. This is attributed to the increasingly lower influence of small-scale scattering defects in the graphene at high frequencies, such as the < 100 nm grain sizes.

5.2 Rectangular Waveguide-based Characterisation in the K_a-Band

5.2.1 Approach

A non-contact approach was devised to evaluate the surface impedance of EG grown on SiC/Si over large areas. This alternative and complementary method enables evaluating the graphene circumventing electrical contacts and the complex fabrication steps required for the CPW approach. The procedure consists of measuring the S-parameters of a graphitised sample and a bare substrate [337], as illustrated in Figure 5-33. An ABCD-matrix model is then used to extract the high-frequency sheet conductivity of the EG. The S-parameter measurements are converted next to an ABCD representation using the two-port-network conversion table in [251] (p.192). Their expressions are:

$$A = \frac{(1+S_{11})(1-S_{22})+S_{12}S_{21}}{2S_{21}} \tag{5.39}$$

$$B = Z_0\frac{(1+S_{11})(1+S_{22})-S_{12}S_{21}}{2S_{21}} \tag{5.40}$$

$$C = Z_0\frac{(1-S_{11})(1-S_{22})-S_{12}S_{21}}{2S_{21}} \tag{5.41}$$

$$D = \frac{(1-S_{11})(1+S_{22})+S_{12}S_{21}}{2S_{21}} \tag{5.42}$$

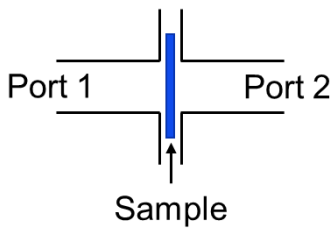

Figure 5-33 S-Parameter measurement of a sample wedged in between two coaxial adaptors.

SiC/Si substrates are a dielectric stack, and the individual layers here need to be modelled individually. Both EG and SiC can be assumed as infinitesimally thin layers as their thickness is significantly smaller than the dielectric wavelength, for example, $t_{SiC} = 500\ \text{nm} \ll \lambda_{d,SiC} = 24\ \mu\text{m}$. Thus, they can be represented as thin-layer admittances, as illustrated in Figure 5-34. The complete equivalent circuit model is thus shown in Figure 5-35.

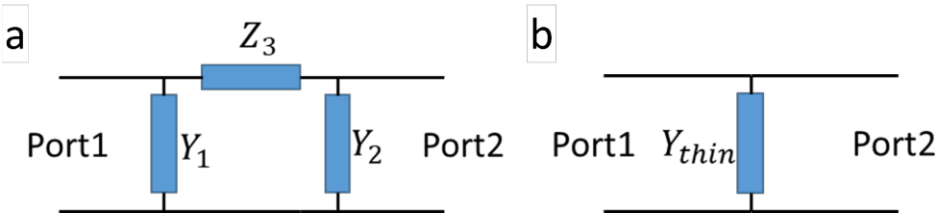

Figure 5-34 ABCD-matrix equivalent circuits used to represent (a) dielectrics, with a so-called π-circuit, and (b) a thin film.

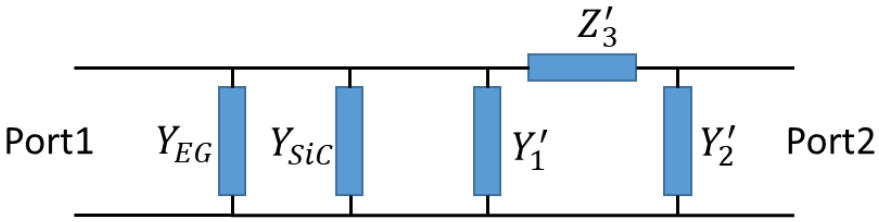

Figure 5-35 Equivalent circuit used to determine the sheet resistance of EG on SiC/Si substrates.

The EG, SiC layer, and bare Si can thus be described in terms of their ABCD-matrixes

$$M_{Si} = \begin{bmatrix} 1 & 0 \\ Y_1 & 1 \end{bmatrix} \begin{bmatrix} 1 & Z_3 \\ 0 & 1 \end{bmatrix} \begin{bmatrix} 1 & 0 \\ Y_2 & 1 \end{bmatrix} = \begin{bmatrix} 1 + Z_3 Y_2 & Z_3 \\ Y_1 + Y_1 Y_2 Z_3 + Y_2 & 1 + Z_3 Y_1 \end{bmatrix} \tag{5.43}$$

$$M_{SiC} = \begin{bmatrix} 1 & 0 \\ Y_{SiC} & 1 \end{bmatrix} \tag{5.44}$$

$$M_{EG} = \begin{bmatrix} 1 & 0 \\ Y_{EG} & 1 \end{bmatrix} \tag{5.45}$$

Each of these terms are determined from their respective measurements. The complete equivalent model is subsequently represented as

$$M = M_{EG} M_{SiC} M_{Si} \tag{5.46}$$

which are individually solved from their respective measurements.

5.2.2 Numerical Modelling

The measurement setup was modelled using ANSYS HFSS. The coaxial adapters and sample were 3D-modelled using exact dimensions determined from manual measurements.

The inside dimensions of the YERKON BJ320 (WR-28) were 7.112 mm $(0.28")\times 3.556$ mm $(0.14")$, they also set the measurement band to be $26.5-40$ GHz. The thickness of the metal was ~ 2 mm, and the flange was 19 mm $\times$ 19 mm. The individual adaptors were modelled as aluminium ($\sigma_{Al} = 3.8 \times 10^7$ S m^{-1}) with a length of 30 mm to accommodate at least a quarter wavelength $\lambda_{26.5\,\mathrm{GHz}}/4 = 1.131$ cm $/4 = 28.25$ mm within each element. A rectangular wave port was placed at either end of the adaptors, and the design was encapsulated by air ($\epsilon_r = 1$) filled cuboid radiation boundary whose length was the sum of the lengths of the coaxial adaptors plus the thickness of the substrate, while the width and height were set to 30 mm. The samples were modelled as a EG on SiC/Si stack. Here, the SiC layer and Si substrate are modelled as cuboids with thicknesses of 500 nm (manufacturer's specification) and 230 µm (measured), respectively, and a width and length of $a = 11$ mm (measured). The dielectric properties were set as $\epsilon_{r,SiC} = 9.7$ and $\epsilon_{r,Si} = 11.7$. Graphene was modelled as an impedance boundary surface with a constant sheet resistance of $R_{sh,Gr} = 2.13$ kΩ, which was previously determined using a DC van-der-Pauw measurement. Figure 5-36 shows the 3D HFSS model used to simulate the characterisation procedure.

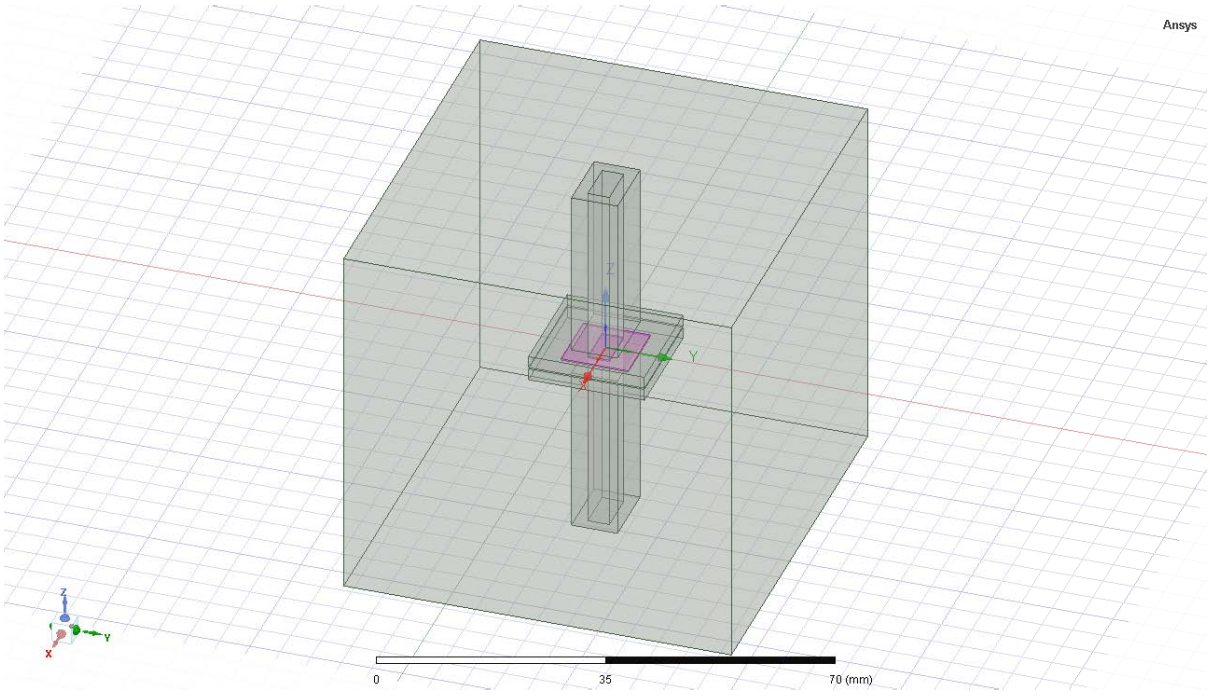

Figure 5-36 HFSS model of EG on SiC/Si sample characterisation using WR-28 coaxial adaptors. The sample is highlighted in purple and wedged in between the adaptors.

A frequency sweep was performed within $26.5-40$ GHz with a 0.1 GHz step size to evaluate the S-parameters. They were extracted for further processing in MATLAB using equations (5.39)-(5.46).

5.2.3 Discussion

S-parameter measurements of EG on intrinsic 3C-(111) SiC/Si, bare intrinsic 3C-(111) SiC/Si, and bulk intrinsic Si(111) using WR-28 coaxial adaptors within $26.5-40$ GHz were performed. Figure 5-37 plots $|S_{11}|$ and $|S_{12}|$ of the three samples. It can be seen that the measurements of the SiC/Si and bulk Si very much align. The slight reduction in both $|S_{11}|$ and $|S_{12}|$ can be associated with slightly higher losses due to the SiC layer. A similar effect is shown using numerical modelling, as illustrated in Figure 5-38. An increased reduction in both $|S_{11}|$ and $|S_{12}|$ is seen for the measurements of the graphitised sample. Here, the change can be associated with resistive losses within the graphene layer. This is also confirmed using numerical modelling, as illustrated in Figure 5-38.

However, the modelling with exact sample dimensions showed distinct differences between the modelled and measured S-parameter values. In particular, the mode where both $|S_{11}|$ and $|S_{12}|$ become smaller appears around ~ 38 GHz in the experimental measurements of the samples, while it appears at ~ 35.3 GHz in the simulation results. Additional simulations have confirmed this mode to be a resonance, see Figure B-5.

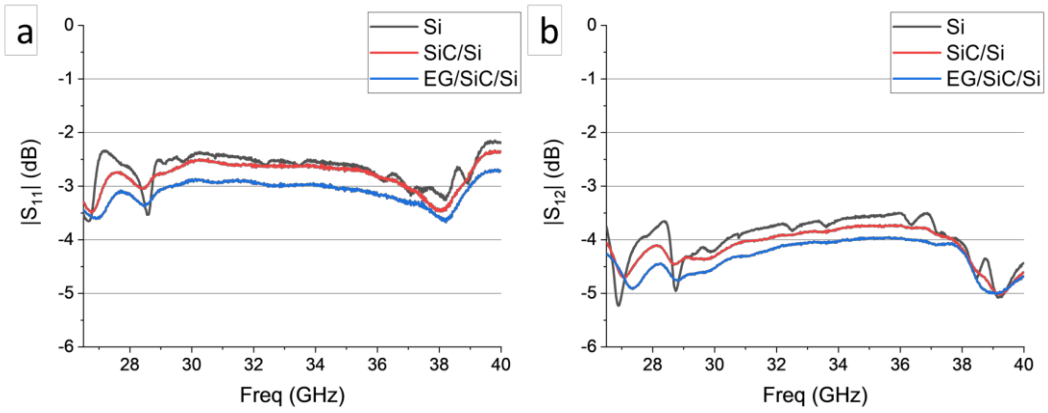

Figure 5-37 S-parameter measurements of EG on intrinsic 3C-(111) SiC/Si, bare intrinsic 3C-(111) SiC/Si, and bulk intrinsic Si(111). (a) $|S_{11}|$ and (b) $|S_{12}|$ parameter.

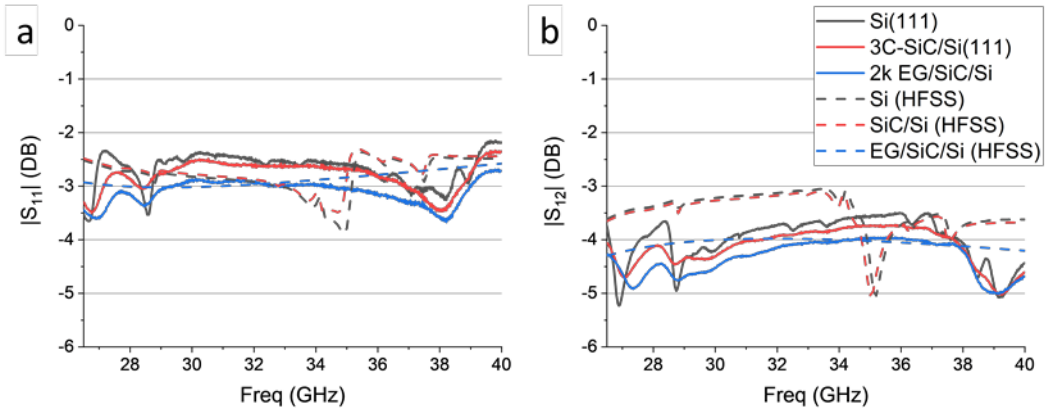

Figure 5-38 Comparison of measured and modelled S-parameters of EG on intrinsic 3C-(111) SiC/Si, bare intrinsic 3C-(111) SiC/Si, and bulk intrinsic Si(111). (a) $|S_{11}|$ and (b) $|S_{12}|$ parameter. (Legend in (b) valid for both graphs)

A parametric analysis of the bare Si substrate side length, thickness, and permittivity, as illustrated in Figure B-6, Figure B-7, and Figure B-8, respectively, identified the dependence of the Si substrate mode on the sample side length and permittivity. The Si thickness inversely influences the magnitude of $|S_{11}|$ and $|S_{12}|$.

Furthermore, an air gap was added in the model between the EG/SiC/Si sample and the coaxial adaptors to represent, e.g., likely surface unevenness due to contamination, surface topography, or insufficient clamping pressure, and to determine its effect on the S-parameter measurements. Figure B-9 shows a logarithmic sweep of the air gap between $0.01 - 10\ \mu m$ and includes a simulation where no air gap is present. Figure B-10 shows a linear sweep within $1 - 10\ \mu m$. As can be seen in Figure B-9, without an air gap, the resonances are absent in the S-parameter measurements. The resonances that are observed in the measured S-parameters appear in the modelled ones with the introduction of the air gap. Furthermore, a strong dependence of the resonance position and the magnitudes of $|S_{11}|$ and $|S_{12}|$ is found.

Adjusting the model by increasing the thickness to $t_{Si} = 240$ µm, with a sample side length to $a = 11$ mm, the relative permittivity of Si being $\epsilon_{r,Si} = 11.9$, and by introducing a $t_{air} = 3\ \mu m$ air gap improved the matching of the measured and modelled S-parameters, as illustrated in Figure 5-39, including the frequency of the resonant modes. The adjusted permittivity value is still within range with previous evaluations [338].

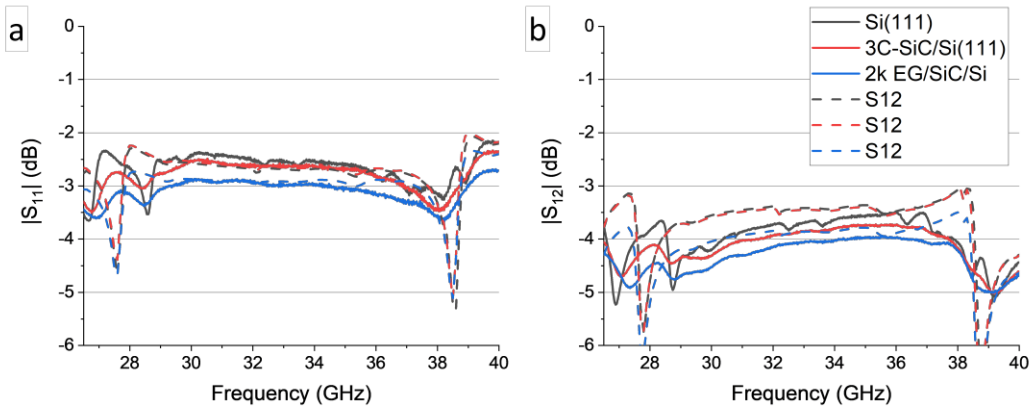

Figure 5-39 Comparison of measured and modelled, using the adjusted model, S-parameters of EG on intrinsic 3C-(111) SiC/Si, bare intrinsic 3C-(111) SiC/Si, and bulk intrinsic Si(111). (a) $|S_{11}|$ and (b) $|S_{12}|$ parameter. (Legend in (b) valid for both graphs)

Finally, an estimate of the surface impedance of the EG layer is extracted from the S-parameter measurements. The real part of the surface impedance averages around ~4.3 kΩ in the evaluated frequency spectrum. Similar to previous measurements and as seen in section 5.1 of this thesis, the high-frequency sheet resistance of graphene, a monotonic decrease in the resistance is observed [36, 39, 331]. The estimate of the real part of the surface impedance using this approach shows a ~2-fold increase compared to the DC value of $R_{sh} \approx 2.13\ k\Omega$.

To determine the cause of the overestimation of the extracted sheet impedance, sensitivity studies of the introduction of an air gap, dimensional variations of the sample thickness, and an offset of the sample from the waveguide centre were performed. Here, a 100 Ω thin film on a 125 μm thick polyimide substrate ($\epsilon_r = 3.2(1 - 0.045)$) is modelled in between two WR-10 coaxial adapters. The surface impedance is extracted at a single frequency point ($f_0 = 90\ GHz$) using the approach introduced earlier in the chapter. Table B-1 shows the extracted sheet impedance for air gaps up to 100 μm; Table B-2 shows the extracted sheet impedance for thickness variations of up to $\pm 20\ \mu m$; and Table B-3 and Table B-4 show the extracted sheet impedance for offsets of the sample from the centre of the waveguide alongside the width a and the height b, respectively.

The uncertainties estimated from the permutations described above (including the air gap considerations) are in the order of only $10 - 25$ %, and are hence not likely to account for the discrepancy between the DC measured and extracted sheet impedance. As mentioned in [339], random noise-type errors introduce an uncertainty in the S-parameter measurements using vector network analyzers. These can lead to significant errors (up to ~50 %) in the extraction

of thin film sheet impedances above $1\ k\Omega$ using rectangular waveguides, and resonant approaches, i.e. using resonant cavities (see 2.3.2.3), are recommended instead.

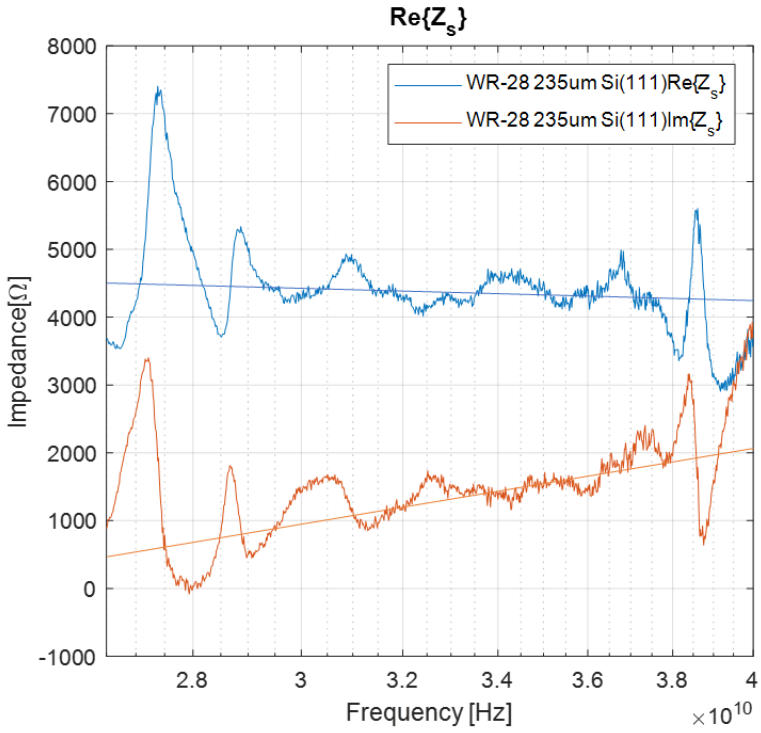

Figure 5-40 Real and imaginary part of the extracted surface impedance of EG grown on intrinsic 3C-(111) SiC/Si without consideration of the air gap. While the DC sheet resistance was characterised to be $R_{sh} \approx 2.13\ k\Omega$, the real part of the extracted surface impedance averages ~4.3 $k\Omega$.

5.2.4 Conclusion

A non-contact approach to determine the high-frequency sheet impedance of large-area graphene on SiC/Si was developed. The sheet impedance is determined from S-parameter measurements, where the graphitised and reference samples are individually wedged between two coaxial adaptors. Modelling the EG on SiC/Si dielectric stack using ABCD-Matrixes allows for the extraction of the sheet resistance by modelling the reference substrate using a transmission line π-model and the graphene layer as a shunt.

Extracting the sheet impedance from the S-parameter measurements shows a ~2-fold increase in the average surface resistance compared to DC measurements. This is attributed to noise-type errors in the S-parameter measurement, as a sensitivity study of various dimensional and alignment variations did not account for the discrepancy. However, with the introduction

of an air gap and minor adjustment of the sample parameters, the modelled S-parameter values are in good agreement with the measured values.

While this approach provides several benefits over the CPW-characterisation introduced in the earlier chapter, i.e., avoiding issues with electrical contacts and complex fabrication, characterising a larger area of the thin film, making it less prone to localised defects by averaging over the waveguide cross-section, it struggles to accurately extract the sheet resistance of EG grown on SiC/Si.

Chapter 6 Modelling of Electromagnetic Graphene Devices in the Terahertz Domain

EG grown on SiC/Si substrates is an emerging platform for electronic, photonic, and bio-sensing components. The THz spectrum is particularly interesting for graphene applications because of the strong plasmonic effect in graphene at those frequencies and the potential for dynamically tuning its electrical properties. In contrast, in the microwave frequency range, graphene behaves like a variable resistor. The development of such devices generally starts with the design, conceptualisation, and analysis using analytical and numerical pathways. In this chapter, two distinct applications for this platform are investigated: a graphene dipole antenna and absorber structures.

6.1 Planar Terahertz Dipole Antenna

6.1.1 Antenna Design

Several planar dipole antennas made of Cu and graphene on top of SiO_2 ($\epsilon_r = 3.9$) as well as SiC ($\epsilon_r = 9.7$) substrates were designed to study the effects of graphene. These included its tunability and the impact of the relatively high permittivity of SiC on the general antenna properties. The latter included the resonance frequency, efficiency, and BW.

The resonance frequency of a planar graphene dipole can be determined from [49]

$$f_{r,Gr} = \sqrt{m\frac{\alpha E_F c_0}{2\pi\hbar l_d \epsilon_{eff}}} \tag{6.1}$$

where m is the order of the resonance mode, α is the fine structure constant, E_F is the Fermi level of graphene, c_0 is the speed of light, $\hbar$ is the reduced Planck constant, l_d is the length of the dipole, and ϵ_{eff} is the effective permittivity.

Similar to the approach of calculating the effective permittivity of the substrate of the CPWs, conformal mapping techniques are employed to calculate the effective permittivity of the substrate for the planar graphene dipole, as described in [340]. The effective capacitance of the dipole can be calculated using

$$C_{eff} = \epsilon_0 w_d[2K_1 + (\epsilon_r - 1)K_2] \tag{6.2}$$

where ϵ_0 is the vacuum permittivity, w_d is the width of the dipole, and ϵ_r is the relative permittivity of the substrate. The terms K_1 and K_2 are given as

$$K_1 = \frac{K(k_1)}{K(k_1')} \tag{6.3}$$

$$K_2 = \frac{K(k_2)}{K(k_2')} \tag{6.4}$$

where $K(k_i)$ is the complete elliptical integral, see 5.1. The moduli $k_1$and k_2 are calculated from

$$k_1 = \frac{l_d - G}{l_d + G} \tag{6.5}$$

$$k_2 = \frac{\sinh\left(\frac{\pi(l_d - G)}{4h}\right)}{\sinh\left(\frac{\pi(l_d + G)}{4h}\right)} \tag{6.6}$$

where l_d is the length of the dipole, G is the gap width, h is the thickness of the substrate, and $k_n' = \sqrt{1 - k_n^2}$. The effective permittivity of the dipole substrate is then determined from the ratio of C_{eff} to the value of an equivalent capacitance in a vacuum $C_{eff,vac}$, i.e., with $\epsilon_r = 1$. The effective permittivity then becomes [340]

$$\epsilon_{eff} = 1 + \left(\frac{\epsilon_r - 1}{2}\right)\frac{K_2}{K_1} \tag{6.7}$$

Considering a 71 µm long and 5 µm wide planar dipole with a $G = 1$ µm feeding gap between the individual arms and substrate thickness of $h = 1$ µm, the effective permittivity of the SiO_2 substrate is $\epsilon_{eff} \approx 1.43$. Together with a typical Fermi level of $E_F = 0.37$ eV of EG on SiC [26], a resonance frequency of $f_{r,Gr} \approx 1.39$ THz was determined. For comparison, the resonance frequency of a centre-fed Cu dipole on the same substrate can be evaluated using [340]

$$f_{r,Cu} = \frac{c}{2l_d\sqrt{\epsilon_{eff}}} \tag{6.8}$$

which gives $f_{r,Cu} \approx 1.77$ THz.

6.1.2 Numerical Modelling

Graphene is modelled using the Drude conductivity model, see 2.1.2. For the initial calculations and the numerical modelling, typical values for EG on SiC are chosen, i.e., $\tau = 1$ ps and $E_F = 0.1 - 0.6$ eV at room temperature ($T = 300$ K). The reason for this is to accurately model the performance of planar dipoles made of EG on SiC/Si substrates, while the simulation of the graphene on SiO_2 is done for a comparison of the influence of the substrate relative permittivity change.

For the simulation, bulk SiO_2 and SiC, with relative permittivities of $\epsilon_{r,SiO_2} = 3.9$ and $\epsilon_{r,SiC} = 9.7$, respectively, are assumed as the substrate material with dimensions 80 µm ×

15 µm × 1 µm. The dipole antennas of both the Cu and graphene have the same dimensions: $l_d = 71$ µm, $w_d = 5$ µm, and $G = 1$ µm. Hence, the individual arms of the dipoles are $l_{arm} = (l_d - G)/2 = 35$ µm. Transition boundary conditions are used for the two antenna arms of the dipoles. The Cu elements are modelled as electrically thick layers using the Drude conductivity model with

$$\sigma_{Cu}(\omega) = \frac{\sigma_{Cu,0}}{1 - i\omega\tau_{Cu}} \tag{6.9}$$

where $\sigma_{Cu} = 5.88 \times 10^7$ S m^{-1} is the DC conductivity of Cu and $\tau_{Cu} = 72.5\, fs$ is its relaxation time [341]. In contrast, the graphene elements are modelled by calculating their conductivity using the Kubo conductivity model, as introduced in 2.1.2, and setting a thickness of $t_{Gr} = 0.34$ nm.

The substrate is surrounded by air ($\epsilon_{r,air} = 1$) and is engulfed with a spherical boundary with a radius of $4 \times l_{arm} = 140$ µm upon which a PML absorbing boundary is specified that is $l_{arm}/5 = 7$ µm thick. For the excitation, a uniform lumped port with dimensions of 1 µm × 5 µm is used. Figure 6-1 illustrates the designed dipole antenna elements on their respective substrate, as well as the PML-covered radiation boundary that surrounds the substrate.

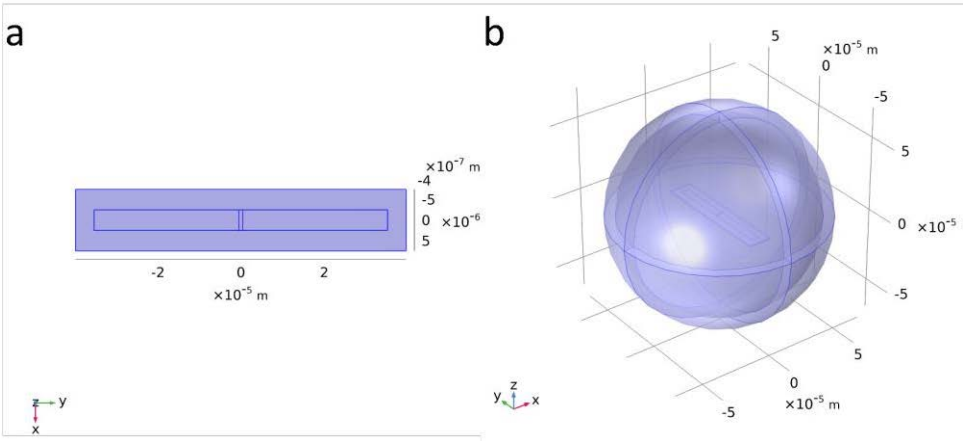

Figure 6-1 (a) Designed centre-fed dipole antenna on top of the substrate. (b) PML covered radiation boundary surrounding the dipole antenna.

To determine the spectral performance of the dipoles and to determine crucial antenna characteristics, $0.4 - 3$ THz frequency sweeps were performed with a 50 GHz step size. The resonant frequency f_r, reflection coefficient $|S_{11}|$, and directivity were obtained for the main Cu and graphene dipoles on the SiO_2 and SiC substrate. Additional $0.1 - 1$ THz frequency sweeps were performed for the graphene dipoles on the SiC substrate to evaluate their

tunability. The efficiency of the individual antennas is calculated from the relation of the port input power P_{in} and the radiated power P_{rad} via $\mu_{eff} = P_{rad}/P_{in}$.

6.1.3 Discussion

Initially, the graphene and Cu-based dipoles were simulated on a SiO_2 substrate, and their simulated reflection coefficient can be seen in Figure 6-2. It is immediately noticeable that the graphene antenna has a significantly lower resonance frequency at $f_{r,Gr} = 0.785$ THz compared to its Cu counterpart at $f_{r,Cu} = 1.725$ THz, which is due to the SPP induced confinement of the EM waves within the graphene. While the resonance of the Cu dipole matches the analytical value well, the resonance of the graphene dipole is significantly lower than the analytically determined value. The reason for this is not clear at this point, but it is assumed to be due to the improper approximation for the SPP wave vector used in the referenced works, which underestimates the confinement of the EM waves in the graphene.

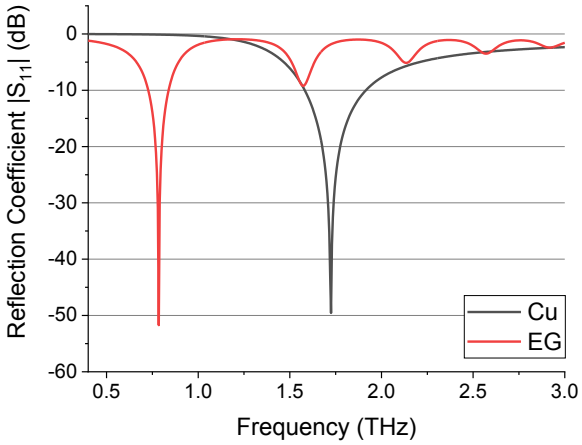

Figure 6-2 Reflection coefficient $|S_{11}|$of copper and graphene dipoles on SiO_2 substrate.

The respective reflection coefficients are $|S_{11,Gr}| = -51.71$ dB and $|S_{11,Cu}| = -49.55$ dB, which indicate good impedance matching to the excitation ports. Here, it should be noted that the characteristic impedances for the Cu and graphene dipoles are $72.06\ \Omega$ and $1291.33\ \Omega$, respectively. The reason for this is the inherently thin layer thickness of the graphene that results in a high surface impedance. However, as mentioned before, this is ideal for impedance matching to photomixers due to their high output impedance [55, 179, 218]. The high surface impedance, on the other hand, also results in high resistive losses, such that the radiation efficiency of the graphene antenna reduces to $\mu_{eff,Gr} = 8.29$ %, compared to $\mu_{eff,Cu} = 95$ % for the Cu antenna. 91.56 % of the input power of the graphene dipole is lost due to the resistive losses. With a 3-dB BW of $BW_{3\,\mathrm{dB},Gr} = 0.347$ THz, the graphene antenna has a significantly

narrower BW compared to the Cu antenna at $BW_{3\,\mathrm{dB},Cu} = 1.26$ THz, which matches the observations made in [49].

Furthermore, the dipoles were simulated on a thin SiC film ($\epsilon_{r,SiC} = 9.7$). This can be easily achieved by back etching the Si of the SiC/Si substrates using SF6-based plasma dry etching [342] or chemical wet etching, such as in a potassium hydroxide solution [343], as illustrated in Figure 6-3. The remaining graphene dipole could potentially be patterned using the process introduced in Chapter 4.

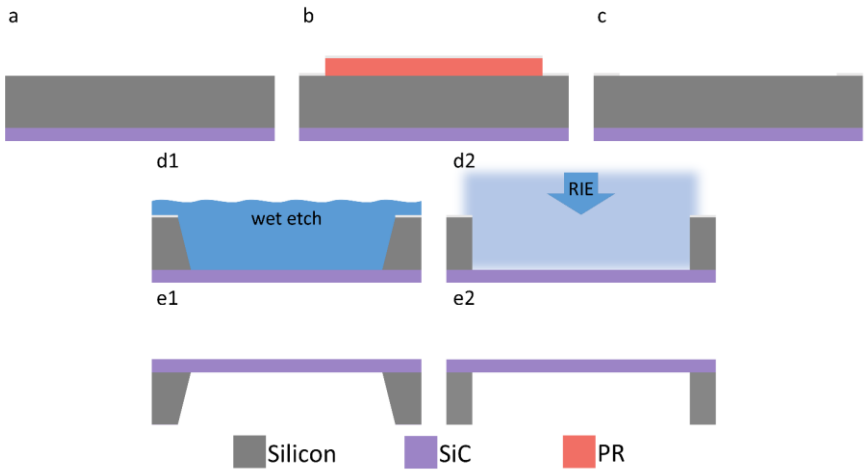

Figure 6-3 Removal of Si layer from SiC/Si substrate using plasma dry or wet etching. (a) bare SiC/Si substrate that is turned upside-down. (b) PR is structured using Lithography, and a metallic masking layer is deposited before it is (c) lift-off to reveal the final etching mask. Then the Si layer can be etched isotopically or anisotropically using (d1) wet chemical etching or (d2) RIE. (e1, e2) The substrate is again turned upside down to reveal the etched substrate for further processing.

Cu and graphene dipoles, with the same parameters as before, are initially simulated, and their reflection coefficients are plotted in Figure 6-4. In comparison to the antennas on SiO_2, the resonance frequencies shift to$f_{r,Cu} = 1.605$ THz and $f_{r,Gr} = 0.61$ THz, respectively, with reflection coefficients of $|S_{11,Cu}| = -55.37$ dB and $|S_{11,Gr}| = -44.74$ dB, which again shows good impedance matching to the excitation port. The reason for the shift in the resonance is the stronger confinement of the EM waves in the dielectric due to the higher relative permittivity of the SiC. While the 3-dB BW of the graphene dipole slightly widens to $BW_{3\,\mathrm{dB},Gr} = 0.36$ THz, it shrinks for the Cu antenna to $BW_{3\,\mathrm{dB},Gr} = 1.05$ THz. The directivity and gain of both the graphene and Cu antennas experience no change compared to the dipoles modelled on

SiO_2. Most notably, the radiation efficiencies of the two dipoles reduce to $\mu_{eff,Cu} = 94.53\ \%$ and $\mu_{eff,Gr} = 7.44\ \%$. Using SiC/Si instead of removing the Si would increase the effective permittivity and thus result in higher confinement of the EM wave within the antenna element. This would lead to a higher redshift of the resonance frequencies.

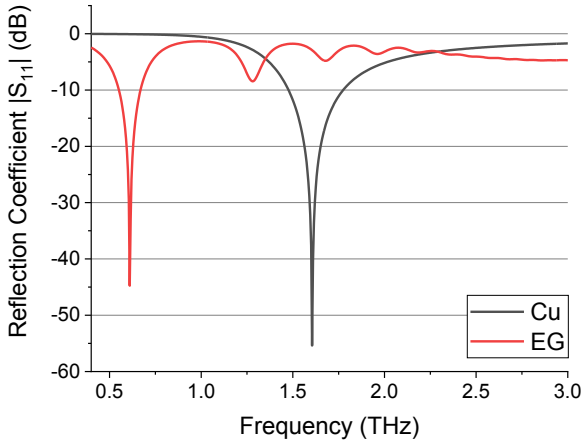

Figure 6-4 Reflection coefficient $|S_{11}|$ of copper and graphene dipoles on a SiC substrate

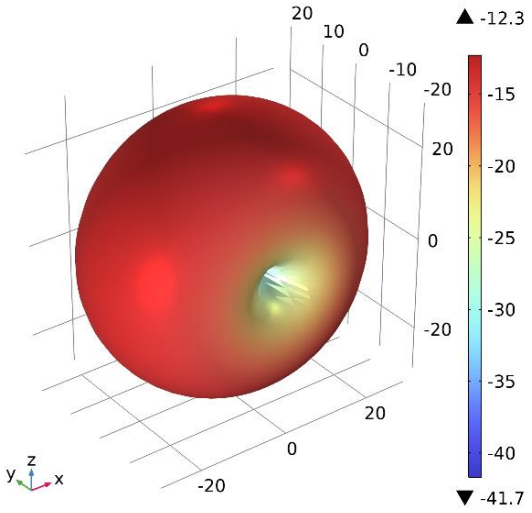

Figure 6-5 3D-far field radiation pattern of EG dipole ($E_F = 0.37\ eV$ and $\tau = 1\ ps$) on SiC at $f_r = 0.61\ THz$.

Biasing is assumed to simulate the tunability of the graphene dipole, such that the Fermi level is varied between $E_F = 0.1 - 0.6$ eV while keeping the characteristic impedance constant at $Z_{0,0.37\,eV} = 464.38\ \Omega$. Figure 6-6 shows the simulated reflection coefficient of the graphene dipole with varying Fermi level E_F. The resonance frequency experiences a strong blueshift with increasing values of E_F, such that it ranges from 0.3 THz for $E_F = 0.1$ eV to 0.77 THz for

$E_F = 0.6$ eV. It should be noted that the reduced reflection coefficient for some values of the Fermi level is due to the impedance mismatch to the port.

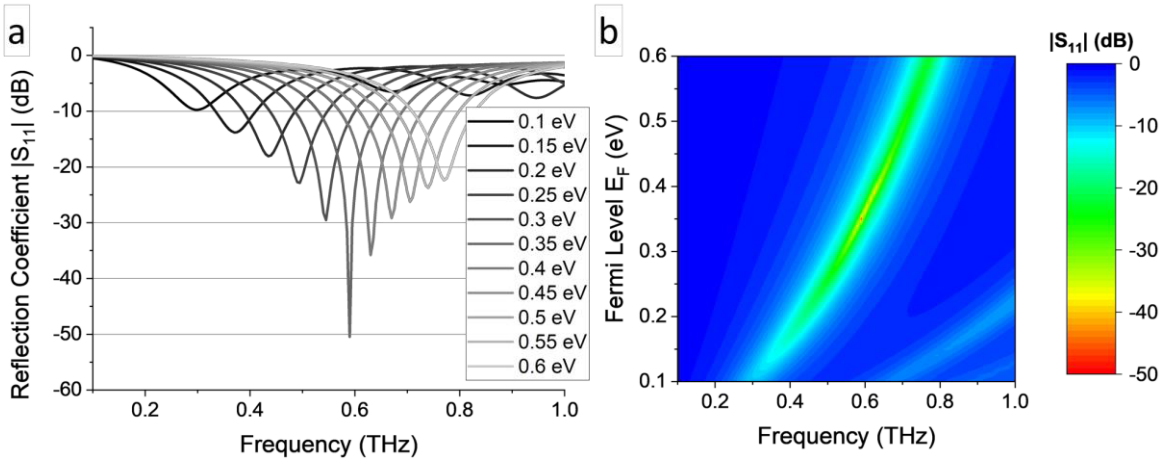

Figure 6-6 Reflection coefficient $|S_{11}|$ of EG dipoles on a SiC substrate with varying Fermi level $E_F = 0.1 - 0.6\ eV$ simulated with constant port impedant $Z_0 = 464.38\ \Omega$. (a) Line plot of $|S_{11}|$ for various values of E_F and (b) 2D heat map showing the Fermi level and frequency dependency of $|S_{11}|$.

The most important characteristics of all designed antennas are summarised in Table 6-1.

Table 6-1 Overview of properties of the main dipole antennas

Antenna	f_r [THz]	$\lvert S_{11,max}\rvert$ [dB]	Directivity [dBi]	Gain [dB]	$BW_{3\text{-}dB}$ [THz]	Z_0 [Ω]	μ_{rad} [%]
Cu on SiO_2	1.725	49.55	2.09	1.73	1.26	72.06	95
EG on SiO_2 $E_F = 0.37\ eV$	0.785	51.71	1.85	-9.99	0.35	1291.33	8.32
Cu on SiC	1.605	55.37	2.08	1.73	1.05	74.17	94.5
EG on SiC $E_F = 0.37\ eV$	0.61	44.74	1.82	-12.3	0.36	464.38	7.44

While these devices are not yet physically feasible, they do provide valuable information about the expected performance and trends of graphene-based EM components at high frequencies. Furthermore, this simulation does not consider biasing the structures to achieve reconfigurable devices by tuning the Fermi level of the graphene, which is another prominent advantage of graphene-based EM devices. The main reason for this is the 3-C SiC/Si substrate and the inherent difficulty of designing bias-feeding structures for antennas as they are not to

impede their operation. One of the most common biasing approaches is the electrostatic biasing via a dielectric and metal gate, such as in a FET. Unless the gate is part of the antenna design, i.e., the ground plane of a microstrip antenna, it would impede the propagation of EM waves. At the same time, the dielectric needs to be insulating, which does not apply to the SiC/Si substrate. Hence, this approach does not work with antennas based on EG grown on SiC/Si.

Biasing using ion gels, on the other hand, has shown to work well on graphene with a high intrinsic Fermi level [344], such as the graphene platform used in this study. However, their EM behaviour and dielectric properties at THz frequencies still need be determined for consideration in modelling.

An alternative biasing approach is optical pumping, which alleviates the need for considering bias feeding structures on the device level. Furthermore, a biasing architecture needs to be engineered if several elements need to be biased individually, such as in an antenna array.

6.1.4 Conclusion

Graphene-based antennas have the potential for significant miniaturisation compared to their metallic counterparts. In addition, they can offer dynamic tunability of their resonance frequency, which is not possible with metallic antennas. However, they suffer from narrow BW and high resistive losses due to their high surface impedance and, thus, low radiation efficiencies. Note also that the graphene is only < 3 nm thick, whereas the Cu antennas were simulated as an electrically thick layer.

In addition, using SiC, with a relatively high permittivity compared to conventional substrate materials, such as FR-4 or SiO_2, as a substrate, the antennas can be further miniaturised, however, at the cost of efficiency reduction.

6.2 Terahertz Absorber Structures

6.2.1 Design

For the basis of the metasurface absorber structure, a Salisbury screen is considered. Generally, it consists of a thin resistive sheet deposited on a metal-backed $\lambda_0/4$ thick dielectric that forms a Fabry-Perot resonator. Since the EM-waves are reflected at the metal backing, they pass through the dielectric layer twice, travelling a total length of $\lambda_0/2$, considering normal incidence. Therefore, the EM waves that manage to exit the structure cancel out the incident EM fields. Their main disadvantage, however, is their sensitivity to the angle of incidence of the fields [263].

The fundamental Fabry-Perot resonance of the Salisbury screen can be determined using [284]

$$f_0 = \frac{c}{4h\sqrt{\epsilon_r}} \tag{6.10}$$

with h being the thickness of the dielectric. The absorption spectrum has periodic zeros at $f_n = (2n-1)f_0,\ (n = 1, 2, \ldots)$. Considering the general relative permittivity of SiC $\epsilon_r = 9.7$ and a dielectric thickness of $h = 7$ µm, the first, second, and third resonances occur at $f_1 = 3.44$ THz, $f_2 = 10.03$ THz, and $f_3 = 17.19$ THz, respectively.

The absorbers are further extended to gratings by creating wells within the SiC layer that are coated with EG. Utilising a layer of graphene on top of SiC gratings has previously been shown to enhance absorption [75]. The SiC gratings can be fully covered with EG using the alloy-mediated graphitisation approach, including the bottom of the wells and their sidewalls.

6.2.2 Numerical Modelling

To reduce the computational burden, the structures are modelled in 2D. Initially, a Salisbury screen with a resistive layer matching the free space impedance $\eta_0 = \sqrt{\mu_0/\epsilon_0} = 376.73\ \Omega$, for optimal coupling of the incident EM-fields into the structure, was simulated. SiC is used as a dielectric. The observed frequency range ($0.1 - 20$ THz, with 0.05 THz step size) approaches the Reststrahlen band of SiC. Since SiC is a polar dielectric, its dielectric function differs from typical Drude materials, such as metals or graphene. It is modelled using the TOLO formalism [248]

$$\epsilon(\omega) = \epsilon_\infty \left(1 + \frac{\omega_{LO}^2 - \omega_{TO}^2}{\omega_{TO}^2 - \omega^2 - i\gamma\omega}\right) \tag{6.11}$$

where $\epsilon_\infty = 6.52$ is the high-frequency permittivity of SiC, $\omega_{TO} = 97.3$ meV (23.9 THz) and $\omega_{LO} = 118$ meV (28.5 THz) are the transverse optical (TO) and LO phonon frequencies, respectively, ω is the angular frequency, and $\gamma = 0.6$ meV (0.15 THz) is the damping constant associated with the optic phonon modes [248]. The dielectric has a thickness of $h = 7$µm and is backed by a PEC boundary. The model width/period was set to $p = 1$ µm and the left and right sides of the model were periodic boundaries to model an infinitely wide structure. A periodic port was placed about 0.1 µm above the resistive layer. It was used to radiate transverse electric (TE) and TM waves with their respective electric field and magnetic field components being perpendicular to the model, such that, $E_{TE} = E_z$ with $E_x = E_z = 0$ and $H_{TM} = -H_z$ with $H_x = H_z = 0$. Parametric sweeps of the incident angle $\theta = 0 - 90°$ $1°$ steps

were performed. Figure 6-7 shows an illustration of the used model. The absorptivity was determined via $A = 1 - R - T$ with $R = |S_{11}^2|$ and $T = 0$ due to the PEC.

Moreover, EG was used as the resistive layer. Here, the same values for modelling graphene were used as before, such that $E_F = 0.37$ eV and $\tau = 1$ ps. Biasing was again assumed to model the tunability of the absorber by varying the Fermi level within $E_F = 0.1 - 0.6$ eV, with a 0.01 eV step size.

To determine the influence of graphitising SiC gratings on their absorptivity, a single well was added to the dielectric of the Salisbury screen absorber and covered with a graphene layer, as illustrated in Figure 6-7. The depth and width were set to $d_{well} = 2$ µm and $w_{well} = 0.1$ µm, respectively. The remaining dimensions and boundaries were taken from the previous model. Here again, parametric sweeps were performed to model the dimensional dependence of absorptivity. The well depth was swept within $d_{well} = 0.25 - 6.75$ µm in 0.25 µm steps, the well width was swept within $w_{well} = 0.05 - 0.95$ µm in 0.05 µm steps, and the period was swept within $p = 0.2 - 3$ µm in 0.2 µm steps.

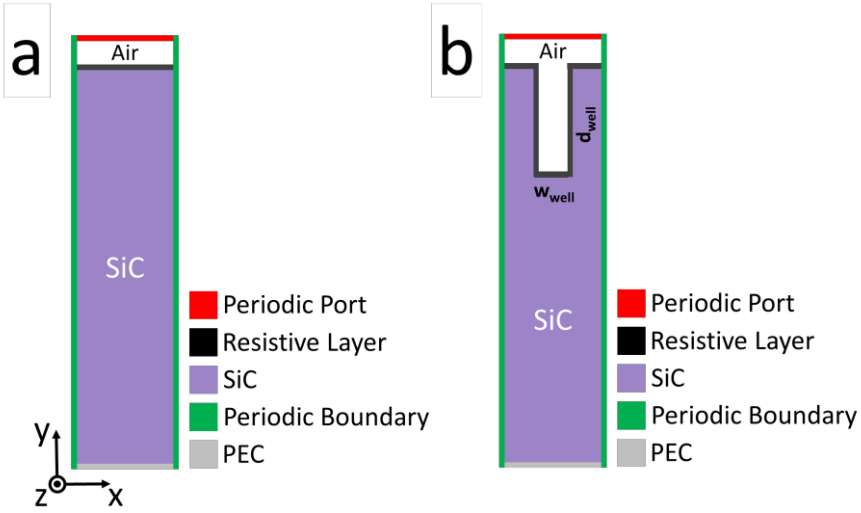

Figure 6-7 Schematic illustration of (a) Salisbury screen and (b) grating-based absorbers. (The coordinate axis from (a) is also valid for (b))

6.2.3 Discussion

The absorptivities of the bare SiC layer, EG on SiC, and the 376.73 Ω resistive layer on SiC are shown in Figure 6-8 for a normally incident ($\theta = 0°$) TE wave. An overview of the first four resonances and their respective values of absorptivity is given in Table 6-2. Here, it can be seen that the absorber that is based on the 376.73 Ω resistive layer behaves very much like an ideal Salisbury screen. Its first resonance at $f_{1,377\,\Omega} = 3.45$ THz matches the ideal Fabry-

Perot resonance very well as the modelled permittivity of the SiC at 3.45 THz is $\epsilon_{r,SiC,3.45\,\mathrm{THz}} = 9.657 - 0.003\mathrm{i}$ and thus very close to the idealised value of $\epsilon_{r,SiC} = 9.7$. As the frequency increases towards the Reststrahen band of SiC, the real part of the permittivity of SiC rapidly increases while the imaginary part decreases. The permittivity for the third resonance becomes $\epsilon_{r,SiC,15.5\,\mathrm{THz}} = 11.94 - 0.039\mathrm{i}$. Therefore, the values of the second and third resonance experience a significant redshift as compared to the analytical values.

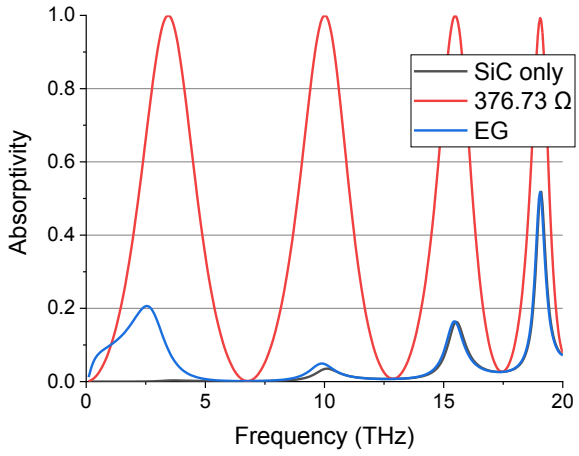

Figure 6-8 Absorptivity of Salisbury screen with no resistive layer, one that matches the free space impedance (376.73 Ω), as well as a layer of EG ($E_F = 0.37\ eV, \tau = 1\ ps$), for normally incident ($\theta = 0°$) TE waves.

Table 6-2 Overview of the first four resonances of the Salisbury screen absorbers

Resistive layer	f_1 **[THz]**	A_1 **[%]**	f_2 **[THz]**	A_2 **[%]**	f_3 **[THz]**	A_3 **[%]**	f_4 **[THz]**	A_4 **[%]**
none	3.7	0.3	10.1	3.5	15.55	16.3	19.1	51.8
EG ($E_F = 0.37$ eV)	2.55	20.6	9.9	4.9	15.45	16.5	19.05	51.8
376.73 Ω	3.45	100	10	100	15.5	99.9	19.05	99.3

The resonances of the bare SiC layer match those of the 376.73 Ω resistive layer quite well, while the EG-based absorber shows a slight redshift in the resonance frequencies. The reason for this is that the intraband contribution of its conductivity passes through the Drude-roll off and is subject to large changes that influence the impedance matching of the EG layer to free space. Furthermore, an enhancement of the absorption, up to ~67-fold for the first mode, is revealed when compared to the bare SiC layer. However, is also directly noticeable that the absorption of the EG-based absorber is much lower compared to the one based on the 376.73 Ω resistive layer, which has a roughly 5-fold higher absorption. The reason for this is again the

impedance mismatch of the EG-layer to free space, which prohibits EM-fields from coupling into the substrate. Hence, less EM-radiation can be cancelled out by the reflected fields.

To analyse the influence of potential biasing, the Fermi level of the EG absorber is varied between $E_F = 0.1 - 0.6$ eV. Figure 6-9 shows the dependence of the absorptivity on graphene's Fermi level. It can be noticed that the resonance frequencies experience a redshift as well as an enhancement of the absorption for resonances other than the fourth-order resonance. This enhancement is particularly strong for the first mode, and the absorptivity increases from 4.5 % at $E_F = 0.1$ eV to 46.6 % at $E_F = 0.6$ eV. It is expected that increasing the Fermi level further would eventually lead to a fully optimized Salisbury screen as the surface impedance of graphene approaches the free-space impedance. However, it is yet to be determined whether the graphene layer can realistically be biased to such an extend using common biasing approaches. Therefore, the device was modelled considering a rather conservative Fermi level range and not further optimised to achieve impedance matching to the free-space.

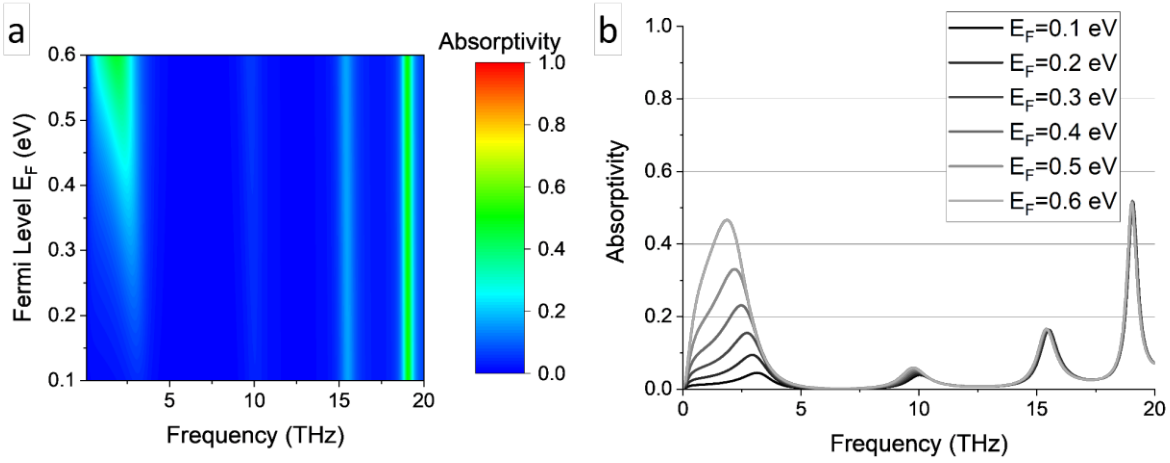

Figure 6-9 Absorptivity of graphene-based Salisbury screen absorber based on a SiC substrate for varying Fermi level $E_F = 0.1 - 0.6$ eV, for normally incident ($\theta = 0°$) TE waves. (a) 2D heat map of the absorptivity depending on E_F and the frequency, and (b) plot of the frequency dependent absorptivity for several values of E_F. A plot of (a) with adjusted absorptivity limits is shown in Figure C-1.

As Salisbury screen absorbers experience a strong dependence on the angle of incidence of the EM fields, the EG and the 376.73 Ω absorbers are modelled for varying values of θ, see Figure 6-10 and Figure 6-11. The 376.73 Ω absorber experiences the expected absorptivity decrease for increasing incident angles, regardless of polarisation. However, the absorptivity

of the EG absorber increases for TE incident waves as θ approaches 90°. On the other hand, the absorptivity of the EG absorber decreases for TM incident waves as θ approaches 90°.

This effect, which is attributed to interband and intraband absorption as indicated by graphene's conductivity model, has previously been demonstrated using numerical simulations [283]. The angle for maximum absorptivity ($\theta_{max.\mathrm{A}}$) was determined using transfer matrix modelling to be [283]

$$\theta_{max.A,TE} = \cos^{-1}(Re\{\sigma_{Gr}\}\eta_0) \tag{6.12}$$

$$\theta_{max.A,TM} = \cos^{-1}(1/Re\{\sigma_{Gr}\}\eta_0) \tag{6.13}$$

where σ_{Gr} is the complex conductivity of graphene and η_0 is the free space impedance. Figure 6-12 plots the frequency-dependent incident angle for maximum absorptivity ($\theta_{max.\mathrm{A}}$) for TE and TM waves. It can be seen that TE waves experience a maximum absorptivity at $\theta_{max.A,TE} \neq 0$ throughout the frequency range, except for frequencies below ~0.6 THz. The effect is the opposite for TM waves, as they experience a maximum absorptivity at $\theta_{max,A,TM} \neq 0$ for frequencies up to ~0.6 THz. This transition aligns with the Drude roll-off of graphene's conductivity model, where the contribution of conduction mechanisms changes from the intraband and interband transitions. Towards grazing incident angles, the absorptivities approach zero again. Furthermore, the resonance at ~13.5 THz and ~18 THz for close-to-grazing angle TM waves are associated with the SiC substrate model [283].

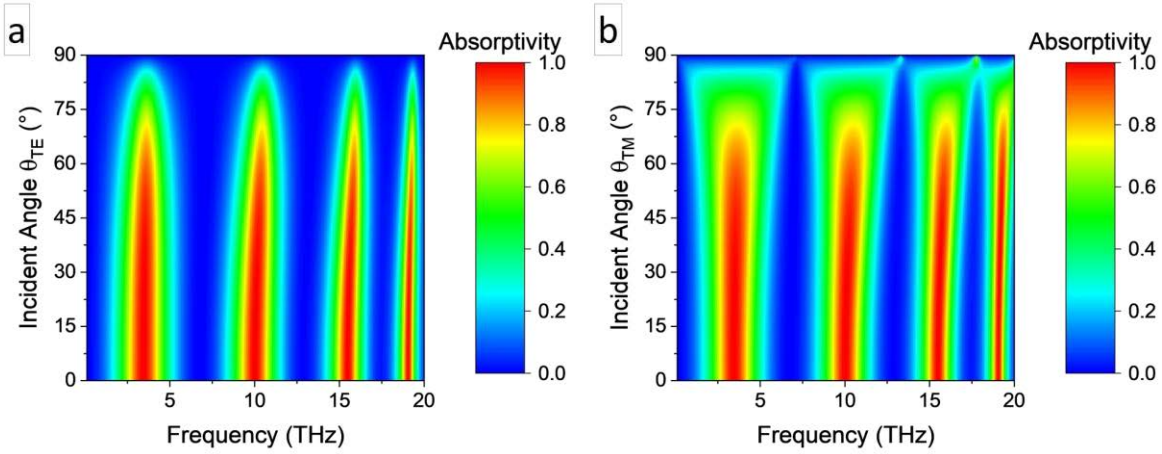

Figure 6-10 2D heat maps of the absorptivity of a Salisbury screen absorber based on a SiC substrate and 376.73 Ω resistive layer for oblique incident (a) TE and (b) TM waves.

In general, the resonances of both structures experience a blueshift for increasing values of θ for either TE or TM waves. Except for the first resonance of the graphene-based absorber for TM waves. As it initially decreases for increasing angles of θ_{TM}, it broadens, and the resonance

reaches a frequency range where $\theta_{max.A,TM} \neq 0$, and the absorptivity increases again for higher values of θ_{TM}.

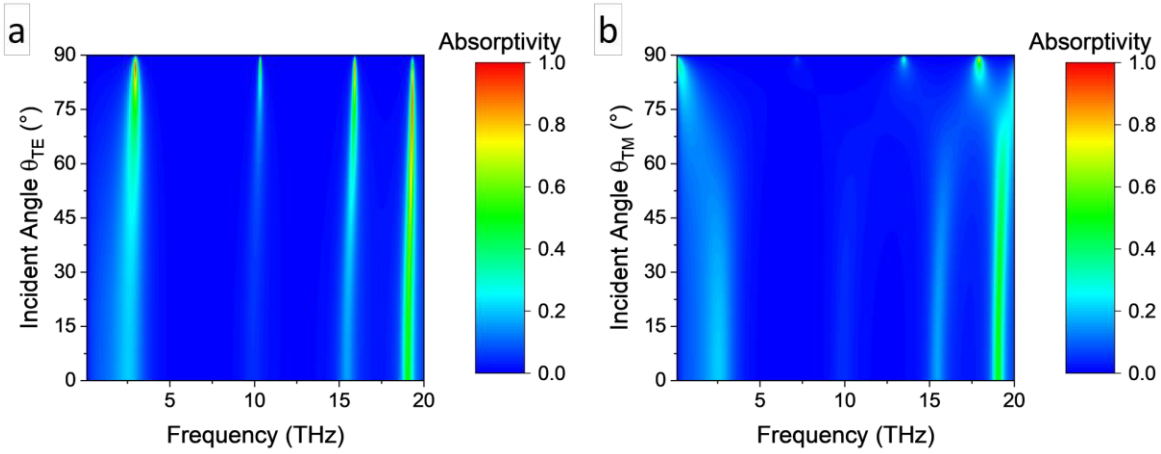

Figure 6-11 2D heat maps of the absorptivity of a graphene-based Salisbury screen absorber based on a SiC substrate for the oblique incident (a) TE and (b) TM waves. A plot of (b) with adjusted absorptivity limits is shown in Figure C-2.

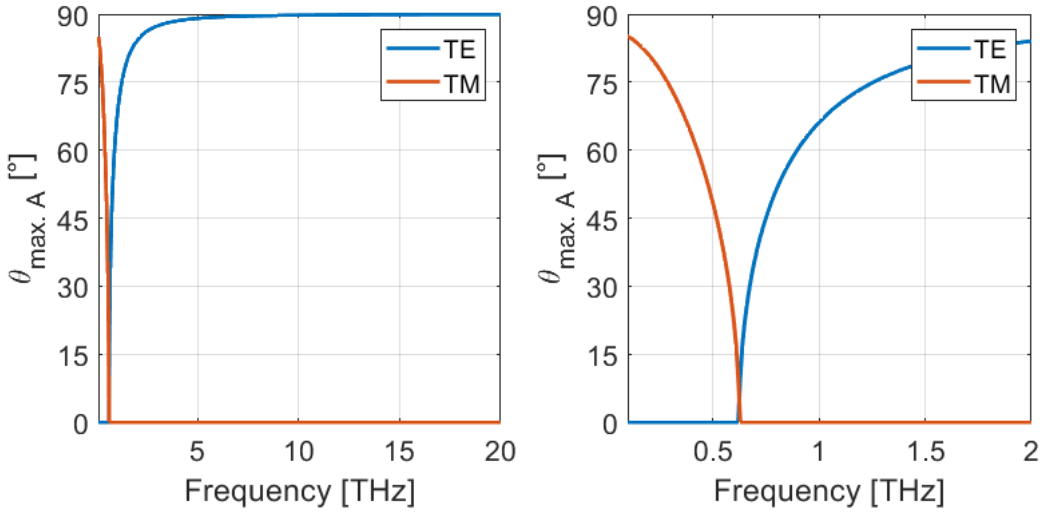

Figure 6-12 Evaluation of the frequency-dependent incident angle for maximum absorptivity ($\theta_{max.A}$) for (a) the complete modelling frequency range, and (b) zooming into the area of interest.

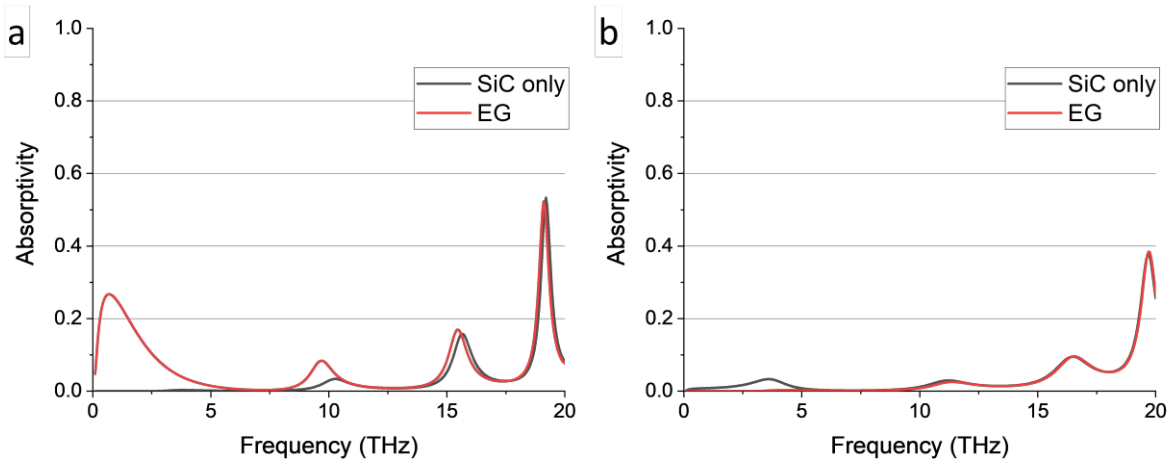

Figure 6-13 Absoptivity of the bare and a graphitised SiC grating absorber for normally incident ($\theta = 0°$) (a) TE and (b) TM waves.

To analyse the absorptivity enhancement of graphitised SiC grating, a bare SiC grating with well dimensions of $d_{well} = 2$ µm and $w_{well} = 0.1$ µm was numerically modelled. The surface of the same grating was covered by a graphene layer with $E_F = 0.37$ eV and $\tau = 1$ ps. Figure 6-13 shows the simulated absorptivity of those two structures for normally incident TE and TM waves (field component along the grating), and Table 6-3 and Table 6-4 give an overview of the first four resonances and absorptivities. The resonances, again, experience a redshift for impinging TE waves on the graphene-based grating absorber when compared to the bare SiC grating, while they barely shift for impinging TM waves. The resonances for TE waves experience an absorption enhancement, up to ~89 fold for the first mode, while the resonances for impinging TM waves show a lower absorptivity.

Table 6-3 Overview of the first four resonances of the SiC grating-based absorbers for normally incident TE waves.

Resistive layer	f_1 **[THz]**	A_1 **[%]**	f_2 **[THz]**	A_2 **[%]**	f_3 **[THz]**	A_3 **[%]**	f_4 **[THz]**	A_4 **[%]**
none	3.75	0.3	10.3	3.37	15.65	15.8	19.2	53.3
EG ($\mu_c = 0.37$ eV)	0.7	26.7	9.7	8.4	15.45	17	19.1	52.3

Table 6-4 Overview of the first four resonances of the SiC grating-based absorbers for normally incident TM waves.

Resistive layer	f_1 [THz]	A_1 [%]	f_2 [THz]	A_2 [%]	f_3 [THz]	A_3 [%]	f_4 [THz]	A_4 [%]
none	3.6	3.3	11.2	3	16.5	9.5	19.7	37.7
EG ($\mu_c = 0.37\ eV$)	4.3	0.3	11.35	2.6	16.5	9.6	19.1	52.3

Again, the tunability of the graphitised SiC gratings was analysed by biasing the graphene layer within $E_F = 0.1 - 0.6$ eV. The resulting absorptivity is illustrated in Figure 6-14. It shows how the resonances experience a redshift for increasing values of E_F and a significant absorptivity enhancement, with the absorption reaching nearly 100 %, as E_F approaches ~0.2 eV for TE waves.. On the other hand, the change in Fermi level induces barely any change for impinging TM waves.

The dependence of the absorptivity on the incident angle of the EM irradiation is plotted in Figure 6-15. The resonance shift and absorptivity enhancement correlate with the graphene Salisbury screen absorbers, see Figure 6-11.

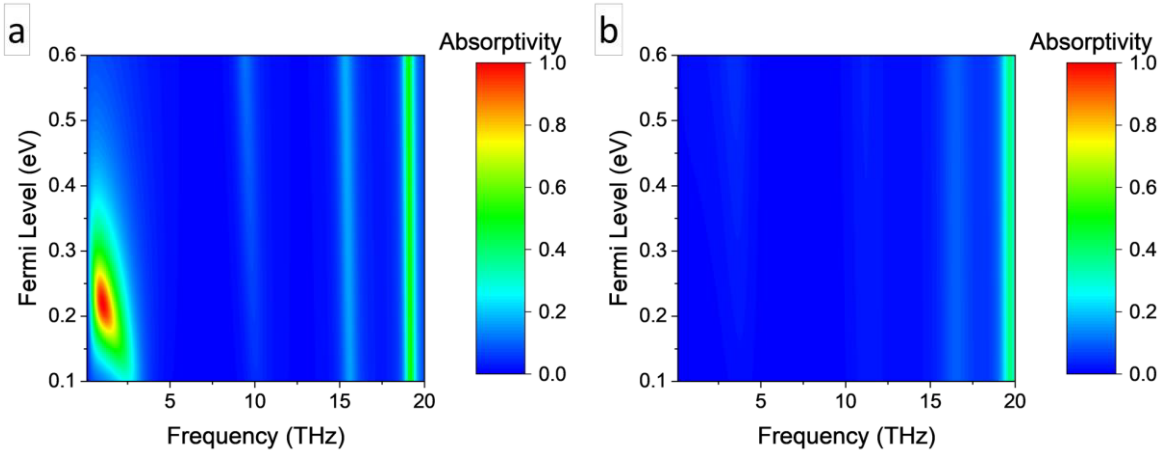

Figure 6-14 2D heat maps of the absorptivity of a graphitised SiC grating absorber for varying Fermi level $E_F = 0.1 - 0.6\ eV$, for normally incident ($\theta = 0°$) (a) TE and (b) TM waves. A plot of (b) with adjusted absorptivity limits is shown in Figure C-3.

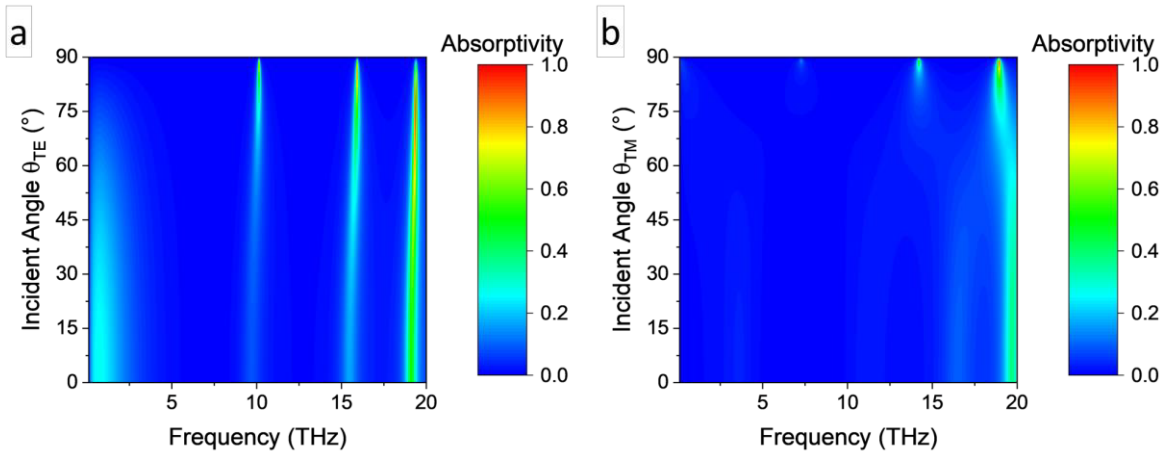

Figure 6-15 2D heat maps of the absorptivity of a graphitised SiC grating absorber for the oblique incident (a) TE and (b) TM waves.

While a change in the dielectric thickness of Salisbury screen absorbers will result in a change in the resonance frequencies, the graphitised SiC gratings provide more degrees of freedom for dimensional tuning. It should be noted that dimensions are set during fabrication and can generally not be tuned dynamically. Figure 6-16 shows the change in the absorptivity of the graphitised SiC gratings for varying well depth $d_{well} = 0.25 - 6.75$ µm, Figure 6-17 shows the change in the absorptivity for varying well width $w_{well} = 0.05 - 0.95$ µm, and Figure 6-18 shows the change in the absorptivity for varying period $p = 0.2 - 3$ µm. The dimensional tuning of d_{well}, w_{well}, and p need to carfully be considered at the design stage as their have a large impact on the absorption behaviour of the designed device. Adjusting the well depth and period of the graphitised SiC gratings absorber can increase the absorptivity to 100 % for impinging TE waves, as shown in Figure 6-16 and Figure 6-18, respectively. In these individual cases, total absorption is achieved without biasing of the graphene layer. In general, all dimensional changes affect the resonance position, but they can also impact their BW. Here a trade-off can be made at the design stage to optimise the dimensions of the gratings for a particular application.

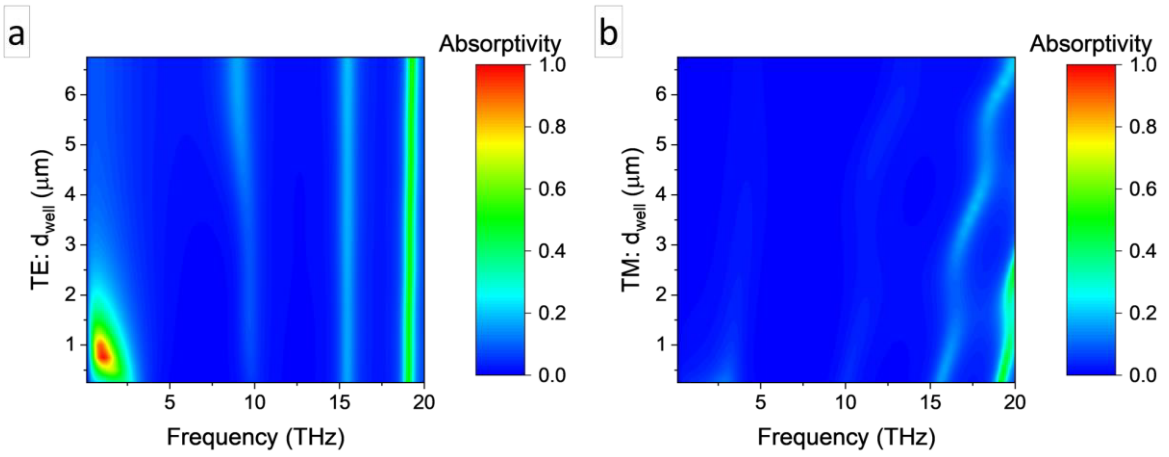

Figure 6-16 2D heat maps of the absorptivity of a graphitised SiC grating absorber under dimensional tunings of the depth d_{well} with constant well width $w_{well} = 0.1\ \mu m$ and period $p = 1\ \mu m$, for normally incident ($\theta = 0°$) (a) TE and (b) TM waves. A plot of (b) with adjusted absorptivity limits is shown in Figure C-4.

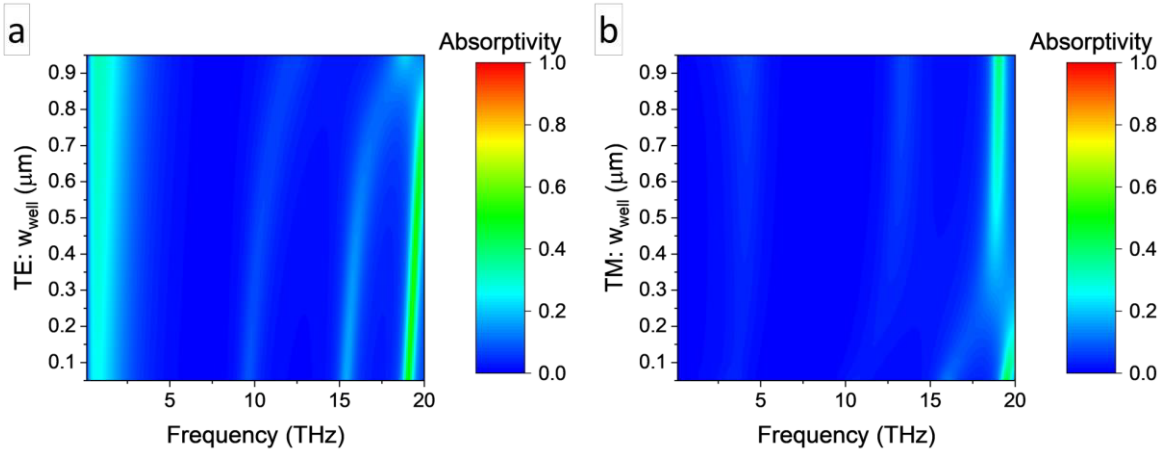

Figure 6-17 2D heat maps of the absorptivity of a graphitised SiC grating absorber under dimensional tunings of the well width $w_{well} = 0.1\ \mu m$ with constant depth $d_{well} = 2\ \mu m$ and period $p = 1\ \mu m$, for normally incident ($\theta = 0°$) (a) TE and (b) TM waves. A plot of (a) and (b) with adjusted absorptivity limits is shown in Figure C-5.

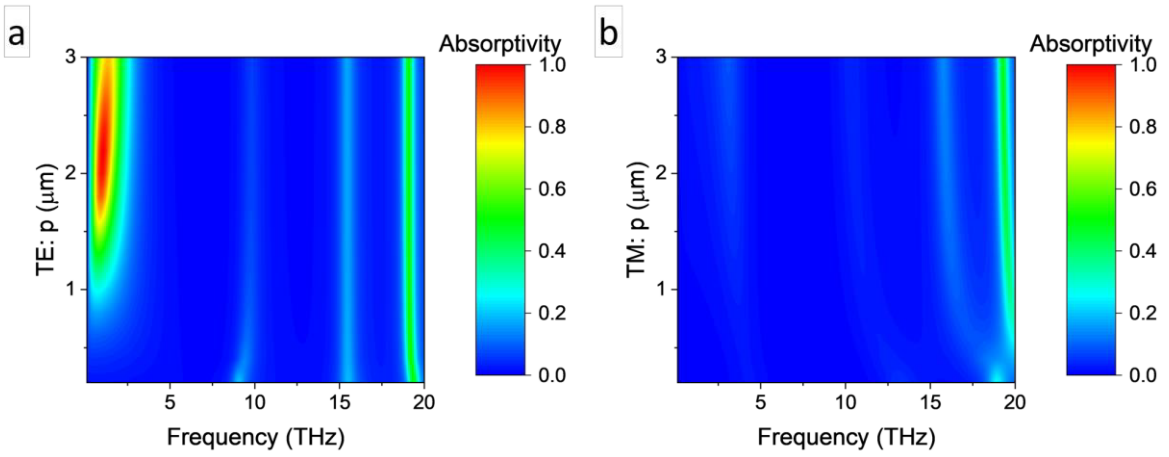

Figure 6-18 2D heat maps of the absorptivity of a graphitised SiC grating absorber under dimensional tunings of the period p with constant depth $d_{well} = 2\ \mu m$ and well width $w_{well} = 0.1\ \mu m$, for normally incident ($\theta = 0°$) (a) TE and (b) TM waves. A plot of (b) with adjusted absorptivity limits is shown in Figure C-6.

6.2.4 Conclusion

Graphene-based absorbers are particularly promising due to their tunability and absorptivity enhancement. In this study, EG on SiC-based absorbers are introduced. Using graphene as the resistive layer of the Salisbury screen absorber structure, up to ~67-fold absorptivity enhancement can be achieved, accompanied by a redshift of the resonances compared to an ungraphitised SiC layer. While the absorptivities of the individual modes are smaller compared to an ideal Salisbury screen absorber, the graphene-based absorber is tunable by varying its Fermi level. Furthermore, the designed graphene-based Salisbury screen absorber shows an absorptivity enhancement and a blueshift for an increasing angle of incidence at the Drude roll-off, which goes against the expectation of the ideal one.

Introducing a well in the SiC layer to create graphitised SiC gratings enables the possibility of achieving much more complex absorption spectra, such that the absorption BW and absorptivity can be engineered at the design stage. Here it is important to note that dynamic dimensional tuning is generally not possible. Therefore, there is a significant interest towards the use of dynamically tunable materials, such as graphene. Comparing a graphitised SiC grating absorber to an ungraphitised SiC grating shows a much stronger enhancement of absorptivity, up to ~89 fold, and redshift for the resonance frequencies, compared to the Salisbury screen structures. On the other hand, both behave very similarly, such that again an absorptivity enhancement, as well as a redshift of the resonance frequencies, can be achieved by biasing the graphene layer, while an absorptivity enhancement and a blueshift are possible

for an increasing angle of incidence. Furthermore, optimising the dimensions of the gratings can result in total absorption without any biasing applied to the graphene layer.

It should be noted that in EM applications, the biasing of the graphene layer has been demonstrated using an ion gel [67]. This would also be a viable option for the designed EG on SiC metasurface absorbers, as the whole structure is biased to the same level.

Chapter 7 Conclusions and Future Works

7.1 Conclusions

One faces several hurdles on the path towards the use of any graphene technology for high-frequency applications. These include the scalable synthesis and patterning of graphene and accurate modelling of its performance. The latter requires appropriate input derived from an in-depth characterisation of graphene's performance at the appropriate EM spectrum.

In order to fill this important gap, first of all, this work introduced a new method for the direct synthesis of planar micro and nanopatterned EG on SiC/Si substrates using simple lithography processes and avoiding graphene etching. As opposed to the previously available route via the pre-patterning of the carbon source, this novel approach can also be used on SiC wafers. In this approach, the catalyst metals are pre-patterned using lithography and lift-off techniques before the graphitisation. This technique also avoids the etching of the graphene, which has been shown to introduce defects, i.e., edge defects and contamination from the etch mask. Masked UV-lithography confirms the possibility of creating millimetre-sized graphene structures and paves the way for wafer-scale graphene patterning for high-frequency device fabrication and commercial applications. EBL-patterned graphene nanostructures suggest a pitch resolution limit of ~ 200 nm. s-SNOM measurements show the formation of graphene that conforms to the shape of the pre-structured metal catalyst and confirms that the flow of the metal catalyst, deposition technique, and lithography process limit the pitch resolution. Further improvements are anticipated by optimising the said parameters.

The patterned synthesis approach developed above was then used to characterise the high-frequency properties of EG grown on SiC/Si substrates. Graphene was employed in metal CPWs as a patch within the centre trace, as well as a shunt between the centre and ground traces. While an initially insufficient quality electrical contact impeded the current injection into the graphene patches, a mild Ar RIE treatment on the graphene at the interface to the metal CPW enabled the contact with the graphene shunts. This finding affirms the importance of contact engineering to achieve a sufficiently low graphene-metal contact resistance for adequate current injection in the 2D material at high frequencies. Furthermore, a wideband evaluation of the sheet resistance showed a strong frequency dependence of graphene's sheet resistance, which is attributed to the increasingly lower influence of small-scale scattering defects in the graphene at high frequencies, such as the < 100 nm grain sizes.

For the characterisation of the intrinsic electrical properties of large-area graphitised SiC/Si coupons without the consideration of the electrical contacts, this work also devises a methodology that uses K_a-band coaxial rectangular waveguide adaptors. S-parameter measurements are taken of a sample wedged in between two waveguide adaptors, and the surface impedance of the EG is determined by modelling the EG/SiC/Si stack using ABCD-Matrix models. Compared to the CPW-based characterisation, it provides several benefits. Such as avoiding contracting issues and complex fabrication and characterising a larger area of the thin film, making it less prone to localised defects by averaging over the waveguide cross-section.

The extraction of the sheet impedance from the S-parameter measurements yielded a ∼2-fold increase in the average surface resistance compared to DC measurements, which is attributed to noise-type errors in the S-parameter measurements. However, with the introduction of an air gap and minor adjustment of the sample parameters, the modelled S-parameters are in very good agreement with the measured values.

Finally, EM devices for application in the THz range were designed and numerically modelled. The THz spectrum is particularly interesting for graphene applications because of the strong plasmonic effect in graphene and the potential for dynamically tuning the properties of the components.

They show that graphene dipoles are dynamically tunable and have the potential for significant miniaturisation compared to metallic ones. However, they suffer from low gain, narrow BW, and high resistive losses due to their high surface impedance and, thus, low radiation efficiencies. Using high permittivity SiC, brings the potential of further miniaturisation, however, at the cost of efficiency reduction. Therefore, a trade-off between miniaturisation and tunability for graphene-based antennas and high radiation efficiency and gain for metallic ones needs to be made.

Numerical modelling of THz metasurface absorbers based on EG on SiC shows the potential for tunability and high absorptivity enhancement. A Salisbury screen absorber structure shows up to ∼67-fold absorptivity enhancement compared to an ungraphitised SiC layer and a redshift of the resonances, which are both dynamically tunable. Introducing a well in the SiC layer to create graphitised SiC gratings would enable the achievement of much more complex absorption spectra, such that the absorption BW and absorptivity can be engineered at the design stage. Here, a ∼89-fold enhancement of absorptivity compared to an ungraphitised SiC grating and redshift of the resonance was shown, again both dynamically tunable.

Note that graphene is commonly modelled as a homogenous layer. However, experimental graphene comprises grain boundaries, defects, surface roughness, and local variations in the number of layers. A lot more work will need to be done in the future by the whole scientific community to gather more specific characteristics of the different types of graphene in the RF and THz ranges, as accurate, predictive models need to be built based on relevant specific experimental input. The technological progress through the introduction of a novel and simple patterning approach, together with the first scientific characterisation of high-frequency properties EG grown using the catalytic ally mediated graphitisation of SiC/Si substrates, as well as the numerical validation of first EM devices, paving the way for high-frequency applications in the microwave to THz range based on this platform.

7.2 Future Works

- Further use of the patterning approach introduced in this thesis to fabricate a variety of electronic devices based on planar EG on SiC/Si structures. This can include, but is not limited to, GFETs, EM components such as for THz to optical frequency ranges, as well as biosensors.
- Thorough experimental evaluation of the graphene devices.
- Design, modelling, and fabrication of metasurface-based EM components for sensing applications.
- Thorough experimental evaluation of the devices' sensitivity to polarisation, phase, and incident angle of impinging EM fields.
- Design and testing of biasing capabilities to examine the possibility of dynamically tuning the properties of fabricated components.

Appendices

Appendix A. Supporting Material for Chapter 4

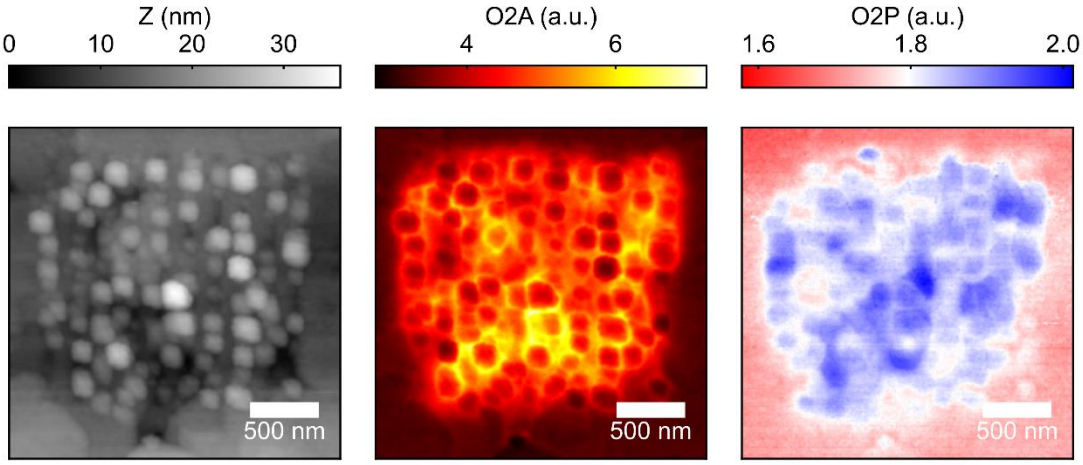

Figure A-1 Near-field imaging characterisation of 100 nm *gratings. For the excitation, a wavelength of* 9.6 μm *was used. The O2A plot shows the amplitude of the measured fields, and the O2P plot shows the phase. The image of the topographical scan is shown on the left.*

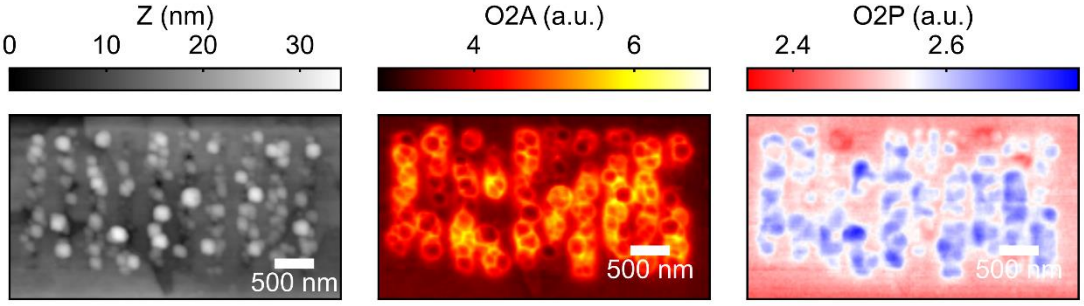

Figure A-2 Near-field imaging characterisation of 200 nm *gratings. For the excitation, a wavelength of* 9.6 μm *was used. The O2A plot shows the amplitude of the measured fields, and the O2P plot shows the phase. The image of the topographical scan is shown on the left.*

Appendix B. Supporting Material for Chapter 5

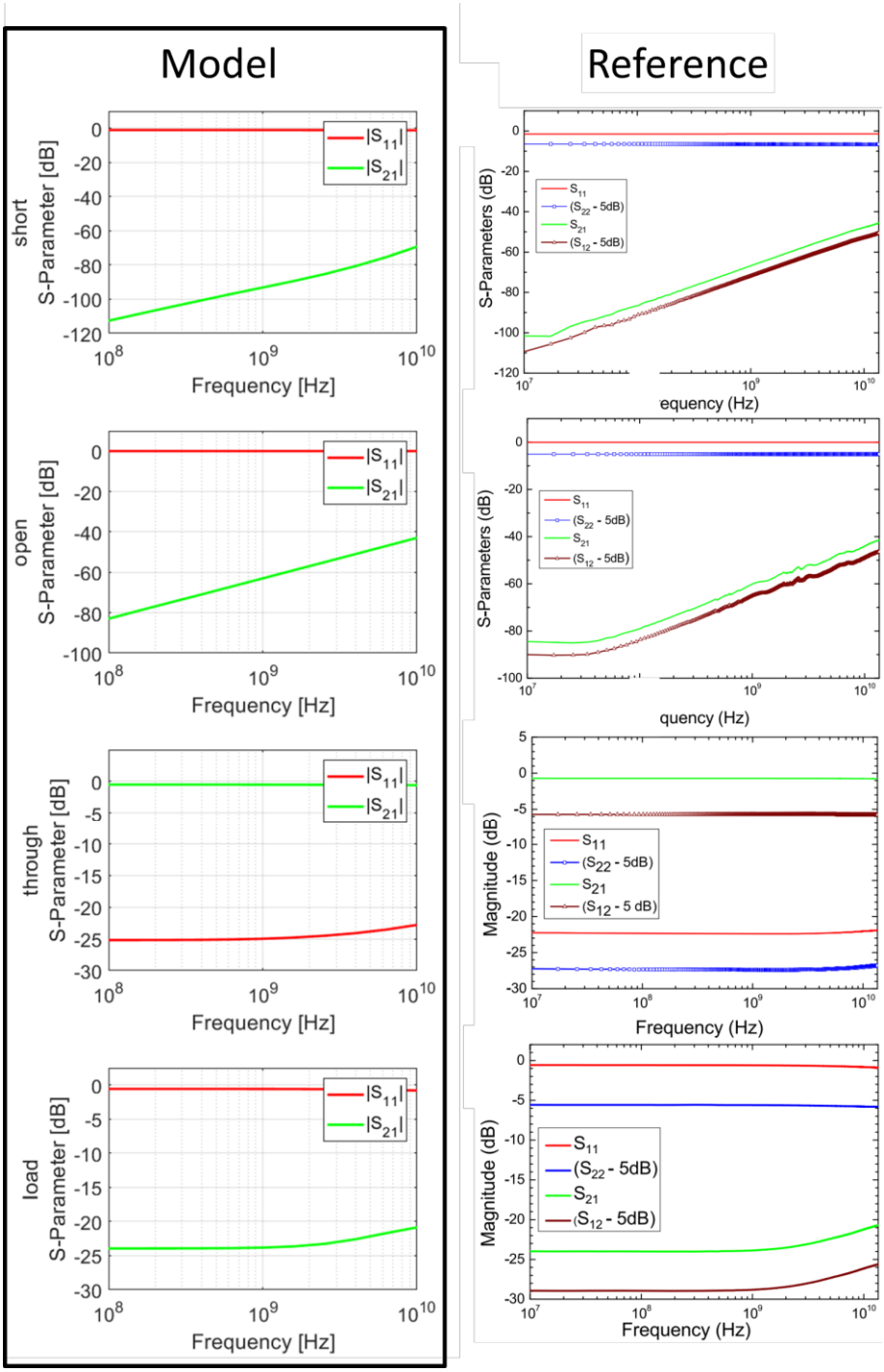

Figure B-1 Comparison of modelled S-parameter values for the SOTL structures using the developed CPW model in COMSOL to reference S-parameter measurement from [35]. CPW dimensions and graphene properties were taken from the study while common values for the other material properties, i.e., conductivities and permittivities, were assumed. The results agree well and validate the used CPW model. Reference plots reprinted from [35].

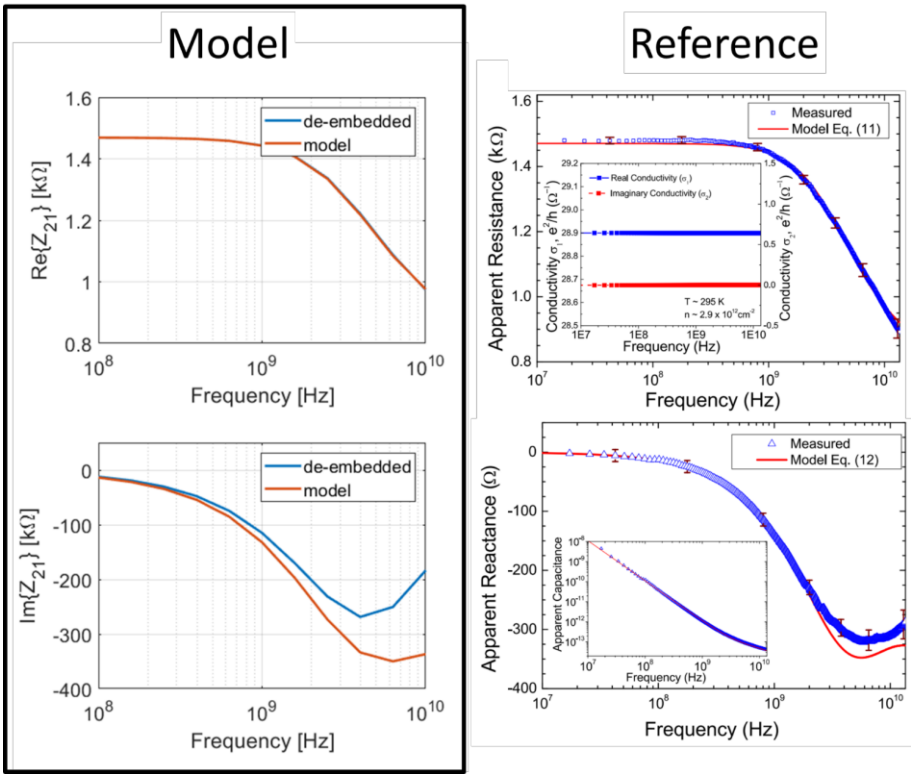

Figure B-2 Comparison of the modelled de-embedding results using the modelled S-parameter values from Figure B-1 to reference values from [35]. Equations (5.11)-(5.19) were used for the de-embedding. Using the equivalent circuit model shown in Figure 5-4 and equations (5.20)-(5.22), the properties of the graphene and graphene-metal contact were determined and plotted, as 'model' in the plots. The results agree well and validate the de-embedding and extracting procedure. Reference plots reprinted from [35].

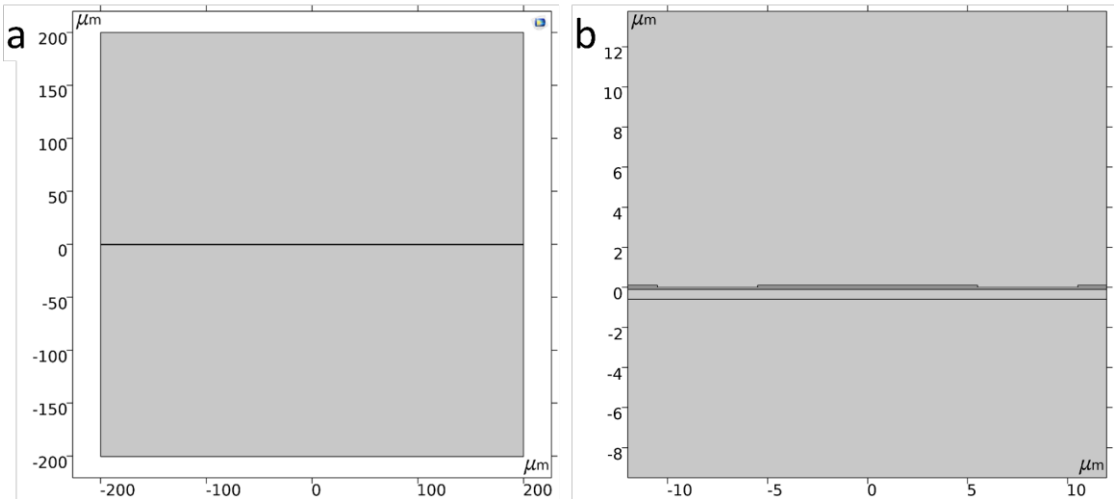

Figure B-3 Illustration of 2D COMSOL model used to determine the characteristic impedance of a CPW. (a) The top half is air, while the bottom part is Si. The separating line is the SiC layer and metal CPW. (b) zoom into the CPW ($S = 25\ \mu m$ and $W = 11\ \mu m$) shows the $100\ nm$ thin metal CPW on top of the $500\ nm$ thick SiC layer. Z_0 is calculated from by determined the RLCG parameters electro and magneto static simulations. It is calculated via $Z_0 = \sqrt{R + j\omega L / G + j\omega C}$.

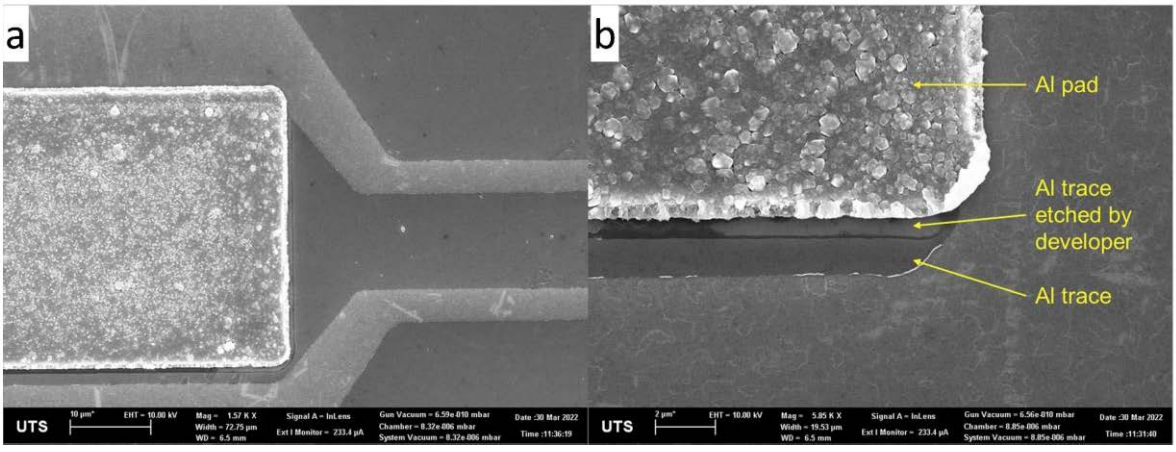

Figure B-4 SEM picture illustrating the etching of the Al CPW traces during the development of the pad lift-off mask. (a) Zoomed out and (b) zoomed-in view.

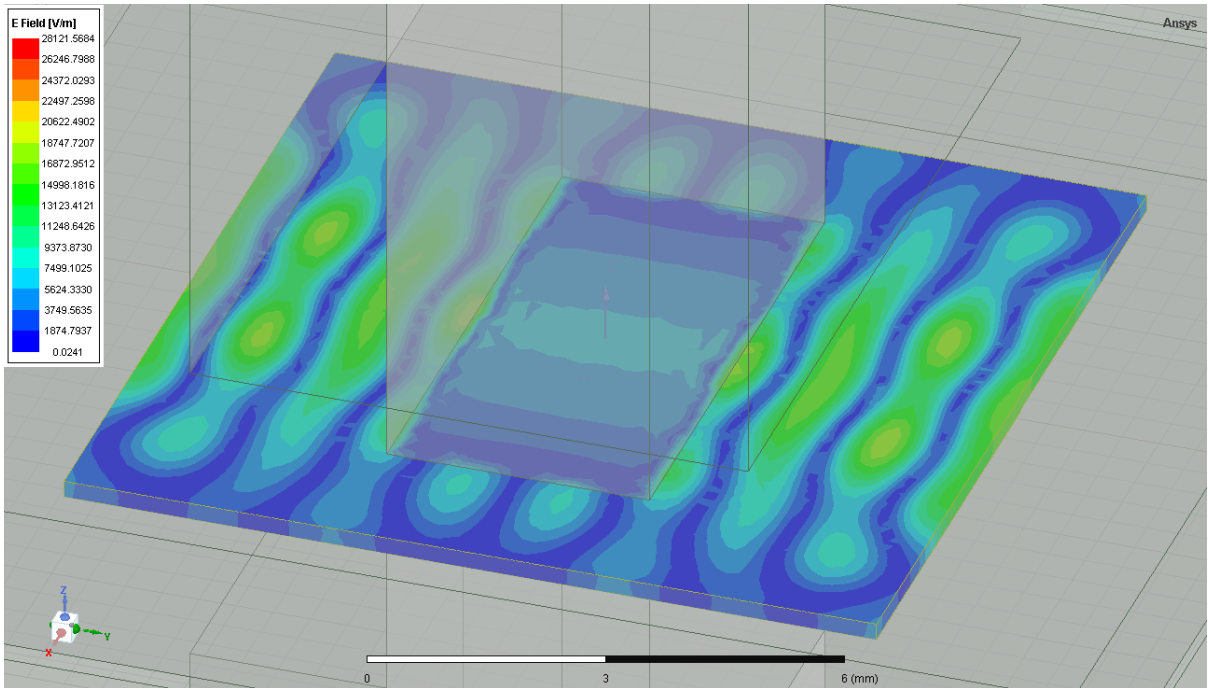

Figure B-5 HFSS simulation of the E-field on the surface of the Si substrate to show the mode at $35.3\ GHz$ *during coaxial waveguide characterisation of the bare Si substrate.*

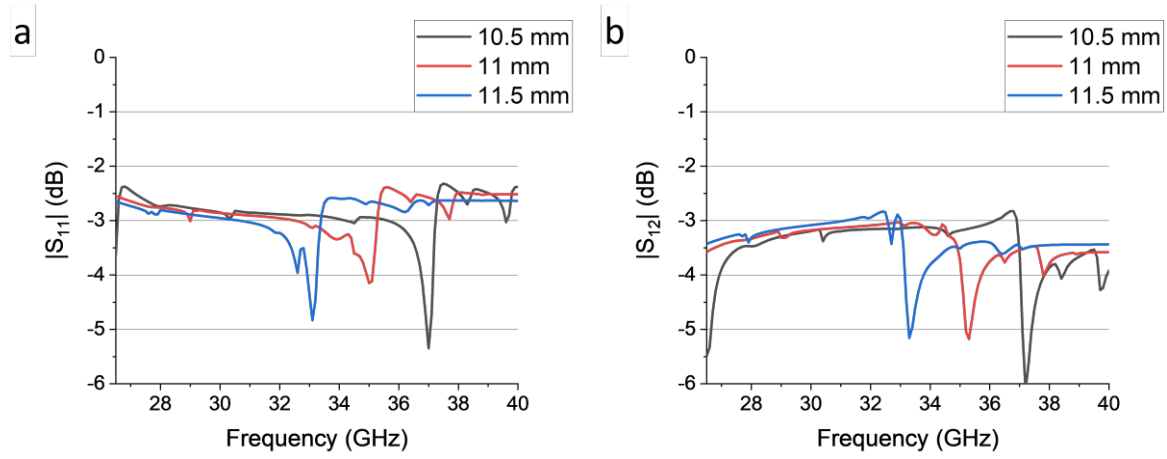

Figure B-6 HFSS Simulation of S-parameters of coaxial waveguide characterisation of bare Si substrate: parametric sweep of sample side length ($a_{Si} = 10.5 - 11.5\ mm$). *Both (a)* $|S_{11}|$ *and (b)* $|S_{21}|$ *shows a significant redshift with increasing side length and another resonance appears at lowest frequencies for* $a_{Si} = 10.5\ mm$.

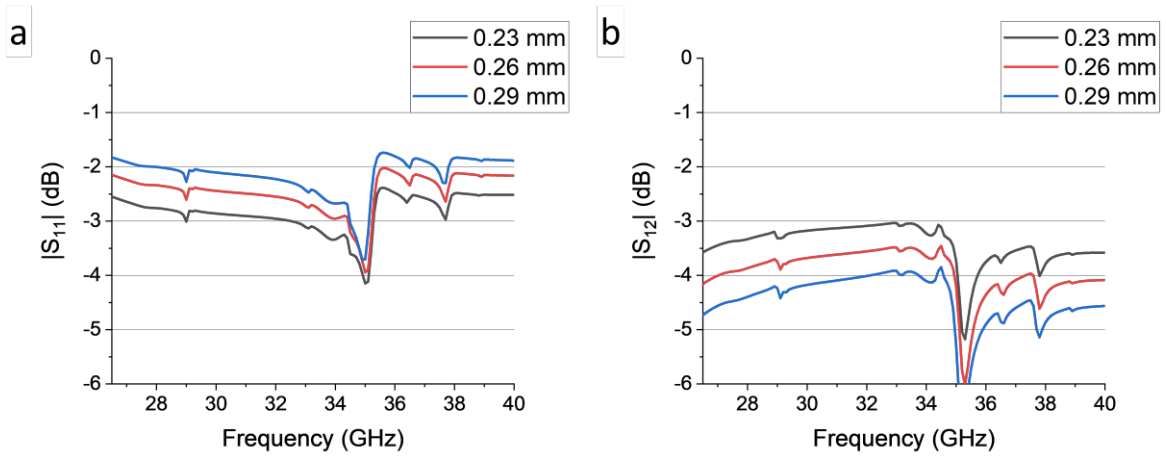

Figure B-7 HFSS Simulation of S-parameters of coaxial waveguide characterisation of bare Si substrate: parametric sweep of sample thickness ($t_{Si} = 230 - 290\ \mu m$). It shows a significant increase of (a) $|S_{11}|$ and decrease of (b) $|S_{21}|$ with increasing thickness.

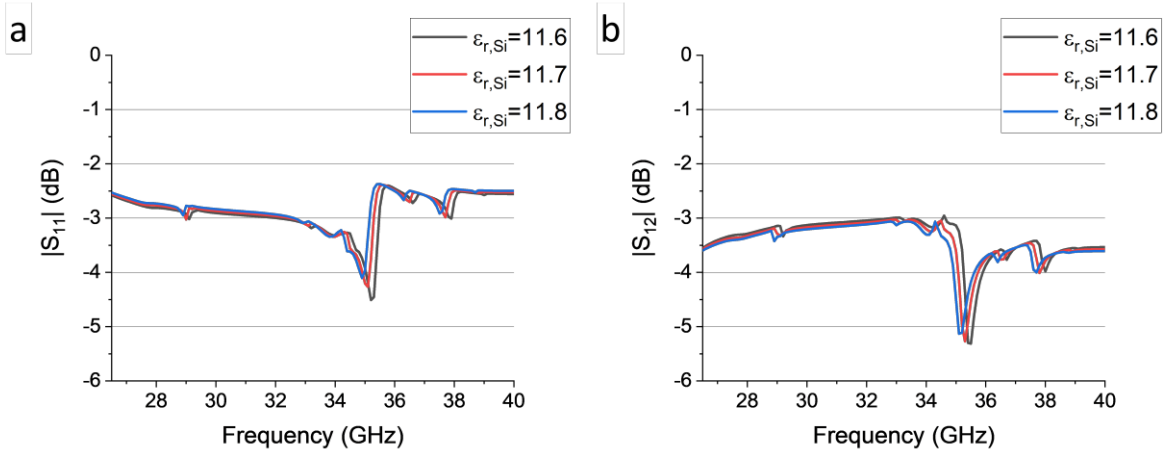

Figure B-8 HFSS Simulation of S-parameters of coaxial waveguide characterisation of bare Si substrate: parametric sweep of Si permittivity ($\epsilon_{r,Si} = 11.6 - 11.8$). It shows a minor resonance redshift for both (a) $|S_{11}|$ and (b) $|S_{21}|$ while, at the same time, $|S_{11}|$ and $|S_{21}|$ slightly decrease at the resonance with increasing permittivity $\epsilon_{r,Si}$.

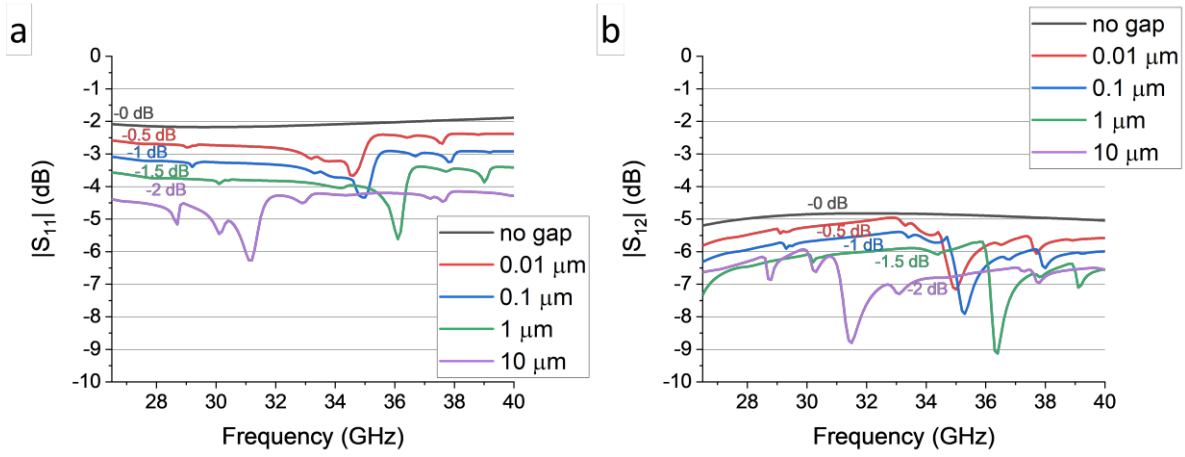

Figure B-9 HFSS Simulation of S-parameters of coaxial waveguide characterisation of EG/SiC/Si: parametric sweep of an air gap ($t_{air} = 0 - 10\ \mu m$) that was introduced in between the substrate and coaxial adaptors. It introduces resonances not present without the air gap, with a significant resonance blue shift observed with increasing gap width for both (a) $|S_{11}|$ and (b) $|S_{21}|$. Furthermore, a second large resonance appears for the $10\ \mu m$ gap at $\sim 31.5\ GHz$ as the main resonance moves outside of the observed frequency spectrum. The individual plots are offset for comparisons.

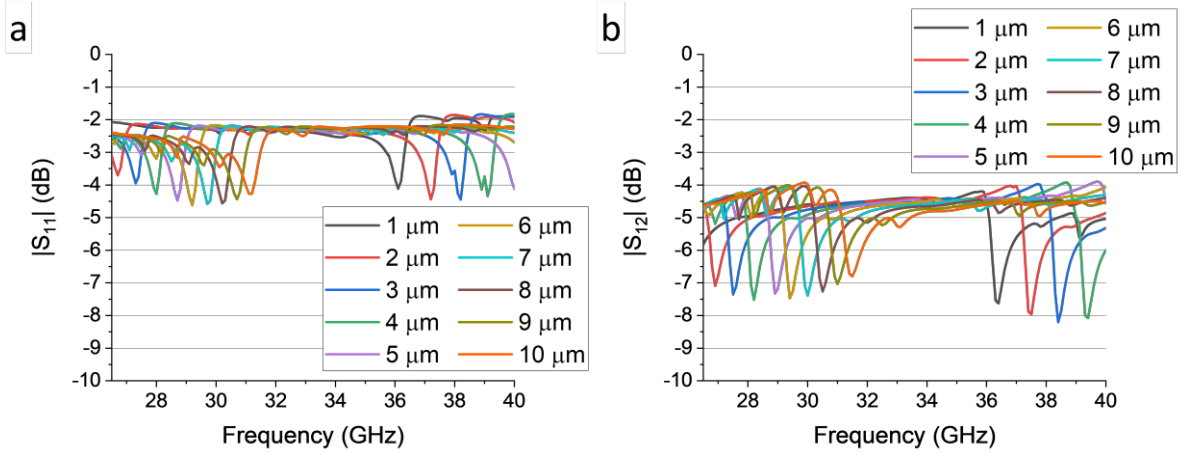

Figure B-10 HFSS Simulation of S-parameters of coaxial waveguide characterisation of EG/SiC/Si: parametric sweep of an air gap ($t_{air} = 1 - 10\ \mu m$) that was introduced in between the substrate and coaxial adaptors. It shows a significant resonance blue shift with increasing gap width for both (a) $|S_{11}|$ and (b) $|S_{21}|$, and the occurrence of a second resonance.

Table B-1 Evaluation of the change in the extracted sheet impedance ($Z_s = 100\ \Omega$) depending on the air gap introduced between the coaxial adapter and sample.

Gap	$Re\{Z_s\}$ [Ohm]	$Im\{Z_s\}$ [Ohm]
-	*94*	*0*
10 nm	86	-4
100 nm	87.8	0
1 µm	92.8	-1.5
10 µm	85.5	-14.4
100 µm	74.6	-24.4

Table B-2 Evaluation of the change in the extracted sheet impedance ($Z_s = 100\ \Omega$) depending on the thickness of the sample. Values in parenthesis identify the change in the thickness as compared to the reference sample

Thickness	$Re\{Z_s\}$ [Ohm]	$Im\{Z_s\}$ [Ohm]
105 µm (*-20 µm*)	96.6	5.7
115 µm (*-10 µm*)	94.5	3
125 µm	*94*	*0*
135 µm (*+10 µm*)	92.8	-2.7
145 µm (*+20 µm*)	88	-5.8

Table B-3 Evaluation of the change in the extracted sheet impedance ($Z_s = 100\ \Omega$) depending on the offset of the sample along the width of the waveguide a from the centre.

Offset (a)	$Re\{Z_s\}$ [Ohm]	$Im\{Z_s\}$ [Ohm]
-	*94*	*0*
200 µm	93.7	0.6
400 µm	92.2	-0.2
600 µm	93.7	*-0.3*
800 µm	91.6	-0.3
1000 µm	92.8	-0.4

Table B-4 Evaluation of the change in the extracted sheet impedance ($Z_s = 100\ \Omega$) depending on the offset of the sample along the heigth of the waveguide b from the centre.

Offset (b)	$Re\{Z_s\}$ [Ohm]	$Im\{Z_s\}$ [Ohm]
-	*94*	*0*
200 µm	93.8	0.3
400 µm	96.7	0.6
600 µm	*96.3*	*1*
800 µm	93.7	0.7
1000 µm	93	0.1

Appendix C. Supporting Material for Chapter 6

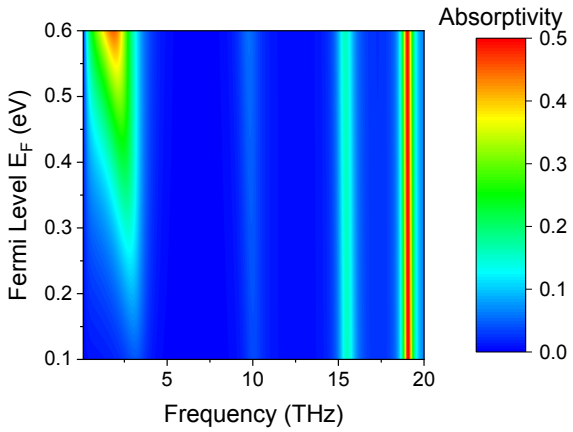

Figure C-1 2D heat map of the absorptivity of graphene-based Salisbury screen absorber based on a SiC substrate for varying Fermi level $E_F = 0.1 - 0.6\ eV$, for normally incident ($\theta = 0°$) TE waves, depending on E_F and the frequency, with adjusted absorptivity limits.

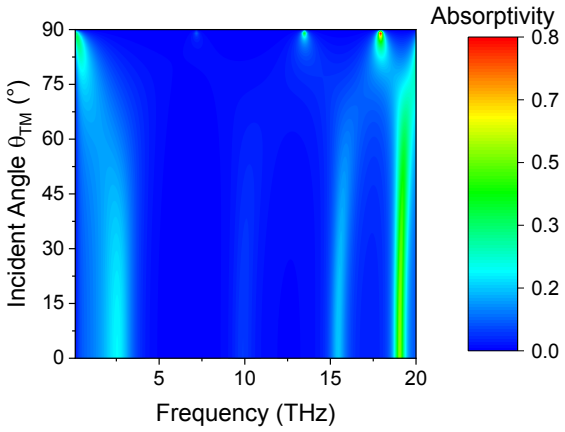

Figure C-2 2D heat map of the absorptivity of a graphene-based Salisbury screen absorber based on a SiC substrate for oblique incident TM waves with adjusted absorptivity limits.

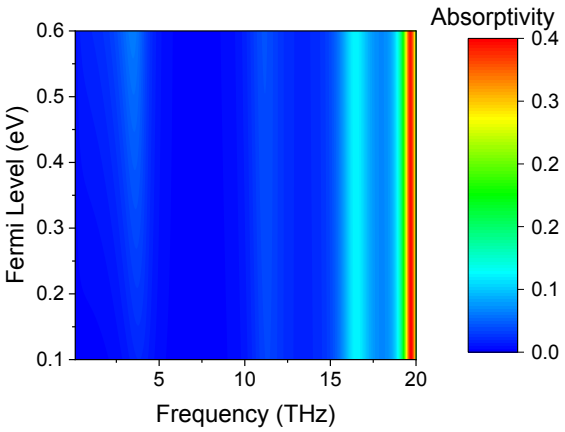

Figure C-3 2D heat map of the absorptivity of a graphitised SiC grating absorber for varying Fermi level $E_F = 0.1 - 0.6\ eV$, for normally incident ($\theta = 0°$) TM waves, depending on E_F and the frequency, with adjusted absorptivity limits.

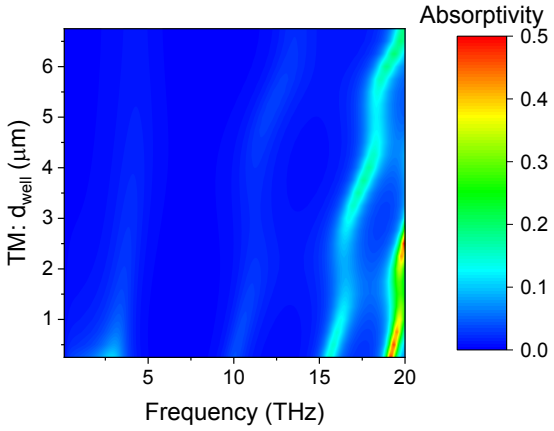

Figure C-4 2D heat map of the absorptivity of a graphitised SiC grating absorber under dimensional tuning of the depth d_{well} with constant well width $w_{well} = 0.1\ \mu m$ and period $p = 1\ \mu m$, for normally incident ($\theta = 0°$)) TM waves, with adjusted absorptivity limits.

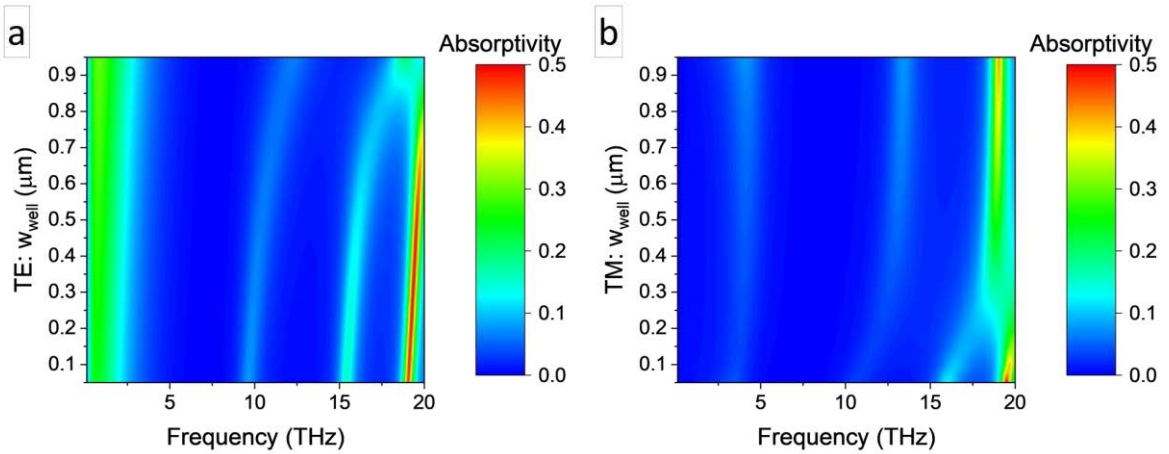

Figure C-5 2D heat maps of the absorptivity of a graphitised SiC grating absorber under dimensional tunings of the well width w_{well} with constant depth $d_{well} = 2\ \mu m$ and period $p = 1\ \mu m$, for normally incident ($\theta = 0°$) (a) TE and (b) TM waves, with adjusted absorptivity limits.

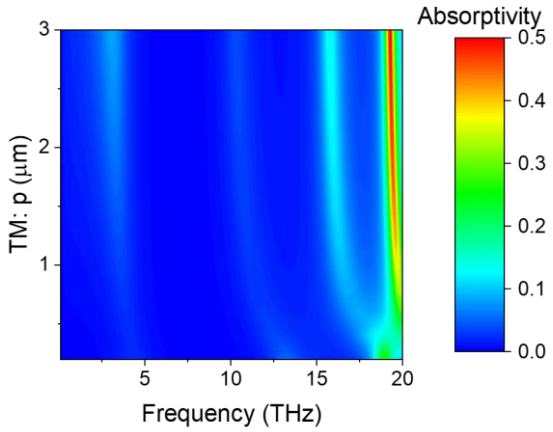

Figure C-6 2D heat map of the absorptivity of a graphitised SiC grating absorber under dimensional tunings of the period p with constant depth $d_{well} = 2\ \mu m$ and well width $w_{well} = 0.1\ \mu m$, for normally incident ($\theta = 0°$) TM waves, with adjusted absorptivity limits.

Bibliography

[1] K. S. Novoselov, A. K. Geim, S. V. Morozov, D. Jiang, Y. Zhang, S. V. Dubonos *et al.*, "Electric field effect in atomically thin carbon films," *Science,* vol. 306, no. 5696, pp. 666-9, Oct 2004.

[2] I. Forbeaux, J. M. Themlin, and J. M. Debever, "Heteroepitaxial graphite on 6H−SiC(0001): Interface formation through conduction-band electronic structure," *Phys. Rev. B,* vol. 58, no. 24, pp. 16396-16406, 1998.

[3] C. Berger, Z. Song, T. Li, X. Li, A. Y. Ogbazghi, R. Feng *et al.*, "Ultrathin epitaxial graphite: 2D electron gas properties and a route toward graphene-based nanoelectronics," *J. Phys. Chem. B,* vol. 108, no. 52, pp. 19912-19916, 2004.

[4] F. Iacopi, N. Mishra, B. V. Cunning, D. Goding, S. Dimitrijev, R. Brock *et al.*, "A catalytic alloy approach for graphene on epitaxial SiC on silicon wafers," *J. Mater. Res.,* vol. 30, no. 5, pp. 609-616, Mar 2015.

[5] A. Hussain, S. M. Mehdi, N. Abbas, M. Hussain, and R. A. Naqvi, "Synthesis of graphene from solid carbon sources: A focused review," *Mater. Chem. Phys.,* vol. 248, p. 122924, Jul 2020.

[6] X. Li, W. Cai, J. An, S. Kim, J. Nah, D. Yang *et al.*, "Large-area synthesis of high-quality and uniform graphene films on copper foils," *Science,* vol. 324, no. 5932, pp. 1312-4, Jun 2009.

[7] T. Kobayashi, M. Bando, N. Kimura, K. Shimizu, K. Kadono, N. Umezu *et al.*, "Production of a 100-m-long high-quality graphene transparent conductive film by roll-to-roll chemical vapor deposition and transfer process," *Appl. Phys. Lett.,* vol. 102, no. 2, p. 023112, 2013.

[8] M. Saeed, Y. Alshammari, S. A. Majeed, and E. Al-Nasrallah, "Chemical vapour deposition of graphene—synthesis, characterisation, and applications: A review," *Molecules,* vol. 25, no. 17, p. 3856, 2020.

[9] J. Hofrichter, B. N. Szafranek, M. Otto, T. J. Echtermeyer, M. Baus, A. Majerus *et al.*, "Synthesis of graphene on silicon dioxide by a solid carbon source," *Nano Lett.,* vol. 10, no. 1, pp. 36-42, Jan 2010.

[10] W. Xiong, Y. S. Zhou, L. J. Jiang, A. Sarkar, M. Mahjouri-Samani, Z. Q. Xie *et al.*, "Single-step formation of graphene on dielectric surfaces," *Adv. Mater.,* vol. 25, no. 4, pp. 630-634, 2013.

[11] V. P. Pham, H.-S. Jang, D. Whang, and J.-Y. Choi, "Direct growth of graphene on rigid and flexible substrates: Progress, applications, and challenges," *Chem. Soc. Rev.,* vol. 46, no. 2, pp. 6276-63, 2017.

[12] R. N. Tiwari, M. Tripathi, M. Yoshimura, and A. Kumar, "Low vacuum annealing of polymer at low temperatures towards direct and scalable growth of graphene," *Mater. Res. Bull.,* vol. 107, pp. 147-153, Nov 2018.

[13] N. Mishra, J. J. Boeckl, A. Tadich, R. T. Jones, P. J. Pigram, M. Edmonds *et al.*, "Solid source growth of graphene with Ni–Cu catalysts: Towards high qualityin situgraphene on silicon," *J. Phys. D,* vol. 50, no. 9, p. 095302, Feb 2017.

[14] D. A. Katzmarek, A. Pradeepkumar, R. W. Ziolkowski, and F. Iacopi, "Review of graphene for the generation, manipulation, and detection of electromagnetic fields from microwave to terahertz," *2D Mater.,* vol. 9, no. 2, p. 022002, Mar 2022.

[15] M. Y. Han, B. Ozyilmaz, Y. Zhang, and P. Kim, "Energy band-gap engineering of graphene nanoribbons," (in eng), *Phys. Rev. Lett.,* vol. 98, no. 20, p. 206805, May 2007.

[16] J. Sun, T. Iwasaki, M. Muruganathan, and H. Mizuta, "Lateral plasma etching enhanced on/off ratio in graphene nanoribbon field-effect transistor," *Appl. Phys. Lett.,* vol. 106, no. 3, p. 33509, 2015.
[17] S. N. Faisal and F. Iacopi, "Thin-film electrodes based on two-dimensional nanomaterials for neural interfaces," *ACS Appl. Nano Mater.,* vol. 5, no. 8, pp. 10137-10150, Aug 2022.
[18] J. Yuan, L.-P. Ma, S. Pei, J. Du, Y. Su, W. Ren *et al.*, "Tuning the electrical and optical properties of graphene by ozone treatment for patterning monolithic transparent electrodes," *ACS Nano,* vol. 7, no. 5, pp. 4233-4241, 2013.
[19] T. Wei, L. Bao, F. Hauke, and A. Hirsch, "Recent advances in graphene patterning," *ChemPlusChem,* vol. 85, no. 8, pp. 1655-1668, Aug 2020.
[20] W. Luo, W. Cai, Y. Xiang, W. Wu, B. Shi, X. Jiang *et al.*, "In-plane electrical connectivity and near-field concentration of isolated graphene resonators realized by ion beams," *Adv. Mater.,* vol. 29, no. 30, pp. 1701083-n/a, 2017.
[21] X. Xu, B. Shi, X. Zhang, Y. Liu, W. Cai, M. Ren *et al.*, "Laser direct writing of graphene nanostructures beyond the diffraction limit by graphene oxidation," *Opt. Express,* vol. 26, no. 16, pp. 20726-20734, 2018.
[22] I. I. Bobrinetskiy, A. V. Emelianov, N. Otero, and P. M. Romero, "Patterned graphene ablation and two-photon functionalization by picosecond laser pulses in ambient conditions," *Appl. Phys. Lett.,* vol. 107, no. 4, p. 43104, 2015.
[23] K. Nakagawa, H. Takahashi, Y. Shimura, and H. Maki, "A light emitter based on practicable and mass-producible polycrystalline graphene patterned directly on silicon substrates from a solid-state carbon source," *RSC Adv.,* 10.1039/C9RA07294B vol. 9, no. 65, pp. 37906-37910, 2019.
[24] K. S. Kim, Y. Zhao, H. Jang, S. Y. Lee, J. M. Kim, K. S. Kim *et al.*, "Large-scale pattern growth of graphene films for stretchable transparent electrodes," *Nature,* vol. 457, no. 7230, pp. 706-710, Feb 2009.
[25] B. V. Cunning, M. Ahmed, N. Mishra, A. R. Kermany, B. Wood, and F. Iacopi, "Graphitized silicon carbide microbeams: Wafer-level, self-aligned graphene on silicon wafers," *Nanotechnology,* vol. 25, no. 32, p. 325301, Jul 2014.
[26] P. Rufangura, I. Khodasevych, A. Agrawal, M. Bosi, T. G. Folland, J. D. Caldwell *et al.*, "Enhanced absorption with graphene-coated silicon carbide nanowires for mid-infrared nanophotonics," *Nanomaterials,* vol. 11, no. 9, p. 2339, 2021.
[27] N. Mishra, S. Jiao, A. Mondal, Z. Khan, J. J. Boeckl, K. D. Gaskill *et al.*, "A graphene platform on silicon for the Internet of Everything," in *2018 IEEE 2nd Electron Devices Technology and Manufacturing Conference (EDTM)*, Kobe, 2018: IEEE, pp. 211-213, doi: 10.1109/EDTM.2018.8421464.
[28] N. Camara, G. Rius, J. R. Huntzinger, A. Tiberj, N. Mestres, P. Godignon *et al.*, "Selective epitaxial growth of graphene on SiC," *Appl. Phys. Lett.,* vol. 93, no. 12, pp. 123503-123503-3, 2008.
[29] M. Sprinkle, M. Ruan, Y. Hu, J. Hankinson, M. Rubio-Roy, B. Zhang *et al.*, "Scalable templated growth of graphene nanoribbons on SiC," (in eng), *Nat. Nanotechnol.,* vol. 5, no. 10, pp. 727-31, Oct 2010.
[30] A. Pradeepkumar, M. Amjadipour, N. Mishra, C. Liu, M. S. Fuhrer, A. Bendavid *et al.*, "P-Type epitaxial graphene on cubic silicon carbide on silicon for integrated silicon technologies," *ACS Appl. Nano Mater.,* vol. 3, no. 1, pp. 830-841, Dec 2020.
[31] J. Krupka and W. Strupinski, "Measurements of the sheet resistance and conductivity of thin epitaxial graphene and SiC films," *Appl. Phys. Lett.,* vol. 96, no. 8, p. 082101, 2010.

[32] L. Hao, J. Gallop, S. Goniszewski, O. Shaforost, N. Klein, and R. Yakimova, "Non-contact method for measurement of the microwave conductivity of graphene," *Appl. Phys. Lett.,* vol. 103, no. 12, p. 123103, 2013.
[33] H. S. Skulason, H. V. Nguyen, A. Guermoune, V. Sridharan, M. Siaj, C. Caloz *et al.*, "110 GHz measurement of large-area graphene integrated in low-loss microwave structures," *Appl. Phys. Lett.,* vol. 99, no. 15, p. 153504, Oct 2011.
[34] H.-J. Lee, E. Kim, J.-G. Yook, and J. Jung, "Intrinsic characteristics of transmission line of graphenes at microwave frequencies," *Appl. Phys. Lett.,* vol. 100, no. 22, p. 223102, Mar 2012.
[35] S. A. Awan, A. Lombardo, A. Colli, G. Privitera, T. S. Kulmala, J. M. Kivioja *et al.*, "Transport conductivity of graphene at RF and microwave frequencies," *2D Mater.,* vol. 3, p. 015010, Feb 2016.
[36] N. Rouhi, S. Capdevila, D. Jain, K. Zand, Y. Y. Wang, E. Brown *et al.*, "Terahertz graphene optics," *Nano Res.,* vol. 5, no. 10, pp. 667-678, Sep 2012.
[37] N. Rouhi, D. Jain, S. Capdevila, L. Jofre, E. Brown, and P. J. Burke, "Broadband conductivity of graphene from DC to THz," presented at the *2011 11th IEEE International Conference on Nanotechnology*, 2011.
[38] J. S. Gómez-Díaz, J. Perruisseau-Carrier, P. Sharma, and A. Ionescu, "Non-contact characterization of graphene surface impedance at micro and millimeter waves," *J. Appl. Phys.,* vol. 111, no. 11, p. 114908, 2012.
[39] J. L. Tomaino, A. D. Jameson, J. W. Kevek, M. J. Paul, A. M. van der Zande, R. A. Barton *et al.*, "Terahertz imaging and spectroscopy of large-area single-layer graphene," *Opt. Express,* vol. 19, no. 1, pp. 141-6, Jan 2011.
[40] H. Yan, F. Xia, W. Zhu, M. Freitag, C. Dimitrakopoulos, A. A. Bol *et al.*, "Infrared spectroscopy of wafer-scale graphene," *ACS Nano,* vol. 5, no. 12, pp. 9854-60, Dec 2011.
[41] M. Liang, Z. Wu, L. Chen, L. Song, P. Ajayan, and H. Xin, "Terahertz Characterization of Single-Walled Carbon Nanotube and Graphene On-Substrate Thin Films," *IEEE Trans. Microwave Theory Tech.,* vol. 59, no. 10, pp. 2719-2725, 2011.
[42] L. Min, T. Mingguang, L. Zhen, S. Cronin, and X. Hao, "Terahertz characterization of graphene thin films on both sides of substrate," presented at the *2012 37th International Conference on Infrared, Millimeter, and Terahertz Waves*, 2012.
[43] X. Feng, M. Hu, J. Zhou, and S. Liu, "Calculation and study of graphene conductivity based on terahertz spectroscopy," *J. Infrared Millim. Terahertz Waves,* vol. 38, no. 7, pp. 874-884, 2017.
[44] L. Ren, Q. Zhang, J. Yao, Z. Sun, R. Kaneko, Z. Yan *et al.*, "Terahertz and infrared spectroscopy of gated large-area graphene," *Nano Lett.,* vol. 12, no. 7, pp. 3711-5, Jul 2012.
[45] H. Choi, F. Borondics, D. A. Siegel, S. Y. Zhou, M. C. Martin, A. Lanzara *et al.*, "Broadband electromagnetic response and ultrafast dynamics of few-layer epitaxial graphene," *Appl. Phys. Lett.,* vol. 94, no. 17, p. 172102, 2009.
[46] K. Arts, R. H. J. Vervuurt, A. Bhattacharya, J. Gómez Rivas, J. W. Oosterbeek, and A. A. Bol, "Broadband optical response of graphene measured by terahertz time-domain spectroscopy and FTIR spectroscopy," *J. Appl. Phys.,* vol. 124, no. 7, p. 73105, 2018.
[47] J. M. Dawlaty, S. Shivaraman, J. Strait, P. George, M. Chandrashekhar, F. Rana *et al.*, "Measurement of the optical absorption spectra of epitaxial graphene from terahertz to visible," *Appl. Phys. Lett.,* vol. 93, no. 13, p. 131905, 2008.
[48] J. Horng, C.-F. Chen, B. Geng, C. Girit, Y. Zhang, Z. Hao *et al.*, "Drude conductivity of Dirac fermions in graphene," *Phys. Rev. B,* vol. 83, no. 16, p. 165113, 2011.

[49] S. Dash and A. Patnaik, "Performance of graphene plasmonic antenna in comparison with their counterparts for low-terahertz applications," *Plasmonics,* vol. 13, no. 6, pp. 2353-2360, 2018.
[50] M. T. Gatte, P. J. Soh, H. A. Rahim, R. B. Ahmad, and F. Malek, "The performance improvement of Thz antenna via modeling and characterization of doped graphene," *Prog. Electromagn. Res. M,* vol. 49, pp. 21-31, Jun 2016.
[51] B. Wu, H. M. Tuncer, A. Katsounaros, W. Wu, M. T. Cole, K. Ying *et al.*, "Microwave absorption and radiation from large-area multilayer CVD graphene," *Carbon,* vol. 77, pp. 814-822, 2014.
[52] M. Grande, G. V. Bianco, D. Laneve, P. Capezzuto, V. Petruzzelli, M. Scalora *et al.*, "Optically transparent wideband CVD graphene-based microwave antennas," *Appl. Phys. Lett.,* vol. 112, no. 25, p. 251103, 2018.
[53] X. Chen, X. Liu, S. Li, W. Wang, D. Wei, Y. Wu *et al.*, "Tunable wideband slot antennas based on printable graphene inks," *Nanoscale,* 10.1039/D0NR00507J vol. 12, no. 20, pp. 10949-10955, May 2020.
[54] M. Yasir, P. Savi, S. Bistarelli, A. Cataldo, M. Bozzi, L. Perregrini *et al.*, "A planar antenna with voltage-controlled frequency tuning based on few-layer graphene," *IEEE Antennas Wirel. Propag. Lett.,* vol. 16, pp. 2380-2383, 2017.
[55] M. Tamagnone, J. S. Gómez-Díaz, J. R. Mosig, and J. Perruisseau-Carrier, "Reconfigurable terahertz plasmonic antenna concept using a graphene stack," *Appl. Phys. Lett.,* vol. 101, no. 21, p. 214102, 2012.
[56] P. Liu, W. Cai, L. Wang, X. Zhang, and J. Xu, "Tunable terahertz optical antennas based on graphene ring structures," *Appl. Phys. Lett.,* vol. 100, no. 15, pp. 153111-153111-5, 2012.
[57] L. Anzi, A. Mansouri, P. Pedrinazzi, E. Guerriero, M. Fiocco, A. Pesquera *et al.*, "Ultra-low contact resistance in graphene devices at the Dirac point," *2D Mater.,* vol. 5, no. 2, p. 025014, Feb 2018.
[58] A. Hsu, H. Wang, K. K. Kim, J. Kong, and T. Palacios, "Impact of graphene interface quality on contact resistance and RF device performance," *IEEE Electron Device Lett.,* vol. 32, no. 8, pp. 1008-1010, Jun 2011.
[59] R. L. Jackson, E. R. Crandall, and M. J. Bozack, "Rough surface electrical contact resistance considering scale dependent properties and quantum effects," *J. Appl. Phys.,* vol. 117, no. 19, p. 195101, 2015.
[60] L. Kogut and K. Komvopoulos, "Electrical contact resistance theory for conductive rough surfaces," *J. Appl. Phys.,* vol. 94, no. 5, pp. 3153-3162, 2003.
[61] X. Hai-qiang, P. Qin-Xu, H. Jun, and Y. Wen-Yan, "Design of a novel graphene terahertz antenna at 500GHz with reconfigurable radiation pattern," presented at the *2015 IEEE International Symposium on Antennas and Propagation & USNC/URSI National Radio Science Meeting*, Vancouver, 2015.
[62] J. S. Gomez-Diaz, M. Esquius-Morote, and J. Perruisseau-Carrier, "Plane wave excitation-detection of non-resonant plasmons along finite-width graphene strips," *Opt. Express,* vol. 21, no. 21, pp. 24856-72, Oct 2013.
[63] M. Esquius-Morote, J. S. Gomez-Diaz, and J. Perruisseau-Carrier, "Sinusoidally modulated graphene leaky-wave antenna for electronic beamscanning at THz," *IEEE Trans. Terahertz Sci. Technol.,* vol. 4, no. 1, pp. 116-122, 2014.
[64] W. Fuscaldo, P. Burghignoli, P. Baccarelli, and A. Galli, "Graphene Fabry–Perot cavity leaky-wave antennas: Plasmonic versus nonplasmonic solutions," *IEEE Trans. Antennas Propag.,* vol. 65, no. 4, pp. 1651-1660, 2017.

[65] B. Hähnlein, B. Händel, J. Pezoldt, H. Töpfer, R. Granzner, and F. Schwierz, "Side-gate graphene field-effect transistors with high transconductance," *Appl. Phys. Lett.,* vol. 101, no. 9, p. 93504, 2012.
[66] L. Long, X. Ying, Y. Yang, and L. Wang, "Tuning the infrared absorption of SiC metasurfaces by electrically gating monolayer graphene with solid polymer electrolyte for dynamic radiative thermal management and sensing applications," *ACS Appl. Nano Mater.,* vol. 2, no. 8, pp. 4810-4817, 2019.
[67] L. Ju, B. Geng, J. Horng, C. Girit, M. Martin, Z. Hao *et al.*, "Graphene plasmonics for tunable terahertz metamaterials," *Nat. Nanotechnol.,* vol. 6, no. 10, pp. 630-634, 2011.
[68] M. Masyukov, A. Vozianova, A. Grebenchukov, K. Gubaidullina, A. Zaitsev, and M. Khodzitsky, "Optically tunable terahertz chiral metasurface based on multi-layered graphene," *Sci. Rep.,* vol. 10, no. 1, p. 3157, Feb 2020.
[69] S. Arezoomandan, H. Condori Quispe, A. Chanana, P. Gopalan, S. Banerji, A. Nahata *et al.*, "Graphene–dielectric integrated terahertz metasurfaces," *Semicond. Sci. Technol.,* vol. 33, no. 10, p. 104007, Sep 2018.
[70] H. Soleimani and H. Oraizi, "A novel 2D leaky wave antenna based on complementary graphene patch cell," *J. Phys. D,* vol. 53, no. 25, p. 255301, 2020.
[71] Z. Chang, B. You, L.-S. Wu, M. Tang, Y.-P. Zhang, and J.-F. Mao, "A reconfigurable graphene reflectarray for generation of vortex THz waves," *IEEE Antennas Wirel. Propag. Lett.,* vol. 15, pp. 1537-1540, 2016.
[72] Z. Bao, J. Wang, Z. D. Hu, A. Balmakou, S. Khakhomov, Y. Tang *et al.*, "Coordinated multi-band angle insensitive selection absorber based on graphene metamaterials," *Opt. Express,* vol. 27, no. 22, pp. 31435-31445, Oct 2019.
[73] S. E. Hosseininejad, K. Rouhi, M. Neshat, R. Faraji-Dana, A. Cabellos-Aparicio, S. Abadal *et al.*, "Reprogrammable graphene-based metasurface mirror with adaptive focal point for THz imaging," *Sci. Rep.,* vol. 9, no. 1, p. 2868, Feb 2019.
[74] X.-C. Wang, W.-S. Zhao, J. Hu, and W.-Y. Yin, "Reconfigurable terahertz leaky-wave antenna using graphene-based high-impedance surface," *IEEE Trans. Nanotechnol.,* vol. 14, no. 1, pp. 62-69, 2015.
[75] B. Zhao, J. M. Zhao, and Z. M. Zhang, "Enhancement of near-infrared absorption in graphene with metal gratings," *Appl. Phys. Lett.,* vol. 105, no. 3, p. 31905, 2014.
[76] A. C. Neto, F. Guinea, and N. M. Peres, "Drawing conclusions from graphene," *Phys. World,* vol. 19, no. 11, pp. 33-37, Now 2006.
[77] A. P. Kauling, A. T. Seefeldt, D. P. Pisoni, R. C. Pradeep, R. Bentini, R. V. B. Oliveira *et al.*, "The worldwide graphene flake production," *Adv. Mater.,* vol. 30, no. 44, p. 1803784, 2018.
[78] A. H. Castro Neto, F. Guinea, N. M. R. Peres, K. S. Novoselov, and A. K. Geim, "The electronic properties of graphene," *Rev. Mod. Phys.,* vol. 81, no. 1, pp. 109-162, 2009.
[79] P. R. Wallace, "The band theory of graphite," *Phys. Rev.,* vol. 71, no. 9, pp. 622-634, 1947.
[80] J. H. Chen, C. Jang, S. Xiao, M. Ishigami, and M. S. Fuhrer, "Intrinsic and extrinsic performance limits of graphene devices on SiO2," *Nat. Nanotechnol.,* vol. 3, no. 4, pp. 206-9, Apr 2008.
[81] V. E. Dorgan, M.-H. Bae, and E. Pop, "Mobility and saturation velocity in graphene on SiO2," *Appl. Phys. Lett.,* vol. 97, no. 8, p. 082112, 2010.
[82] Y. Wu, K. A. Jenkins, A. Valdes-Garcia, D. B. Farmer, Y. Zhu, A. A. Bol *et al.*, "State-of-the-art graphene high-frequency electronics," *Nano Lett.,* vol. 12, no. 6, pp. 3062-7, Jun 2012.
[83] F. V. Kusmartsev, W. M. Wu, M. P. Pierpoint, and K. C. Yung, "Application of graphene within optoelectronic devices and transistors," in *Applied Spectroscopy and*

the Science of Nanomaterials, P. Misra Ed. Singapore: Springer Singapore, 2015, pp. 191-221.
[84] A. K. Geim and K. S. Novoselov, "The rise of graphene," *Nat. Mater.,* vol. 6, no. 3, pp. 183-91, Mar 2007.
[85] V. P. Gusynin and S. G. Sharapov, "Unconventional integer quantum Hall effect in graphene," *Phys. Rev. Lett.,* vol. 95, no. 14, p. 146801, Sep 2005.
[86] V. P. Gusynin and S. G. Sharapov, "Transport of Dirac quasiparticles in graphene: Hall and optical conductivities," *Phys. Rev. B,* vol. 73, no. 24, p. 245411, 2006.
[87] L. A. Falkovsky and A. A. Varlamov, "Space-time dispersion of graphene conductivity," *Eur. Phys. J. B,* vol. 56, no. 4, pp. 281-284, 2007.
[88] V. P. Gusynin, S. G. Sharapov, and J. P. Carbotte, "Magneto-optical conductivity in graphene," *J. Phys. Condens. Matter,* vol. 19, no. 2, p. 026222, 2007.
[89] G. W. Hanson, "Dyadic Green's functions and guided surface waves for a surface conductivity model of graphene," *J. Appl. Phys.,* vol. 103, no. 6, p. 064302, 2008.
[90] M. Jablan, H. Buljan, and M. Soljačić, "Plasmonics in graphene at infrared frequencies," *Phys. Rev. B,* vol. 80, no. 24, p. 245435, 2009.
[91] B. Vasic, G. Isic, and R. Gajic, "Localized surface plasmon resonances in graphene ribbon arrays for sensing of dielectric environment at infrared frequencies," *J. Appl. Phys.,* vol. 113, no. 1, p. 13110, 2013.
[92] F. J. G. de Abajo, "Graphene plasmonics: Challenges and opportunities," *ACS Photonics,* vol. 1, no. 3, pp. 135-152, 2014.
[93] Z. Fei, A. S. Rodin, M. M. Fogler, A. H. Castro, C. N. Lau, F. Keilmann *et al.*, "Gate-tuning of graphene plasmons revealed by infrared nano-imaging," *Nature,* vol. 487, no. 7405, pp. 82-85, 2012.
[94] C. Jianing, M. Badioli, A. Zurutuza Elorza, N. Camara, F. J. Garcia De Abajo, R. Hillenbrand *et al.*, "Optical nano-imaging of gate-tunable graphene plasmons," *Nature,* vol. 487, no. 7405, pp. 77-81, 2012.
[95] A. Barua, M. S. Hossain, K. I. Masood, and S. Subrina, "Thermal management in 3-D integrated circuits with graphene heat spreaders," *Phys. Procedia,* vol. 25, pp. 311-316, 2012.
[96] A. A. Balandin, S. Ghosh, W. Bao, I. Calizo, D. Teweldebrhan, F. Miao *et al.*, "Superior thermal conductivity of single-layer graphene," *Nano Lett.,* vol. 8, no. 3, pp. 902-7, Mar 2008.
[97] C. Lee, X. Wei, J. W. Kysar, and J. Hone, "Measurement of the elastic properties and intrinsic strength of monolayer graphene," *Science,* vol. 321, no. 5887, pp. 385-8, Jul 2008.
[98] K. S. Novoselov, V. I. Fal'ko, L. Colombo, P. R. Gellert, M. G. Schwab, and K. Kim, "A roadmap for graphene," *Nature,* vol. 490, no. 7419, pp. 192-200, Oct 2012.
[99] S. E. Hosseininejad, M. Neshat, R. Faraji-Dana, M. Lemme, P. Haring Bolivar, A. Cabellos-Aparicio *et al.*, "Reconfigurable THz plasmonic antenna based on few-layer graphene with high radiation efficiency," *Nanomaterials,* vol. 8, no. 8, p. 577, Jul 2018.
[100] A. Pradeepkumar, D. K. Gaskill, and F. Iacopi, "Electronic and transport properties of epitaxial graphene on SiC and 3C-SiC/Si: A review," *Appl. Sci.,* vol. 10, no. 12, p. 4350, 2020.
[101] X. Xu, Z. Zhang, J. Dong, D. Yi, J. Niu, M. Wu *et al.*, "Ultrafast epitaxial growth of metre-sized single-crystal graphene on industrial Cu foil," *Sci. Bull.,* vol. 62, no. 15, pp. 1074-1080, 2017.
[102] Z.-Y. Juang, C.-Y. Wu, C.-W. Lo, W.-Y. Chen, C.-F. Huang, J.-C. Hwang *et al.*, "Synthesis of graphene on silicon carbide substrates at low temperature," *Carbon,* vol. 47, no. 8, pp. 2026-2031, 2009.

[103] L. Wang, S. Dimitrijev, J. Han, A. Iacopi, L. Hold, P. Tanner *et al.*, "Growth of 3C–SiC on 150-mm Si(100) substrates by alternating supply epitaxy at 1000 °C," *Thin Solid Films,* vol. 519, no. 19, pp. 6443-6446, 2011.
[104] V. Y. Aristov, G. Urbanik, K. Kummer, D. V. Vyalikh, O. V. Molodtsova, A. B. Preobrajenski *et al.*, "Graphene synthesis on cubic SiC/Si wafers. perspectives for mass production of graphene-based electronic devices," *Nano Lett.,* vol. 10, no. 3, pp. 992-5, Mar 2010.
[105] M. Suemitsu and H. Fukidome, "Epitaxial graphene on silicon substrates," *J. Phys. D,* vol. 43, no. 37, p. 374012, Sep 2010.
[106] H. Fukidome, T. Kinoshita, T. Otsuji, M. Suemitsu, Y. Kawai, H. Handa *et al.*, "Site-selective epitaxy of graphene on Si wafers," *Proc. IEEE,* vol. 101, no. 7, pp. 1557-1566, 2013.
[107] B. Gupta, M. Notarianni, N. Mishra, M. Shafiei, F. Iacopi, and N. Motta, "Evolution of epitaxial graphene layers on 3C SiC/Si (111) as a function of annealing temperature in UHV," *Carbon,* vol. 68, pp. 563-572, 2014.
[108] M. Suemitsu, Y. Miyamoto, H. Handa, and A. Konno, "Graphene formation on a 3C-SiC(111) thin film grown on Si(110) substrate," *E-J. Surf. Sci. Nanotechnol.,* vol. 7, pp. 311-313, 2009.
[109] J. S. Moon, D. Curtis, M. Hu, D. Wong, C. McGuire, P. M. Campbell *et al.*, "Epitaxial-graphene RF field-effect transistors on Si-face 6H-SiC substrates," *IEEE Electron Device Lett.,* vol. 30, no. 6, pp. 650-652, 2009.
[110] Y. Hernandez, V. Nicolosi, M. Lotya, F. M. Blighe, Z. Sun, S. De *et al.*, "High-yield production of graphene by liquid-phase exfoliation of graphite," *Nat. Nanotechnol.,* vol. 3, no. 9, pp. 563-8, Sep 2008.
[111] X. Huang, T. Leng, M. Zhu, X. Zhang, J. Chen, K. Chang *et al.*, "Highly flexible and conductive printed graphene for wireless wearable communications applications," *Sci. Rep.,* vol. 5, no. 1, p. 18298, Dec 2015.
[112] X. Huang, T. Leng, X. Zhang, J. C. Chen, K. H. Chang, A. K. Geim *et al.*, "Binder-free highly conductive graphene laminate for low cost printed radio frequency applications," *Appl. Phys. Lett.,* vol. 106, no. 20, p. 203105, 2015.
[113] K. Pan, Y. Fan, T. Leng, J. Li, Z. Xin, J. Zhang *et al.*, "Sustainable production of highly conductive multilayer graphene ink for wireless connectivity and IoT applications," *Nat. Commun.,* vol. 9, no. 1, p. 5197, Dec 2018.
[114] R. Song, C. Liu, J. Zhang, C. Liu, D. He, and Z. Wu, "Flexible graphene based films for microstrip array antennas," in *2017 Sixth Asia-Pacific Conference on Antennas and Propagation (APCAP)*, Xi'an, 2017: IEEE, pp. 1-3, doi: 10.1109/APCAP.2017.8420634.
[115] S. N. H. Sa'don, M. R. Kamarudin, F. Ahmad, M. Jusoh, and H. A. Majid, "Graphene array antenna for 5G applications," *Appl. Phys. A,* vol. 123, no. 2, pp. 1-4, 2017.
[116] L. Jiao, L. Zhang, X. Wang, G. Diankov, and H. Dai, "Narrow graphene nanoribbons from carbon nanotubes," (in eng), *Nature,* vol. 458, no. 7240, pp. 877-80, Apr 2009.
[117] S. Pang, H. N. Tsao, X. Feng, and K. Müllen, "Patterned graphene electrodes from solution-processed graphite oxide films for organic field-effect transistors," *Adv. Mater.,* vol. 21, no. 34, pp. 3488-3491, 2009.
[118] M. C. Prado, D. Jariwala, T. J. Marks, and M. C. Hersam, "Optimization of graphene dry etching conditions via combined microscopic and spectroscopic analysis," *Appl. Phys. Lett.,* vol. 102, no. 19, p. 193111, 2013.
[119] Y. Zheng, H. Wang, S. Hou, and D. Xia, "Lithographically defined graphene patterns," *Adv. Mater. Technol.,* vol. 2, no. 5, p. 1600237, 2017.

[120] J. Wang and J. Du, "Plasmonic and dielectric metasurfaces: Design, fabrication and applications," *Appl. Sci.,* vol. 6, no. 9, p. 239, 2016.
[121] W. S. Hwang, K. Tahy, X. Li, H. Xing, A. C. Seabaugh, C. Y. Sung *et al.*, "Transport properties of graphene nanoribbon transistors on chemical-vapor-deposition grown wafer-scale graphene," *Appl. Phys. Lett.,* vol. 100, no. 20, pp. 203107-203107-3, 2012.
[122] W. S. Hwang, K. Tahy, L. O. Nyakiti, V. D. Wheeler, R. L. Myers-Ward, C. R. Eddy *et al.*, "Fabrication of top-gated epitaxial graphene nanoribbon FETs using hydrogen-silsesquioxane," *Journal of Vacuum Science & Technology B,* vol. 30, no. 3, p. 3, 2012.
[123] T. Wei, F. Hauke, and A. Hirsch, "Evolution of graphene patterning: From dimension regulation to molecular engineering," *Adv. Mater.,* vol. 33, no. 45, p. 2104060, 2021.
[124] A. Choi, A. T. Hoang, T. T. Ngoc Van, B. Shong, L. Hu, K. You Thai *et al.*, "Residue-free photolithographic patterning of graphene," *J. Chem. Eng.,* vol. 429, p. 132504, Feb 2022.
[125] C. X. Cong, T. Yu, Z. H. Ni, L. Liu, Z. X. Shen, and W. Huang, "Fabrication of graphene nanodisk arrays using nanosphere lithography," *J. Phys. Chem. C,* vol. 113, no. 16, pp. 6529-6532, Apr 2009.
[126] J. Bai, X. Duan, and Y. Huang, "Rational fabrication of graphene nanoribbons using a nanowire etch mask," (in eng), *Nano Lett.,* vol. 9, no. 5, pp. 2083-7, May 2009.
[127] C. Liu, B. Yao, T. Dong, H. Ma, S. Zhang, J. Wang *et al.*, "Highly stretchable graphene nanoribbon springs by programmable nanowire lithography," *NPJ 2D Mater. Appl.,* vol. 3, no. 1, p. 23, Mar 2019.
[128] Y. K. Lee, H. Choi, C. Lee, H. Lee, K. C. Goddeti, S. Y. Moon *et al.*, "Charge transport-driven selective oxidation of graphene," (in eng), *Nanoscale,* vol. 8, no. 22, pp. 11494-502, Jun 2016.
[129] L. Wang, J. Zhang, N. Liu, Y. Wang, P. Hu, and Z. Wang, "Fast patterned graphene ribbons via soft–lithography," *Procedia CIRP,* vol. 42, pp. 428-432, Jan 2016.
[130] M. W. Jung, S. Myung, K. W. Kim, W. Song, Y. Y. Jo, S. S. Lee *et al.*, "Fabrication of graphene-based flexible devices utilizing a soft lithographic patterning method," (in eng), *Nanotechnology,* vol. 25, no. 28, p. 285302, Jul 2014.
[131] C. Wang, K. J. Morton, Z. Fu, W. D. Li, and S. Y. Chou, "Printing of sub-20 nm wide graphene ribbon arrays using nanoimprinted graphite stamps and electrostatic force assisted bonding," (in eng), *Nanotechnology,* vol. 22, no. 44, p. 445301, Nov 2011.
[132] X. Liang, Y. S. Jung, S. Wu, A. Ismach, D. L. Olynick, S. Cabrini *et al.*, "Formation of bandgap and subbands in graphene nanomeshes with sub-10 nm ribbon width fabricated via nanoimprint lithography," (in eng), *Nano Lett.,* vol. 10, no. 7, pp. 2454-60, Jul 2010.
[133] M. E. P. Tweedie, C. S. Lau, L. Hou, X. Wang, Y. Sheng, and J. H. Warner, "Transparent ultrathin all-two-dimensional lateral Gr:WS2:Gr photodetector arrays on flexible substrates and their strain induced failure mechanisms," *Mater. Today,* vol. 6, p. 100067, Jun 2020.
[134] A. I. Dago, S. Sangiao, R. Fernández-Pacheco, J. M. De Teresa, and R. Garcia, "Chemical and structural analysis of sub-20 nm graphene patterns generated by scanning probe lithography," *Carbon,* vol. 129, pp. 281-285, 2018.
[135] M. Zhang, M. Yang, Y. Okigawa, T. Yamada, H. Nakajima, Y. Iizumi *et al.*, "Patterning of graphene using wet etching with hypochlorite and UV light," *Sci. Rep.,* vol. 12, no. 1, p. 4541, Mar 2022.
[136] S. Konishi, W. Sugimoto, Y. Murakami, and Y. Takasu, "Catalytic creation of channels in the surface layers of highly oriented pyrolytic graphite by cobalt nanoparticles," *Carbon,* vol. 44, no. 11, pp. 2338-2340, Sep 2006.

[137] N. Severin, S. Kirstein, I. M. Sokolov, and J. P. Rabe, "Rapid trench channeling of graphenes with catalytic silver nanoparticles," (in eng), *Nano Lett.,* vol. 9, no. 1, pp. 457-61, Jan 2009.
[138] G. Cheng, I. Calizo, and A. R. Hight Walker, "Metal-catalyzed etching of graphene governed by metal–carbon interactions: A comparison of Fe and Cu," *Carbon,* vol. 81, pp. 678-687, Jan 2015.
[139] P. Solís-Fernández, K. Yoshida, Y. Ogawa, M. Tsuji, and H. Ago, "Dense arrays of highly aligned graphene nanoribbons produced by substrate-controlled metal-assisted etching of graphene," (in eng), *Adv. Mater.,* vol. 25, no. 45, pp. 6562-8, Dec 2013.
[140] L. C. Campos, V. R. Manfrinato, J. D. Sanchez-Yamagishi, J. Kong, and P. Jarillo-Herrero, "Anisotropic etching and nanoribbon formation in single-layer graphene," *Nano Lett.,* vol. 9, no. 7, pp. 2600-2604, 2009.
[141] G. Cheng, I. Calizo, C. A. Hacker, C. A. Richter, and A. R. Hight Walker, "Fe-catalyzed etching of exfoliated graphite through carbon hydrogenation," (in eng), *Carbon,* vol. 96, pp. 311-315, Jan 2016.
[142] L. Ci, Z. Xu, L. Wang, W. Gao, F. Ding, K. F. Kelly *et al.*, "Controlled nanocutting of graphene," *Nano Res.,* vol. 1, no. 2, pp. 116-122, Aug 2008.
[143] L. Gao, W. Ren, B. Liu, Z. S. Wu, C. Jiang, and H. M. Cheng, "Crystallographic tailoring of graphene by nonmetal SiO(x) nanoparticles," (in eng), *J. Am. Chem. Soc.,* vol. 131, no. 39, pp. 13934-6, Oct 2009.
[144] D. V. Kosynkin, A. L. Higginbotham, A. Sinitskii, J. R. Lomeda, A. Dimiev, B. K. Price *et al.*, "Longitudinal unzipping of carbon nanotubes to form graphene nanoribbons," (in eng), *Nature,* vol. 458, no. 7240, pp. 872-6, Apr 2009.
[145] Y. S. Li, J. L. Liao, S. Y. Wang, and W. H. Chiang, "Intercalation-assisted longitudinal unzipping of carbon nanotubes for green and scalable synthesis of graphene nanoribbons," (in eng), *Sci. Rep.,* vol. 6, p. 22755, Mar 2016.
[146] D. B. Shinde, M. Majumder, and V. K. Pillai, "Counter-ion dependent, longitudinal unzipping of multi-walled carbon nanotubes to highly conductive and transparent graphene nanoribbons," (in eng), *Sci. Rep.,* vol. 4, p. 4363, Mar 2014.
[147] L. Jiao, X. Wang, G. Diankov, H. Wang, and H. Dai, "Facile synthesis of high-quality graphene nanoribbons," (in eng), *Nat. Nanotechnol.,* vol. 5, no. 5, pp. 321-5, May 2010.
[148] R. S. Singh, V. Nalla, W. Chen, A. T. Wee, and W. Ji, "Laser patterning of epitaxial graphene for Schottky junction photodetectors," (in eng), *ACS Nano,* vol. 5, no. 7, pp. 5969-75, Jul 2011.
[149] J. Ye, H. Tan, S. Wu, K. Ni, F. Pan, J. Liu *et al.*, "Direct laser writing of graphene made from chemical vapor deposition for flexible, integratable micro-supercapacitors with ultrahigh power output," *Adv. Mater.,* vol. 30, no. 27, pp. e1801384-n/a, 2018.
[150] T. He, Y. Yi, C.-H. Zhang, Z. Yuegang, X. I. E. Dan, T.-L. Ren *et al.*, "Laser directed lithography of asymmetric graphene ribbons on a polydimethylsiloxane trench structure," *Phys. Chem. Chem. Phys.,* vol. 15, no. 18, pp. 6825-6830, 2013.
[151] J. Aumanen, A. Johansson, J. Koivistoinen, P. Myllyperkiö, and M. Pettersson, "Patterning and tuning of electrical and optical properties of graphene by laser induced two-photon oxidation," *Nanoscale,* vol. 7, no. 7, pp. 2851-2855, 2015.
[152] M. C. Lemme, D. C. Bell, J. R. Williams, L. A. Stern, B. W. Baugher, P. Jarillo-Herrero *et al.*, "Etching of graphene devices with a helium ion beam," (in eng), *ACS Nano,* vol. 3, no. 9, pp. 2674-6, Sep 2009.
[153] L. Scipioni, L. Stern, and J. Notte, "Applications of the helium ion microscope," *Micros. Today,* vol. 15, no. 6, pp. 12-15, 2007.

[154] N. Kalhor, S. A. Boden, and H. Mizuta, "Sub-10nm patterning by focused He-ion beam milling for fabrication of downscaled graphene nano devices," *Microelectron. Eng.,* vol. 114, pp. 70-77, Feb 2014.
[155] Y. Naitou and S. Ogawa, "Anderson localization of graphene by helium ion irradiation," *Appl. Phys. Lett.,* vol. 108, no. 17, p. 171605, 2016.
[156] D. Tosic, Z. Markovic, S. Jovanovic, J. Prekodravac, M. Budimir, D. Kepic *et al.*, "Rapid thermal annealing of nickel-carbon nanowires for graphene nanoribbons formation," *Synth. Met.,* vol. 218, pp. 43-49, Aug 2016.
[157] T. Kato and R. Hatakeyama, "Site- and alignment-controlled growth of graphene nanoribbons from nickel nanobars," (in eng), *Nat. Nanotechnol.,* vol. 7, no. 10, pp. 651-6, Oct 2012.
[158] Z. Yan, Y. Liu, J. Lin, Z. Peng, G. Wang, E. Pembroke *et al.*, "Hexagonal graphene onion rings," (in eng), *J. Am. Chem. Soc.,* vol. 135, no. 29, pp. 10755-62, Jul 2013.
[159] M. D. S. Lakshad Wimalananda, J. K. Kim, and J. M. Lee, "Selective growth of monolayer and bilayer graphene patterns by a rapid growth method," (in eng), *Nanoscale,* vol. 11, no. 14, pp. 6727-6736, Apr 2019.
[160] H. Lim, J. Jung, H. J. Yang, and Y. Kim, "Lattice-contraction-induced Moiré patterns in direction-controlled epitaxial graphene on Cu(111)," *Adv. Mater. Interfaces,* vol. 1, no. 2, p. 1300080, 2014.
[161] X. Zhou, Y. Qi, J. Shi, J. Niu, M. Liu, G. Zhang *et al.*, "Modulating the electronic properties of monolayer graphene using a periodic quasi-one-dimensional potential generated by hex-reconstructed Au(001)," (in eng), *ACS Nano,* vol. 10, no. 8, pp. 7550-7, Aug 2016.
[162] J. M. Ha, H. San Lim, J. W. Park, H. J. Kim, and S. O. Cho, "Freestanding graphene nanosheets and large-area/patterned graphene nanofilms from indium-catalyzed graphite," *RSC Adv.,* 10.1039/C6RA08526A vol. 6, no. 50, pp. 44788-44793, 2016.
[163] R. M. Jacobberger, B. Kiraly, M. Fortin-Deschenes, P. L. Levesque, K. M. McElhinny, G. J. Brady *et al.*, "Direct oriented growth of armchair graphene nanoribbons on germanium," (in eng), *Nat. Commun.,* vol. 6, p. 8006, Aug 2015.
[164] J. K. Choi, J. Kwak, S. D. Park, H. D. Yun, S. Y. Kim, M. Jung *et al.*, "Growth of wrinkle-free graphene on texture-controlled platinum films and thermal-assisted transfer of large-scale patterned graphene," (in eng), *ACS Nano,* vol. 9, no. 1, pp. 679-86, Jan 2015.
[165] D. A. Katzmarek, A. Mancini, S. A. Maier, and F. Iacopi, "Direct synthesis of nanopatterned epitaxial graphene on silicon carbide," *Nanotechnology,* vol. 34, no. 40, p. 405302, Jul 2023.
[166] A. Narita, X. Feng, Y. Hernandez, S. A. Jensen, M. Bonn, H. Yang *et al.*, "Synthesis of structurally well-defined and liquid-phase-processable graphene nanoribbons," (in eng), *Nat. Chem.,* vol. 6, no. 2, pp. 126-32, Feb 2014.
[167] K.-Y. Yoon and G. Dong, "Liquid-phase bottom-up synthesis of graphene nanoribbons," *Mater. Chem. Front.,* vol. 4, no. 1, pp. 29-45, 2020.
[168] B. Shi, W. Cai, X. Zhang, Y. Xiang, Y. Zhan, J. Geng *et al.*, "Tunable band-stop filters for graphene plasmons based on periodically modulated graphene," *Sci. Rep.,* vol. 6, no. 1, pp. 26796-26796, 2016.
[169] X. Xu, C. Wang, Y. Liu, X. Wang, N. Gong, Z. Zhu *et al.*, "A graphene P-N junction induced by single-gate control of dielectric structures," *J. Mater. Chem. C,* vol. 7, no. 29, pp. 8796-882, 2019.
[170] A. Vakil and N. Engheta, "Transformation optics using graphene," *Science,* vol. 332, no. 6035, pp. 1291-1294, 2011.

[171] J. Krupka, W. Strupinski, and N. Kwietniewski, "Microwave conductivity of very thin graphene and metal films," *J. Nanosci. Nanotechnol.,* vol. 11, no. 4, pp. 3358-62, Apr 2011.
[172] M. B. Klarskov, H. F. Dam, D. H. Petersen, T. M. Hansen, A. Lowenborg, T. J. Booth *et al.*, "Fast and direct measurements of the electrical properties of graphene using micro four-point probes," *Nanotechnology,* vol. 22, no. 44, p. 445702, Nov 2011.
[173] A. Pradeepkumar, M. Amjadipour, N. Mishra, C. Liu, M. S. Fuhrer, A. Bendavid *et al.*, "p-type Epitaxial Graphene on Cubic Silicon Carbide on Silicon for Integrated Silicon Technologies," *ACS Applied Nano Materials,* vol. 3, no. 1, 2019.
[174] H. Cho and D. E. Burk, "A three-step method for the de-embedding of high-frequency S-parameter measurements," *IEEE Trans. Electron Devices,* vol. 38, no. 6, pp. 1371-1375, 1991.
[175] M. C. A. M. Koolen, J. A. M. Geelen, and M. P. J. G. Versleijen, "An improved de-embedding technique for on-wafer high-frequency characterization," in *Proceedings of the 1991 Bipolar Circuits and Technology Meeting*, 1991: IEEE, pp. 188-191, doi: 10.1109/BIPOL.1991.160985.
[176] E. P. Vandamme, D. M. M. P. Schreurs, and G. Van Dinther, "Improved three-step de-embedding method to accurately account for the influence of pad parasitics in silicon on-wafer RF test-structures," *IEEE Trans. Electron Devices,* vol. 48, no. 4, pp. 737-742, 2001.
[177] C. N. Santos, F. Joucken, D. De Sousa Meneses, P. Echegut, J. Campos-Delgado, P. Louette *et al.*, "Terahertz and mid-infrared reflectance of epitaxial graphene," *Sci. Rep.,* vol. 6, no. 1, p. 24301, Apr 2016.
[178] C. A. Balanis, *Modern Antenna Handbook*. Oxford: Wiley-Blackwell, 2008.
[179] G. J. Nissiyah and M. G. Madhan, "Graphene-based photoconductive antenna structures for directional terahertz emission," *Plasmonics,* vol. 14, no. 4, pp. 891-900, 2018.
[180] S. Kosuga, R. Suga, O. Hashimoto, and S. Koh, "Graphene-based optically transparent dipole antenna," *Appl. Phys. Lett.,* vol. 110, no. 23, p. 233102, 2017.
[181] S. Kosuga, K. Suga, R. Suga, T. Watanabe, O. Hashimoto, and S. Koh, "Radiation characteristics of optically transparent dipole antenna fabricated using CVD monolayer graphene," presented at the *2018 Asia-Pacific Microwave Conference (APMC)*, Kyoto, 2018.
[182] H.-R. Zu, B. Wu, Y.-H. Zhang, Y.-T. Zhao, R.-G. Song, and D.-P. He, "Circularly polarized wearable antenna with low profile and low specific absorption Rate using highly conductive graphene film," *IEEE Antennas Wirel. Propag. Lett.,* vol. 19, no. 12, pp. 2354-2358, 2020.
[183] R. Goyal and D. K. Vishwakarma, "Design of a graphene-based patch antenna on glass substrate for high-speed terahertz communications," *Microw. Opt. Technol. Lett.,* vol. 60, no. 7, pp. 1594-1600, 2018.
[184] S. K. Tripathi, M. Kumar, and A. Kumar, "Graphene based tunable and wideband terahertz antenna for wireless network communication," *Wirel. Netw.,* vol. 25, no. 7, pp. 4371-4381, 2019.
[185] M. Dragoman, A. A. Muller, D. Dragoman, F. Coccetti, and R. Plana, "Terahertz antenna based on graphene," *J. Appl. Phys.,* vol. 107, no. 10, p. 104313, 2010.
[186] Y. Luo, Q. Zeng, X. Yan, Y. Wu, Q. Lu, C. Zheng *et al.*, "Graphene-based multi-beam reconfigurable THz antennas," *IEEE Access,* vol. 7, pp. 30802-30808, 2019.
[187] T. Cusati, G. Fiori, A. Gahoi, V. Passi, M. C. Lemme, A. Fortunelli *et al.*, "Electrical properties of graphene-metal contacts," *Sci. Rep.,* vol. 7, no. 1, p. 5109, Jul 2017.

[188] D. Neumaier and H. Zirath, "High frequency graphene transistors: can a beauty become a cash cow?," *2D Mater.,* vol. 2, no. 3, p. 030203, Jul 2015.
[189] H. Lyu, Q. Lu, J. Liu, X. Wu, J. Zhang, J. Li *et al.*, "Deep-submicron graphene field-effect transistors with state-of-art fmax," *Sci. Rep.,* vol. 6, no. 1, p. 35717, Oct 2016.
[190] J. Jiang, J. Kang, W. Cao, X. Xie, H. Zhang, J. H. Chu *et al.*, "Intercalation doped multilayer-graphene-nanoribbons for next-generation interconnects," *Nano Lett.,* vol. 17, no. 3, pp. 1482-1488, Mar 2017.
[191] Q. Qiaofeng, W. Zidong, J. Yuehui, P. Pei, G. Xin, R. Liming *et al.*, "Impacts of dimensions, number of layers and contact structures on the loss of graphene-based coplanar waveguides through simulations," in *2015 IEEE 16th International Conference on Communication Technology (ICCT)*, 2015, pp. 255-257, doi: 10.1109/ICCT.2015.7399836.
[192] A. Katsounaros, M. T. Cole, H. M. Tuncer, W. I. Milne, and Y. Hao, "Near-field characterization of chemical vapor deposition graphene in the microwave regime," *Appl. Phys. Lett.,* vol. 102, no. 23, p. 233104, 2013.
[193] C. A. Balanis, *Antenna Theory : Analysis and Design*, 4th ed. Hoboken: Wiley, 2015.
[194] M. Dragoman, D. Neculoiu, A.-C. Bunea, G. Deligeorgis, M. Aldrigo, D. Vasilache *et al.*, "A tunable microwave slot antenna based on graphene," *Appl. Phys. Lett.,* vol. 106, no. 15, p. 153101, 2015.
[195] N. Guan, H. Furuya, D. Delaune, and K. Ito, "Antennas made of transparent conductive films," *Prog. Electromagn. Res. Symp.,* vol. 4, no. 1, pp. 116-120, 2008.
[196] Y. Yao, W. Chen, X. Chen, and J. Yu, "Design of optically transparent antenna with directional radiation patterns," *Int. J. Antennas Propag.,* vol. 2017, pp. 1-7, 2017.
[197] S. Hong, Y. Kim, and C. W. Jung, "Transparent microstrip patch antennas with multilayer and metal-mesh films," *IEEE Antennas Wirel. Propag. Lett.,* vol. 16, pp. 772-775, 2017.
[198] M. S. A. Rani, S. K. A. Rahim, M. R. Kamarudin, T. Peter, S. W. Cheung, and B. M. Saad, "Electromagnetic behaviors of thin film CPW-fed CSRR loaded on UWB transparent antenna," *IEEE Antennas Wirel. Propag. Lett.,* vol. 13, pp. 1239-1242, 2014.
[199] G. Clasen and R. Langley, "Meshed patch antennas," *IEEE Trans. Antennas Propag.,* vol. 52, no. 6, pp. 1412-1416, 2004.
[200] Y. Song and C. Huang, "Research on high-performance antennas based on graphene materials," *J. Phys. Conf. Ser,* vol. 2138, no. 1, p. 12006, 2021.
[201] S. G. Kirtania, A. W. Elger, M. R. Hasan, A. Wisniewska, K. Sekhar, T. Karacolak *et al.*, "Flexible antennas: A review," *Micromachines,* vol. 11, no. 9, p. 847, 2020.
[202] X. Huang, T. Leng, K. H. Chang, J. C. Chen, K. S. Novoselov, and Z. Hu, "Graphene radio frequency and microwave passive components for low cost wearable electronics," *2D Mater.,* vol. 3, no. 2, p. 025021, 2016.
[203] T. T. Tung, S. J. Chen, C. Fumeaux, and D. Losic, "Scalable realization of conductive graphene films for high-efficiency microwave antennas," *J. Mater. Chem. C,* vol. 4, no. 45, pp. 10620-10624, 2016.
[204] D. Tang, Q. Wang, Z. Wang, Q. Liu, B. Zhang, D. He *et al.*, "Highly sensitive wearable sensor based on a flexible multi-layer graphene film antenna," *Sci. Bull.,* vol. 63, no. 9, pp. 574-579, 2018.
[205] J. Zhang, R. Song, X. Zhao, R. Fang, B. Zhang, W. Qian *et al.*, "Flexible graphene-assembled film-based antenna for wireless wearable sensor with miniaturized size and high sensitivity," *ACS Omega,* vol. 5, no. 22, pp. 12937-12943, Jun 2020.

[206] W. Wang, C. Ma, X. Zhang, J. Shen, N. Hanagata, J. Huangfu *et al.*, "High-performance printable 2.4 GHz graphene-based antenna using water-transferring technology," *Sci. Technol. Adv. Mater.,* vol. 20, no. 1, pp. 870-875, 2019.
[207] C. Fan, B. Wu, Y. Hu, Y. Zhao, and T. Su, "Millimeter-wave pattern reconfigurable Vivaldi antenna using tunable resistor based on graphene," *IEEE Trans. Antennas Propag.,* vol. 68, no. 6, pp. 4939-4943, 2020.
[208] A. Bunea, D. Neculoiu, M. Dragoman, G. Konstantinidis, and G. Deligeorgis, "X band tunable slot antenna with graphene patch," in *2015 European Microwave Conference (EuMC)*, Paris, 2015: IEEE, pp. 614-617, doi: 10.1109/EuMC.2015.7345838.
[209] M. Grande, G. V. Bianco, D. Laneve, P. Capezzuto, V. Petruzzelli, M. Scalora *et al.*, "Gain and phase control in a graphene-loaded reconfigurable antenna," *Appl. Phys. Lett.,* vol. 115, no. 13, p. 133103, 2019.
[210] N. Qasem and H. M. Marhoon, "Simulation and optimization of a tuneable rectangular microstrip patch antenna based on hybrid metal-graphene and FSS superstrate for fifth-generation applications," *Telkomnika,* vol. 18, no. 4, pp. 1719-1730, 2020.
[211] A. Hassan, S. Ali, G. Hassan, J. Bae, and C. H. Lee, "Inkjet-printed antenna on thin PET substrate for dual band Wi-Fi communications," *Microsyst. Technol.,* vol. 23, no. 8, pp. 3701-3709, 2016.
[212] Y. Zhang, S. Li, Z. Q. Yang, X. Y. Qu, and W. H. Zong, "A coplanar waveguide-fed flexible antenna for ultra-wideband applications," *Int. J. RF Microw. Comput.-Aided Eng.,* vol. 30, no. 8, 2020.
[213] W. Lin, S.-L. Chen, R. W. Ziolkowski, and Y. J. Guo, "Reconfigurable, wideband, low-profile, circularly polarized antenna and array enabled by an artificial magnetic conductor ground," *IEEE Trans. Antennas Propag.,* vol. 66, no. 3, pp. 1564-1569, 2018.
[214] J. Wang, W.-B. Lu, Z.-G. Liu, A.-Q. Zhang, and H. Chen, "Graphene-based microwave antennas with reconfigurable pattern," *IEEE Trans. Antennas Propag.,* vol. 68, no. 4, pp. 2504-2510, 2020.
[215] J. M. Kovitz, H. Rajagopalan, and Y. Rahmat-Samii, "Design and implementation of broadband MEMS RHCP/LHCP reconfigurable arrays using rotated E-shaped patch elements," *IEEE Trans. Antennas Propag.,* vol. 63, no. 6, pp. 2497-2507, 2015.
[216] W. A. Awan, S. I. Naqvi, W. A. E. Ali, N. Hussain, A. Iqbal, H. H. Tran *et al.*, "Design and realization of a frequency reconfigurable antenna with wide, dual, and single-band operations for compact sized wireless applications," *Electronics,* vol. 10, no. 11, p. 1321, 2021.
[217] I. Llatser, C. Kremers, A. Cabellos-Aparicio, J. M. Jornet, E. Alarcón, and D. N. Chigrin, "Graphene-based nano-patch antenna for terahertz radiation," *Photonics Nanostructures: Fundam. Appl.,* vol. 10, no. 4, pp. 353-358, 2012.
[218] M. Tamagnone, J. S. Gómez-Díaz, J. R. Mosig, and J. Perruisseau-Carrier, "Analysis and design of terahertz antennas based on plasmonic resonant graphene sheets," *J. Appl. Phys.,* vol. 112, no. 11, p. 114915, 2012.
[219] T. Zhou, Z. Cheng, H. Zhang, M. Le Berre, L. Militaru, and F. Calmon, "Miniaturized tunable terahertz antenna based on graphene," *Microw. Opt. Technol. Lett.,* vol. 56, no. 8, pp. 1792-1794, 2014.
[220] S. Anand, D. Sriram Kumar, R. J. Wu, and M. Chavali, "Graphene nanoribbon based terahertz antenna on polyimide substrate," *Optik,* vol. 125, no. 19, pp. 5546-5549, 2014.
[221] A. S. Thampy, M. S. Darak, and S. K. Dhamodharan, "Analysis of graphene based optically transparent patch antenna for terahertz communications," *Physica E Low Dimens. Syst. Nanostruct.,* vol. 66, pp. 67-73, 2015.
[222] M. Dashti and J. D. Carey, "Graphene microstrip patch ultrawide band antennas for THz communications," *Adv. Funct. Mater.,* vol. 28, no. 11, p. 1705925, 2018.

[223] S. Dash and A. Patnaik, "Sub-wavelength graphene planar nanoantenna for THz application," *Mater. Today: Proc.,* vol. 18, pp. 1336-1341, 2019.
[224] M. A. K. Khan, T. A. Shaem, and M. A. Alim, "Analysis of graphene based miniaturized terahertz patch antennas for single band and dual band operation," *Optik,* vol. 194, p. 163012, 2019.
[225] B. Zhang, J. Zhang, C. Liu, Z. Wu, and D. He, "Equivalent resonant circuit modeling of a graphene-based bowtie antenna," *Electronics,* vol. 7, no. 11, p. 285, 2018.
[226] I. Ahmad, S. Ullah, S. Ullah, U. Habib, S. Ahmad, A. Ghaffar *et al.*, "Design and analysis of a photonic crystal based planar antenna for THz applications," *Electronics,* vol. 10, no. 16, p. 1941, 2021.
[227] S. Anand, D. Sriram Kumar, R. J. Wu, and M. Chavali, "Analysis and design of optically transparent antenna on photonic band gap structures," *Optik,* vol. 125, no. 12, pp. 2835-2839, 2014.
[228] A. H. Radwan, M. D. Amico, and G. G. Gentili, "Reconfigurable THz Yagi antenna based on hybrid graphene-metal layout," in *2014 Loughborough Antennas and Propagation Conference (LAPC)*, Loughborough, 2014: IEEE, pp. 671-675, doi: 10.1109/LAPC.2014.6996483.
[229] Y. Wu, M. Qu, L. Jiao, Y. Liu, and Z. Ghassemlooy, "Graphene-based Yagi-Uda antenna with reconfigurable radiation patterns," *AIP Adv.,* vol. 6, no. 6, pp. 65308-065308-11, 2016.
[230] S. E. Hosseininejad, S. Abadal, M. Neshat, R. Faraji-Dana, M. C. Lemme, C. Suessmeier *et al.*, "MAC-oriented programmable terahertz PHY via graphene-based Yagi-Uda antennas," presented at the *2018 IEEE Wireless Communications and Networking Conference (WCNC)*, Barcelona, 2018.
[231] A. Oliner and A. Hessel, "Guided waves on sinusoidally-modulated reactance surfaces," *IEEE Trans. Antennas Propag.,* vol. 7, no. 5, pp. 201-208, 1959.
[232] D. A. Chu, P. W. C. Hon, T. Itoh, and B. S. Williams, "Feasibility of graphene CRLH metamaterial waveguides and leaky wave antennas," *J. Appl. Phys.,* vol. 120, no. 1, p. 13103, 2016.
[233] D. Correas-Serrano, J. S. Gomez-Diaz, D. L. Sounas, Y. Hadad, A. Alvarez-Melcon, and A. Alu, "Nonreciprocal graphene devices and antennas based on spatiotemporal modulation," *IEEE Antennas Wirel. Propag. Lett.,* vol. 15, pp. 1529-1532, 2016.
[234] S. K. Patel, V. Sorathiya, T. Guo, and C. Argyropoulos, "Graphene-based directive optical leaky wave antenna," *Microw. Opt. Technol. Lett.,* vol. 61, no. 1, pp. 153-157, 2018.
[235] S. van Berkel, E. S. Malotaux, C. De Martino, M. Spirito, D. Cavallo, A. Neto *et al.*, "Wideband double leaky slot lens antennas in CMOS technology at submillimeter wavelengths," *IEEE Trans. Terahertz Sci. Technol.,* vol. 10, no. 5, pp. 540-553, 2020.
[236] M. K. Mohsen, M. S. M. Isa, A. A. M. Isa, M. K. Abdulhameed, and M. L. Attiah, "Achieving fixed-frequency beam scanning with a microstrip leaky-wave antenna using double-gap capacitor technique," *IEEE Antennas Wirel. Propag. Lett.,* vol. 18, no. 7, pp. 1502-1506, 2019.
[237] S.-L. Chen, D. K. Karmokar, P.-Y. Qin, R. W. Ziolkowski, and Y. J. Guo, "Polarization-reconfigurable leaky-wave antenna with continuous beam scanning through broadside," *IEEE Trans. Antennas Propag.,* vol. 68, no. 1, pp. 121-133, 2020.
[238] P. Lu, T. Haddad, B. Sievert, B. Khani, S. Makhlouf, S. Dulme *et al.*, "InP-based THz beam steering leaky-wave antenna," *IEEE Trans. Terahertz Sci. Technol.,* vol. 11, no. 2, pp. 218-230, 2021.

[239] N. J. Karl, R. W. McKinney, Y. Monnai, R. Mendis, and D. M. Mittleman, "Frequency-division multiplexing in the terahertz range using a leaky-wave antenna," *Nat. Photonics,* vol. 9, no. 11, pp. 717-720, 2015.
[240] P. Lu, T. Haddad, J. Tebart, M. Steeg, B. Sievert, J. Lackmann *et al.*, "Mobile THz communications using photonic assisted beam steering leaky-wave antennas," *Opt. Express,* vol. 29, no. 14, pp. 21629-21638, 2021.
[241] T. Zvolensky, D. Chicherin, A. V. RÄIsÄNen, and C. Simovski, "Leaky-wave antenna based on micro-electromechanical systems-loaded microstrip line," *IET Microw. Antennas Propag.,* vol. 5, no. 3, pp. 357-363, 2011.
[242] K. Han, T. K. Nguyen, I. Park, and H. Han, "Terahertz Yagi-Uda antenna for high input resistance," *J. Infrared Millim. Terahertz Waves,* vol. 31, no. 4, pp. 441-454, 2009.
[243] S. Poorgholam-Khanjari, F. B. Zarrabi, and S. Jarchi, "Compact and wide-band quasi Yagi-Uda antenna based on periodic grating ground and coupling method in terahertz regime," *Optik,* vol. 203, p. 163990, 2020.
[244] Y. Torabi, G. Dadashzadeh, M. Hadeie, H. Oraizi, and A. Lalbakhsh, "A wide-angle scanning sub-terahertz leaky-wave antenna based on a multilayer dielectric image waveguide," *Electronics,* vol. 10, no. 17, p. 2172, 2021.
[245] T. Karacolak, R. V. K. G. Thirumalai, J. N. Merrett, Y. Koshka, and E. Topsakal, "Silicon carbide (SiC) antennas for high-temperature and high-power applications," *IEEE Antennas Wirel. Propag. Lett.,* vol. 12, pp. 409-412, 2013.
[246] S. E. Saddow, M. Gazziro, C. L. Frewin, S. Thomas, F. Araujo Cespedes, and E. Bernadin, "SiC for biomedical applications," *Mater. Sci. Forum,* vol. 858, pp. 1010-1014, 2016.
[247] V. Parshin, E. Serov, G. Denisov, B. Garin, R. Denisyuk, V. V'Yuginov *et al.*, "Silicon carbide for high-power applications at MM and THz ranges," *Diam. Relat. Mater.,* vol. 80, pp. 1-4, 2017.
[248] P. Rufangura, T. G. Folland, A. Agrawal, J. D. Caldwell, and F. Iacopi, "Towards low-loss on-chip nanophotonics with coupled graphene and silicon carbide: a review," *J. Phys. Mater.,* vol. 3, no. 3, p. 32005, 2020.
[249] D. Headland, Y. Monnai, D. Abbott, C. Fumeaux, and W. Withayachumnankul, "Tutorial: Terahertz beamforming, from concepts to realizations," *APL Photonics,* vol. 3, no. 5, p. 051101, May 2018.
[250] D. Berry, R. Malech, and W. Kennedy, "The reflectarray antenna," *IEEE Trans. Antennas Propag.,* vol. 11, no. 6, pp. 645-651, 1963.
[251] D. M. Pozar, *Microwave Engineering*, 4th ed. Hoboken: Wiley, 2011.
[252] L. Deng, Y. Zhang, J. Zhu, and C. Zhang, "Wide-band circularly polarized reflectarray using graphene-based Pancharatnam-Berry phase unit-cells for terahertz communication," *Materials,* vol. 11, no. 6, p. 956, Jun 2018.
[253] J. Zhang, H. Zhang, W. Yang, K. Chen, X. Wei, Y. Feng *et al.*, "Dynamic scattering steering with graphene-based coding metamirror," *Adv. Opt. Mater.,* vol. 8, no. 19, pp. 2000683-n/a, 2020.
[254] M. Tamagnone, S. Capdevila, A. Lombardo, J. Wu, A. Centeno, A. Zurutuza *et al.*, "Graphene reflectarray metasurface for terahertz beam steering and phase modulation," ed. arXiv:1806.02202, 2018.
[255] L. Deng, Y. Wu, C. Zhang, W. Hong, B. Peng, J. Zhu *et al.*, "Manipulating of different-polarized reflected waves with graphene-based plasmonic metasurfaces in terahertz regime," *Sci. Rep.,* vol. 7, no. 1, p. 10558, Sep 2017.
[256] E. Carrasco, M. Tamagnone, and J. Perruisseau-Carrier, "Tunable graphene reflective cells for THz reflectarrays and generalized law of reflection," *Appl. Phys. Lett.,* vol. 102, no. 10, p. 104103, 2013.

[257] E. Carrasco and J. Perruisseau-Carrier, "Reflectarray antenna at terahertz using graphene," *IEEE Antennas Wirel. Propag. Lett.,* vol. 12, pp. 253-256, 2013.
[258] H. Chen, W.-B. Lu, Z.-G. Liu, and M.-Y. Geng, "Microwave programmable graphene metasurface," *ACS Photonics,* vol. 7, no. 6, pp. 1425-1435, 2020.
[259] H. Chen, Z. Liu, W. Lu, A. Zhang, X. Li, and J. Zhang, "Microwave beam reconfiguration based on graphene ribbon," *IEEE Trans. Antennas Propag.,* vol. 66, no. 11, pp. 6049-6056, 2018.
[260] S. R. Biswas, C. E. Gutiérrez, A. Nemilentsau, I.-H. Lee, S.-H. Oh, P. Avouris *et al.*, "Tunable graphene metasurface reflectarray for cloaking, illusion, and focusing," *Phys. Rev. Appl.,* vol. 9, no. 3, p. 034021, 2018.
[261] S. Han, S. Kim, S. Kim, T. Low, V. W. Brar, and M. S. Jang, "Complete complex amplitude modulation with electronically tunable graphene plasmonic metamolecules," *ACS Nano,* vol. 14, no. 1, pp. 1166-1175, Jan 2020.
[262] Z. Sun, F. Huang, and Y. Fu, "Graphene-based active metasurface with more than 330° phase tunability operating at mid-infrared spectrum," *Carbon,* vol. 173, pp. 512-520, 2021.
[263] B. Munk, *Frequency Selective Surfaces Theory and Design*. New York: Wiley, 2005.
[264] S. A. Kuznetsov, M. A. Astafev, M. Beruete, and M. Navarro-Cía, "Planar holographic metasurfaces for terahertz focusing," *Sci. Rep.,* vol. 5, no. 1, pp. 7738-7738, 2015.
[265] H. Hasani, M. Tamagnone, S. Capdevila, C. F. Moldovan, P. Maoddi, A. M. Ionescu *et al.*, "Tri-band, polarization-independent reflectarray at terahertz frequencies: Design, fabrication, and measurement," *IEEE Trans. Terahertz Sci. Technol.,* vol. 6, no. 2, pp. 268-277, 2016.
[266] Z. Ma, S. M. Hanham, P. Albella, B. Ng, H. T. Lu, Y. Gong *et al.*, "Terahertz all-dielectric magnetic mirror metasurfaces," *ACS Photonics,* vol. 3, no. 6, pp. 1010-1018, 2016.
[267] S. V. Hum, M. Okoniewski, and R. J. Davies, "Realizing an electronically tunable reflectarray using varactor diode-tuned elements," *IEEE Microw. Wirel. Compon. Lett.,* vol. 15, no. 6, pp. 422-424, 2005.
[268] O. Bayraktar, O. A. Civi, and T. Akin, "Beam switching reflectarray monolithically integrated with RF MEMS switches," *IEEE Trans. Antennas Propag.,* vol. 60, no. 2, pp. 854-862, 2012.
[269] G. Perez-Palomino, P. Baine, R. Dickie, M. Bain, J. A. Encinar, R. Cahill *et al.*, "Design and experimental validation of liquid crystal-based reconfigurable reflectarray elements with improved bandwidth in F-band," *IEEE Trans. Antennas Propag.,* vol. 61, no. 4, pp. 1704-1713, 2013.
[270] L. Dai, B. Wang, M. Wang, X. Yang, J. Tan, S. Bi *et al.*, "Reconfigurable intelligent surface-based wireless communications: antenna design, prototyping, and experimental results," *IEEE Access,* vol. 8, pp. 45913-45923, 2020.
[271] C. Huang, A. Zappone, G. C. Alexandropoulos, M. Debbah, and C. Yuen, "Reconfigurable intelligent surfaces for energy efficiency in wireless communication," *IEEE Trans. Wirel. Commun.,* vol. 18, no. 8, pp. 4157-4170, 2019.
[272] Y.-L. Xu, X.-C. Wei, and E.-P. Li, "Three-dimensional tunable frequency selective surface based on vertical graphene micro-ribbons," *J. Electromagn. Waves Appl.,* vol. 29, no. 16, pp. 2130-2138, 2015.
[273] S. AbdollahRamezani, K. Arik, S. Farajollahi, A. Khavasi, and Z. Kavehvash, "Beam manipulating by gate-tunable graphene-based metasurfaces," *Opt. Lett.,* vol. 40, no. 22, pp. 5383-6, Nov 2015.

[274] Y. Liu, X. Xu, D. Yang, X. Zhang, M. Ren, N. Gong *et al.*, "Multifunctional and tunable trigate graphene metamaterial with “Lakes of Wada” topology," *Opt. Express,* vol. 28, no. 17, pp. 24772-24788, 2020.
[275] M. R. Tavakol and A. Khavasi, "Reconfigurable meta-coupler employing hybrid metal-graphene metasurfaces," *Sci. Rep.,* vol. 10, no. 1, p. 7684, May 2020.
[276] T. Guo and C. Argyropoulos, "Broadband polarizers based on graphene metasurfaces," *Opt. Lett.,* vol. 41, no. 23, pp. 5592-5595, Dec 2016.
[277] J. Neu, R. Beigang, and M. Rahm, "Metamaterial-based gradient index beam steerers for terahertz radiation," *Appl. Phys. Lett.,* vol. 103, no. 4, p. 41109, 2013.
[278] S. Liu, Q. Cheng, Q. Xu, T. Q. Wang, L. L. Du, K. Luan *et al.*, "Free-standing metasurfaces for high-efficiency transmitarrays for controlling terahertz waves," *Adv. Opt. Mater.,* vol. 4, no. 3, pp. 384-390, 2016.
[279] M. Wang, S. Xu, F. Yang, N. Hu, W. Xie, and Z. Chen, "A novel 1-Bit reconfigurable transmitarray antenna using a C-shaped probe-fed patch element with broadened bandwidth and enhanced efficiency," *IEEE Access,* vol. 8, pp. 120124-120133, 2020.
[280] S. K. Hong, K. Y. Kim, T. Y. Kim, J. H. Kim, S. W. Park, J. H. Kim *et al.*, "Electromagnetic interference shielding effectiveness of monolayer graphene," *Nanotechnology,* vol. 23, no. 45, p. 455704, Oct 2012.
[281] O. Balci, E. O. Polat, N. Kakenov, and C. Kocabas, "Graphene-enabled electrically switchable radar-absorbing surfaces," *Nat. Commun.,* vol. 6, no. 1, p. 6628, Mar 2015.
[282] C. M. Watts, X. Liu, and W. J. Padilla, "Metamaterial electromagnetic wave absorbers," *Adv. Mater.,* vol. 24, no. 23, pp. OP98-OP120, 2012.
[283] X. Ying, Y. Pu, Z. Li, Z. Liu, and Y. Jiang, "Absorption enhancement of graphene Salisbury screen in the mid-infrared regime," *J. Opt.,* vol. 44, no. 1, pp. 59-67, Mar 2015.
[284] B. Wu, H. M. Tuncer, M. Naeem, B. Yang, M. T. Cole, W. I. Milne *et al.*, "Experimental demonstration of a transparent graphene millimetre wave absorber with 28% fractional bandwidth at 140 GHz," *Sci. Rep.,* vol. 4, no. 1, p. 4130, Feb 2014.
[285] S. Barzegar-Parizi, "Realization of wide-angle and wideband absorber using metallic and graphene-based metasurface for mid-infrared and low THz frequency," *Opt. Quantum Electron.,* vol. 50, no. 10, pp. 1-12, 2018.
[286] O. Balci, N. Kakenov, and C. Kocabas, "Controlling phase of microwaves with active graphene surfaces," *Appl. Phys. Lett.,* vol. 110, no. 16, p. 161102, 2017.
[287] J. Zhang, X. Wei, M. Premaratne, and W. Zhu, "Experimental demonstration of an electrically tunable broadband coherent perfect absorber based on a graphene-electrolyte-graphene sandwich structure," *Photonics Res.,* vol. 7, no. 8, pp. 868-874, Aug 2019.
[288] C. Huang, J. Song, C. Ji, J. Yang, and X. Luo, "Simultaneous control of absorbing frequency and amplitude using graphene capacitor and active frequency-selective surface," *IEEE Trans. Antennas Propag.,* vol. 69, no. 3, pp. 1793-1798, 2021.
[289] J. Zhang, X. Wei, I. D. Rukhlenko, H.-T. Chen, and W. Zhu, "Electrically tunable metasurface with independent frequency and amplitude modulations," *ACS Photonics,* vol. 7, no. 1, pp. 265-271, 2020.
[290] R. Alaee, M. Farhat, C. Rockstuhl, and F. Lederer, "A perfect absorber made of a graphene micro-ribbon metamaterial," *Opt. Express,* vol. 20, no. 27, pp. 28017-24, Dec 2012.
[291] A. Andryieuski and A. V. Lavrinenko, "Graphene metamaterials based tunable terahertz absorber: effective surface conductivity approach," *Opt. Express,* vol. 21, no. 7, pp. 9144-55, Apr 2013.

[292] A. Ahmadivand, R. Sinha, M. Karabiyik, P. K. Vabbina, B. Gerislioglu, S. Kaya *et al.*, "Tunable THz wave absorption by graphene-assisted plasmonic metasurfaces based on metallic split ring resonators," *J. Nanopart. Res.,* vol. 19, no. 1, pp. 1-14, 2016.
[293] S. K. Ghosh, S. Das, and S. Bhattacharyya, "Graphene based metasurface with near unity broadband absorption in the terahertz gap," *Int. J. RF Microw. Comput.-Aided Eng.,* vol. 30, no. 12, p. 22436, 2020.
[294] L. La Spada and L. Vegni, "Metamaterial-based wideband electromagnetic wave absorber," *Opt. Express,* vol. 24, no. 6, pp. 5763-72, Mar 2016.
[295] C. Lu, Q. Fu, S. Huang, and J. Liu, "Polymer electrolyte-gated carbon nanotube field-effect transistor," *Nano Lett.,* vol. 4, no. 4, pp. 623-627, 2004.
[296] L. P. Wang and Z. M. Zhang, "Phonon-mediated magnetic polaritons in the infrared region," *Opt. Express,* vol. 19, no. S2, pp. A126-35, Mar 2011.
[297] J. Yan, M. H. Kim, J. A. Elle, A. B. Sushkov, G. S. Jenkins, H. M. Milchberg *et al.*, "Dual-gated bilayer graphene hot-electron bolometer," *Nat. Nanotechnol.,* vol. 7, no. 7, pp. 472-8, Jun 2012.
[298] S. Yuan, R. Yu, C. Ma, B. Deng, Q. Guo, X. Chen *et al.*, "Room temperature graphene mid-infrared bolometer with a broad operational wavelength range," *ACS Photonics,* vol. 7, no. 5, pp. 1206-1215, 2020.
[299] G. Skoblin, J. Sun, and A. Yurgens, "Graphene bolometer with thermoelectric readout and capacitive coupling to an antenna," *Appl. Phys. Lett.,* vol. 112, no. 6, p. 63501, 2018.
[300] F. H. Koppens, T. Mueller, P. Avouris, A. C. Ferrari, M. S. Vitiello, and M. Polini, "Photodetectors based on graphene, other two-dimensional materials and hybrid systems," *Nat. Nanotechnol.,* vol. 9, no. 10, pp. 780-93, Oct 2014.
[301] M. Dyakonov and M. Shur, "Detection, mixing, and frequency multiplication of terahertz radiation by two-dimensional electronic fluid," *IEEE Trans. Electron Devices,* vol. 43, no. 3, pp. 380-387, 1996.
[302] M. Amiri, F. Tofigh, N. Shariati, J. Lipman, and M. Abolhasan, "Wide-angle metamaterial absorber with highly insensitive absorption for TE and TM modes," *Sci. Rep.,* vol. 10, no. 1, pp. 13638-13638, 2020.
[303] G. Deng, H. Hu, H. Mo, J. Xu, Z. Yin, H. Lu *et al.*, "Tunable terahertz metamaterial wideband absorber with liquid crystal," *Opt. Mater. Express,* vol. 11, no. 12, pp. 4026-4035, Dec 2021.
[304] Z. Ren, L. Cheng, L. Hu, C. Liu, C. Jiang, S. Yang *et al.*, "Photoinduced broad-band tunable terahertz absorber based on a VO2 thin film," *ACS Appl. Mater. Interfaces,* vol. 12, no. 43, pp. 48811-48819, 2020.
[305] E. J. Lee, K. Balasubramanian, R. T. Weitz, M. Burghard, and K. Kern, "Contact and edge effects in graphene devices," *Nat. Nanotechnol.,* vol. 3, no. 8, pp. 486-90, Aug 2008.
[306] F. Xia, T. Mueller, Y. M. Lin, A. Valdes-Garcia, and P. Avouris, "Ultrafast graphene photodetector," *Nat. Nanotechnol.,* vol. 4, no. 12, pp. 839-43, Dec 2009.
[307] N. M. Gabor, J. C. Song, Q. Ma, N. L. Nair, T. Taychatanapat, K. Watanabe *et al.*, "Hot carrier-assisted intrinsic photoresponse in graphene," *Science,* vol. 334, no. 6056, pp. 648-52, Nov 2011.
[308] F. Bianco, D. Perenzoni, D. Convertino, S. L. De Bonis, D. Spirito, M. Perenzoni *et al.*, "Terahertz detection by epitaxial-graphene field-effect-transistors on silicon carbide," *Appl. Phys. Lett.,* vol. 107, no. 13, p. 131104, 2015.
[309] D. A. Bandurin, D. Svintsov, I. Gayduchenko, S. G. Xu, A. Principi, M. Moskotin *et al.*, "Resonant terahertz detection using graphene plasmons," *Nat. Commun.,* vol. 9, no. 1, p. 5392, Dec 2018.

[310] A. El Fatimy, A. Nath, B. D. Kong, A. K. Boyd, R. L. Myers-Ward, K. M. Daniels *et al.*, "Ultra-broadband photodetectors based on epitaxial graphene quantum dots," *Nanophotonics,* vol. 7, no. 4, pp. 735-740, 2018.
[311] R. M. G K, P. Deshmukh, S. S. Prabhu, and P. K. Basu, "Antenna coupled graphene-FET as ultra-sensitive room temperature broadband THz detector," *AIP Adv.,* vol. 8, no. 12, pp. 125122-125122-7, 2018.
[312] A. Zak, M. A. Andersson, M. Bauer, J. Matukas, A. Lisauskas, H. G. Roskos *et al.*, "Antenna-integrated 0.6 THz FET direct detectors based on CVD graphene," *Nano Lett.,* vol. 14, no. 10, pp. 5834-8, Oct 2014.
[313] W. Miao, H. Gao, Z. Wang, W. Zhang, Y. Ren, K. M. Zhou *et al.*, "A graphene-based terahertz hot electron bolometer with Johnson noise readout," *J. Low Temp. Phys.,* vol. 193, no. 3-4, pp. 387-392, 2018.
[314] D. Spirito, D. Coquillat, S. L. De Bonis, A. Lombardo, M. Bruna, A. C. Ferrari *et al.*, "High performance bilayer-graphene terahertz detectors," *Appl. Phys. Lett.,* vol. 104, no. 6, p. 61111, 2014.
[315] S. Cakmakyapan, P. K. Lu, A. Navabi, and M. Jarrahi, "Gold-patched graphene nano-stripes for high-responsivity and ultrafast photodetection from the visible to infrared regime," *Light Sci. Appl.,* vol. 7, no. 1, p. 20, 2018.
[316] E. D. Walsh, W. Jung, G. H. Lee, D. K. Efetov, B. I. Wu, K. F. Huang *et al.*, "Josephson junction infrared single-photon detector," *Science,* vol. 372, no. 6540, pp. 409-412, Apr 2021.
[317] W. Li, J. Wang, J. Gou, Z. Huang, and Y. Jiang, "Fabrication and characterization of linear terahertz detector arrays based on lithium tantalate crystal," *J. Infrared Millim. Terahertz Waves,* vol. 36, no. 1, pp. 42-48, 2015.
[318] A. W. M. Lee, B. S. Williams, S. Kumar, H. Qing, and J. L. Reno, "Real-time imaging using a 4.3-THz quantum cascade laser and a 320 /spl times/ 240 microbolometer focal-plane array," *IEEE Photon. Technol. Lett.,* vol. 18, no. 13, pp. 1415-1417, 2006.
[319] L.-J. Xu, F.-C. Tong, X. Bai, and Q. Li, "Design of miniaturised on-chip slot antenna for THz detector in CMOS," *IET Microw. Antennas Propag.,* vol. 12, no. 8, pp. 1324-1331, 2018.
[320] F. Schuster, D. Coquillat, H. Videlier, M. Sakowicz, F. Teppe, L. Dussopt *et al.*, "Broadband terahertz imaging with highly sensitive silicon CMOS detectors," *Opt. Express,* vol. 19, no. 8, pp. 7827-7832, 2011.
[321] D. Čibiraitė-Lukenskienė, K. Ikamas, T. Lisauskas, V. Krozer, H. G. Roskos, and A. Lisauskas, "Passive detection and imaging of human body radiation using an uncooled field-effect transistor-based THZ detector," *Sensors,* vol. 20, no. 15, pp. 1-14, 2020.
[322] A. Pradeepkumar, M. Zielinski, M. Bosi, G. Verzellesi, D. K. Gaskill, and F. Iacopi, "Electrical leakage phenomenon in heteroepitaxial cubic silicon carbide on silicon," *J. Appl. Phys.,* vol. 123, no. 21, p. 215103, 2018.
[323] L. G. Cançado, K. Takai, T. Enoki, M. Endo, Y. A. Kim, H. Mizusaki *et al.*, "General equation for the determination of the crystallite size L a of nanographite by Raman spectroscopy," *Appl. Phys. Lett.,* vol. 88, no. 16, pp. 163106-163106-3, 2006.
[324] A. Mancini, L. Nan, F. J. Wendisch, R. Berté, H. Ren, E. Cortés *et al.*, "Near-field retrieval of the surface phonon polariton dispersion in free-standing silicon carbide thin films," *ACS Photonics,* vol. 9, no. 11, pp. 3696-3704, 2022.
[325] G. Hu, Q. Ou, G. Si, Y. Wu, J. Wu, Z. Dai *et al.*, "Topological polaritons and photonic magic angles in twisted α-MoO3 bilayers," *Nature,* vol. 582, no. 7811, pp. 209-213, Jun 2020.
[326] L. Huang, D. Zhang, F. H. Zhang, Z. H. Feng, Y. D. Huang, and Y. Gan, "High-contrast SEM Imaging of supported few-layer graphene for differentiating distinct layers and

sesolving fine features: There is plenty of room at the bottom," *Small,* vol. 14, no. 22, pp. e1704190-n/a, 2018.
[327] R. Hillenbrand, T. Taubner, and F. Keilmann, "Phonon-enhanced light–matter interaction at the nanometre scale," *Nature,* vol. 418, no. 6894, pp. 159-162, Jul 2002.
[328] R. Simons, *Coplanar Waveguide Circuits, Components, and Systems* (Wiley Series in Microwave and Optical Engineering ; 152). Hoboken: Wiley, 2001.
[329] S. Gevorgian, L. J. P. Linner, and E. L. Kollberg, "CAD models for shielded multilayered CPW," *IEEE Trans. Microwave Theory Tech.,* vol. 43, no. 4, pp. 772-779, 1995.
[330] T. C. Edwards and M. B. Steer, *Foundations for Microstrip Circuit Design*, 4th ed. (Wiley - IEEE). Chichester: Wiley-IEEE Press, 2016.
[331] D. A. Katzmarek, Y. Yang, M. B. Ghasemian, K. Kalantar-Zadeh, R. W. Ziolkowski, and F. Iacopi, "Characteristics of epitaxial graphene on SiC/Si substrates in the radio frequency spectrum," *IEEE Electron Device Lett.,* vol. 44, pp. 297-300, Feb 2023.
[332] W. R. Eisenstadt and Y. Eo, "S-parameter-based IC interconnect transmission line characterization," *IEEE Trans. Components, Hybrids Manuf. Technol.,* vol. 15, no. 4, pp. 483-490, Aug 1992.
[333] J. A. Robinson, M. LaBella, M. Zhu, M. Hollander, R. Kasarda, Z. Hughes *et al.*, "Contacting graphene," *Appl. Phys. Lett.,* vol. 98, no. 5, pp. 053103-053103-3, 2011.
[334] D. W. Yue, C. H. Ra, X. C. Liu, D. Y. Lee, and W. J. Yoo, "Edge contacts of graphene formed by using a controlled plasma treatment," *Nanoscale,* 10.1039/C4NR05725B vol. 7, no. 2, pp. 825-831, Nov 2014.
[335] W. S. Leong, C. T. Nai, and J. T. L. Thong, "What does annealing do to metal–graphene contacts?," *Nano Lett.,* vol. 14, no. 7, pp. 3840-3847, Jul 2014.
[336] J. Yang, P. Hu, and G. Yu, "Perspective of graphene-based electronic devices: Graphene synthesis and diverse applications," *APL Mater.,* vol. 7, no. 2, p. 020901, Feb 2019.
[337] X. c. Wang, A. Díaz-Rubio, and S. Tretyakov, "Microwave and millimeter-wave characterization of conductive ink film in rectangular waveguide," in *2017 47th European Microwave Conference (EuMC)*, 2017, pp. 843-846, doi: 10.23919/EuMC.2017.8230976.
[338] X. Yang, X. Liu, S. Yu, L. Gan, J. Zhou, and Y. Zeng, "Permittivity of undoped silicon in the millimeter wave range," *Electronics,* vol. 8, no. 8, p. 886, 2019.
[339] X. C. Wang, A. Díaz-Rubio, and S. A. Tretyakov, "An Accurate Method for Measuring the Sheet Impedance of Thin Conductive Films at Microwave and Millimeter-Wave Frequencies," *IEEE Trans. Microwave Theory Tech.,* vol. 65, no. 12, pp. 5009-5018, 2017.
[340] A. Abbosh, "Accurate effective permittivity calculation of printed center-fed dipoles and its application to quasi Yagi-Uda antennas," *IEEE Trans. Antennas Propag.,* vol. 61, no. 4, pp. 2297-2300, 2013.
[341] M. A. Ordal, L. L. Long, R. J. Bell, S. E. Bell, and R. R. Bell, "Optical Properties of the Metals Al, Co, Cu, Au, Fe, Pb, Ni, Pd, Pt, Ag, Ti and W in the Infrared and Far Infrared," *Appl. Opt.,* vol. 22, pp. 1099-1119, 1983.
[342] R. D. Mansano, P. Verdonck, H. S. Maciel, and M. Massia, "Anisotropic inductively coupled plasma etching of silicon with pure SF6," *Thin Solid Films,* vol. 343-344, pp. 378-380, Apr 1999.
[343] N. F. M. Nasir, C. M. Shah, P. W. Leech, G. K. Reeves, E. Pirogova, T. Istivan *et al.*, "Fabrication of 3C-silicon carbide membranes: Towards development of novel microdevices for biomedical applications," in *2012 International Conference on*

Biomedical Engineering (ICoBE), 2012, pp. 589-593, doi: 10.1109/ICoBE.2012.6178985.

[344] H. Hu, F. Zhai, D. Hu, Z. Li, B. Bai, X. Yang *et al.*, "Broadly tunable graphene plasmons using an ion-gel top gate with low control voltage," *Nanoscale,* vol. 7, no. 46, pp. 19493-19500, 2015.